UNIVERSITY OF CALIFORNIA, SAN DIEGO

Central and South Pacific Plate Tectonic Reconstructions

A dissertation submitted in partial satisfaction of the requirements for the degree of

Doctor of Philosophy

in

Earth Sciences

by

Marcel Bernard Croon

Committee in charge:

Steven C. Cande, Chair
Donna K. Blackman
Jeffrey S. Gee
Laurence B. Milstein
David T. Sandwell

2011

The Dissertation of Marcel Bernard Croon is approved, and it is acceptable in quality and form for publication on microfilm and electronically:

_____

_____

_____

_____

_____
Chair

University of California, San Diego

2011

To Rose,
for many, many reasons

EPIGRAPH

The happiness of your life depends upon the quality of your thoughts.

Marcus Aurelius

TABLE OF CONTENTS

LIST OF FIGURES AND TABLES

ACKNOWLEDGMENTS

As a graduate student at Scripps I have met many wonderful people along the way, who have provided assistance, guidance, encouragement and friendship. I would like to thank first and foremost, my committee members for helping me with my research projects and for giving feedback on the dissertation manuscript. I am very grateful to Donna Blackman and Dave Sandwell, who have given me valuable advise on how to interpret ridge-transform-intersections. In particular, Jeff Gee was of invaluable assistance for the Central Pacific plate reconstruction project. I relied on him heavily. My advisor, Steve Cande, has had the largest impact on my development as a scientist and I have learned a tremendous amount from him: how to maximize valuable ship time, interpreting marine magnetic anomalies and how to write concise scientific publications.

Numerous other people at GRD and the SIO Graduate Office were there for all the more mundane aspects of surviving graduate school. The many friends I have met at Scripps have made my stay in sunny San Diego near the beach pleasant and I will miss the get-togethers.

Finally, I wish to thank my family and in particular my wife, Rose, for providing love and support throughout the years.

The first two chapters have been published:

Croon, M. B., S. C. Cande, and J. M. Stock (2008), Revised Pacific-Antarctic plate motions and geophysics of the Menard Fracture Zone, *Geochemistry Geophysics Geosystems, 9*, Q07001, DOI: 10.1029/2008gc002019.

Croon, M. B., S. C. Cande, and J. M. Stock (2010), Abyssal hill deflections at Pacific-Antarctic ridge-transform intersections, *Geochemistry Geophysics Geosystems, 11*, Q11004, DOI: 10.1029/2010gc003236.

VITA

2000	Bachelor and Master of Science, Free University Amsterdam, The Netherlands
2000-2004	Geologist and Geotechnical Engineer, Fugro Engineers B.V., Leidschendam, The Netherlands
2011	Doctor of Philosophy, University of California, San Diego

PUBLICATIONS

Croon, M. B., Hillier, J. K., and Sclater, J. G. (2011), Comment on “Mantle Flow Drives the Subsidence of Oceanic Plates”, *Science*, DOI: 10.1126/science.1193587.

Croon, M. B., S. C. Cande, and J. M. Stock (2010), Abyssal Hill Deflections at Pacific-Antarctic Ridge-Transform Intersections, *Geochemistry Geophysics Geosystems*, DOI: 10.1029/2010GC003236.

Croon, M. B., S. C. Cande, and J. M. Stock (2008), Revised Pacific-Antarctic plate motions and geophysics of the Menard Fracture Zone, *Geochemistry Geophysics Geosystems, 9*, Q07001, DOI: 10.1029/2008gc002019.

FIELDS OF STUDY

Studies in Plate Tectonic Reconstructions
Professor Steven C. Cande

Studies in Marine Geomagnetics
Professors Steven C. Cande and Jeffrey S. Gee

ABSTRACT OF THE DISSERTATION

Central and South Pacific Plate Tectonic Reconstructions

By

Marcel Bernard Croon

Doctor of Philosophy in Earth Sciences

University of California, San Diego, 2011

Professor Steven C. Cande, Chair

Several aspects of the plate tectonic evolution of the ridge systems and structural development of oceanic crust in the Central and South Pacific basins are investigated. In the South Pacific surveys of magnetic anomaly data and multibeam bathymetry of the Menard and Pitman Fracture Zones, ~3500 km apart, allowed for significant refinement of the Pacific-Antarctic plate motion history over the last 44 million years. We tested the predictive quality of the high-resolution plate motion model at the southwestern end of the Pacific-Antarctic Ridge close to the Macquarie Triple Junction and showed that reconstructions predict phases of transform fault motion and extension to great detail. In particular, the most recent period of extension since 10 million years ago occurred when a ~1200 km long transform fault was replaced an array of 15 transform faults and short spreading centers.

The detailed plate motion model for the Pacific-Antarctic Ridge was used to test whether abyssal hill tip curvatures correlate to changes in plate motion direction, which lead to periods of transtension and transpression. The tip of the ridge axis can deflect up to 60° into the transform fault in response to changes in the stress field at ridge-transform-intersections. This is observed to have occurred in particular during periods of significant transtension. In addition, abyssal hill curvatures in the opposite sense are observed to have developed during periods of transpression when increased coupling across an oceanic transform fault is partially accommodated by distributed strike-slip deformation rather than solely by discontinuous displacement at the transform fault.

In the equatorial Pacific region, where the total field magnetic anomalies are very small for oceanic crust formed at the North-South striking East Pacific Rise, towed and aeromagnetic vector magnetometer data allowed for better constraints of the relative motions of the Pacific-Cocos Ridge near the Galapagos Triple Junction. These data in combination with available magnetic anomaly profiles for most of the East Pacific ridge were used to improve plate reconstructions for the Pacific-Cocos, Pacific-Nazca, Cocos-Nazca, Pacific-Antarctic, Chile Ridge and Mathematician Paleo-Ridge since 9 Ma.

INTRODUCTION

AN INTRODUCTION TO PLATE TECTONICS

Plate tectonics refers to how the Earth's surface is composed of rigid plates on top of hotter more mobile mantle material. The idea that the lithosphere forms a strong thermal boundary layer on top of a convecting system led to linear models for mantle convection [e.g., *McKenzie et al.*, 1973], which agreed well with observations of seafloor bathymetry and heat flow [*Sclater and Francheteau*, 1970; *Sclater et al.*, 1971].

Hess [1962] and *Dietz* [1961] suggested that seafloor is created at mid-oceanic ridges, spreads away with age and is subducted in trenches. Based on this concept, *Wilson* [1965] proposed that active mobile belts, where plates are created at ridges and destroyed at trenches marked by active seismicity, separate the Earth into a set of rigid tectonic plates. Specifically, *Vine and Matthews* [1963] supported the idea of seafloor spreading with marine magnetic anomaly data. Building on the seafloor spreading hypothesis and the remarkable symmetry found in a magnetic anomaly profile across the Pacific-Antarctic Ridge [*Pitman and Heirtzler*, 1966], the first geomagnetic polarity time scale was proposed by *Heirtzler et al.* [1968].

When the concept that tectonic plates are internally rigid is valid, Euler's theorem allows us to model the relative motions between plates quantitatively. In Euler's theorem the motion of a plate, which is the rigid cap at the surface of a sphere, can be described by the rotation about a virtual axis that passes through the center of the sphere. The intersection of the rotation axis with the Earth defines the Euler pole rotation and the angular velocity vector describes the plate motions.

RELATIVE PLATE MOTIONS

Present-day plate motions can be accurately measured in real time using satellite technology. However, constraining the relative motion between two tectonic plates in the geologic past can be a challenging task. *Bullard et al.* [1965] constructed a computer-generated quantitative model, which involved fitting the pre-breakup coastlines on either side of the Atlantic ocean. *Hellinger* [1981] proposed a more advanced method with fitting criteria determined by dividing the data into multiple segments and fitting great circles to reconstructed data in each segment. Magnetic anomalies and fracture zone crossings define the segments. Fracture zone segments, located between the same magnetic isochron on either side, are typically identified by following their trace on a map with mulitbeam bathymetry data or, when not available, on a map with the less accurate (for this task) satellite-derived, free-air gravity field [*Sandwell and Smith*, 2009]. Fracture zones are ideally represented by small circles, but with the exception of some very long offsets, the difference between small and great circle segments is negligible for most fracture zones. Great circle segments are easier to handle computationally and are used in the *Hellinger* [1981] method. This method heavily relies on the correct identification of data points that belong to the same isochron and are part of the same segment on both conjugate plates. The resulting reconstructed rotation pole is computed by minimization of the sum of misfits between conjugate magnetic anomaly and fracture zone segments. The method of *Hellinger* [1981] was implemented by *Chang* [1987; 1988] and *Royer and Chang* [1991] to describe the uncertainties of a rotation by a covariance matrix. The advantage of this method is that uncertainties in a rotation are expressed in terms of the

deviations of the rotation from the best-fitting rotation, which is reflected by the size of an ellipse-shaped confidence region, where a smaller region represents a better fit.

SEAFLOOR MORPHOLOGY, THE STRESS FIELD AND CHANGES IN RELATIVE PLATE MOTIONS

The three main types of plate boundaries that separate tectonic plates are: (1) divergent boundaries where new crust is generated as plates are pulled apart, (2) convergent boundaries where crust is destroyed and recycled back into the earth interior at subduction zones and (3) transform fault boundaries where two plates slip horizontally past each other. The concept of transform faults, which offset active spreading ridges, originated with *Wilson* [1965]. Diffuse deformation at mid-ocean ridges only occurs in few restricted places [*Gordon*, 2000]. It is therefore assumed that the oceanic upper lithosphere behaves rigidly except at oceanic plate boundaries, which are typically narrow zones of deformation. Although most deformation is localized in these narrow boundaries, additional broad zones of deformation occur within traditionally defined plates, e.g., within a large part of the Indo-Australia plate [*Jellinek et al.*, 2006]. *Fujita and Sleep* [1978] used an anisotropic two-dimensional finite element model to examine the response of the stress field around ridge-transform intersections to changes in the direction of regional stress. Based on earthquake focal mechanisms the largest component of the horizontal stress field is typically ridge-perpendicular near mid-oceanic ridge axes [*Sykes*, 1967]. However, at ridge-transform intersections and non-transform offsets, the tensile stresses are often strongly deviated [*Crane*, 1976; *Lonsdale*, 1978; *Tucholke and Schouten*, 1988] up to 45° [*Grindlay et al.*, 1991; *Haxby and Parmentier*, 1988; *Karson and Dick*, 1983; *Searle and Laughton*, 1977; *Searle*, 1986], which is

typically associated with strike-slip shear stresses along the transform fault [*Fujita and Sleep*, 1978; *Grindlay and Fox*, 1993; *Phipps Morgan and Parmentier*, 1984] or normal stresses related to the transform [*Gudmundsson*, 1993]. Changes in the direction of regional stress, as suggested by a change in direction of relative plate motion [*Menard and Atwater*, 1968], lead to a period of extension at a clockwise change in direction of motion and compression at a counterclockwise change for a right-stepping offset. Since the availability of multibeam data, it has become practical to make high-resolution maps of the seafloor, allowing for detailed analysis of seafloor structures such as normal faults, median ridges and abyssal hill structures, which can be associated with the changes in the stress field at ridge-transform interactions. This allows for comparison of a model of relative plate motion to seafloor structures observed from shipboard bathymetry data to better understand these observations.

THESIS APPROACH

In this thesis I investigate the relative plate motions of Central and South Pacific ridge systems and the structural development of the oceanic crust near ridge-transform intersections associated with changes in these plate motions. For the Pacific-Antarctic Ridge (Chapter 1) refinement of rotation parameters is based primarily on a detailed geophysical survey of the Pitman fracture zone (FZ) in combination with extensive new shipboard magnetic anomaly and multibeam bathymetry data along the right-stepping Menard FZ, which developed at the northern side of the Pacific-Antarctic Ridge since ~44 million years ago. Data from these two fracture zones in particular allows for analysis of changes in plate motions along the Pacific-Antarctic Ridge in great detail.

The Pacific-Antarctic Ridge, where the oceanic crust morphology at Menard and Pitman FZs is clearly visible in the multibeam bathymetry data, is an excellent plate pair to study the correlation between adjustments in relative plate motion direction and seafloor structures associated with changes in the stress field. In particular, the nature and magnitude of abyssal hill tip deflections at ridge-transform intersections responds to these changes. In Chapter 2 I analyze abyssal hill deflections at the Pacific-Antarctic Ridge and compare the observed trends in changes in abyssal hill curvature with the relative plate motion model in order to determine which geologic processes and what parameters are responsible for the observed abyssal hill morphology.

In Chapter 3 I use the available magnetic anomaly data to better understand the complex relative plate motions between the Pacific, Cocos, Nazca and Antarctic plates since ~9 million years ago. This is challenging since a large part of that study area is located near the magnetic equator (~7°S). Total field magnetic anomalies are very small at low magnetic latitudes when formed at approximately north-south striking bodies such as the East Pacific Rise. To address this problem I evaluate and use towed and aero vector magnetic data, for which the component anomalies are significantly larger near the magnetic equator. I include the extra magnetic anomaly identifications from these data to better constrain the plate reconstruction model. This analysis includes 3-plate solutions for the Pacific-Nazca-Antarctic and the Pacific-Cocos-Nazca circuits. A 3-plate solution allows for testing if the three plates are rigid and if the plate geometry and input data are correct and, consequently, whether the circuit is ‘closed’.

REFERENCES

Bullard, E., J. E. Everett, and A. G. Smith (1965), The fit of the continents around the Atlantic, in *Philosophical Transactions of the Royal Society of London. Series A, Mathematical and Physical Sciences, vol. 258, no. 1088, A Symposium on Continental Drift*, edited by P. M. S. Blackett, E. Bullard and S. K. Runcorn, pp. 41-51.

Chang, T. (1987), On the statistical properties of estimated rotations, *Journal of Geophysical Research-Solid Earth and Planets*, *92*(B7), 6319-6329.

Chang, T. (1988), Estimating the Relative Rotations of Two Tectonic Plates from Boundary Crossings, *Journal of the American Statistical Association*, *83*(404), 1178-1183.

Crane, K. (1976), Intersection of Siqueiros Transform Fault and East Pacific Rise, *Marine Geology*, *21*(1), 25-46.

Dietz, R. S. (1961), Continent and Ocean Basin Evolution by Spreading of Sea Floor, *Nature, 190*(477), 854-857, DOI: 10.1038/190854a0.

Fujita, K., and N. H. Sleep (1978), Membrane stresses near mid-ocean ridge-transform intersections, *Tectonophysics*, *50*(2-3), 207-221.

Gordon, R. G. (2000), Diffuse oceanic plate boundaries: strain rates, vertically averaged rheology, and comparison with narrow plate boundaries and stable plate interiors in the history and dynamics of global plate motions, in *History and Dynamics of Global Plate Motions, Geophysical Monograph 121*, edited by M. A. Richards, R. G. Gordon and R. D. Van der Hilst, pp. 143-159.

Grindlay, N. R., P. J. Fox, and K. C. Macdonald (1991), 2nd-Order Ridge Axis Discontinuities in the South-Atlantic - Morphology, Structure, and Evolution, *Marine Geophysical Researches*, *13*(1), 21-49.

Grindlay, N. R., and P. J. Fox (1993), Lithospheric stresses associated with nontransform offsets of the mid-atlantic ridge-implications from a finite-element analysis, *Tectonics*, *12*(4), 982-1003.

Gudmundsson, A. (1993), On the Structure and Formation of Fracture-Zones, *Terra Nova*, *5*(3), 215-224.

Haxby, W. F., and E. M. Parmentier (1988), Thermal Contraction and the State of Stress in the Oceanic Lithosphere, *Journal of Geophysical Research-Solid Earth and Planets*, *93*(B6), 6419-6429.

Heirtzler, J. R., G. O. Dickson, E. M. Herron, W. C. Pitman, and X. Le Pichon (1968), Marine Magnetic Anomalies Geomagnetic Field Reversals and Motions of Ocean

Floor and Continents, *Journal of Geophysical Research, 73*(6), 2119-2136, DOI: 10.1029/JB073i006p02119.

Hellinger, S. J. (1981), The uncertainties of finite rotations in plate tectonics, *Journal of Geophysical Research*, *86*(NB10), 9312-9318.

Hess, H. H. (1962), History of ocean basins, *Geological Society of America Bulletin; Petrologic Studies: A Volume to Honour A.F. Buddington*, 559-620.

Jellinek, A. M., R. G. Gordon, and S. Zatman (2006), Experimental tests of simple models for the dynamics of diffuse oceanic plate boundaries, *Geophysical Journal International, 164*(3), 624-632, DOI: 10.1111/j.1365-246X.2005.02840.x.

Karson, J. A., and H. J. B. Dick (1983), Tectonics of Ridge-Transform Intersections at the Kane Fracture-Zone, *Marine Geophysical Researches*, *6*(1), 51-98.

Lonsdale, P. (1978), Near-bottom reconnaissance of a fast-slipping transform fault zone at the Pacific-Nazca Plate boundary, *Journal of Geology*, *86*(4), 451-472.

McKenzie, D., J. Roberts, and N. Weiss (1973), Numerical Models of Convection in Earths Mantle, *Tectonophysics, 19*(2), 89-103, DOI: 10.1016/0040-1951(73)90034-6.

Menard, H. W., and T. Atwater (1968), Changes in Direction of Sea Floor Spreading, *Nature, 219*(5153), 463-467, DOI: 10.1038/219463a0.

Phipps Morgan, J., and E. M. Parmentier (1984), Lithospheric stress near a ridge-transform intersection, *Geophysical Research Letters, 11*(2), 113-116, DOI: 10.1029/GL011i002p00113.

Pitman, W. C., and J. R. Heirtzler (1966), Magnetic Anomalies over the Pacific-Antarctic Ridge, *Science, 154*(3753), 1164-1171, DOI: 10.1126/science.154.3753.1164.

Royer, J. Y., and T. Chang (1991), Evidence for relative motions between the Indian and Australian Plates during the last 20 m.y. From plate tectonic reconstructions: Implication for the deformation of the Indo-Australian plate, *Journal of Geophysical Research-Solid Earth and Planets*, *96*(B7), 11779-11802.

Sandwell, D. T., and W. H. F. Smith (2009), Global marine gravity from retracked Geosat and ERS-1 altimetry: Ridge segmentation versus spreading rate, *Journal of Geophysical Research-Solid Earth, 114*, B01411, DOI: 10.1029/2008jb006008.

Sclater, J. G., and J. Francheteau (1970), The Implications of Terrestrial Heat Flow Observations on Current Tectonic and Geochemical Models of Crust and Upper Mantle of Earth, *Geophysical Journal of the Royal Astronomical Society, 20*(5), 509-542, DOI: 10.1111/j.1365-246X.1970.tb06089.x.

Sclater, J. G., R. N. Anderson, and M. L. Bell (1971), Elevation of Ridges and Evolution of Central Eastern Pacific, *Journal of Geophysical Research, 76*(32), 7888-7915, DOI: 10.1029/JB076i032p07888.

Searle, R. C., and A. S. Laughton (1977), Sonar Studies of Mid-Atlantic Ridge and Kurchatov Fracture Zone, *Journal of Geophysical Research*, *82*(33), 5313-5328.

Searle, R. C. (1986), GLORIA Investigations of Oceanic Fracture-Zones - Comparative-Study of the Transform-Fault Zone, *Journal of the Geological Society*, *143*, 743-756.

Sykes, L. R. (1967), Mechanism of Earthquakes and Nature of Faulting on Mid-Oceanic Ridges, *Journal of Geophysical Research*, *72*(8), 2131-2153.

Tucholke, B. E., and H. Schouten (1988), Kane Fracture Zone, *Marine Geophysical Researches, 10*(1-2), 1-39, DOI: 10.1007/BF02424659.

Vine, F. J., and D. H. Matthews (1963), Magnetic Anomalies over Oceanic Ridges, *Nature, 199*(489), 947-949, DOI: 10.1038/199947a0.

Wilson, J. T. (1965), A New Class of Faults and Their Bearing on Continental Drift, *Nature, 207*(4995), 343-347, DOI: 10.1038/207343a0.

CHAPTER 1

Revised Pacific-Antarctic Plate Motions and Geophysics of the Menard Fracture Zone

ABSTRACT

A reconnaissance survey of multibeam bathymetry and magnetic anomaly data of the Menard Fracture Zone allows for significant refinement of plate motion history of the South Pacific over the last 44 million years. The right-stepping Menard Fracture Zone developed at the northern end of the Pacific-Antarctic Ridge within a propagating rift system that generated the Hudson microplate and formed the conjugate Henry and Hudson Troughs as a response to a major plate reorganization ~45 million years ago. Two splays, originally about 30 to 35 km apart, narrowed gradually to a corridor of 5 to 10 km width, while lineation azimuths experienced an 8° counterclockwise reorientation owing to changes in spreading direction between chrons C13o and C6C (33 to 24 million years ago). We use the improved Pacific-Antarctic plate motions to analyze the development of the southwest end of the Pacific-Antarctic Ridge. Owing to a 45° counterclockwise reorientation between chrons C27 and C20 (61 to 44 million years ago) this section of the ridge became a long transform fault connected to the Macquarie Triple Junction. Following a clockwise change starting around chron C13o (33 million years ago), the transform fault opened. A counterclockwise change starting around chron C10y (28 millions years ago) again led to a long transform fault between chrons C6C and C5y (24 to 10 million years ago). A second period of clockwise reorientation starting around chron C5y (10 million years ago) put the transform fault into extension forming an array of 15 en echelon transform faults and short linking spreading centers.

1.1 INTRODUCTION

The Pacific-Antarctic Ridge (PAR) (Figure 1.1) is one of the major branches in the global ridge system and links the Pacific basins to the Earth's other tectonic plates [*Pitman et al.*, 1968]. *Molnar et al.* [1975] first estimated rotation parameters for the PAR, calculating rotations for six chrons, the oldest being C31 (68 Ma; *Cande and Kent* [1995]), as well as a fit of the Campbell Plateau and Marie Byrd Land. *Cande et al.* [1995] significantly improved constraints for Pacific-Antarctic plate motions back to chron C31 (68 Ma) based on data from a detailed geophysical survey of the Pitman Fracture Zone (FZ). In this paper we present a refinement of Pacific-Antarctic plate rotations since ~44 Ma based primarily on new shipboard magnetic anomaly and multibeam bathymetry data along the right-stepping Menard FZ, which developed at the northern side of the PAR within a propagating rift system that generated the conjugate Henry and Hudson Troughs as a response to a major plate reorganization around chron C21 (~45 Ma) [*Cande et al.*, 1982; *Eakins*, 2002].

Based on the new magnetic anomaly and FZ data we calculated 49 new rotations for chrons C20o to C1o (43.8 to 0.78 Ma). This allowed us to analyze changes in plate motion along the PAR in detail during this time period. In this paper we present detailed bathymetric and magnetic anomaly data along the Menard FZ, which shows the response of the FZ to adjustments in plate motion. Changes in spreading direction at chrons C13o and C6C (33.5 Ma and 24.1 Ma) are observed at FZs along the entire PAR. We then use these rotations to investigate the tectonic evolution of the southwesternmost section of the PAR, a region which underwent a significant clockwise change in spreading direction during the Late Miocene [*Cande et al.*, 1995; *Lodolo and*

Coren, 1997]. Being close to the rotation poles, this area is ideal for testing the predictive quality of the new rotation parameters for changes in plate motion and observed tectonic features related to these changes. We show that a clockwise change in plate motion starting around chron C5y (9.7 Ma) opened up an array of 15 en echelon transform faults and 15 short linking spreading centers.

1.2 DATA

The most recent major revision to Pacific-Antarctic rotation parameters [*Cande et al.*, 1995] was based on P-code GPS-navigated R/V Maurice Ewing data for the Pitman FZ plus older geomagnetic data from available cruises where navigation was less precise. For this study we used the R/V Maurice Ewing data plus new data from 11 transits of the NSF OPP (Office of Polar Programs) operated R/VIB Nathaniel B. Palmer that are all GPS-navigated and include multibeam bathymetry. These data are mainly concentrated along the Menard FZ and were collected during five R/VIB Nathaniel B. Palmer transits between Lyttelton, New Zealand and Punta Arenas, Chile from 1997 to 2005. In addition we used R/VIB Nathaniel B. Palmer data from eight transits at the southwest end of the PAR (from 1995 to 2007), one transit along the Vacquier FZ (2006) and one transit south of the Hollister FZ (1998). *Cande and Stock* [2004a; b] calculated Pacific-Antarctic rotations for a small set of chrons using data from a limited number of R/VIB Nathaniel B. Palmer transits available at that time. Those rotations are not as well constrained as the rotations presented here. Figure 1.2 shows ship tracks of all cruises we used for this study. We also used GEOSAT and ERS 1 gravity anomaly data derived from satellite altimetry [*McAdoo and Laxon*, 1997; *Sandwell and Smith*, 1997], for interpretation of tectonic features where magnetic anomaly and bathymetric data were

sparse or unavailable. The principal new data set from the Menard FZ mapped seafloor of the Pacific and Antarctic plates back to its original appearance at ~45 Ma between chrons C20o and C21y (43.8 to 46.3 Ma). Besides the R/VIB Nathaniel B. Palmer data we included multibeam bathymetry data from a R/V Thomas Washington along-axis survey of the northern section of the PAR [*Lonsdale*, 1994b], a N/O Atalante cruise in 2005 [*Klingelhoefer et al.*, 2006] at the Menard transform fault and a R/V Melville cruise in 1994 [*Lonsdale*, 1994a] that crossed the Menard FZ on Antarctic plate crust formed around chron C5. The only transit satellite navigated data used in the solutions were from a R/V Robert D. Conrad cruise in 1974 that ran south of the Menard FZ on the Antarctic plate between chrons C12o and C20o (30.9 to 43.8 Ma). These data agree well with a parallel GPS-navigated R/VIB Nathaniel B. Palmer track. The magnetic anomaly data and identified anomaly points are shown on Figure 1.3, which is an overview of both the Pacific and Antarctic limbs of the FZ on a GEOSAT gravity background. Detailed multibeam bathymetry (Figure 1.4a-e) reveals several prominent features along the Menard FZ including a deep transform fault graben, a westward ridge jump south of the FZ around chron C7 (24.8 Ma) and the presence of two splays, 30 km apart at chron C20o (43.8 Ma), that narrowed to a 5 to 10 km corridor by chron C6C (23.8 Ma).

The other area with considerable new data is at the southwest end of the PAR. In this region a change in spreading direction around chron C5y (9.8 Ma) put a large transform fault under extension, forming a set of short ridge segments. The FZs and several prominent tectonic features are imaged in GEOSAT gravity [*Sandwell and Smith*, 1997] (Figure 1.5a). The FZ traces are based on the sparse multibeam bathymetry and GEOSAT gravity data (Figures 1.5b and c). Pronounced axial grabens are observed for the ridge segments between FZ E, the Emerald FZ and FZ F, whereas smooth triangular

morphology with an axial high [*Macdonald et al.*, 1988] is observed for ridge segments between FZs C and D, FZs H and I and FZs K and L. Troughs of 5000 to 6000 m depth and parallel ridges that reach up to about 1000 m below sealevel mark the boundaries of the en echelon right-stepping FZs.

The preservation of both flanks of the Pacific-Antarctic spreading center allows us to match FZ trails on each flank with the other and compare them with modeled synthetic flowlines [*Cande et al.*, 1988; *Cande et al.*, 1995]. The FZs were digitized from the detailed topography in combination with magnetic anomaly data. We used the geophysical data collected along Menard, Vacquier, Hollister, Pitman, Emerald, C, D, F, H, I and J FZs to calculate a revised set of rotation parameters. A combination of detailed topography, magnetics and minima in GEOSAT gravity data was used to maximize coverage. A total of 49 rotations describe the relative plate motion. Since the Menard FZ, along which most new data were collected, opened at about 45 Ma the oldest improved rotation parameter is chron C20o (43.8 Ma). We identified the magnetic anomalies according to the scheme for the North Pacific initiated by *Atwater and Severinghaus* [1989].

1.3 FINITE ROTATIONS

The finite rotations (Table 1) were calculated using the fitting criteria of *Hellinger* [1981] as implemented by *Chang* [1987; 1988] and *Royer and Chang* [1991]. In this method, reconstruction parameters are determined by dividing the data into multiple segments and fitting great circles to reconstructed data in each segment. Magnetic anomalies and FZ crossings define the segments. Based on the multibeam bathymetry we digitized the FZs and also the abyssal hills where magnetic anomaly data were

sparse. Table 1.1 shows the number of segments used for each individual finite rotation. We assigned an average uncertainty estimate of 0.7 to 1.2 km for magnetic anomaly picks, which mainly reflects the ambiguities in identifying specific points on the magnetic anomaly profiles. For FZ crossings a larger 1.7 to 3 km estimate was assigned since the structure of a FZ depends on the geologic history of the transform fault and may change with time [*Lonsdale*, 1994a]. For certain segments only a single track of magnetic anomaly data was available. For these segments abyssal hill morphology was used to extrapolate the magnetic anomaly pick to the outer edges of the multibeam swath generating two extra picks at that location. A 1.7 to 3 km uncertainty was assigned for these picks. Using the *Chang* [1987; 1988] method, a statistical parameter $\hat{\kappa}$ is returned with the solution. $\hat{\kappa}$ is a statistical parameter related to the error values; errors are overestimated when $\hat{\kappa} \gg 1$, errors are underestimated when $\hat{\kappa} \ll 1$. The $\hat{\kappa}$ values we present range between 1 and 3 indicating our error values were somewhat overestimated.

In Figure 1.6 we compare the newly calculated finite rotation poles with those of *Cande et al.* [1995]. Owing to the large number of constraints on rotation parameters along the PAR, the error ellipses are very small. Our rotations generally agree well with those of *Cande et al.* [1995], but deviate considerably for times younger than chron C5A (12.3 Ma). This reflects the fact that the trace of the Menard FZ was not well constrained without multibeam bathymetry data. The differences are illustrated (Figure 1.6) by the 95% error ellipses for chron C5A and younger from Cande et al. [1995]. Rotation parameters between chrons C13o and C20o (33.5 to 43.8 Ma) were not constrained in the *Cande et al.* [1995] study. However the pole positions for chrons C13o and C20o are close to our new rotation poles.

The high density of shipboard magnetic anomaly and multibeam bathymetry data on the Menard and Pitman FZs allowed us to address an issue related to intraplate deformation. In particular, Géli et al. [1998] suggested that the Hollister Ridge, a prominent volcanic lineament that cuts through 0.5 to 20 Ma old crust near the Hollister FZ (Figure 1.1), may have been caused by a period of intraplate deformation starting around 3 Ma. We followed the method of *Goodwillie and Parsons* [1992] and *Gans et al.* [2003] and used a comparison of the separation distances between the Menard and Pitman FZs on conjugate portions of the Pacific and Antarctic plates to place an upper limit on the amount of intraplate deformation that may have taken place. The geometrical setup of the *Chang* [1987; 1988] method is ideal for this analysis since the computation for each segment includes the distance between each data point and a great circle that best fits the data in the segment. Thus, the combined misfit of the great circle segments corresponding to the Menard and Pitman FZs is a direct computation of the difference in separation distances between the FZs, which are roughly 3500 km apart. Intraplate deformation should appear as a systematic change in the average amount of misfit between the FZs. When we plot the individual and combined misfits in the FZ segments for all 49 rotations (Figure 1.7), we noted that the combined misfits are generally about 1.5 km, with no obvious trend to the misfits through time. Although it is difficult to estimate the amount of systematic error in picking the FZ location from the bathymetry because of such tectonic complexities as overshot ridges at ridge-transform intersections [*Gallo et al.*, 1986; *Lonsdale*, 1994a], the lack of any trend to the combined misfit between Menard and Pitman FZs over 45 Ma suggests that the systematic error is small and that any intraplate deformation is less than 1.5 km. The lack of any trend to the misfit also places a lower limit on plate rigidity. A strain of 1.5 km over a distance of 3500

km over 45 Ma corresponds to a strain rate of 9.5 x 10^{-12}/a, which is within the range suggested for the interior of rigid plates by *Gordon* [1998].

1.4 STAGE ROTATIONS

To evaluate the predictive quality of the new finite rotations we calculated stage rotations and used these to generate synthetic flowlines (Figure 1.8). These tracks plotted relative to the Pacific and Antarctic plates indicate slow to intermediate spreading rates close to the stage poles (Emerald and Pitman FZs) to intermediate spreading rates further away from the stage poles (Menard and Hollister FZs). Between chrons C20o and C16y (43.8 to 35.7 Ma) the stage poles moved eastwards. They experienced a rapid shift westward away from the ridge between chrons C16y and C10y (35.7 to 28.3 Ma). From chrons C8o to C6C (26.6 to 23.1 Ma) the stage poles rapidly moved southeast. Between chrons C6o and C5A (20.1 to 12.3 Ma) they remained relatively stationary. Since chron C5A (12.3 Ma) the stage poles have migrated relatively continuously north-northwest, with a slight change in direction to the north since chron C5y (9.7 Ma). Figure 1.8 also shows the calculated synthetic flowlines from the stage poles for several FZs along the PAR. The synthetic flowline data fit well with the Menard, Hollister and Pitman FZs. Only the left-stepping Vacquier FZ does not follow a simple synthetic flowline. However, propagating rifts complicated the evolution of the Vacquier FZ between chrons C6C (22.2 Ma) and C5A (12.3 Ma).

1.5 VARIATIONS IN SPREADING RATES

Using new rotation parameters, we examined the half-spreading rates along the PAR since the opening of the Menard FZ at about 45 Ma. We determined the half-spreading rates for ridge segments bounding the Menard, Hollister, Pitman and Emerald

FZs along synthetic flowlines, using the *Cande and Kent* [1995] (CK95) geomagnetic polarity timescale with revisions for chrons C3Ay and C3Ao as given in *Krijgsman et al.* [1999] (Figure 1.9). The intermediate spreading rate of the PAR at the latitude of the Menard FZ is comparable to the northern part of the Pacific-Cocos [*Weiland and Macdonald*, 1996] and Australian-East Antarctic [*Cochran and Sempéré*, 1997] boundaries. From chrons C20o to C17y (43.8 to 36.6 Ma) the half-spreading rate was fairly constant at about 27 mm/yr. Between chrons C17y and C12o (36.6 to 30.9 Ma) the half-spreading rate gradually increased to 40 mm/yr. At chron C9o (28.0 Ma) it dropped to 33 mm/yr and remained constant until chron C6C (24.1 Ma). Between chrons C6C and C5Cy (24.1 to 16.2 Ma) half-spreading rates were 28 mm/yr. *DeMets et al.* [1990] and *Lonsdale* [1994b] reported symmetric spreading at an average half-spreading rate of 47 mm/yr since chron C5A (12.3 Ma) just north of the Menard FZ. Our new data show that since chron C5Cy half-spreading rates increased from 36 to about 43 mm/yr at chron C3o (5.1 Ma) and remained constant from then until present.

Large fluctuations in spreading rate of short durations (e.g. between chrons C17y and C15y) are probably not real but a result of small errors in magnetic anomaly picks, which are reflected in a larger error in the spreading rate calculation for short time intervals of about 1 m.y. In Figure 1.9 we excluded some of the 49 new rotations for chrons spaced at time intervals on the order of 0.5 m.y. in order to smooth unrealistically large fluctuations. Small fluctuations in spreading rate, such as those between chrons C5Cy and C5o, may reflect small errors in magnetic anomaly picks or errors in the timescale. In order to evaluate the effect of timescale error we also looked at the Geologic Time Scale (GTS2004, red line on Figure 1.9) [*Ogg and Smith*, 2004], which includes the astronomically tuned timescale for the Neogene [*Lourens et al.*, 2004]. We

found that spreading rate fluctuations are still present. The GTS2004 timescale leads to larger spreading rate fluctuations than the CK95 timescale for the PAR between chrons C5Cy and C4 (16.2 and 7.9 Ma), while the opposite is true between chrons C6B and C5Cy (23.1 and 16.2 Ma for CK95). However, these fluctuations in spreading rate over short time intervals are similar to the magnitude of the 95% confidence limits based on stage rotations (Figure 1.9).

We used half-spreading rates based on the synthetic flowline to compute age vs. distance, and compared these to observations from R/VIB Nathaniel B. Palmer cruise NBP9707. This cruise followed a track perpendicular to spreading lineation azimuths just north of Menard FZ and has a continuous magnetic anomaly record until chron C18o (40.1 Ma) on both the Pacific and Antarctic plates. The observed and predicted distances (Figure 1.10) show a good correlation, which is expected since the NBP9707 data were used in the calculation of the rotation parameters. Since chron C18o a total of 1460 km of Antarctic and 1350 km of Pacific oceanic crust has been accreted north of the Menard FZ. Apparently the PAR at this latitude has spread slightly asymmetrically since 40 Ma with more material accreted to the Antarctic plate.

1.6 RECONSTRUCTION OF THE MENARD FZ

The spreading ridge adjacent to the Menard FZ accreted almost 3000 km of oceanic crust since chron C20o (43.8 Ma). Seafloor depths range from about 2300 m at the axis (Figure 1.4c) to 5200 m at the oldest parts of the ocean floor near the FZ (Figures 1.4a and e). The ridge exhibits a smooth triangular morphology with an axial high [*Klingelhoefer et al.*, 2006; *Macdonald et al.*, 1988]. Troughs as deep as 6500 m

mark the intersection of the FZ with the Henry and Hudson Troughs on the Pacific and Antarctic plates, respectively [*Cande et al.*, 1982; *Eakins*, 2002].

The Menard FZ experienced adaptations to changes in plate motion. At its start, the FZ consisted of two splays, 30 km apart. Figure 1.11 shows the lineation azimuths based on the synthetic flowline and the ridge offset calculated from magnetic anomaly points across the Menard FZ during the last 40 Ma for both the Pacific and Antarctic plates. The ridge offsets on the two flanks should be the same; small differences reflect the uncertainties in the magnetic anomaly picks. The eastward drift of the stage poles between chrons C18o and C16y (40.1 to 35.7 Ma) put the FZ slightly under extension and the distance separating the two splays grew to about 35 km. During this period the ridge offset decreased from 150 to 130 km, corresponding to a 2° clockwise change in lineation azimuths. On the Pacific plate parallel to the northern splay at -46.2° S and 229.8° E (Figure 1.4a) a ridge rises 1200 m above the seafloor. This ridge possibly formed by transtension during the rotation. However, no prominent ridges are observed at the southern splay on the Pacific plate or at the conjugate splays on the Antarctic plate (Figure 1.4e). Note that there is a gap in multibeam bathymetry data on the location of much of the southern splay (Figure 1.4e). Ridges that rise up to 500 m above the surrounding seafloor are observed along most of the FZ splays. This relief can be explained by differential cooling and flexure of the rise flanks [*Sandwell*, 1984]. South of the Menard FZ no ridge offset data are available between 27 and 24 Ma owing to a ridge jump, which is possibly related to a propagating ridge around chron C7 (24.8 Ma). The westward ridge jump (Figure 1.4a) transferred about 65 km of former Pacific oceanic crust to the Antarctic plate (Figure 1.4d), which increased the ridge offset to about 230 km. A bathymetric deep of 800 m below the surrounding oceanic crust (Figure 1.4a)

reveals the topographic scar of this jump on the Pacific plate. Chaotic magnetic anomalies and large changes in relief up to 1000 m characterize the captured former Pacific oceanic crust on the Antarctic plate south of the southern splay (Figure 1.4d).

Between chrons C13o and C6C (33.5 to 24.1 Ma) the stage poles drifted westwards, away from the plate boundary, with respect to both plates, which put the FZ under compression. Lineation azimuths experienced a counterclockwise change of about 15° and the corridor between the two splays gradually narrowed to a width of 5 to 10 km by chron C6C (23.1 Ma). The counterclockwise rotation is consistent with observations of *Cande et al.* [1995] and *Lonsdale* [*Lonsdale*, 1994b] for the northern part of the PAR; our study shows that this reorientation occurred progressively between 34 and 26 Ma. Between 24 and 11 Ma the ridge offset increased gradually from 230 to 260 km. This slight increase in transform fault offset at the right-stepping Menard FZ could indicate transpression. However, the spreading direction of the ridge segments near the Menard FZ remained fairly constant between chrons C6C and C3o (23.1 to 5.1 Ma) with only a 3° clockwise rotation as opposed to the Pitman and Emerald FZs [*Cande et al.*, 1995], which lie closer to the stage poles and underwent significant clockwise rotations since 10 Ma. During this period the ridge offset of Menard FZ gradually decreased to its modern value of 215 km. A 3° clockwise rotation since chron C3o (5.1 Ma) indicates the Menard transform fault is under transtension. At 4.9 Ma, after a remarkable 18 Myr lifespan of the narrow corridor, the northern splay of the Menard FZ ceased to exist leaving a single transform fault. The extensional period since chron C3o is reflected in a 5500 m deep Menard transform fault graben (Figure 1.4c) bounded by a transverse ridge on the north side that rises up to 2500 m below sealevel (Figure 1.4c). Moreover, a seamount peaks 2500 m below sea surface in the middle of the graben. A possible explanation for this

feature is a leaky transform fault as envisioned by *Menard and Atwater* [1969] and *Menard and Chase* [1970].

1.7 RECONSTRUCTION OF THE EMERALD FZ

The southwestern section of the PAR, between the Terror FZ and the Macquarie Triple Junction, which links the Pacific, Antarctic and Australian plates, is located close to the rotation poles. This area has alternated periods of motion along a large transform fault with periods of spreading. Its complex tectonic history is therefore useful to test the predictive quality of the new rotation parameters. At present the area is characterized by multiple NNW-SSE striking en echelon faults and short spreading links. *Menard and Atwater* [1969] described how an opening of a transform fault in response to a change in plate motion creates an array of en echelon faults with the new spreading-parallel azimuth and short linking spreading axes between them. Multiple en echelon faults and short spreading links were also considered for the Valdivia FZ System during the Neogene at the Antarctic-Nazca boundary [*Tebbens and Cande*, 1997; *Tebbens et al.*, 1997], for the Molokai and Mendocino-Pau-Pioneer systems during the late Cretaceous [*Atwater et al.*, 1993; *Searle et al.*, 1993] in the North Pacific and for the Andrew Bain FZ area during the late Cretaceous [*Bernard et al.*, 2005; *Royer et al.*, 1988] at the Southwest Indian Ridge. We reconstructed the evolution of the Emerald FZ based on the synthetic flowlines with the Antarctic plate kept fixed. Figure 1.12 shows the evolution of the PAR close to the Macquarie Triple Junction since chron C24o (53.3 Ma). The major plate reorganization at ~45 Ma resulted in a 30° counterclockwise change in spreading direction. As a response, a transform fault of about 450 km offset formed between the Macquarie Triple Junction and the Emerald, E and Terror FZs (Figure 1.12 - 43.8 Ma).

Between chrons C20o and C13o (43.8 to 33.5 Ma) the transform fault lengthened to about 700 km. Around chron C13o a gradual 20° clockwise change in spreading direction put the transform fault under extension. The change in direction was small and it is not clear if distinct transform faults and ridges formed. A gradual 20° counterclockwise change in spreading direction starting around chron C10y (28.3 Ma) led once more to the formation of a single long transform fault between the Macquarie Triple Junction and Terror FZ by chron C6C (24.1 Ma) (Figure 1.12: 24.1 Ma). The transform fault grew to a length of about 1200 km between chrons C6C and C5y (24.1 to 9.7 Ma). *Symons et al.* [2004] considered a leaky transform fault between 26.6 and 10.9 Ma accommodating some divergence between the Pacific and Antarctic plates and evolution of the transform fault into a spreading ridge since 5.9 Ma. Our observations suggest that there was pure transform motion during most of this period. Since chron C5y (9.7 Ma) the southwestern section of the PAR was subject to almost 30° of clockwise change in spreading direction. The change in spreading direction, starting around chron C5y, is associated with the northward migration of stage poles since that time, which put the long transform fault under extension and replaced it with an array of 15 transform faults and short ridge segments (Figure 1.12 for 9.7, 6.7 and 3.6 Ma and Figure 1.5 for 0 Ma). Ridges that run parallel to the original locations of the transform fault were most likely formed as flexural responses to the extension and related opening of the transform fault around chrons C13o and C5y (33.5 and 9.8 Ma). Similar extensional ridges are observed along the Udintsev FZ [*Lonsdale*, 1986; 1994a].

1.8 EFFECTS ELSEWHERE ON THE PAR

The effects of the clockwise change in spreading direction starting around chron C5y (9.7 Ma) associated with the northward migration of the stage poles since that time, continued with the increase in spreading rate around chron C4 (7.9 Ma) and are observed elsewhere on the PAR. South of the Heirtzler FZ this recent change in plate motion led to the formation of a short right-stepping ridge offset around chron C3Ay (6.0 Ma) and propagating rifts around chrons C2Ay and C1o (2.6 and 0.78 Ma) [*Briais et al.*, 2002]. The pattern of en echelon right-stepping faults and short spreading segments for Heezen, Udintsev and Raitt transform faults and the exceptional 6000 m depth of the Heezen and Tharp transform fault valleys, which are part of the Eltanin Fault System, have also been attributed to extension resulting from the clockwise change in spreading direction during the Pliocene [*Lonsdale*, 1986; 1994a].

1.9 GLOBAL TECTONICS

Atwater and Molnar [1973] and *Stock and Molnar* [1988] pointed out the importance of the reconstruction of the PAR for motion of the Pacific plate relative to western North America. The rotation parameters based on the Pitman FZ [*Cande et al.*, 1995] were used by *Royer et al.* [2006] to revise the North America - Nubia - Antarctica - Pacific - North America plate circuit. Our Pacific-Antarctic rotation parameters are slightly different than the Pacific-Antarctic component of the plate circuit published by *Royer et al.* [2006], whose study focused on the effect of significantly modifying rotation parameters for the Southwest Indian Ridge. The effect of using our revised Pacific-Antarctic rotations is small compared to the effect of the significant changes in Southwest Indian Ridge rotation parameters proposed by *Royer et al.* [2006].

1.10 SUMMARY AND CONCLUSIONS

In this study we determined 49 rotations that describe the relative motion between the Pacific and Antarctic plates since ~44 Ma in detail. We used data along the entire PAR, but the rotations were primarily constrained by the new detailed data set along the Menard FZ in combination with the Pitman FZ data. These two FZs are located ~3500 km apart and therefore cover a large area of PAR oceanic crust, allowing for tight constraints on rotation parameters. An outcome of this study is that our high resolution plate motion model for the PAR can predict the plate tectonic history along the entire ridge in great detail. We tested the predictive quality of the stage rotations and synthetic flowlines based on these new rotation parameters at the southwestern end of the PAR close to the Macquarie Triple Junction. Reconstructions show that this section of the ridge twice became a single, long transform fault (between 44 and 33 Ma and between 24 and 10 Ma), followed by plate motion changes that put the transform fault into extension (between 33 and 28 Ma and from 10 Ma to present). During the most recent period of extension the transform fault was replaced by an array of 15 transform faults and short spreading centers. The earlier period of extension was not as long nor characterized by as large a change in direction and it is not clear if distinct transform faults and spreading ridges formed.

1.11 ACKNOWLEDGMENTS

This study was made possible through a series of grants from the NSF-Office of Polar Programs supporting the acquisition of geophysical data along transits of the R/VIB Nathaniel B. Palmer : grant numbers OPP-0338317, OPP-0338346, OPP-0126334 and OPP-0126340. We thank the officers, crew and scientific staff of the R/VIB

Nathaniel B. Palmer and the many students who sailed on these cruises. Caltech contribution number 9005.

This chapter has been published: Croon, M. B., S. C. Cande, and J. M. Stock (2008), Revised Pacific-Antarctic plate motions and geophysics of the Menard Fracture Zone, *Geochemistry Geophysics Geosystems, 9*, Q07001, DOI: 10.1029/2008gc002019.

1.12 FIGURES

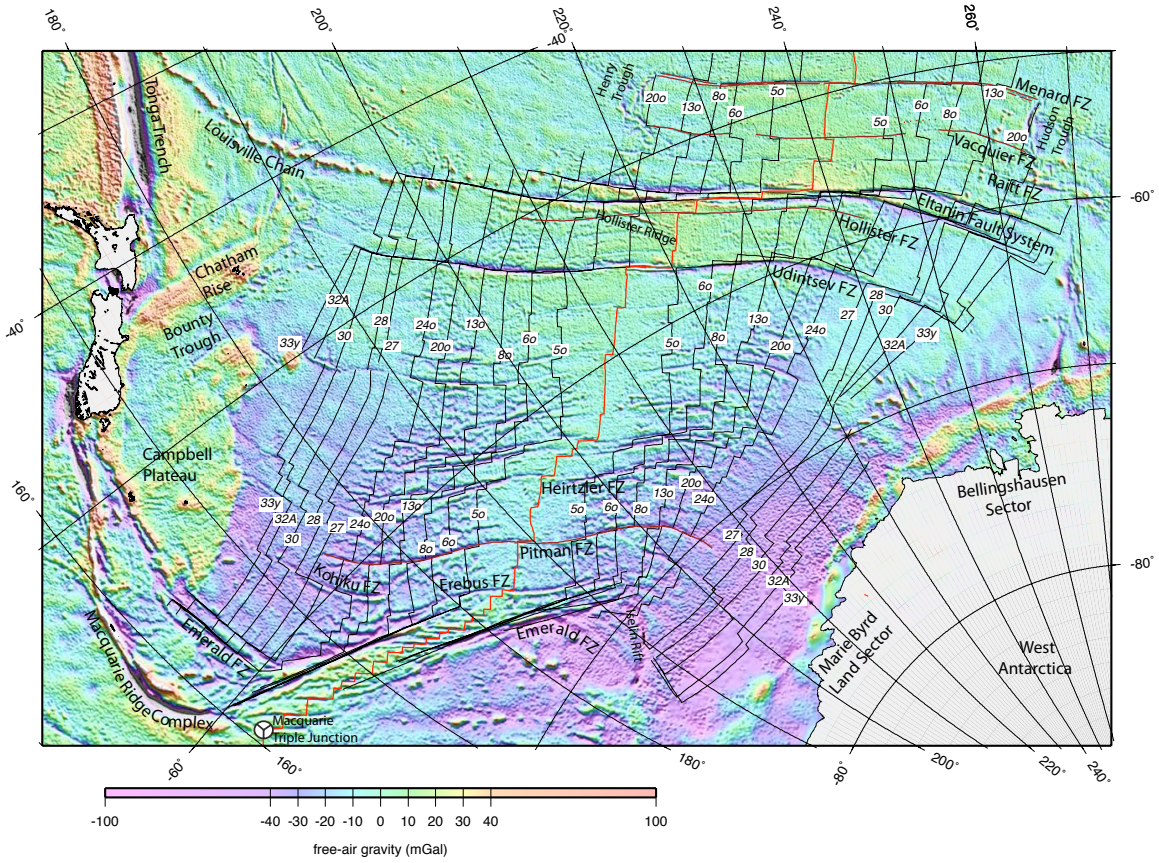

Figure 1.1: Map of the Pacific-Antarctic Ridge, on an image of the satellite-derived, free-air gravity field, summarizing the location of magnetic anomaly isochrons. The traces of the Menard, Vacquier, Hollister and Pitman FZs are highlighted in red. Map is in an oblique Mercator projection about a pole at 66.8° N, 81.7° W, near the pole of rotation of Pacific to Antarctica at chron C3A.

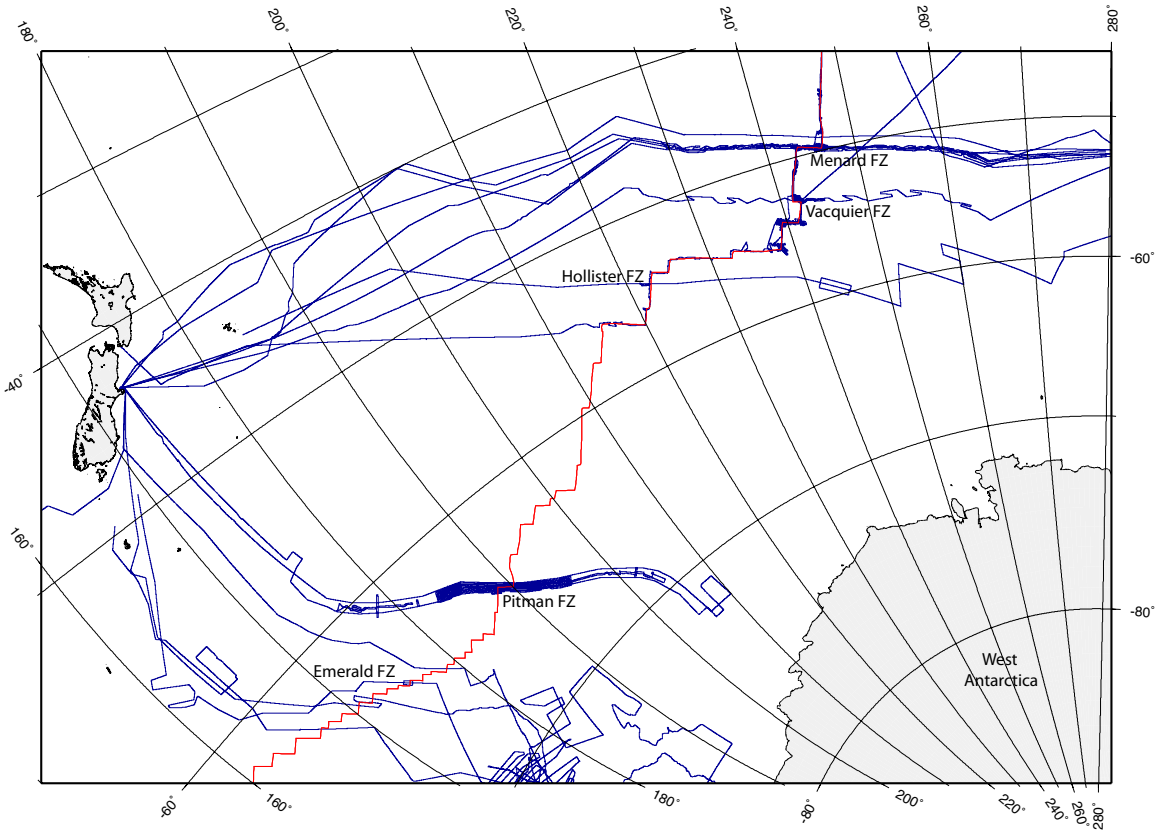

Figure 1.2: Overview of ship tracks (blue lines) with geophysical data used to improve Pacific-Antarctic rotation parameters. Included are following cruises (NBP = R/VIB Nathaniel B. Palmer, MV = R/V Melville, WT = R/V Thomas Washington, RC = R/V Robert D. Conrad, EW = R/V Maurice Ewing): NBP9707, NBP0007B, NBP0403, NBP0501B, NBP0507, WEST03MV, RAPA03WT and RC1714 at Menard FZ, NBP0607A at Vacquier FZ, NBP9804 south of Hollister FZ, EW9201 at Pitman FZ and NBP9702, NBP0209, NBP0501A and NBP0701 near Emerald FZ. The present location of the Pacific-Antarctic Ridge is highlighted in red. Map projection same as in Figure 1.1.

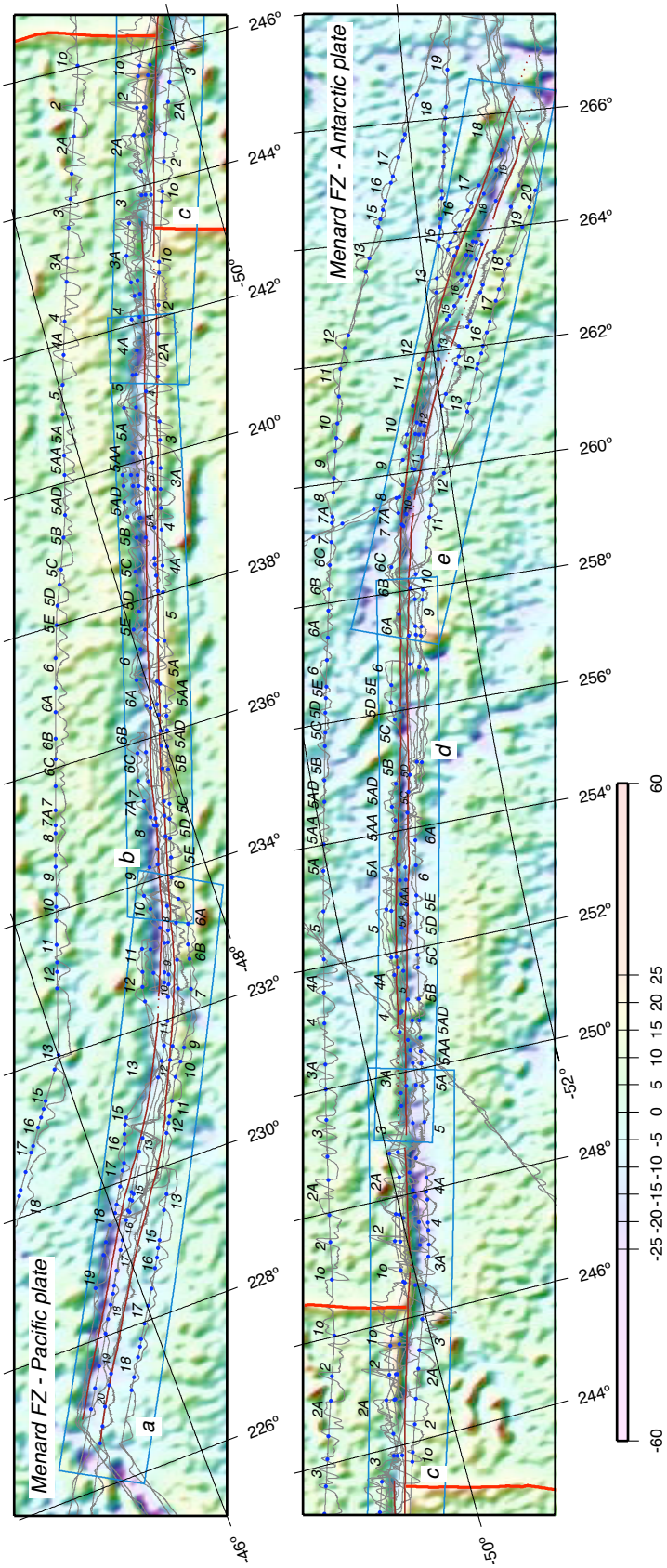

Figure 1.3: The ship tracks (NBP9707, NBP0007B, NBP0403, NBP0501B, NBP0507, WEST03MV, RAPA03WT and RC1714) and magnetic anomaly wiggles (grey) along the two splays of the Menard FZ (dark red lines), on an image of the satellite-derived, free-air gravity field. The blue dots represent magnetic anomaly picks and the Pacific-Antarctic Ridge is highlighted with thick red lines. The blue boxes show the locations of the multibeam bathymetry maps in Figure 1.4. Map projection same as in Figures 1.1 and 1.2.

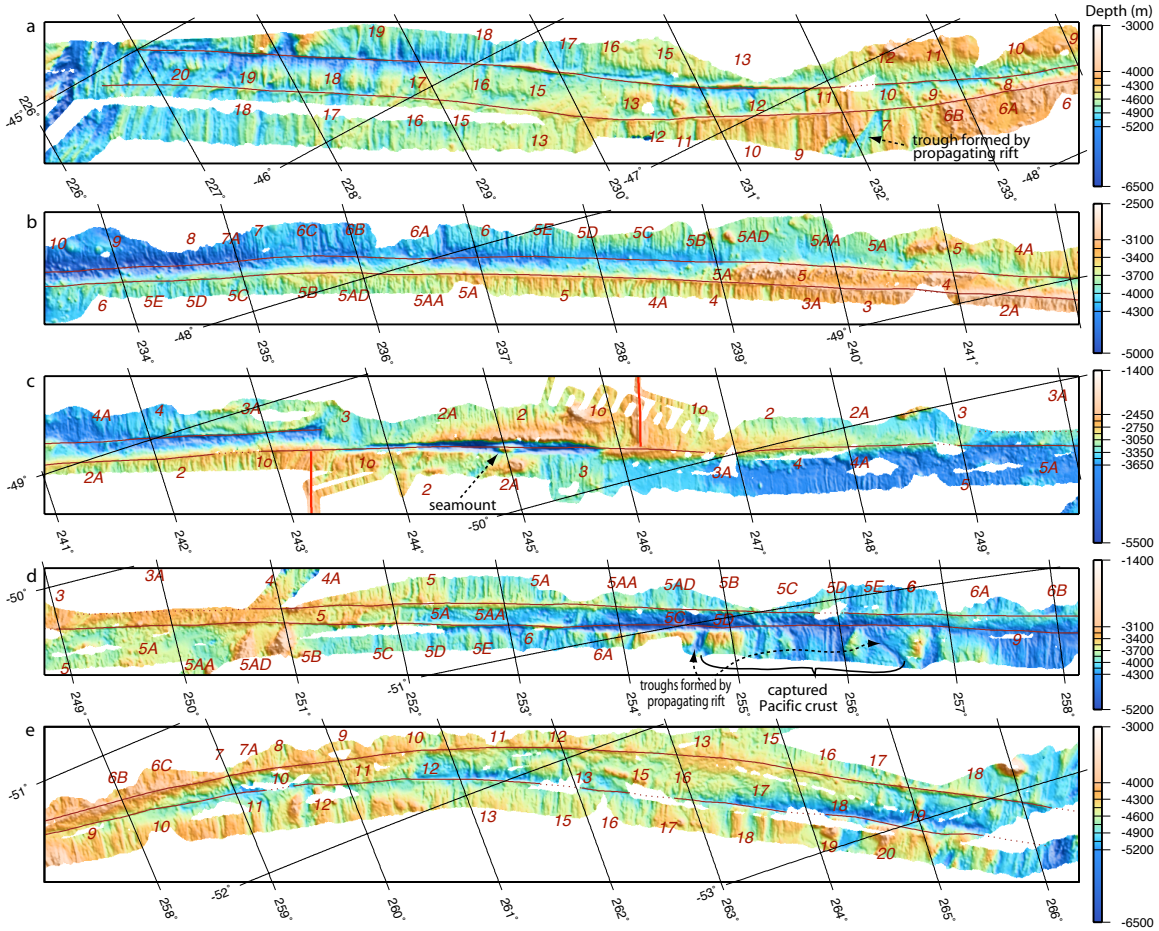

Figure 1.4: Multibeam bathymetry data from NBP9707, NBP0007B, NBP0403, NBP0501B, NBP0507, WEST03MV, Pacantarctic2 and RAPA03WT cruises at the two splays of the Menard FZ (dark red lines). The red numbers show magnetic anomaly identifications and the Pacific-Antarctic Ridge is highlighted with thick red lines.

Figure 1.5: Emerald, Terror and Erebus FZs and FZs A through O (black lines) on an image of the satellite-derived, free-air gravity field. The black tagged lines are isochrons based on magnetic anomaly picks and the Pacific-Antarctic Ridge is highlighted with thick red lines. Red tagged lines are synthetic flowlines generated from the stage rotations; blue dots mark the center points of the flowlines. Blue lines mark the edges of the array of FZs A through O and the bounding transverse ridges are contoured light blue. Inset in [a]: map of seafloor spreading provinces. The blue and purple regions were generated by Pacific-Antarctic spreading, the yellow and light green regions by Australia-East Antarctic spreading, the green region by Australia-Antarctic spreading before chron C8 (26.6 Ma) , the dark green region by Australia-Lord Howe Rise (Tasman Sea) spreading and the pink region by Australia-Pacific spreading between chrons C20 and C8 (43.8 to 26.6 Ma). Detailed maps [b] and [c] show the available multibeam bathymetry data from NBP9407, NBP9702, NBP9909, NBP0209, NBP0305A, NBP0402, NBP0501A and NBP0701 cruises on an image of the satellite-derived, free-air gravity field. Map projection same as in Figures 1.1, 1.2 and 1.3.

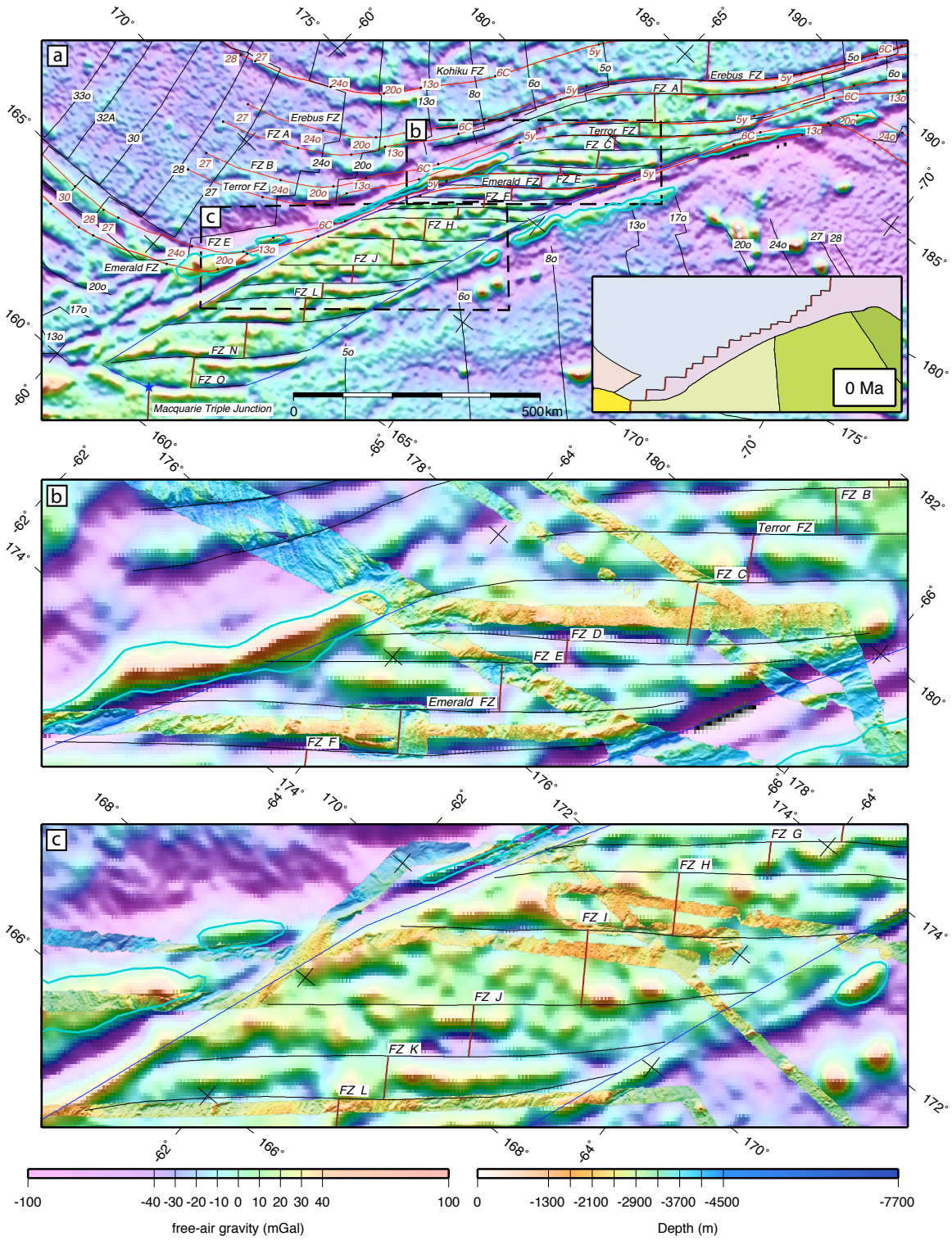
a
b
c
Kohiku FZ
Erebus FZ
FZ A
FZ B
Terror FZ
FZ C
Emerald FZ
FZ E
FZ F
FZ H
FZ J
FZ L
FZ N
FZ O
Macquarie Triple Junction
0
500km
0 Ma
FZ B
Terror FZ
FZ C
FZ D
FZ E
Emerald FZ
FZ F
FZ G
FZ H
FZ I
FZ J
FZ K
FZ L
-100 -40 -30 -20 -10 0 10 20 30 40 100
free-air gravity (mGal)
0 -1300 -2100 -2900 -3700 -4500 -7700
Depth (m)

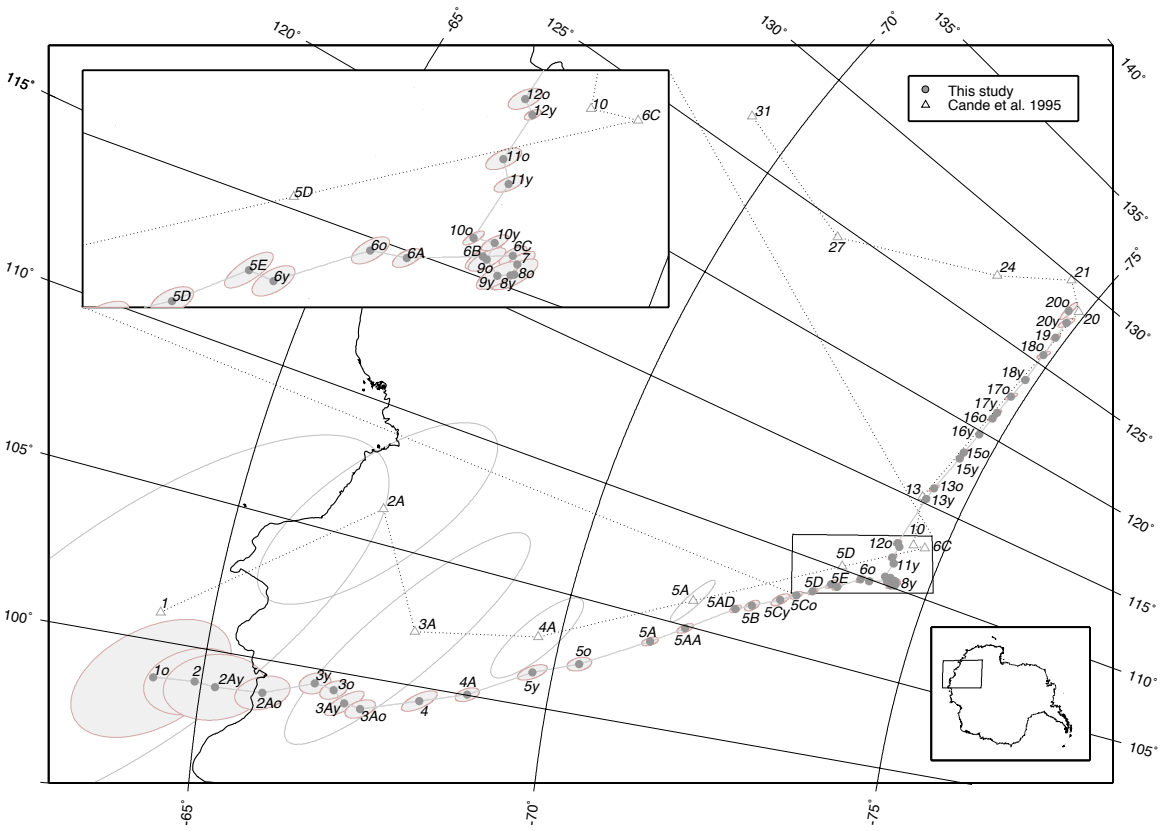

Figure 1.6: Comparison of our rotation poles (solid line) with the *Cande et al.* [1995] poles (dashed line) for the Pacific-Antarctic Ridge. Shaded ellipses show 95% confidence regions associated with the new poles. Open ellipses represent 95% confidence regions for chron C5A (12.3 Ma) and younger from *Cande et al.* [1995]. All poles are antipodal to those listed in Table 1.1. Map projection is stereographic centered on 69° S, 180° W.

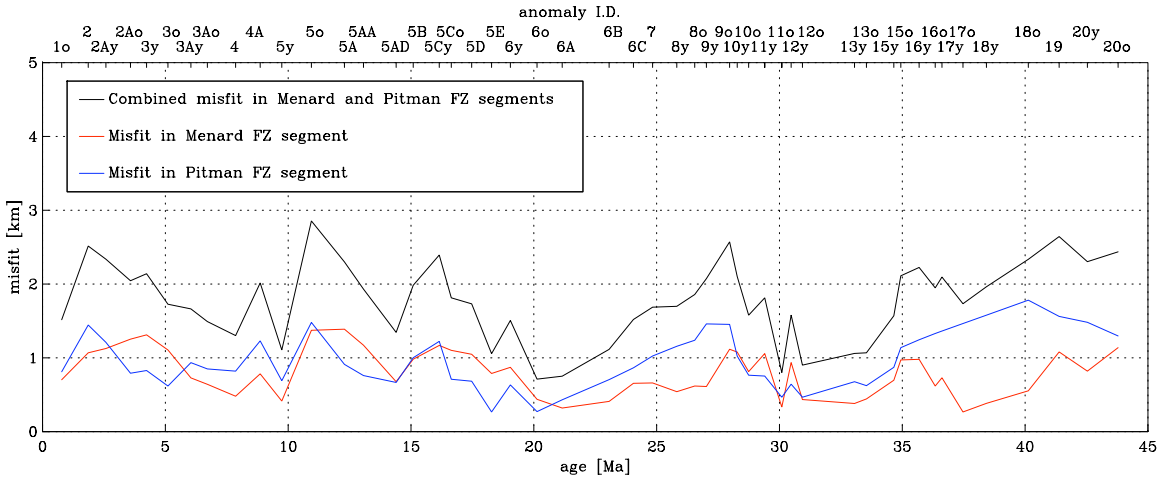

Figure 1.7: Individual and combined misfit in the Menard and Pitman FZ segments according to the *Chang* [1987; 1988] method.

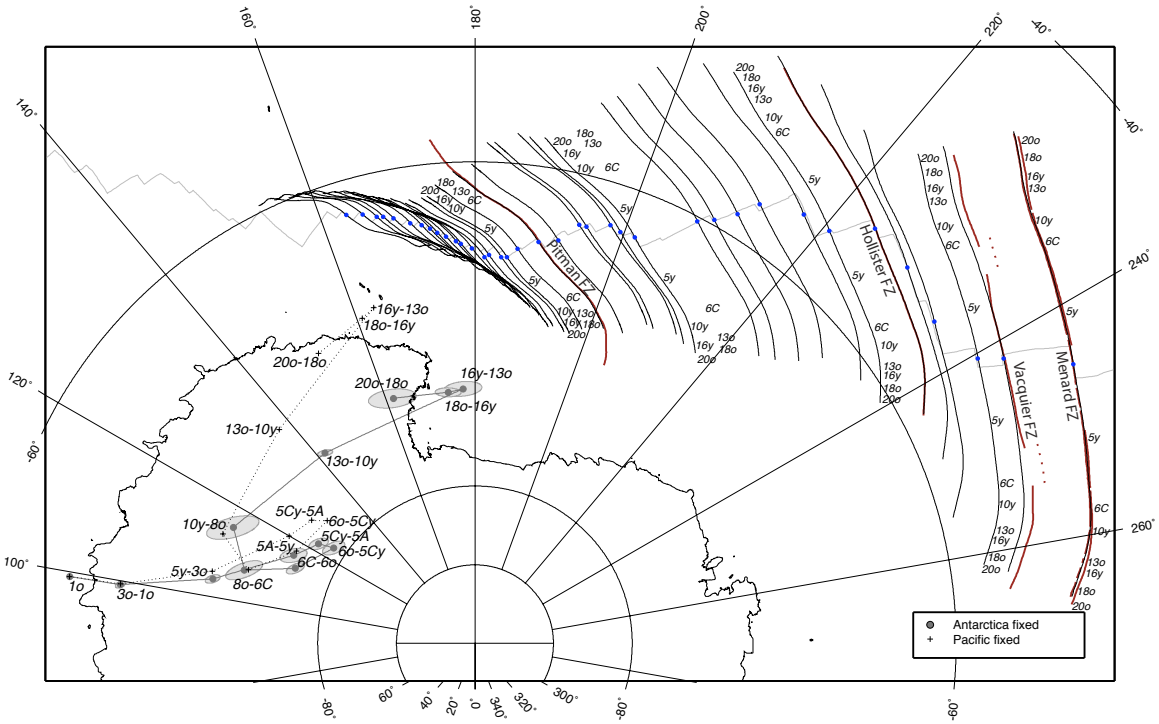

Figure 1.8: Stage poles for Pacific-Antarctic relative displacements. Grey dots and crosses are poles in the Antarctic plate and Pacific plate reference frames respectively. Synthetic flowlines (black) based on the poles are plotted for many of the present day ridge offsets. Blue dots mark the center points of the flowlines. The traces of the Menard, Vacquier, Hollister and Pitman FZs are highlighted in red. 95% confidence regions are shown for the stage poles in the Antarctic reference frame. Pacific-fixed 95% confidence regions are similar in size but are omitted for clarity. Map projection same as in Figure 1.6.

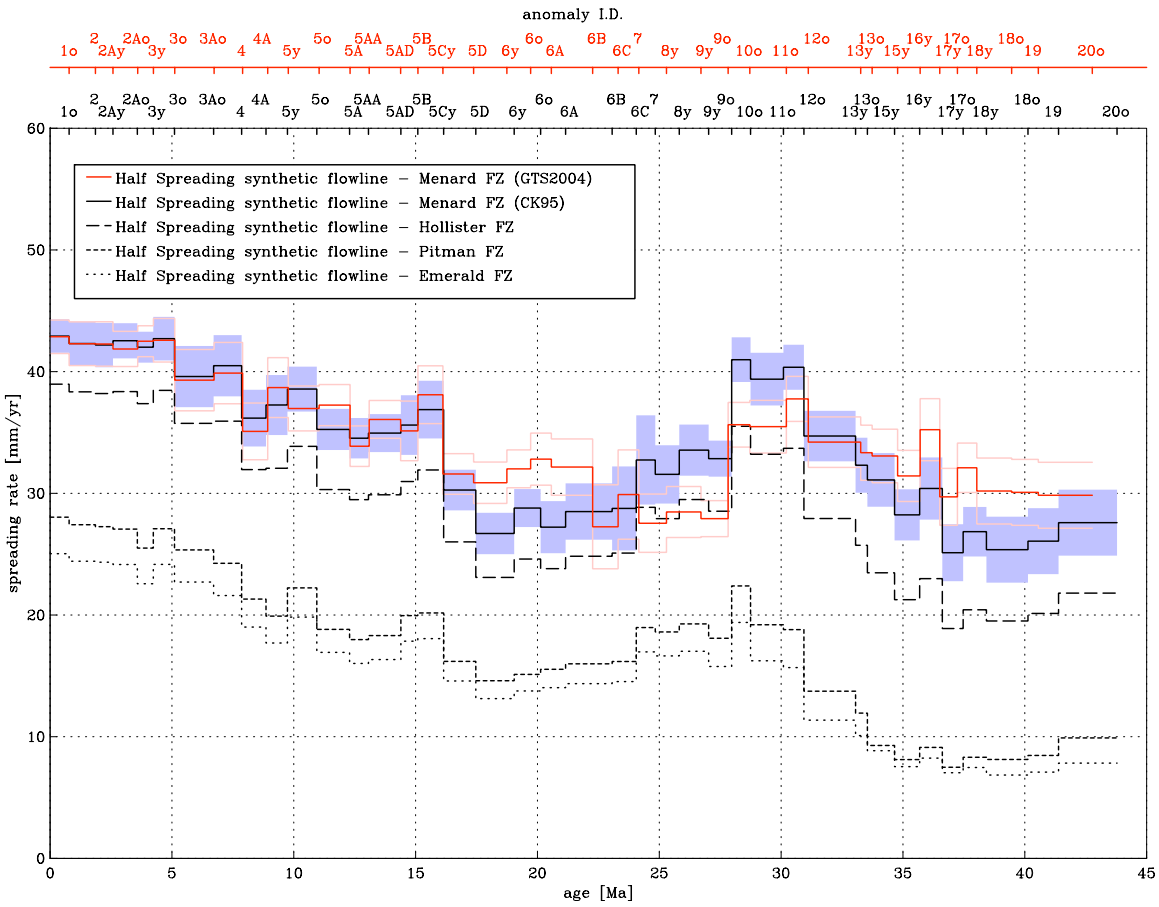

Figure 1.9: Half-spreading rates calculated from the rotation parameters along flowlines at the Menard, Hollister, Pitman and Emerald FZs. Black lines represent spreading rates based on the CK95 timescale [Cande and Kent, 1995] and the red line represents spreading rates based on the GTS2004 timescale [Ogg and Smith, 2004]. Shading and pink lines are the 95% confidence limits based on stage rotations for the CK95 and GTS2004 timescales respectively.

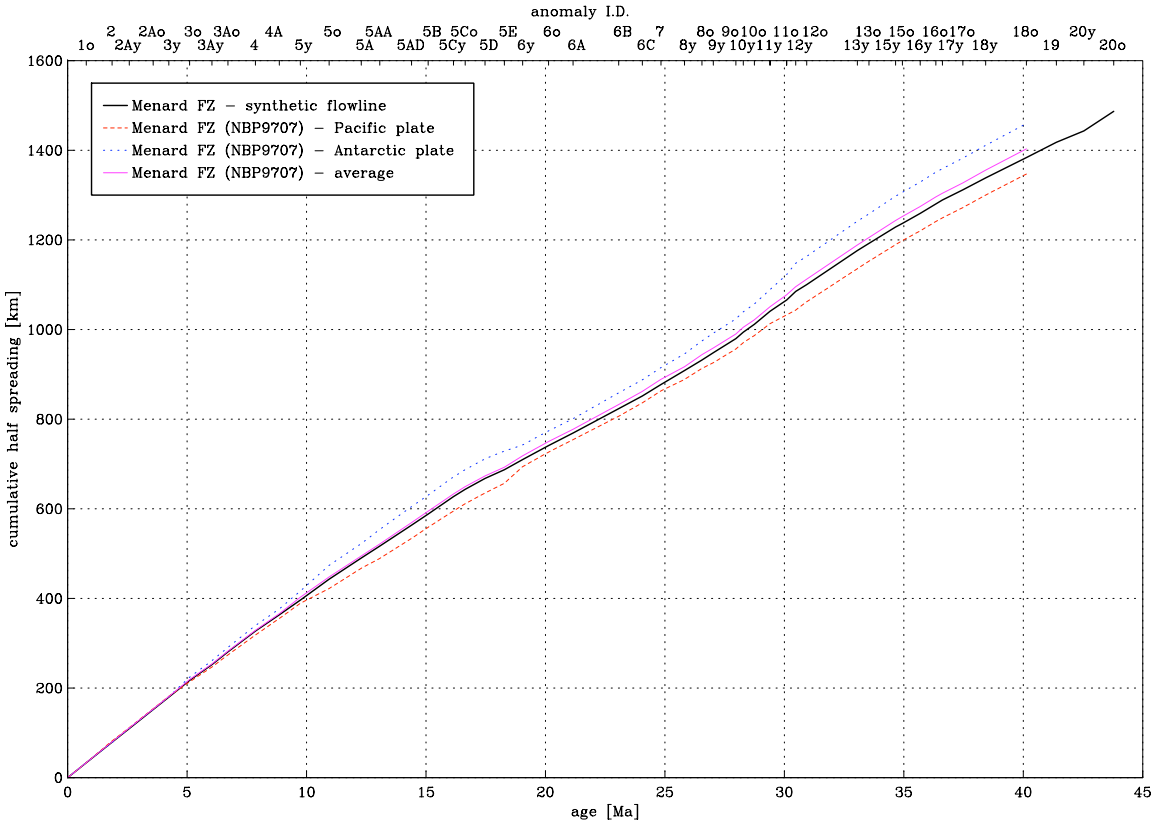

Figure 1.10: Cumulative half-spreading based on the flowline at the Menard FZ in comparison with the NBP9707 ship track that followed a route perpendicular to spreading lineation azimuths about 100 km north of the FZ.

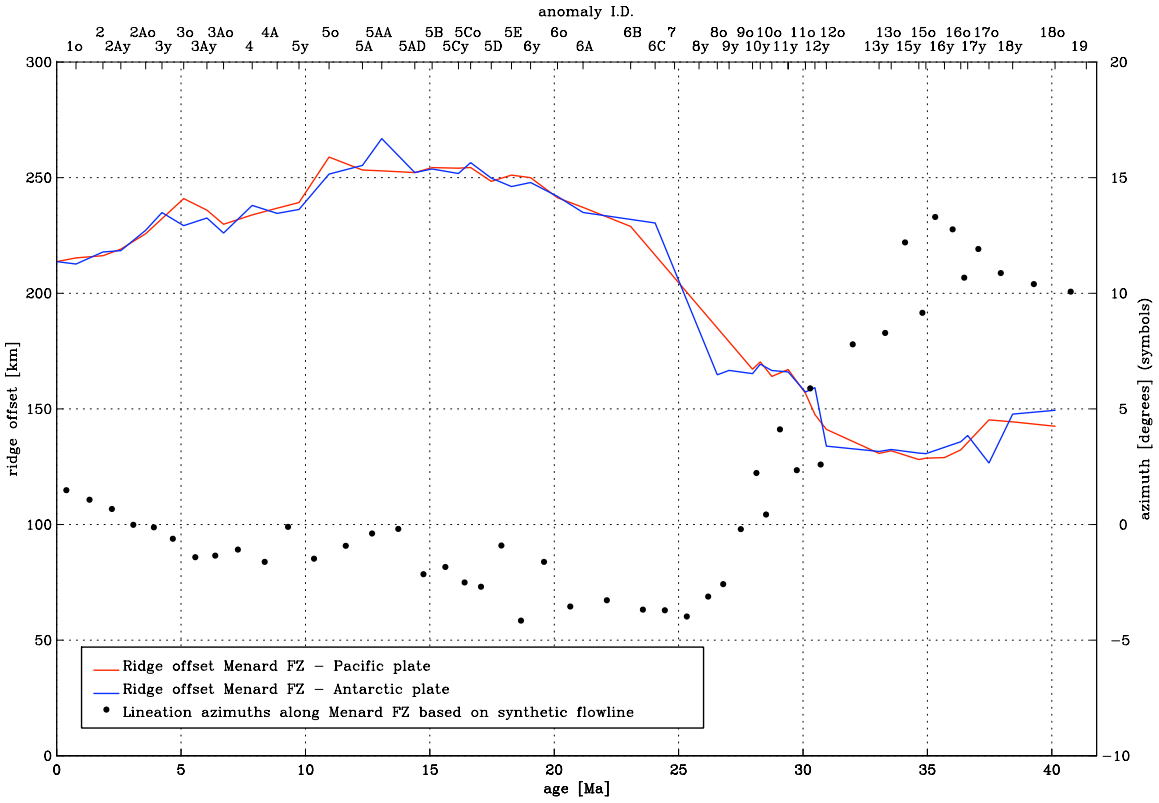

Figure 1.11: Ridge offset (lines) and lineation azimuths (dots) calculated from the rotation parameters at the Menard FZ. Oblique Mercator projection used to calculate lineation azimuths same as in Figures 1.1, 1.2, 1.3 and 1.5.

Figure 1.12: Reconstruction of the Emerald, Terror, Erebus and Kohiku FZs and FZs A through O (red flowlines and tags) based on the rotation parameters in Table 1.1. Antarctic plate is fixed. Frames show configurations at 3.6 Ma (chron C2Ao), 6.7 Ma (chron C3Ao), 9.7 Ma (chron C5y), 24.1 Ma (chron C6C), 33.1 Ma (chron C13o), 43.8 Ma (chron C20o) and 53.3 Ma (chron C24o). Blue dots mark the center points of the flowlines. The black tagged lines are isochrons based on magnetic anomaly picks and the location of paleo-spreading ridges is highlighted with thick red lines. Dark blue lines mark the edges of the array of FZs A through O and the bounding transverse ridges are contoured light blue. Colors represent the seafloor spreading provinces: blue and purple regions were generated by Pacific-Antarctic spreading, the yellow and light green regions by Australia-East Antarctic spreading, the yellowish brown and green regions by Australia-Antarctic spreading before chron C8 (26.6 Ma), the dark green and orange regions by Australia-Lord Howe Rise (Tasman Sea) spreading and the pink region by Australia-Pacific spreading between chrons C20 and C8 (43.8 to 26.6 Ma). The Iselin Rift, an extensional plate boundary between West and East Antarctica prior to chron C24 (53.3 Ma) [*Marks and Stock*, 1997], is shown as a dark grey dashed line. Map projection same as in Figures 1.1, 1.2, 1.3 and 1.5. See Figure 1.5 for the present configuration of these transform faults.

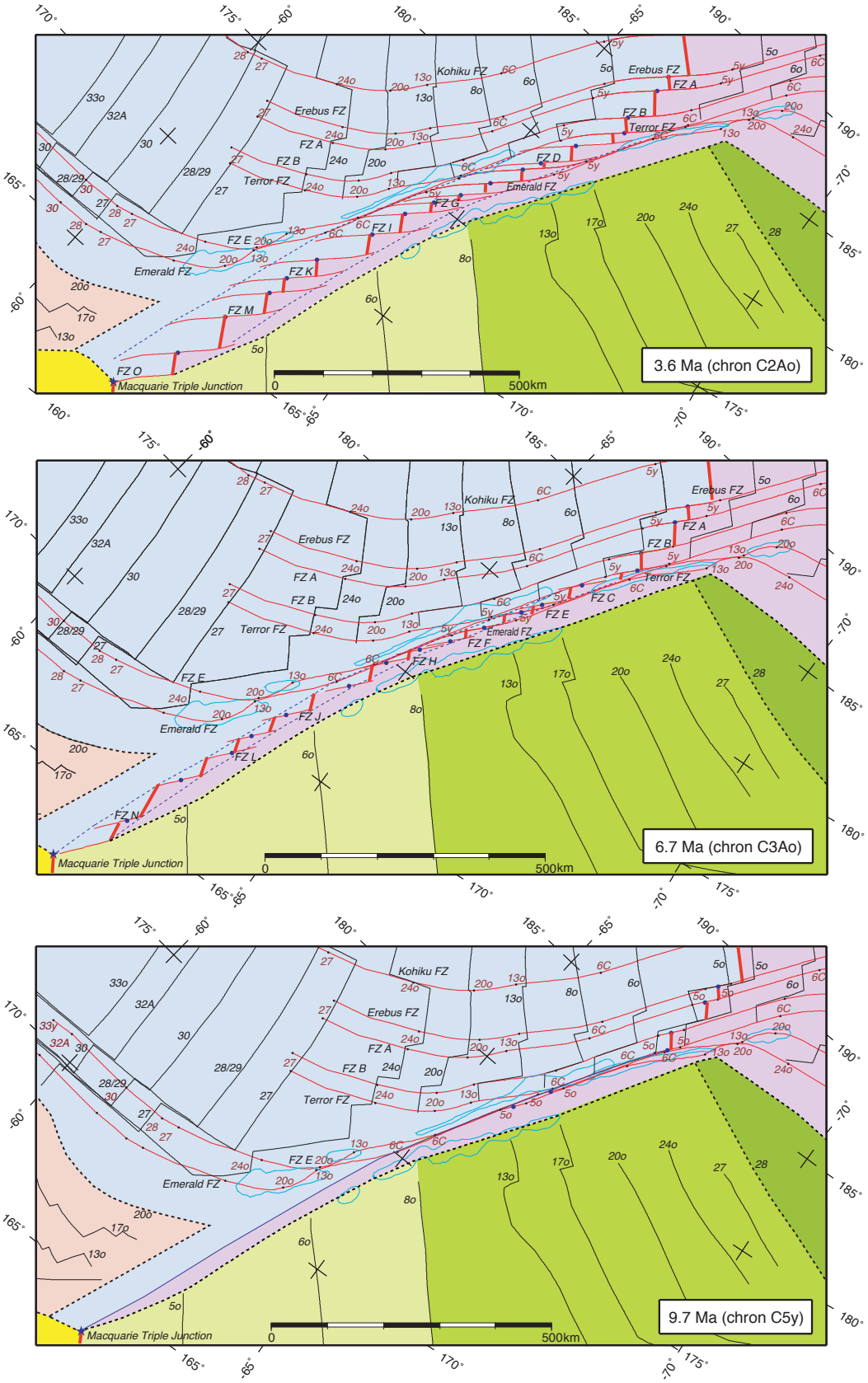
Kohiku FZ
Erebus FZ
FZ A
FZ B
Terror FZ
FZ D
Emerald FZ
FZ G
FZ I
FZ E
FZ K
FZ M
FZ O
Macquarie Triple Junction
0
500km
3.6 Ma (chron C2Ao)
Kohiku FZ
Erebus FZ
FZ A
FZ B
Terror FZ
FZ C
FZ E
Emerald FZ
FZ F
FZ H
FZ J
FZ L
FZ N
Macquarie Triple Junction
0
500km
6.7 Ma (chron C3Ao)
Kohiku FZ
Erebus FZ
FZ A
FZ B
Terror FZ
FZ E
Emerald FZ
Macquarie Triple Junction
0
500km
9.7 Ma (chron C5y)

Figure 1.12 (continued)

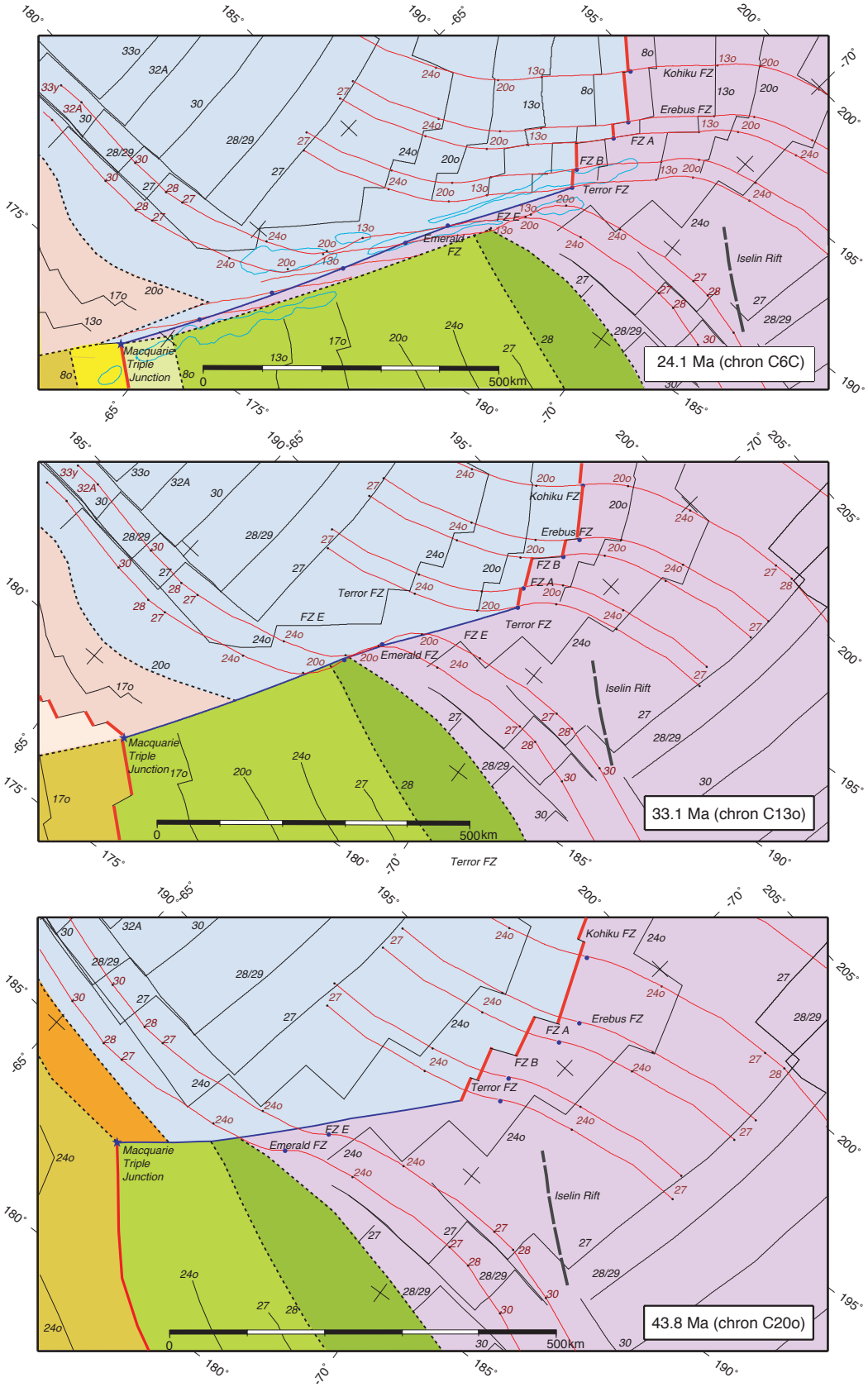
24.1 Ma (chron C6C)
33.1 Ma (chron C13o)
43.8 Ma (chron C20o)
Kohiku FZ
Erebus FZ
FZ A
FZ B
Terror FZ
FZ E
Emerald FZ
Iselin Rift
Macquarie Triple Junction
0
500km

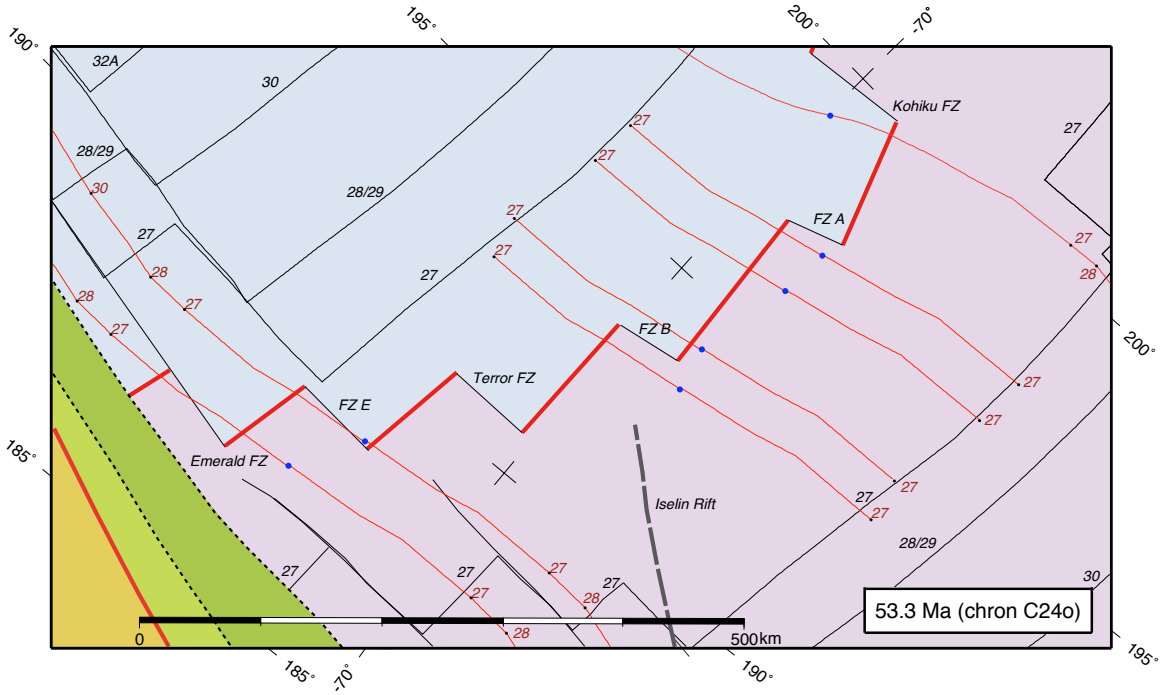

Figure 1.12 (continued)

Table 1.1: Finite rotations and covariance matrices of the Pacific plate relative to the Antarctic plate.

Age (Ma)	Mag. an.	Polarity Chron	Lat. (°N)	Long. (°E)	Angle (deg)	$\hat{k}$	a	b	c	d	e	f	g	Mag. Pts	FZ Pts	Ab. Hill Pts	Mag. Segs	FZ Segs
0.78	1o	C1n (o)	64.303	-81.212	0.676	2.62	1.18	.647	1.59	4.26	7.92	4.43	9	43	45	2	9	3
1.86	2	C2n (m)	64.901	-81.138	1.606	1.21	9.05	.251	8.38	6.54	9.72	3.00	9	34	32	1	6	2
2.58	2Ay	C2An.1n (y)	65.204	-81.225	2.227	2.05	27.8	-0.669	2.00	2.37	3.41	8.94	9	32	31	1	5	2
3.58	2Ao	C2An.3n (o)	65.897	-81.165	3.109	1.38	10.4	.661	12.3	8.30	13.1	42.8	9	31	34	1	6	2
4.24	3y	C3n.1n (m)	66.624	-80.533	3.702	2.43	10.0	.662	10.1	7.62	11.4	34.4	9	29	35	8	4	2
5.11	3o	C3n.4n (m)	66.909	-80.658	4.480	2.62	13.6	1.47	19.6	7.24	13.3	58.6	9	30	39	1	5	3
6.04	3Ay	C3An.1n (y)	67.091	-81.081	5.211	2.91	3.53	2.55	4.27	3.23	4.07	8.12	8	28	39	6	4	3
6.71	3Ao	C3An.2n (o)	67.331	-81.202	5.808	1.48	1.32	.240	2.17	.821	1.54	6.55	8	26	41	7	4	3
7.86	4	C4n.2n (m)	68.162	-80.540	6.830	1.41	2.38	.954	4.41	1.50	2.67	11.8	8	30	41	9	5	3
8.86	4A	C4An (m)	68.833	-79.969	7.639	1.34	1.12	.339	1.69	.968	1.56	5.03	8	29	44	1	5	3
9.74	5y	C5n.1n (y)	69.707	-78.566	8.417	1.01	1.59	.597	3.17	1.22	2.32	8.91	8	28	45	9	5	3
10.95	5o	C5n.2n (o)	70.356	-77.813	9.481	1.75	2.52	.662	3.49	2.72	3.92	10.6	8	31	47	7	4	3
12.29	5A	C5An.2n (m)	71.293	-76.115	10.631	1.25	.964	.497	1.45	1.12	1.60	3.84	8	29	52	1	5	3
13.06	5AA	C5AAn (m)	71.746	-75.122	11.283	1.37	1.55	.850	2.19	1.34	1.92	5.25	8	21	53	1	5	3
14.39	5AD	C5ADn (m)	72.381	-73.576	12.420	2.13	1.43	.702	1.60	1.11	1.55	3.61	8	22	54	1	5	3
15.09	5B	C5Bn.2n (m)	72.601	-73.192	13.012	2.78	4.48	1.92	4.50	2.97	4.15	9.77	8	24	53	1	6	3
16.1	5Cy	C5Cn.1n (m)	72.974	-72.498	13.948	2.27	6.11	3.17	7.43	4.10	5.52	16.3	8	18	53	1	5	3
16.64	5Co	C5Cn.3n (m)	73.181	-72.032	14.344	1.47	1.66	.802	2.28	1.21	1.75	5.33	8	18	51	1	5	3
17.4	5D	C5Dn (m)	73.394	-71.580	14.929	1.47	1.47	.678	1.72	1.04	1.47	3.97	8	17	52	1	5	3
18.28	5E	C5En (y)	73.617	-70.909	15.418	1.88	3.33	1.92	3.18	1.90	2.40	4.94	8	12	52	1	4	3
19.05	6y	C6n (y)	73.712	-70.936	15.946	1.41	2.02	.876	2.31	1.18	1.65	4.44	8	13	50	2	5	3
20.13	6o	C6n (o)	74.001	-70.157	16.727	1.93	2.00	.848	2.37	1.13	1.54	4.65	8	10	51	1	4	3
21.1	6A	C6An.2n (m)	74.133	-70.089	17.381	2.66	1.68	.796	2.09	1.14	1.58	4.36	8	12	52	1	4	3
23.07	6B	C6Bn.2n (o)	74.385	-69.727	18.675	2.83	3.51	1.83	4.07	1.95	1.71	9.31	8	10	55	1	4	3
24.06	6C	C6Cn.3n (m)	74.482	-69.581	19.347	2.08	2.33	1.21	2.56	1.36	1.77	4.59	8	9	55	1	3	3
24.84	7	C7n.2n (y)	74.509	-69.664	19.923	2.45	3.89	1.35	6.05	1.82	.416	1.86	8	9	56	1	4	3
25.82	8y	C8n.1n (y)	74.499	-69.836	20.625	2.03	4.18	2.23	4.20	2.04	2.35	6.79	8	12	59	9	3	3
26.55	8o	C8n.2n (o)	74.511	-69.806	21.175	1.12	2.73	1.51	3.01	1.63	2.13	5.22	8	15	60	1	4	3
27.03	9y	C9n (y)	74.455	-69.900	21.531	1.30	2.75	1.54	3.04	1.64	2.03	5.38	8	11	58	1	4	3
27.97	9o	C9n (o)	74.401	-69.747	22.234	1.30	2.42	1.44	2.63	1.57	2.08	4.34	8	14	60	1	4	3
28.28	10y	C10n.1n (y)	74.407	-69.504	22.575	1.58	2.13	1.32	2.28	1.51	2.03	3.88	8	17	59	1	5	3
28.75	10o	C10n.2n (o)	74.330	-69.543	22.953	2.92	2.33	1.32	2.48	1.36	1.77	3.95	8	13	67	1	5	3
29.40	11y	C11n.1n (y)	74.378	-68.714	23.662	2.20	1.81	1.09	2.14	1.42	1.91	4.16	8	18	57	2	6	3
30.10	11o	C11n.2n (o)	74.329	-68.430	24.232	1.12	1.94	.960	2.34	1.25	1.67	4.75	8	16	56	2	6	3
30.48	12y	C12n (y)	74.366	-67.750	24.708	2.67	1.97	1.00	2.10	1.30	1.74	3.88	8	16	48	1	5	3
30.94	12o	C12n (o)	74.320	-67.593	25.058	1.15	1.92	1.00	1.99	1.30	1.74	3.95	8	17	46	1	5	3
33.06	13y	C13n (y)	74.444	-64.739	26.969	1.83	3.27	1.67	3.13	1.63	2.17	4.92	8	16	45	2	7	3
33.55	13o	C13n (o)	74.479	-64.015	27.395	1.57	5.29	3.16	4.72	2.68	3.37	6.19	8	15	49	2	6	3
34.66	15y	C15n (y)	74.621	-61.886	28.395	1.11	4.21	2.70	4.19	2.47	3.27	5.61	8	18	56	2	6	3
34.94	15o	C15n (o)	74.634	-61.485	28.615	2.77	1.22	.805	1.21	.738	.956	1.64	7	14	57	1	4	3
35.69	16y	C16n.2n (y)	74.702	-60.180	29.234	1.46	4.22	2.73	4.36	2.54	3.22	6.03	8	10	60	1	3	3
36.34	16o	C16n.2n (o)	74.750	-59.047	29.808	2.96	1.27	.852	1.30	.801	1.03	1.80	7	11	59	1	3	3
36.62	17y	C17n.1n (y)	74.763	-58.638	30.049	1.15	4.14	2.73	4.31	2.55	3.36	5.90	8	14	60	1	4	3
37.47	17o	C17n.1n (o)	74.816	-57.440	30.678	2.01	1.32	.885	1.37	.825	1.08	1.89	7	14	58	1	4	3
38.43	18y	C18n.1n (y)	74.855	-56.211	31.411	2.13	4.11	3.04	4.83	3.05	4.02	7.09	8	11	70	1	4	4
40.13	18o	C18n.2n (o)	74.868	-54.460	32.620	2.77	1.48	1.04	1.61	.982	1.34	2.24	7	16	58	2	6	4
41.39	19	C19n (m)	74.859	-53.254	33.532	1.01	4.91	2.75	5.98	2.72	4.00	9.71	8	15	49	1	7	4
42.54	20y	C20n (y)	74.856	-52.225	34.217	1.85	3.21	1.60	3.94	1.48	1.94	6.15	7	16	30	1	6	3
43.79	20o	C20n (o)	74.775	-51.610	35.288	1.06	5.71	.227	8.84	.258	.295	14.6	7	8	14	1	3	1

Ages are from *Cande et al*. [1995] except for chrons C3Ay and C3Ao, which are from *Krijgsman et al.* [1999]. Mag. an. = magnetic anomaly. (y), (o) and (m) = young and old ends and middle of Polarity Chron, respectively. Mag. Pts, FZ Pts and Ab. hill Pts = the number of magnetic anomaly, fracture zone and abyssal hill points, respectively. Mag. Segs and FZ Segs = the number of segments with magnetic anomaly and fracture zone data, respectively. The covariance matrix is given by the formula

$$\frac{1}{\hat{k}} * \begin{pmatrix} a & b & c \\ b & d & e \\ c & e & f \end{pmatrix} * 10^{-g}$$, where the values of a-f are given in radians squared.

1.14 REFERENCES

Atwater, T., and P. Molnar (1973), Relative motion of the Pacific and North American plates deduced from sea-floor spreading in the Atlantic, Indian and South Pacific Oceans, in *Proceedings of the Conference on Tectonic Problems of the San Andreas Fault, Geological Sciences, vol. XIII*, edited by R. L. Kovach and A. Nur, pp. 136-148, Stanford University Publications in Geological Sciences, Stanford, CA.

Atwater, T., and J. Severinghaus (1989), Tectonic maps of the Northeast Pacific, in *The Eastern Pacific Ocean and Hawaii, vol. N*, edited by E. L. Winterer, D. M. Hussong and R. W. Decker, pp. 15-20, Geological Society of America, Boulder, Colorado, The Geology of North America.

Atwater, T., J. Sclater, D. Sandwell, J. Severinghaus, and M. S. Marlow (1993), Fracture zone traces across the North Pacific Cretaceous Quiet Zone and their tectonic implications, in *The Mesozoic Pacific: Geology, Tectonics, and Volcanism, Geophysical Monograph 77*, edited by M. S. Pringle, W. W. Sager, W. V. Sliter and S. Stein, pp. 137-154, American Geophysical Union, Washington, DC.

Bernard, A., M. Munschy, Y. Rotstein, and D. Sauter (2005), Refined spreading history at the Southwest Indian Ridge for the last 96 Ma, with the aid of satellite gravity data, *Geophysical Journal International, 162*(3), 765-778, DOI: 10.1111/j.1365-246X.2005.02672.x.

Briais, A., D. Aslanian, L. Géli, and H. Ondréas (2002), Analysis of propagators along the Pacific-Antarctic Ridge: evidence for triggering by kinematic changes, *Earth and Planetary Science Letters, 199*(3-4), 415-428, DOI: 10.1007/BF00286203.

Cande, S. C., E. M. Herron, and B. R. Hall (1982), The early Cenozoic tectonic history of the Southeast Pacific, *Earth and Planetary Science Letters, 57*(1), 63-74, DOI: 10.1016/0012-821X(82)90173-X.

Cande, S. C., J. L. LaBrecque, and W. F. Haxby (1988), Plate kinematics of the South Atlantic: Chron C34 to present, *Journal of Geophysical Research-Solid Earth and Planets*, *93*(B11), 13479-13492.

Cande, S. C., and D. V. Kent (1995), Revised calibration of the geomagnetic polarity timescale for the Late Cretaceous and Cenozoic, *Journal of Geophysical Research-Solid Earth, 100*(B4), 6093-6095, DOI: 10.1029/94JB03098.

Cande, S. C., C. A. Raymond, J. M. Stock, and W. F. Haxby (1995), Geophysics of the Pitman Fracture-Zone and Pacific-Antarctic plate motions during the Cenozoic, *Science, 270*(5238), 947-953, DOI: 10.1126/science.270.5238.947.

Cande, S. C., and J. M. Stock (2004a), Pacific-Antarctic-Australia motion and the formation of the Macquarie Plate, *Geophysical Journal International, 157*(1), 399-414, DOI: 10.1111/j.1365-2699.2006.01643.x.

Cande, S. C., and J. M. Stock (2004b), Cenozoic reconstructions of the Australia-New Zealand-South Pacific Sector of Antarcticas, in *The Cenozoic Southern Ocean: Tectonics, Sedimentation and Climate Change Between Australia and Antarctica, AGU Monograph Series, vol. 151*, edited by N. Exxon, J. Kennett and M. Malone, pp. 5-15, American Geophysical Union, Washington, DC.

Chang, T. (1987), On the statistical properties of estimated rotations, *Journal of Geophysical Research-Solid Earth and Planets*, *92*(B7), 6319-6329.

Chang, T. (1988), Estimating the Relative Rotations of Two Tectonic Plates from Boundary Crossings, *Journal of the American Statistical Association*, *83*(404), 1178-1183.

Cochran, J. R., and J. C. Sempéré (1997), The southeast Indian ridge between 88°E and 118°E: Gravity anomalies and crustal accretion at intermediate spreading rates, *Journal of Geophysical Research-Solid Earth, 102*(B7), 15463-15487, DOI: 10.1029/97JB00511.

DeMets, C., R. G. Gordon, D. F. Argus, and S. Stein (1990), Current plate motions, *Geophysical journal international*, *101*(2), 425-478.

Eakins, B. W. (2002), Structure and Development of Oceanic Rifted Margins, 174 pp, Ph.D. Thesis, Scripps Institution of Oceanography.

Gallo, D. G., P. J. Fox, and K. C. MacDonald (1986), A sea beam investigation of the Clipperton Transform Fault: The morphotectonic expression of a fast slipping transform boundary, *Journal of Geophysical Research-Solid Earth and Planets*, *91*(B3), 3455-3468.

Gans, K. D., D. S. Wilson, and K. C. Macdonald (2003), Pacific Plate gravity lineaments: Diffuse extension or thermal contraction?, *Geochemistry Geophysics Geosystems, 4*, 1074, DOI: 10.1029/2002GC000465.

Géli, L., D. Aslanian, J. L. Olivet, I. Vlastelic, L. Dosso, H. Guillou, and H. Bougault (1998), Location of Louisville hotspot and origin of Hollister ridge: geophysical constraints, *Earth and Planetary Science Letters, 164*(1-2), 31-40, DOI: 10.1016/S0012-821X(98)00217-9.

Goodwillie, A. M., and B. Parsons (1992), Placing bounds on lithospheric deformation in the Central Pacific-Ocean, *Earth and Planetary Science Letters, 111*(1), 123-139, DOI: 10.1016/0012-821X(92)90174-T.

Gordon, R. G. (1998), The plate tectonic approximation: Plate nonrigidity, diffuse plate boundaries, and global plate reconstructions, *Annual Review of Earth and Planetary Sciences, 26*, 615-642, DOI: 10.1146/annurev.earth.26.1.615.

Hellinger, S. J. (1981), The uncertainties of finite rotations in plate tectonics, *Journal of Geophysical Research*, *86*(NB10), 9312-9318.

Klingelhoefer, H., H. Ondréas, A. Briais, C. Hamelin, and L. Dosso (2006), New Structural and Geochemical Observations from the Pacific-Antarctic Ridge between 52°45'S and 41°15'S, *Geophysical Research Letters, 33*, 1-5, DOI: 10.1029/2006GL027335.

Krijgsman, W., F. J. Hilgen, I. Raffi, F. J. Sierro, and D. S. Wilson (1999), Chronology, causes and progression of the Messinian salinity crisis, *Nature, 400*(6745), 652-655, DOI: 10.1038/23231.

Lodolo, E., and F. Coren (1997), A Late Miocene plate boundary reorganization along the westernmost Pacific-Antarctic ridge, *Tectonophysics, 274*(4), 295-305, DOI: 10.1016/S0040-1951(97)00005-X.

Lonsdale, P. (1986), Tectonic and magmatic ridges in the eltanin fault system, South Pacific, *Marine Geophysical Researches, 8*(3), 203-242, DOI: 10.1007/BF00305484.

Lonsdale, P. (1994a), Structural geomorphology of the eltanin fault system and adjacent transform faults of the Pacific-Antarctic plate boundary, *Marine Geophysical Researches, 16*(2), 105-143, DOI: 10.1007/BF01224756.

Lonsdale, P. (1994b), Geomorphology and structural segmentation of the crest of the southern (Pacific-Antarctic) East Pacific Rise, *Journal of Geophysical Research-Solid Earth*, *99*(B3), 4683-4702.

Lourens, L. J., F. Hilgen, N. J. Shackleton, J. Laskar, and D. S. Wilson (2004), The Neogene Period, in *A Geological Time Scale*, edited by F. M. Gradstein, J. G. Ogg and A. G. Smith, pp. 409-440, Cambridge University Press, Cambridge.

Macdonald, K. C., P. J. Fox, L. J. Perram, M. F. Eisen, R. M. Haymon, S. P. Miller, S. M. Carbotte, M. H. Cormier, and A. N. Shor (1988), A New View of the Mid-Ocean Ridge from the Behavior of Ridge-Axis Discontinuities, *Nature*, *335*(6187), 217-225.

Marks, K. M., and J. M. Stock (1997), Early Tertiary gravity field reconstructions of the Southwest Pacific, *Earth and Planetary Science Letters, 152*(1-4), 267-274, DOI: 10.1016/S0012-821X(97)00139-8.

McAdoo, D., and S. Laxon (1997), Antarctic Tectonics: Constraints from an ERS-1 Satellite Marine Gravity Field, *Science, 276*(5312), 556-560, DOI: 10.1126/science.276.5312.556.

Menard, H. W., and T. Atwater (1969), Origin of Fracture Zone Topography, *Nature, 222*(5198), 1037-1040, DOI: 10.1038/2221037a0.

Menard, H. W., and T. E. Chase (1970), Fracture Zones, in *The Sea, vol. 4, part 1*, edited by A. E. Maxwell, pp. 421-444, Wiley Interscience, New York, NY.

Molnar, P., T. Atwater, J. Mammerickx, and S. M. Smith (1975), Magnetic Anomalies, Bathymetry and the Tectonic Evolution of the South Pacific since the Late Cretaceous, *Geophysical Journal of the Royal Astronomical Society, 40*(3), 383-420, DOI: 10.1111/j.1365-246X.1975.tb04139.x.

Ogg, J. G., and A. G. Smith (2004), The geomagnetic polarity time scale, in *A Geological Time Scale*, edited by F. M. Gradstein, J. G. Ogg and A. G. Smith, pp. 63-86, Cambridge University Press, Cambridge.

Pitman, W. C., E. M. Herron, and J. R. Heirtzler (1968), Magnetic anomalies in Pacific and sea floor spreading, *Journal of Geophysical Research, 73*(6), 2069-2085, DOI: 10.1126/science.154.3753.1164.

Royer, J. Y., P. Patriat, H. W. Bergh, and C. R. Scotese (1988), Evolution of the Southwest Indian Ridge from the Late Cretaceous (anomaly 34) to the Middle Eocene (anomaly 20), *Tectonophysics*, *155*(1-4), 235-260.

Royer, J. Y., and T. Chang (1991), Evidence for relative motions between the Indian and Australian Plates during the last 20 m.y. From plate tectonic reconstructions: Implication for the deformation of the Indo-Australian plate, *Journal of Geophysical Research-Solid Earth and Planets*, *96*(B7), 11779-11802.

Royer, J. Y., R. G. Gordon, and B. C. Horner-Johnson (2006), Motion of nubia relative to antarctica since 11 Ma: Implications for Nubia-Somalia, Pacific-North America, and India-Eurasia motion, *Geology, 34*(6), 501-504, DOI: 10.1046/j.1365-246X.2003.01917.x.

Sandwell, D. T. (1984), Thermomechanical evolution of oceanic fracture zones, *Journal of Geophysical Research*, *89*(NB13), 1401-1413.

Sandwell, D. T., and W. H. F. Smith (1997), Marine gravity anomaly from Geosat and ERS 1 satellite altimetry, *Journal of Geophysical Research-Solid Earth, 102*(B5), 10039-10054, DOI: 10.1029/96JB03223.

Searle, R. C., R. T. Bird, R. I. Rusby, and D. F. Naar (1993), The development of 2 oceanic microplates - Easter and Juan-Fernandez microplates, East Pacific Rise, *Journal of the Geological Society, 150*, 965-976, DOI: 10.1144/gsjgs.150.5.0965.

Stock, J., and P. Molnar (1988), Uncertainties and implications of the late Cretaceous and Tertiary position of North America relative to the Farallon, Kula, and Pacific plates, *Tectonics*, *7*(6), 1339-1384.

Symons, C. M., T. A. Meckel, S. Mosher, and M. F. Coffin (2004), Plate Kinematic Model and Resulting Evolution of Oceanic Transform Fault Tectonics Adjacent to the Macquarie Triple Junction, SW Pacific, *EOS Trans., AGU*, *85*(47).

Tebbens, S. F., and S. C. Cande (1997), Southeast Pacific tectonic evolution from early Oligocene to present, *Journal of Geophysical Research-Solid Earth, 102*(B6), 12061-12084, DOI: 10.1029/96JB02582.

Tebbens, S. F., S. C. Cande, L. Kovacs, J. C. Parra, J. L. LaBrecque, and H. Vergara (1997), The Chile ridge: A tectonic framework, *Journal of Geophysical Research-Solid Earth, 102*(B6), 12035-12059, DOI: 10.1029/96JB02581.

Weiland, C. M., and K. C. Macdonald (1996), Geophysical study of the East Pacific Rise 15°N-17°N: An unusually robust segment, *Journal of Geophysical Research-Solid Earth, 101*(B9), 20257-20273, DOI: 10.1029/96JB01756.

CHAPTER 2

Abyssal Hill Deflections at Pacific-Antarctic Ridge-Transform Intersections

ABSTRACT

Nearly complete coverage of shipboard multibeam bathymetry data at the right-stepping Menard and Pitman Fracture Zones allowed us to map abyssal hill deviations along their traces. In this study we distinguish between (a) J-shaped curvatures at their origin, where modeling is addressing primary volcanism and faulting following a curved zone and (b) straight abyssal hills getting bent in anti J-shaped curvatures, in response to increased coupling across the transform fault, after they were formed. We compared the mapped abyssal hill deflections to a detailed plate motion model for the Pacific-Antarctic Ridge to test how abyssal hill curvature correlates to changes in plate motion direction, which lead to periods of transtension or transpression. This test was based on the number and size of the abyssal hill deflections. The observations show a high abundance of J-shaped abyssal hills during periods of significant clockwise change in plate motion direction, which leads to transtension. The tip of the ridge axis can deflect up to 60° into the transform fault in response to changes in the stress field at Ridge-Transform Intersections. This is observed, in particular, at the Pitman Fracture Zone where there has been a ~15° clockwise rotation of the spreading direction azimuth during the last 9 Ma. In addition, we observed anti J-shaped curvatures at Menard, Pitman and Heirtzler Fracture Zones during periods of transpression when increased coupling across an oceanic transform fault is partially accommodated by distributed strike-slip deformation rather than solely by discontinuous displacement at the transform

fault. Anti J-shaped deflections typically develop in seafloor less than 2 million years (m.y.) old when the oceanic lithosphere is thin.

2.1 INTRODUCTION

Abyssal hills are topographic highs, oriented approximately parallel to the spreading axis, which cover most of the ocean floor except where buried beneath sediment [*Dietz et al.*, 1954; *Goff*, 1992; *Menard*, 1960; *Searle*, 1984]. They form within ~6 km of the spreading axis and the shape depends on the spreading rate [*Macdonald et al.*, 1996]. Abyssal hills often deviate from the regional trend at Ridge-Transform Intersections (RTIs) curving into the transform fault [*Crane*, 1976; *Fornari et al.*, 1989; *Fox and Gallo*, 1984; *Lonsdale*, 1977]. This curvature is typically explained by the transition from the extensional stress regime at the ridge axis to the shear stress field at the transform fault and is observed at both slow and fast spreading centers [*Fox and Gallo*, 1984; *Phipps Morgan and Parmentier*, 1984; *Tamsett and Searle*, 1988]. At RTIs and non-transform fault offsets, the direction of least horizontal principal stress (maximum tensile stress), S_h, is often strongly deviated [*Crane*, 1976; *Lonsdale*, 1978; *Tucholke and Schouten*, 1988] up to 45° from the spreading direction [*Grindlay et al.*, 1991; *Haxby and Parmentier*, 1988; *Karson and Dick*, 1983; *Searle and Laughton*, 1977; *Searle*, 1986], which is typically associated with strike-slip shear stress along the transform fault [*Fujita and Sleep*, 1978; *Grindlay and Fox*, 1993; *Phipps Morgan and Parmentier*, 1984] or normal stress related to the transform fault [*Gudmundsson*, 1993].

Grindlay and Fox [1993] predicted that the area of deformation and curvature of faults increases as a function of transform fault length and that larger ridge offsets will more likely result in stronger deformation in response to changes in relative plate motion.

Changes of the far-field stress in response to a counter-clockwise change in relative plate motion direction would result in compression across a right-stepping transform fault, increasing shear stress along the offset [*Tucholke and Schouten*, 1988]. The resulting transpressional forces increase coupling across the transform fault, which could result in distributed strike-slip deformation away from the transform fault and deflection of abyssal hills in anti J-shapes [*Sonder and Pockalny*, 1999]. On the other hand a clockwise change in relative plate motion direction is expected to result in extension of a right-stepping transform fault offset. The S_h direction, which is generally orthogonal to the ridge axis, tends to rotate clockwise near the RTI at right-stepping offsets [*Fujita and Sleep*, 1978] leading to J-shaped ridge curvature.

In this study, we analyze deflections and compare the observed trends in changes in abyssal hill curvature in order to determine which geologic processes and what parameters are responsible for the observed abyssal hill morphology at Pacific-Antarctic Ridge (PAR) right-stepping Fracture Zones (FZs). We will distinguish between the cases of (1) abyssal hills formed with a J-shaped curvature at their origin, where modeling is addressing primary volcanism and faulting following a curved zone and (2) straight abyssal hills getting bent in anti J-shaped curvatures, in response to increased coupling across the transform fault, after they were formed. Note that the sense of deflection in J-shaped or anti J-shaped abyssal hills is opposite at left-stepping FZ offsets. However, all of the PAR FZs that we described in this study have right-stepping offsets. Therefore we believe that using the J- and anti J-shape terminology is the clearest way to describe the abyssal hills that we have observed.

The PAR (Figure 2.1) is an excellent plate pair to study the correlation between changes of the far-field stress in response to adjustments in relative plate motion

direction and the nature and magnitude of abyssal hill tip deflections at RTIs. Extensive shipboard multibeam bathymetric coverage is available for the Menard and Pitman traces for oceanic crust younger than 45 Ma (during chron C20r; for this study we used the geomagnetic polarity timescale by *Cande and Kent* [1995] with revisions for chrons C3Ay and C3Ao as given by *Krijgsman et al.* [1999]). Moreover, the oceanic crust morphology at Menard and Pitman FZs is clearly visible in the multibeam bathymetry data for the most part since sediments are generally thinner than 200 m in the South Pacific basins [*Hayes and LaBrecque*, 1991; *Hayes et al.*, 2009]. Significantly thicker sediments are only found on oceanic crust formed before ~33 Ma (chron C13y) at Pitman FZ on the Antarctic plate.

J-shaped abyssal hills are typically observed in outer RTI corners where they are not overprinted by transform fault tectonics. An excellent example of J-shaped abyssal hill curvatures is available at the well-mapped Pitman Fracture Zone (FZ) [*Cande et al.*, 1995; *Macario et al.*, 1994] (Figure 2.2a). Each mapped J-shaped abyssal hill curvature in this study has been defined by the surface area (in km^2) enclosed by the curved part of the abyssal hill, the lineation azimuth trend and the FZ (Figure 2.2a inset). We chose to quantify the magnitude of abyssal hill deflection this way since the calculated surface area under abyssal hills that start curving at a greater distance from the FZ is significantly larger. For example, in the Figure 2.2a inset the left curvature starts at ~5 km from the FZ vs ~1 km for the middle curvature, a factor of 5 difference in distance. Correspondingly, the calculated area under these curved abyssal hills is 4.3 vs 0.3 km^2, a significantly larger factor of 12 difference. Another advantage of using this method is that errors in mapping the trend of the tip of the abyssal hill curvature are minimized. Mapping the abyssal hill curvature tips was difficult for some of the observed abyssal

hills since their traces could not be followed all the way to the FZ intersection. Furthermore, cracks that run from the FZ at low oblique angles such as Riedel shears (described in the "Transtension at Pitman Fracture Zone" and "Transtensional cracks and Riedel shears" sections) often merge with the tips of the observed abyssal hills. However, an error, if any, in the mapped trend of the tip of the curved abyssal hill has a small effect on the total surface area under the abyssal hill.

Anti J-shaped abyssal hills correlate well with transpressional periods and are observed in crust formed at the inner RTI corners. The best example of a transform fault experiencing transpression is the well-surveyed Clipperton FZ at the East Pacific Rise (EPR) (Figure 2.2b). Each mapped anti J-shaped abyssal hill curvature in this study has been defined by the angle between the abyssal hill trend lineation azimuth and the azimuth of the maximal deflection of the tip of the abyssal hill (Figure 2.2b inset). The curvature in the trace of Clipperton FZ suggests that the transpressional phase started at about 10 Ma, following a counter-clockwise reorientation of the EPR [*Pockalny*, 1997; *Wilson*, 1996]. Morphologic evidence for the recent compression at the Clipperton transform fault has been mapped in the form of anti J-shaped abyssal hill deflections, and a transpressional ridge [*Pockalny*, 1997] that overprinted the original structures (Figure 2.2b). Note that we took a different approach than our method to map J-shaped abyssal hills in order to compare our observed anti J-shaped abyssal hill curvatures to a model of distributed deformation of oceanic lithosphere near the transform fault [*Sonder and Pockalny*, 1999], which we describe in the "Modeling of anti-J shaped abyssal hill deflections" section. Moreover, the traces of anti J-shaped abyssal hill curvatures can be mapped accurately and their tips do not merge with cracks that formed by other processes, as can be the case for J-shaped abyssal hill observations.

Several studies have examined the changes in the stress field and corresponding ridge or abyssal hill tip deflections [*Grindlay and Fox*, 1993; *Neves et al.*, 2004; *Phipps Morgan and Parmentier*, 1984; *Sonder and Pockalny*, 1999]. However, these studies focused on observations from present day RTIs. The effective deflections resulting from changes in the relative plate motion, ridge offset and spreading rate over timescales of tens of m.y. remain unclear. In this paper we address this issue by quantifying the observed J-shaped abyssal hills that formed during periods of transtension and intervals when little change in relative plate motion occurred, and by quantifying anti J-shaped abyssal hill deflections that formed during periods of transpression at the PAR. *Croon et al.* [2008] determined 49 rotations that describe the relative motion between the Pacific and Antarctic plates in detail, mostly based on surveys of the Pitman and Menard FZs. We use this model in combination with the available shipboard bathymetry and magnetic anomaly data to better understand the observations.

2.2 TECTONIC EVOLUTION OF MENARD AND PITMAN FRACTURE ZONES

Shipboard multibeam bathymetry data were collected at most PAR transform fault offsets and ridge segments (Figure 2.1) between the Pitman and Udintsev FZs by *Géli et al.* [1997] and between the Udintsev FZ and the northern end of the PAR by *Lonsdale* [1994a; b]. Abyssal hill deflections have been observed near all PAR transform faults. However, for this study we focused on the Menard and Pitman FZs since these are the only two offsets with extensive shipboard multibeam bathymetry and magnetic anomaly data coverage along most of the FZ traces, which allowed us to study abyssal hill curvatures throughout their history. These data were used by *Croon et al.* [2008] to establish a detailed plate motion model for the PAR and allowed us to calculate the

changes in spreading rate, ridge offset and lineation azimuth, which is generally orthogonal to the spreading direction, for the Menard and Pitman FZs. A plate reorganization initiated the Pitman FZ around chron C27 (61 Ma) [*Cande et al.*, 1995]. However, the Menard FZ, which constrains a major component of the plate motion model by *Croon et al.* [2008], started at ~45 Ma (during chron C20r). Therefore, we only considered the time period between 45 and 0 Ma for this study. We used the plate motion model for the PAR by *Croon et al.* [2008] to calculate a high density of synthetic flowlines along the PAR in order to evaluate periods of transtension and transpression at the PAR. We interpolated the stage rotations from *Croon et al.* [2008] to a constant 2 m.y. interval in order to smooth the changes in lineation azimuths over time. At shorter time intervals small errors in magnetic anomaly picks or errors in the timescale would be reflected in unrealistically large fluctuations. A grid of the synthetic flowlines shows the changes in lineation azimuths in degrees per m.y. (Figure 2.3). The importance of the detailed plate motion model for the understanding of changes in the far-field stress is illustrated in Figure 2.3 since periods of transpression and transtension at the southwestern (Pitman FZ) and northeastern ends (Menard FZ) of the PAR start at separate times and have different durations and intensities.

The Menard FZ (Figures 2.4a-e) developed as a double splay, ~20 km apart, within a propagating rift system that generated the Henry and Hudson Troughs (Figure 2.1) following its start around 45 Ma [*Croon et al.*, 2008; *Eakins*, 2002]. Between 45 and 35 Ma (~chron C20r to C15o) Menard FZ experienced hardly any changes in lineation azimuths or ridge offset (~140 km) (Figure 2.5a). The half spreading rate at the latitude of Menard FZ was about 30 mm/a during this period. Between 35 and 25 Ma (~chron C15yo to C7) a 16° counterclockwise reorientation of the lineation azimuths put the right-

stepping Menard FZ under transpression. In response, the ridge offset grew from ~140 to 230 km while the distance between the two FZ splays decreased from 20 to 5-10 km. A big part of the increase in ridge offset occurred at the end of the transpressional period around 25 Ma (~chron C7) when a propagating rift south of Menard FZ (Figure 2.4a) transferred 65 km of former Pacific crust to the Antarctic plate [*Croon et al.*, 2008]. An increase in half spreading rate to ~40 mm/a between 35 and 30 Ma (~chron C15o to C11o) was followed by a drop to ~32 mm/a around 28 Ma (~chron C9o). Since 25 Ma, the lineation azimuth and ridge offset only experienced small changes. The most prominent event occurred around 5 Ma (~chron C3o) when the northern splay ceased to exist leaving a single FZ offset of about 220 km. Even though the Menard FZ experienced only a modest 2° clockwise reorientation of the lineation azimuths since 5 Ma (chron C3o), it put the 220 km long single offset under transtension, as reflected by a 5500 m deep transform fault valley, bounded by a transverse ridge on the north side. The seamount in the middle of the valley (Figure 2.4c) is possibly explained by a leaky transform fault as envisioned by *Menard and Atwater* [1969] and *Menard and Chase* [1970]. Since 25 Ma (~chron C7) the half spreading rate gradually increased from ~30 to 43 mm/a at present.

While crust at the latitude of Menard FZ has formed at intermediate spreading rates, at Pitman FZ (Figures 2.4f-h), which is located closer to the PAR finite rotation pole, crust accreted at slow ~10 mm/a half spreading rates starting around 45 Ma (Figure 2.5b). Between 45 and 31 Ma (~chron C20r to C12o) the lineation azimuths experienced modest reorientations, while the ridge offset remained relatively constant between 90 and 110 km. Around 35 Ma (~chron C15o) the half spreading rate gradually increased to 15 mm/a and jumped to 20 mm/a at 31 Ma (~chron C12o). A 12°

counterclockwise reorientation of the lineation azimuths between 31 and 23 Ma (~chron C12o to C6B) put the Pitman FZ under transpression. However, the ridge offset remained constant at ~100 km and the half spreading rate remained slow to intermediate at ~20 mm/a. Between 23 and 9 Ma (~chron C6B to C4A) the lineation azimuths, half spreading rate and ridge offset remained relatively constant. Since 9 Ma (~chron C4A) a ~15° clockwise reorientation of the lineation azimuths put significant transtension on the Pitman FZ. During this period the intermediate half spreading rate increased from 20 to 27 mm/a. The ridge offset decreased from ~100 km around 4 Ma (~chron C3y) to 70 km at present in response to recent ridge jumps.

2.3 J-SHAPED ABYSSAL HILL CURVATURE DATA

J-shaped abyssal hills are preserved in the crust at the outer RTI corner, where they were not overprinted by transform fault tectonics, during the last 45 Ma at the Menard and Pitman FZs (Figure 2.4). We digitized the trace of the top of each abyssal hill where the trend can be clearly followed from the straight part of the abyssal hill to its tip at the FZ intersection. We calculated the surface area (in km^2) enclosed by the curved part of the abyssal hill, the lineation azimuth trend and the FZ (Figure 2.2a inset) and compared this to the age of origin of each abyssal hill (Figure 2.6).

Because these abyssal hills are found at the outer RTI corner, they lie on the south side of the FZ on the Pacific plate and on the north side of the FZ on the Antarctic plate (Figure 2.6). We included straight abyssal hills (0 km^2 surface area in Figure 2.6) in our dataset for completeness. At Menard FZ we mapped 116 J-shaped and 17 straight abyssal hills south of the FZ on the Pacific plate and only 23 J-shaped and 9 straight abyssal hill north of the FZ on the Antarctic plate (Figures 2.6a & 2.4a-e). The unequal

number of observations per plate is due to insufficient or lacking multibeam bathymetry data north of significant parts of Menard FZ on the Antarctic plate, corresponding to large gaps in the observations (red symbols in Figure 2.6a). In contrast the observations south of Menard FZ (blue symbols in Figure 2.6b) on the Pacific plate are almost complete and significant gaps are only present before 40 Ma (~chron C18o). Only a few abyssal hills are observed inside the central corridor of Menard FZ (Figure 2.4a-e), which started as a ~20 km wide segment at 45 Ma (during chron C20r) and ceased to exist as a 5-10 km wide segment around 5 Ma (~chron C3o). The same behavior for formation of abyssal hill curvatures is expected in this narrow corridor. The lack of J-shaped abyssal hill observations in the central corridor can be explained by overshot volcanism from the large ridge segments on either side of the central corridor, which overprinted most of the abyssal hill traces. Therefore, we did not consider the observations from inside the Menard FZ central corridor in this study.

At Pitman FZ we mapped 86 J-shaped and 25 straight abyssal hills south of the FZ on the Pacific plate and 92 J-shaped and 7 straight abyssal hills north of the FZ on the Antarctic plate (Figures 2.6b & 2.4f-h). Large gaps in the observations south of Pitman FZ (blue symbols in Figure 2.6b) on the Pacific plate are mainly due to the lack of multibeam bathymetry data for crust older than 14 Ma (~chron C5AD). No observations are available north of Pitman FZ on the Antarctic plate (red symbols in Figure 2.6a) before ~33 Ma (chron C13y) since the abyssal hill morphology in that area is masked by thick sediments from West Antarctica.

Not all of the mapped J-shaped abyssal hills at the PAR formed at the ridge axis or very close by (within a few kilometers). Changes in ridge offset of more than 5 km occur frequently at Menard and Pitman FZs (Figure 2.5), which demonstrates that small ridge

jumps are common at the PAR. A significant number of our measured J-shaped abyssal hills probably have been formed as the propagating tip of a ridge-parallel crack, which started at a distance of more than 5 km from the ridge axis in response to a small ridge jump. However, it is very difficult to pick which J-shaped abyssal hills formed as the tip of a propagating crack. In Appendix A we discuss the role of propagating cracks in the formation of J-shaped abyssal hills in more detail.

A main objective of this study is to evaluate the effect of transtension on J-shaped abyssal hill formation. To some extend there are J-shaped abyssal hills present even when there is no or little transtension. To estimate the structures that represent transtension we have calculated the average area (as defined previously) for periods of no or little transpression or transtension at Pitman FZ. This arithmetic mean (0.8 km^2, standard deviation = 1.1 km^2) is drawn as a solid purple line in Figure 2.6b. We did not calculate this average at Menard FZ since no period of significant transtension occurred during its evolution. At Pitman FZ a large number of J-shaped abyssal hill curvatures that formed since 9 Ma (~chron C4A) are significantly bigger than 2 km^2 and represent the effect of transtension during that period.

2.4 CHANGES IN THE STRESS FIELD AT MENARD AND PITMAN RIDGE-TRANSFORM INTERSECTIONS

At Menard and Pitman FZs the magnitude of the abyssal hill deflections changed rapidly over time throughout the evolution of the FZs. Changes of 1-2 km^2 in the area (as defined previously) over short periods of time (~0.1 m.y.) are very common (Figure 2.6) and extreme changes up to 8 km^2 occurred in less than one m.y. (detailed examples are illustrated by Figures 2.4b2, 2.4e2, 2.4g2 and 2.4g3). These rapid changes in abyssal

hill curvature area are remarkable and suggest that the stress field at the RTI changed rapidly over time periods of one m.y. Processes that could have changed the stress field at Menard and Pitman RTIs include (1) transform fault locking (2) changes in transform fault length, (3) changes in spreading rate, (4) and changes in absolute plate motion.

The mechanism which best explains the rapid changes in the principal stress directions at RTIs is (process 1) transform locking. A transform fault without friction has a minor influence on the stress field at the ridge crest since the principal stresses will align perpendicular and parallel to the planes of zero strength: the plate boundaries at the ridge and transform fault [*Neves et al.*, 2004]. Abyssal hills formed under such stress conditions with no transform fault friction are expected to be straight. Focal mechanisms of earthquakes at oceanic transform faults show that most strike-slip events have one nodal plane parallel to the transform fault [*Thatcher and Hill*, 1995] implying low coefficients of friction [*Behn et al.*, 2002]. Studies of the San Andreas Fault show low values of generated frictional heat [*Brune et al.*, 1969; *Lachenbruch*, 1981; *Reasenberg and Simpson*, 1992] and an angle of 68-85° between the greatest horizontal principal compressive stress and the fault strike [*Townend and Zoback*, 2004], implying a low value of the coefficient of friction at the fault. At oceanic RTIs the coefficient of friction may be higher when newly formed lithosphere periodically welds to the older juxtaposed plate, which creates a shear couple in the underlying lithosphere, thereby reorienting S_h [*Fox and Gallo*, 1984]. The shear couple is short-lived since the mantle weld will be continually broken by ongoing strike-slip-induced strain, which may explain the large variety in obliquity of the abyssal hill deflections at Menard and Pitman FZs (Figure 2.6) over time scales of less than one m.y. In a partially locked system the S_h direction may strongly vary near the RTI, tending to be perpendicular to the transform fault in the

unlocked section but rotated up to 60° from ridge parallel in the locked section [*Neves et al.*, 2004]. The upper boundary of 60° for rotation of the S_h direction at RTIs correlates well with the measured maximum abyssal hill obliquity of the abyssal hill deflections at Menard and Pitman FZs, where we measured maximum difference in azimuth of the straight part of the abyssal hill and its curved tip of 57° and 55°, respectively. Between 41 and 35 Ma (~chron C19 to C15o), during the period of little change in lineation azimuths, several J-shaped abyssal hills formed at both the Pacific and Antarctic plates at Menard FZ. Interestingly, the area (as defined previously) of abyssal hills that formed at the Pacific plate ranges between 1.2 and 7.5 km^2 while at the Antarctic plate the range falls between 0 and 1.8 km^2 (Figure 2.6a). A possible explanation for this difference is that the southern splay of the Menard FZ, along which the J-shaped abyssal hills on the Pacific plate formed, was (partially) locked during that time period, while at the same time the northern splay, along which the J-shaped abyssal hills on the Antarctic plate formed, experienced low frictional resistance.

The other three processes seem unlikely to be able to explain rapid changes in the stress field. Changes in transform fault length (process 2) are expected to scale geometrically with lithospheric stress distributions [*Phipps Morgan and Parmentier*, 1984], e.g. the horizontal principal stress direction at a longer transform fault is expected to rotate more at the RTIs resulting in larger J-shaped abyssal hill curvatures. However, the ridge offset at Pitman FZ hardly changed throughout the evolution of the FZ (Figure 2.5b) and at Menard FZ only gradual changes in ridge offset have been observed, except for one 65 km ridge jump around 25 Ma (~chron C7) (Figure 2.5a). Therefore, it is unlikely that changes in the ridge offset were responsible for the large fluctuations in abyssal hill curvature area over short timescales at the PAR.

RTIs at faster spreading ridges have an increased tendency for ridge propagation, oblique normal faulting and ridge curvature [*Neves et al.*, 2004]. However, changes in spreading rate (process 3) (Figure 2.5) are unlikely to explain the observed frequent fluctuations in the stress field at the Pitman and Menard FZs since these changes were mostly gradual and over longer timescales. The largest fluctuations in half spreading rate are small, on the order of 5 mm/a for time intervals of about 1 m.y. Significant changes in the lineation azimuths, which were responsible for periods of transtension and transpression, also occurred gradually over time periods on the order of 5 or 10 m.y. at the PAR (Figures 2.5 & 2.6), which rules out the possibility that changes in the far field stress would have caused rapid changes in abyssal hill curvature area. In Appendix B we present multibeam bathymetry data from Murray FZ. While higher spreading rates may enhance the curvature of abyssal hills over time periods on the order of 5 or 10 m.y., plate kinematic changes leading to periods of transtension are the dominant mechanism for a gradual increase in number and size of J-shaped abyssal hills.

Migration of the ridge relative to the asthenosphere (process 4) can produce asymmetries in the rotation of the S_h direction near the ridge tips if there is a component of motion parallel to the ridge axis [*Tucholke and Schouten*, 1988]. We made an attempt to evaluate the effects of absolute plate motion on the stress field at the Menard and Pitman RTIs. In Appendix C we show that this effect, if any, on changes in size and number of J-shaped abyssal hill curvatures at the intermediate spreading PAR cannot be quantified due to the limited multibeam bathymetry dataset and significant uncertainty in the considered absolute Pacific plate motion models [*Andrews et al.*, 2006; *Koppers et al.*, 2001; *Wessel and Kroenke*, 2008].

2.5 TRANSTENSION AT PITMAN FRACTURE ZONE

During transtensional periods the clockwise rotation of the S_h direction is enhanced near the RTIs of right-stepping offsets. Since about 9 Ma (~chron C4A) the lineation azimuths at Pitman FZ underwent ~15° clockwise rotation (Figures 2.5b and 2.6b) resulting in significant transtension on the transform fault. The high number of curved J-shaped abyssal hills, which formed at the Pitman FZ on both the Pacific and Antarctic plates (Figures 2.4g and 2.6b), with areas (as defined previously) larger than two km^2 strongly correlates with this transtensional period. In particular between 9 and 7 Ma (~chron C4A to C3Ao) the lineation azimuth rotated 6°. In Pacific plate crust formed between 7.4 to 6.0 Ma (chron C4 to C3Ay) we observed a zone of deformation with several large faults as far away as 30 km north of Pitman FZ (Figure 2.4g4). This morphology suggests that the transform fault zone during that time period formed a broad diffuse boundary unlike the classic single, few-kilometers wide strike-slip deformation zone with dip-slip faults produced by FZ-normal extension as envisioned by *Fox and Gallo* [1984] for oceanic transform faults. Complex multi-fault oceanic strike-slip boundaries such as the Romanche [*Bonatti et al.*, 1994], Andrew Bain [*Sclater et al.*, 2005], Tharp and Udintsev [*Lonsdale*, 1994b] transform faults typically have large offsets of several hundreds of kilometers. *Ligi et al.* [2002] suggested that wide multi-fault boundaries develop when the age offset is above a threshold value of ~30 m.y. for extra long (> 500 km) slow-slip transform faults. However, the ridge and age offsets at the slow-to-intermediate slipping Pitman FZ have only been on the order of 100 km and 2 to 3 m.y., respectively, throughout the evolution of the FZ. We argue that the broad zone of deformation at Pitman FZ formed in response to the continuing clockwise reorientation of the PAR plate motion direction since 9 Ma (~chron C4A). Multiple clockwise adjustments

in orientation of the transform fault plate boundary placed the right-stepping Pitman transform fault offset under transtension (Figure 2.3), similar to processes reported by *Tucholke and Schouten* [1988]. As a consequence strike-slip faults within the transform fault tectonized zone opened and facilitated dip-slip motion. We interpret the faults in the ~30 km wide zone north of Pitman FZ (Figure 2.4g4), which formed at an angle of up to 20° counterclockwise of the main trend of the FZ as Riedel shears. Such faults typically have both strike-slip and extensional offsets [*Tchalenko and Ambraseys*, 1970] and they form during the early stages of strike-slip rifting [*Wilcox et al*., 1973]. At the PAR, Riedel fractures formed at the Eltanin Fault System (Figure 2.1) in response to the clockwise plate reorientation during the Pliocene [*Lonsdale*, 1986; 1994b], which also caused the transtension at Pitman FZ.

A non-transform left-stepping fault with an offset of about 5 to 10 km was observed in the sparsely available multibeam data on the Pacific side of the ridge about 50 km north of the Pitman transform fault (Figure 2.4g4). Around chron C1A (1.1 Ma) a ridge jump straightened the ridge segment north of the Pitman FZ and the left-stepping non-transform fault offset vanished. No other multibeam or magnetic data are available to confirm the start of this offset but a plausible explanation is that the offset started as a Riedel shear and evolved into a left-stepping offset. The multibeam data also revealed that the right-stepping Pahemo FZ, located at about ~80 km north of Pitman FZ (Figure 2.4g), ceased to exist around 6.0 Ma (chron C3Ay), which is 1 m.y. later than the cessation of the most significant clockwise reorientation between 9 and 7 Ma (~chron C4A to C3Ao) at Pitman FZ (Figure 2.6b).

Morphologic evidence for accommodation of the transtension in response to the continuing clockwise rotation in recent times include short-lived non-transform fault

offsets associated with curved abyssal hill fabric and several ridge jumps (Figure 2.4g). Since 2.6 Ma (chron C2Ao) ridge jumps transferred Pacific lithosphere to the Antarctic plate [*Ryan et al.*, 1992] reducing the ridge offset from 95 km to the present 70 km (Figure 2.5b). These ridge jumps were related to the clockwise (extensional) change in spreading direction. The extension was also responsible for a wide zone of strike-slip faults in the modern transform fault tectonized zone (Figure 2.7) and facilitation of dip-slip fault motion and intra-transform fault basin formation [*Tucholke and Schouten*, 1988]. This deformational zone is not as broad as the ~30 km wide zone with several faults north of Pitman FZ (Figure 2.4g4) but it formed under similar transtensional conditions. Following this logic, observations of sub-parallel cracks are expected in oceanic crust formed near Pitman FZ since the start of the transtensional period around 9 Ma (~chron C4A). However, the wide zone of cracks, which formed around 7 Ma (~chron 3Ao) in Pacific crust north of Pitman FZ on the Pacific plate, is the only area with clear observational evidence for a broad deformational transform fault zone in the inactive part of the FZ. A plausible explanation for the lack of observations of more sub-parallel cracks near Pitman FZ is that the multi-fault transform zone, which probably developed during most of the transtensional period, was significantly narrower and has been covered by overshot ridge volcanism during continued plate motion. On oceanic crust that formed near Pitman FZ around 7 Ma (~chron 3Ao) during the period of the most extreme clockwise plate reorientation and the highest transtensional stress, the zone of deformation may have been broad enough that many of the cracks have not been covered by overshot ridge volcanism and therefore have remained visible in the multibeam bathymetry data (Figure 2.4g4).

Around chron C1A (1.1 Ma) the transtension led to a reorganization of the Pitman transform fault. The morphological evidence for the recent transtension in the form of a wide zone of strike-slip faults with a component of dip-slip fault motion is supported by the orientation of the current transform fault zone at ~1° clockwise relative to the youngest portion of the synthetic flowline (< 0.78 Ma; chron C1o) [*Croon et al.*, 2008] (Figure 2.7). This suggests that the clockwise reorientation of the lineation azimuths and the related period of transtension continued since 0.78 Ma. Morphologic highs in combination with a positive magnetic anomaly (Figure 2.7), characteristic for the crest of the oceanic ridge system [*Klitgord*, 1976], indicate that a recent (< 0.1 Ma) northwestward ridge jump occurred north of Pitman FZ. Moreover, two dredges during the EW9201 geophysical survey recovered basalts with abundant fresh glass at the new ridge crest [*Ferguson and Klein*, 1993].

The transverse ridge that bounds the south side of the Pitman transform fault was most likely formed as a response to the extension and related widening of the transform fault tectonized zone (profile on Figure 2.7). Similar ridges have been observed along the Menard and Emerald FZs [*Croon et al.*, 2008] and the Udintsev, Tharp and Heezen FZs [*Lonsdale*, 1986; 1994b].

2.6 TRANSPRESSION AND ANOMALOUS ABYSSAL HILL DEFLECTION

If a transform fault experiences significant transpression, crustal blocks in its vicinity rotate about a vertical axis [*Garfunkel*, 1974; *Ron et al.*, 1984; *Ron et al.*, 1986]. It has been hypothesized by Sonder and Pockalny [1999] that during periods of transpression increased coupling across an oceanic transform fault is partially accommodated by distributed strike-slip deformation rather than solely by discontinuous

displacement at the transform fault. Such periods of transpression occur at oceanic transform faults in response to changes in plate motion direction [*Tucholke and Schouten*, 1988] and result in anti J-shaped abyssal hill curvature (as illustrated in Figure 2.2b) in the vicinity of a right-stepping transform fault [*Sonder and Pockalny*, 1999].

2.6.1 Curvature Data for Anti J-shaped Abyssal Hills

At both Menard and Pitman FZs we see abyssal hill deflections in the opposite sense to the J-shaped curvature. The anti J-shaped deflections differ measurably from the regional trend within about 10 km of the FZ, with the amount of deflection increasing towards the FZ. We mapped 19 anti J-shaped abyssal hill curvatures at Menard FZ (Figures 2.8a and b) and 15 at Pitman FZ (Figures 2.8c and d), respectively. Other than at Menard and Pitman FZs, few data are available at the PAR to study anti J-shaped abyssal hill deflections. A multibeam bathymetry dataset at the Pacific limb of Heirtzler FZ features anti J-shaped deflections as well. However, the measurements at Heirtzler FZ are limited to 6 deflections (Figure 2.8e) since only a small portion of the Pacific limb of the FZ has been mapped by shipboard multibeam bathymetry data.

Anti J-shapes are observed in crust formed at the inner RTI corner, which slipped along the transform fault during the first several m.y. of its evolution. The formation of these anti J-shaped abyssal hills correlates well with the transpressional period between 35 and 25 Ma (~chron C15o to C7) at Menard FZ (Figure 2.9a), and 31 and 23 Ma (~chron C12o to C6B) at Pitman and Heirtzler FZs (Figure 2.9b and c). Counter-clockwise reorientation of the lineation azimuths at Menard FZ (16°) and at Pitman and Heirtzler FZs (12°) occurred during the periods of transpression (Figures 2.3 and 2.9)

according to the plate motion model for the PAR [*Croon et al.*, 2008]. The maximum measured anti J-shaped deflection relative to the regional abyssal hill trend at the three FZs varied between 22° and 63° (Figure 2.9) and the most extreme deflections have been measured at Pitman FZ. Considerable transpression is also expected at Pitman and Heirtzler FZ before 45 Ma (during chron C20r) based on the synthetic flowline model (red areas at the edges of the model at Pitman FZ in Figure 2.3). However, since only limited multibeam bathymetry data is available on the Pacific plate at Pitman FZ we won't consider this oldest period of transpression for this study. The correlation between the age of the observed anti J-shaped abyssal hill deflections, which formed since 45 Ma, and the predicted periods of transpression based on the synthetic plate motion model (Figures 2.3 and 2.9) at Pitman, Menard and Heirtzler FZs is remarkably strong.

2.6.2 Modeling of Anti J-shaped Abyssal Hill Deflections

The observation of 40 anti J-shaped abyssal hill deflections at three FZs at the PAR in combination with the PAR plate motion model allowed us to test a model by *Sonder and Pockalny* [1999] who presented analytical solutions for distributed deformation of a thin layer driven by stress on its side. They approximated very young (< 2 Ma) oceanic lithosphere as a thin layer [*England and McKenzie*, 1982; *Grindlay and Fox*, 1993]. The angular deflection of an abyssal hill initially perpendicular to the transform fault [*McKenzie and Jackson*, 1983; *Nelson and Jones*, 1987] is

$$\theta = \arctan\left[\left(-2D\sqrt{n}\,\frac{\pi}{L}\right)e^{\left(-2D\sqrt{n}\frac{\pi y}{L}\right)}\right] \quad (1)$$

where D is the horizontal displacement of the abyssal hill since its formation along the transform fault under transpression of length, L, y is the distance of the deflection to the transform fault and *n* is the effective stress exponent; *n* = 3 reflects lithospheric strength controlled by ductile deformation, while *n* >> 3 reflects lithospheric strength dominated by fault slip [*Sonder and England*, 1986; *Sonder and Pockalny*, 1999]. Paleo-transform fault length, L, is the same as the ridge offset (Figure 2.9). We measured the distance of the anti J-shapes to the FZ, y, and the deflection angle θ, for each anti J-shaped abyssal hill curvature (Figure 2.10) visible on the gridded multibeam bathymetry data (Figure 2.8). Based on the measured values of L, θ and y for each of the 10 mapped groups of anti J-shaped curvatures we derived the transform fault displacement, D, and the stress exponent, *n*, by fitting curves of Equation 1 with values for D and n that fit the data best (red lines in Figure 2.10). This analysis shows that displacement D on average is about 5 km at both Menard and Pitman FZs and 3.5 km at Heirtzler. However, the average stress exponent, *n*, is significantly larger at Pitman FZ ($n \approx 12$) than at Menard FZ ($n \approx 7$) and Heirtzler FZ ($n \approx 4$). It is difficult to interpret *n* quantitatively [*Sonder and England*, 1986] but it increases with lithospheric age due to cooling. In Figure 2.10, the best fitting curves for the 10 groups are compared to the calculated relationship of stress exponent, *n*, with lithospheric age [Fig. 4, *Sonder and Pockalny*, 1999]. The data generally fit the theoretical curves. However, the values of *n* obtained from the abyssal hill deflections for Pitman FZ are generally higher than the theoretical lithospheric strength curves. A plausible explanation is the influence of the colder lithosphere on the opposite side of the Pitman transform fault. The age offset at the Pitman FZ during the period of formation of the anti-J shaped deflections was about 5 Ma. In contrast, at the time of formation of the anti J-shapes the age offset at both Menard and Heirtzler FZs was ~2.5 Ma.

Consequently, the values of *n* from the anti J-shaped abyssal hill deflections at these FZs fit the theoretical curves better.

2.6.3 Transtensional Cracks and Riedel Shears

Sonder and Pockalny [1999] argued that a counterclockwise change in spreading direction around 1 Ma (chron C1r.1n) put the Pitman transform fault under transpression to explain several apparent anti J-shaped curvatures at the Pitman transform fault. However, we have demonstrated that the Pitman FZ experienced transtension in response to a clockwise rotation of the lineation azimuths since 9 Ma (~chron C4A) (Figures 2.3 and 2.9). Some of the structures mapped by *Sonder and Pockalny* [1999] as anti J-shaped deflections adjacent to the Pitman transform fault curve less than 5° and can be explained by small irregularities in straightness of the abyssal hills at their formation as opposed to the significant anti J-shaped deflections up to 63° measured at Pitman FZ (Figures 2.8c-d and 2.9b) during the transpressional period between 31 and 23 Ma (~chron C12o to C6B). An exception is one group of ~30° curved anti J-shaped abyssal hills formed in oceanic crust on the young side of chron C2 (1.9 Ma) on the Pacific plate north of the Pitman transform fault (Figure 2.7). We conclude that the adjustments in location and orientation of the transform fault in response to the clockwise reorientation, which started around 9 Ma (~chron C4A), led to significant transtensional stress on the transform fault zone, which is characterized by several faults with a strike-slip as well as a dip-slip component, which offset the abyssal hill fabric and formed apparent anti-J shaped morphology. The cracks that offset the abyssal hills are oriented up to 40° oblique to the Pitman transform fault and we interpret them as Riedel shears. Even though the zone of Riedel shears north of the Pitman transform fault is only about

10 km wide compared to the 30 km wide tectonized area mapped in oceanic crust of 7.4 to 6.0 Ma (chron C4 to C3Ay) north of Pitman FZ on the Pacific plate (Figure 2.4g4) we conclude that the transtensional stress conditions responsible for forming these cracks are similar. It is remarkable that the Riedel shears have only been observed north of Pitman FZ in Pacific oceanic crust. The few available multibeam data reveal a left-stepping 5 km non-transform fault offset at about 40 km south of Pitman FZ (Figure 2.4g) in oceanic crust of about 6.7 to 6 Ma age (chron C3Ao to C3Ay). This left-stepping offset ceased to exist because a propagating rift straightened the ridge around 5.1 Ma (chron C3o). Since about 0.8 Ma (chron C1o) a right-stepping ~5 km non-transform fault offset started to evolve at about 60 km south of Pitman FZ (Figure 2.4g). The changes in the regional stress field south of Pitman FZ due to the clockwise reorientation of the PAR since 9 Ma (~chron C4A) were possibly accommodated by these offsets.

2.7 CONCLUSIONS

In this study we quantitatively analyzed more than 300 mapped abyssal hill deflections formed at RTIs at the Menard and Pitman FZs. On the basis of our observations we draw the following conclusions:

1. The J-shaped abyssal hill curvatures formed at Menard and Pitman FZs during the last 45 Ma (during chron C20r) are explained by the local changes in the least horizontal compression (S_h) direction, which tends to rotate clockwise into right-stepping offsets. This rotation is enhanced when the transform fault is under transtension. The greatest number and largest sizes of J-shaped deflections are observed at Pitman FZ during the period of transtension since 9 Ma (~chron C4A) in response to ~15° clockwise rotation of the direction of spreading.

2. The observations of J-shaped abyssal hill curvatures show that the amount of curvature can change rapidly (up to 8 km^2 in size) over short time intervals of less than one m.y. A plausible mechanism to explain the large observed variety in obliquity of the abyssal hill curvatures at the RTIs of Menard and Pitman FZs is temporary locking of the transform fault. When newly formed lithosphere periodically welds to the older juxtaposed plate, a short-lived shear couple changes the stress field. Since the shear couple is continually broken by ongoing strike-slip induced strain, the stress tensor strongly varies over short periods of time.
3. A zone of cracks, which is significantly wider than a classic narrow strike-slip deformation zone with dip-slip faults produced by FZ-normal extension, has been observed north of Pitman FZ on the Pacific plate in crust formed between 7.4 to 6.0 Ma (~chron C4 to C3Ay) during the period of transtension. We conclude that this broad deformational zone formed in response to the significant clockwise change in relative plate motion direction. We interpret the cracks, which formed in a 30 km wide deformed zone at an angle of up to 20° oblique to the Pitman FZ, as Riedel shears.
4. Anti J-shaped deflections are expected to form in oceanic crust near RTIs during periods of transpression in seafloor less than 2 m.y. old when the oceanic lithosphere is thin. The correlation between the mapped anti-J shaped abyssal hill deflections at Menard, Pitman and Heirtzler FZs and the modeled period of transpression in response to the counter-clockwise change in lineation azimuth based on the plate tectonic model of the PAR is excellent.

5. The theoretical lithospheric strength is generally lower than expected from the amount of deflection of the observed anti-J shaped abyssal hills at Pitman FZ. This can be explained by the influence of the colder lithosphere on the opposite side of the Pitman FZ. At Menard and Heirtzler FZ the age offset was less than at Pitman FZ and consequently the calculated values for lithospheric strength from the anti J-shaped abyssal hill deflections fit the theoretical curves better.

2.8 ACKNOWLEDGMENTS

This study was made possible through a series of grants from the NSF-office of Polar Programs, which supported the acquisition of geophysical data along transits of the R/VIB Nathaniel B. Palmer: grants OPP-0338317, OPP-0338346, OPP-0126334, and OPP-0126340. We are grateful to Ifremer (Institut français de Recherche pour l'Exploitation de la Mer) for providing multibeam bathymetry data from the PACANTARCTIC 1 and 2 cruises. We thank the officers, crew, and scientific staff of the R/VIB Nathaniel B. Palmer and the many students who sailed on these cruises. Comments from Jeff Gee, Donna Blackman, Roi Granot and two anonymous reviewers helped us make a number of improvements to the manuscript. Caltech contribution 9005.

This chapter has been published: Croon, M. B., S. C. Cande, and J. M. Stock (2010), Abyssal hill deflections at Pacific-Antarctic ridge-transform intersections, *Geochemistry Geophysics Geosystems, 11*, Q11004, DOI: 10.1029/2010gc003236.

APPENDIX 2A: The Propagation of Cracks

Some of the mapped curved abyssal hills at the Menard and Pitman FZs are J-shaped deflected tips of propagating rifts that did not reach the FZ. One well-mapped

example south of Menard FZ on the Pacific Plate is a rift, which initiated north of Vacquier FZ (Figure 2.1) and propagated northward toward the southern splay of Menard FZ around 25 Ma (~chron C7) (Figure 2.4a). As a result, 65 km of Pacific crust was captured by the Antarctic plate [*Croon et al.*, 2008]. Another example is a recent (<0.1 Ma) propagating rift north of Pitman FZ on the Antarctic plate, which decreased the Pitman FZ ridge offset by 10 km (Figure 2.7). The propagator started to curve clockwise into the transform fault at 4.8 km north of Pitman FZ. While the propagator south of Menard FZ is a clearly distinct feature, the J-shaped abyssal hill curvature at Pitman FZ looks very similar to most of the mapped J-shapes at Menard and Pitman FZs. However, it seems likely that the J-shaped abyssal hills formed as the curved propagating tip of a crack at ~10 km distance from the ridge axis. Therefore, the crack propagated through significantly older lithosphere. The evidence for the recent ridge jump can not be found in the morphology but in two dredges during the EW9201 geophysical survey, which recovered basalts with abundant fresh glass at the new ridge crest [*Ferguson and Klein*, 1993].

Several studies modeled propagating cracks where spreading centers are considered as giant cracks with the tip propagating in a tensile stress field as the plates are pulled apart [*Abelson and Agnon*, 1997; *Abelson et al.*, 2002; *Macdonald et al.*, 1991; *Pollard and Aydin*, 1984; *Sempéré and Macdonald*, 1986]. While we did not compare our measurements to such models it is important to note that a significant number of our measured J-shaped abyssal hills probably have been formed as the propagating tip of a ridge-parallel crack, which started at a distance of more than 5 km from the ridge axis in response to a small ridge jump. Unfortunately, the morphology of that type of J-shaped deflection looks identical to the rest of the J-shapes, which formed

at or within a few kilometers of the spreading axis. A method to figure out which J-shaped deflections formed more than 5 km away from the ridge axis would be to analyze changes in the ridge offset, which is based on the offset in magnetic anomalies across the FZ. Unfortunately, the interpretation of magnetic anomalies near the FZ is difficult due to FZ complexities such as overshot ridge volcanism. Therefore, if no morphologic or other evidence is available it is very difficult to pick which J-shaped abyssal hills formed as the tip of a propagating crack. Hence, in this study we did not compare J-shaped abyssal hills, which may have formed as the curved tip of a propagator, to a model of propagating cracks.

APPENDIX 2B: Stress Field Dependency on Spreading Rate at Ridge-Transform Intersections

Based on finite element modeling *Neves et al.* [2004] pointed out that RTIs at faster spreading ridges have an increased tendency for ridge propagation, oblique normal faulting and ridge curvature. Curved ridge tips have indeed been observed at several fast slipping FZs, including Siqueiros [*Fornari et al.*, 1989], Clipperton [*Kastens et al.*, 1986] and Quebrada [*Lonsdale*, 1978] FZs. We observed no significant increase or decrease in the number and size of curved J-shaped abyssal hills at Menard FZ, which slipped at intermediate spreading rates throughout its history. However, Pitman FZ slipped at slow spreading rates (< 40 mm/a) between 45 and 11 Ma (~chron C20r to C5o), after which it increased to intermediate spreading rates (> 40 mm/a) (Figure 2.5b). This period of intermediate spreading overlaps with the transtensional period at Pitman FZ in response to ~15° change in lineation azimuths since 9 Ma (~chron 4A). To test whether the transtension or the increase in spreading rate is the dominant mechanism

for the increase in number and size of curved abyssal hills, we analyzed abyssal hill deflections at the right-stepping Murray FZ in the North Pacific (Figure 2B1). The Murray FZ is one of the few FZs where significant multibeam bathymetry data are available to study changes in abyssal hill mophology during time intervals of several m.y. The ridge near the Murray FZ has been fast spreading (> 80 mm/a) throughout its evolution. Therefore, if high spreading rate would be a dominant factor for the number and size of curved abyssal hills, J-shaped abyssal hill deflections would be expected along the entire Murray FZ. This is not the case. Before 45 Ma (during chron C20r), hardly any significant J-shaped abyssal hill deflections are observed (Figure 2B1) along both splays of Murray FZ. However, a significant increase in J-shapes is observed in oceanic crust younger than 45 Ma. At Murray FZ a ~5° clockwise reorientation around 45 Ma, which was a time of global plate reorganization [*Atwater and Severinghaus*, 1989; *Cande et al.*, 1982; *Whittaker et al.*, 2007], led to a period of transtension. While higher spreading rates may enhance the likelihood of formation of J-shaped abyssal hill deflections, we conclude based on the observations at Murray FZ that reorientations, which lead to periods of transtension, are the dominant mechanism for increase in number and size of J-shaped abyssal hills. Therefore, the ~15° change in lineation azimuth at Pitman FZ since 9 Ma (~chron 4A) is probably responsible for the dramatic increase in number and size of J-shaped curved abyssal hills (Figure 2.6b). The modest increase in spreading rate starting around 11 Ma (~chron C5o, Figure 2.5b) had no major effect.

APPENDIX 2C: Changes in Absolute Plate Motion

Melt at slower migrating ridges, such as the EPR, equilibrates deeper in the mantle and is more extensive than at fast migrating ridges like the PAR [*Schouten et al.*, 1987].

The PAR is one of the fastest migrating ridges relative to a fixed spot in the mantle. Therefore, the PAR sequesters material from a broad shallow lateral region of the underlying asthenospere [*Small and Danyushevsky*, 2003]. In particular *Tucholke and Schouten* [1988] suggested, based on observations at the Kane FZ at the slow spreading Mid-Atlantic Ridge, that migration of the ridge relative to the asthenosphere can produce asymmetries in the rotation of the S_h direction near the ridge tips if there is a component of motion parallel to the ridge axis. In this case the ridge tip that migrates away from the underlying heat anomaly in the asthenosphere tends to be straighter.

In order to evaluate the effect of absolute plate motion at the Menard and Pitman FZs we calculated the migration of the ridge axis relative to a fixed spot in the mantle. We assumed symmetric spreading of the PAR and summed the relative plate motion model [*Croon et al.*, 2008], using half-angle rotations, with the absolute Pacific plate motion rotations of *Koppers et al.* [2001], *Andrews et al.* [2006] and WK08-A [*Wessel and Kroenke*, 2008] (Figure 2C1a). The ridge migration rate at the latitude of Menard FZ has been fast at about 40 to 50 mm/a since 48 Ma (~chron C21o). At Menard FZ, the area (as defined previously) is less than two km^2 (Figure 2.6a). Fast migration away from the underlying heat anomaly in the asthenosphere at Menard FZ might have had an attenuating effect on the rotation of the stress field at the Menard RTIs, which could explain the moderate amount of deflection of the J-shaped abyssal hills during the evolution of Menard FZ. The ridge migration rate at the latitude of the Pitman FZ has been significantly slower at about 25 to 35 mm/a since 48 Ma. At Pitman FZ the area under many of the curved abyssal hills is significantly larger than two km^2, especially since 9 Ma. However, this coincides with a period of significant transtension at Pitman FZ.

The azimuth of the absolute Pacific plate migration relative to a fixed spot in the mantle according to the *Koppers et al.* [2001], *Andrews et al.* [2006] and WK08-A [*Wessel and Kroenke*, 2008] models is similar to the azimuth of the Pacific plate relative to the Antarctic plate [*Croon et al.*, 2008] during most of the evolution of Menard FZ (Figure 2C1b). The significant change in azimuth of Pacific absolute plate motion was placed at 43 Ma at the landmark Hawaii-Emperor chain bend by *Koppers et al.* [2001]. Note that a revision of seamount ages placed the initiation of the bend at 50 Ma [*Sharp and Clague*, 2006]. The azimuth for absolute plate motion according to the WK08-A model [*Wessel and Kroenke*, 2008] deviates up to 25° from the azimuth of the relative PAR plate motion model [*Croon et al.*, 2008] for the Pacific plate since 2.6 Ma (chron C2Ay), which is the result of a more northward absolute motion of the Pacific plate. At the latitude of Pitman FZ (Figure 2C1c) the difference in azimuth between the three absolute plate motion models and the PAR relative plate motion model is the largest for the WK08-A model. This difference in azimuth is 30° to 45° between 45 and 17.5 Ma (~chron C20r to C5D) and 30° after 0.78 Ma (chron C1o). According to the WK08-A model both ridge tips would have migrated northward relative to a fixed spot in the mantle (Figure 2C1d). Effectively the southeast ridge tip would have overridden relatively hot asthenosphere under the ridge segment to the northeast while the northwest ridge tip would have migrated away from the ridge segment to its southwest and over relatively cold asthenosphere. If *Tucholke and Schouten's* [1988] model of asymmetries in the rotation of the S_h direction at both ridge tips in response to ridge migration relative to the asthenosphere would be applicable in this situation, we expect to see differences in the straightness of abyssal hills at both RTIs. However, we see no significant difference in J-shaped abyssal hill size on the Pacific and Antarctic plates at Pitman FZ (Figure 2.6b).

This could mean that the WK08-A model [*Wessel and Kroenke*, 2008] is incorrect or that the effect of asymmetry in abyssal hill straightness as observed at the Kane FZ by *Tucholke and Schouten* [1988] is not present here perhaps because the asthenosperic heat anomaly underneath the slow spreading Mid-Atlantic Ridge is significantly smaller than at the intermediate spreading PAR. Too few multibeam bathymetry data are available at Menard FZ on the Antarctic plate (Figures 2.4c and 2.6a) to evaluate the difference in absolute Pacific plate motion and PAR relative plate motion with respect to changes in J-shaped abyssal hill curvatures.

2.9 FIGURES

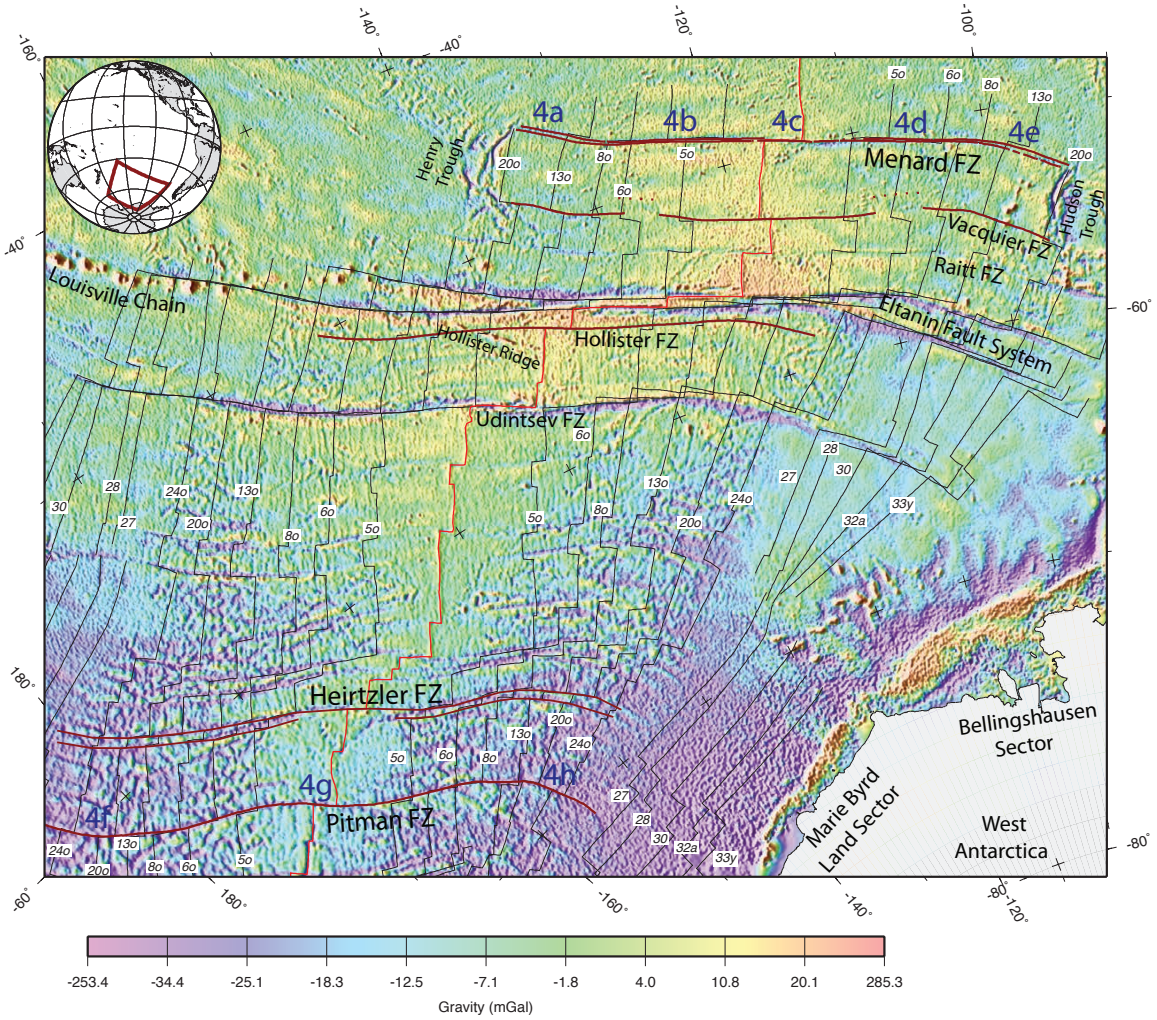

Figure 2.1: Map of the Pacific-Antarctic Ridge, on an image of the GEOSAT and ERS 1 satellite-derived, free-air gravity field [*McAdoo and Laxon*, 1997; *Sandwell and Smith*, 1997], summarizing the location of magnetic anomaly isochrons. The traces of the Menard, Pitman and Heirtzler FZs are highlighted in red. The 4a-h annotations refer to the detailed maps in Figure 2.4. Oblique Mercator projection about a pole at 66.8°N, 81.7°W, near the pole of rotation of Pacific relative to Antarctica at chron C3A [*Croon et al.*, 2008].

Figure 2.2: Examples of J-shaped and anti J-shaped abyssal hill curvatures. Figure a presents J-shaped abyssal hill deflections (black dashed lines) just east of the Pacific-Antarctic Ridge segment (solid dark red line) north of Pitman FZ (solid red line). The inset in Figure 2.2a illustrates how mapped J-shaped abyssal hill curvatures in this study have been defined by the surface area (in km^2) enclosed by the curved part of the abyssal hill, the lineation azimuth trend and the FZ. Figure 2.2b shows anti J-shaped abyssal hill deflections (red dashed lines) at Clipperton transform fault that offsets the East Pacific Rise (EPR), which is marked with a solid dark red line. The inset in Figure 2.2b illustrates how each mapped anti J-shaped abyssal hill curvature in this study has been defined by the angle between the abyssal hill trend lineation azimuth and the azimuth of the maximal curvature of the tip of the abyssal hill. Multibeam bathymetry data at Pitman FZ from EW9201 and at Clipperton FZ from EW9405 and EW9708 cruises. Map projection in Figure 2.2a same as in Figure 2.1. Map in Figure 2.2b is in a Mercator projection. The insets are cartoons of ridge-transform fault-ridge intersections (modified after *Sonder and Pockalny* [1999]). The ridge axes are represented with thick solid lines and the transform fault tectonized zone by grey shading. J-shaped abyssal hills are represented with thin dashed lines in Figure 2.2a. In Figure 2.2b solid lines represent anti J-shaped abyssal hills.

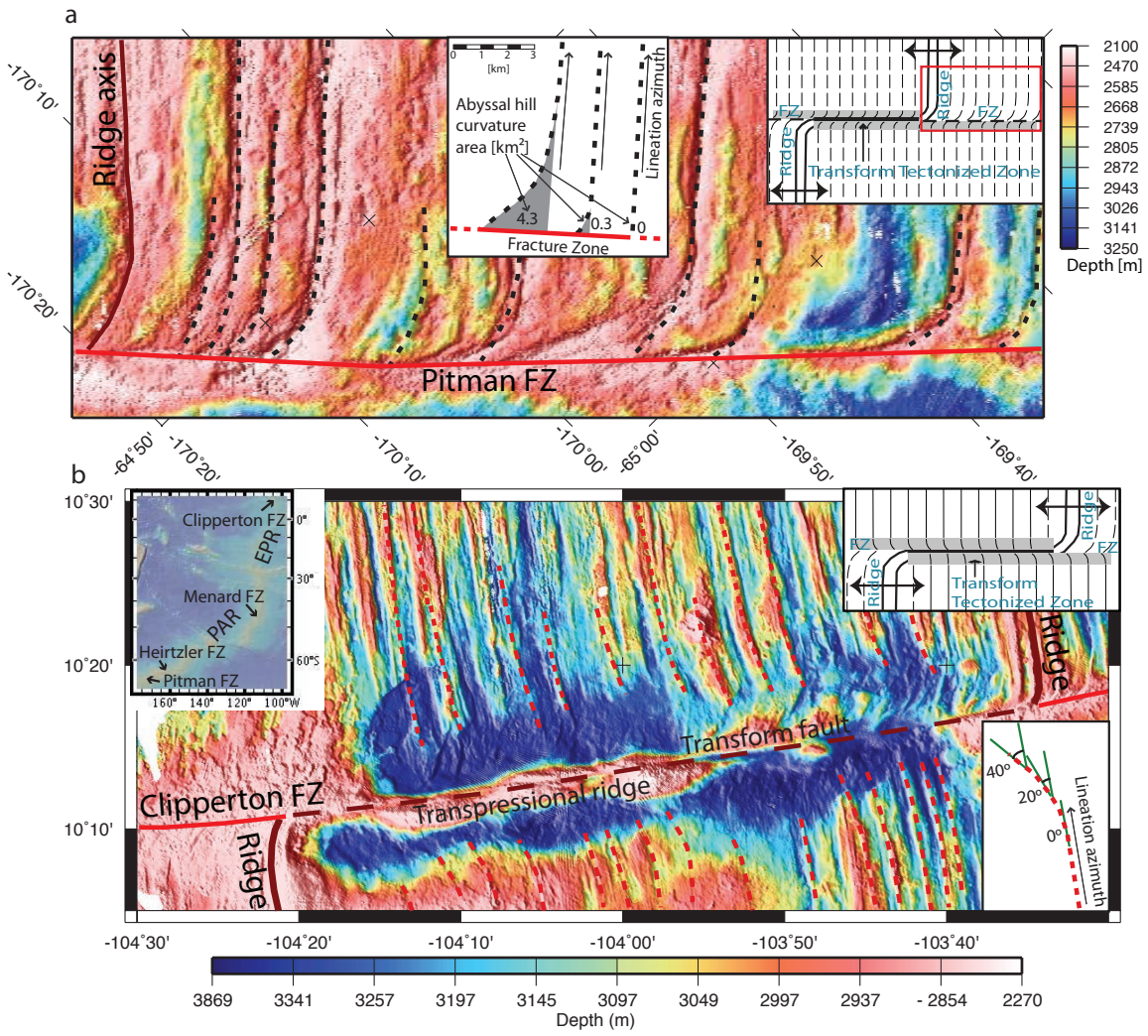
a
Ridge axis
Pitman FZ
Abyssal hill curvature area [km²]
Lineation azimuth
Fracture Zone
Transform Tectonized Zone
Ridge
FZ
Depth [m]
-170°10'
-170°20'
-64°50'
-170°20'
-170°10'
-170°00'
-65°00'
-169°50'
-169°40'
b
Clipperton FZ
EPR
Menard FZ
PAR
Heirtzler FZ
Pitman FZ
Transform fault
Transpressional ridge
Clipperton FZ
Ridge
Transform Tectonized Zone
Lineation azimuth
10°30'
10°20'
10°10'
-104°30'
-104°20'
-104°10'
-104°00'
-103°50'
-103°40'
Depth (m)

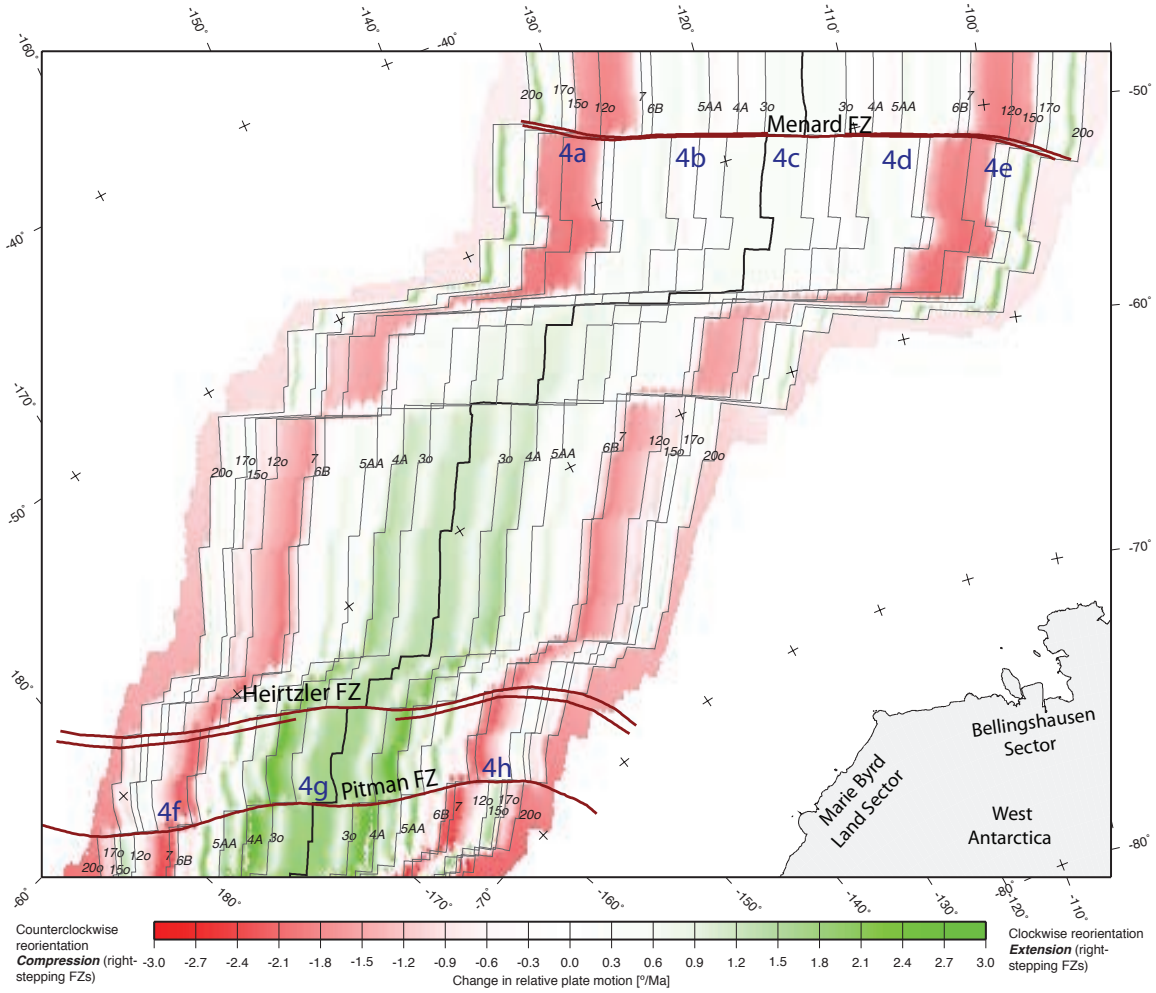

Figure 2.3: Grid based on a very high density of synthetic flowlines representing changes in lineation azimuths in degrees per m.y.. Clockwise changes in lineation azimuths are positive (green) and counter-clockwise changes in lineation azimuths are negative (red). Thin lines represent magnetic anomaly isochrons of the synthetic flowline model for the PAR [*Croon et al.*, 2008] near moments when changes in lineation azimuths occurred. The traces of the Menard, Pitman and Heirtzler FZs are highlighted in red. The 4a-h annotations refer to the detailed maps in Figure 2.4. Map projection same as in Figure 2.1.

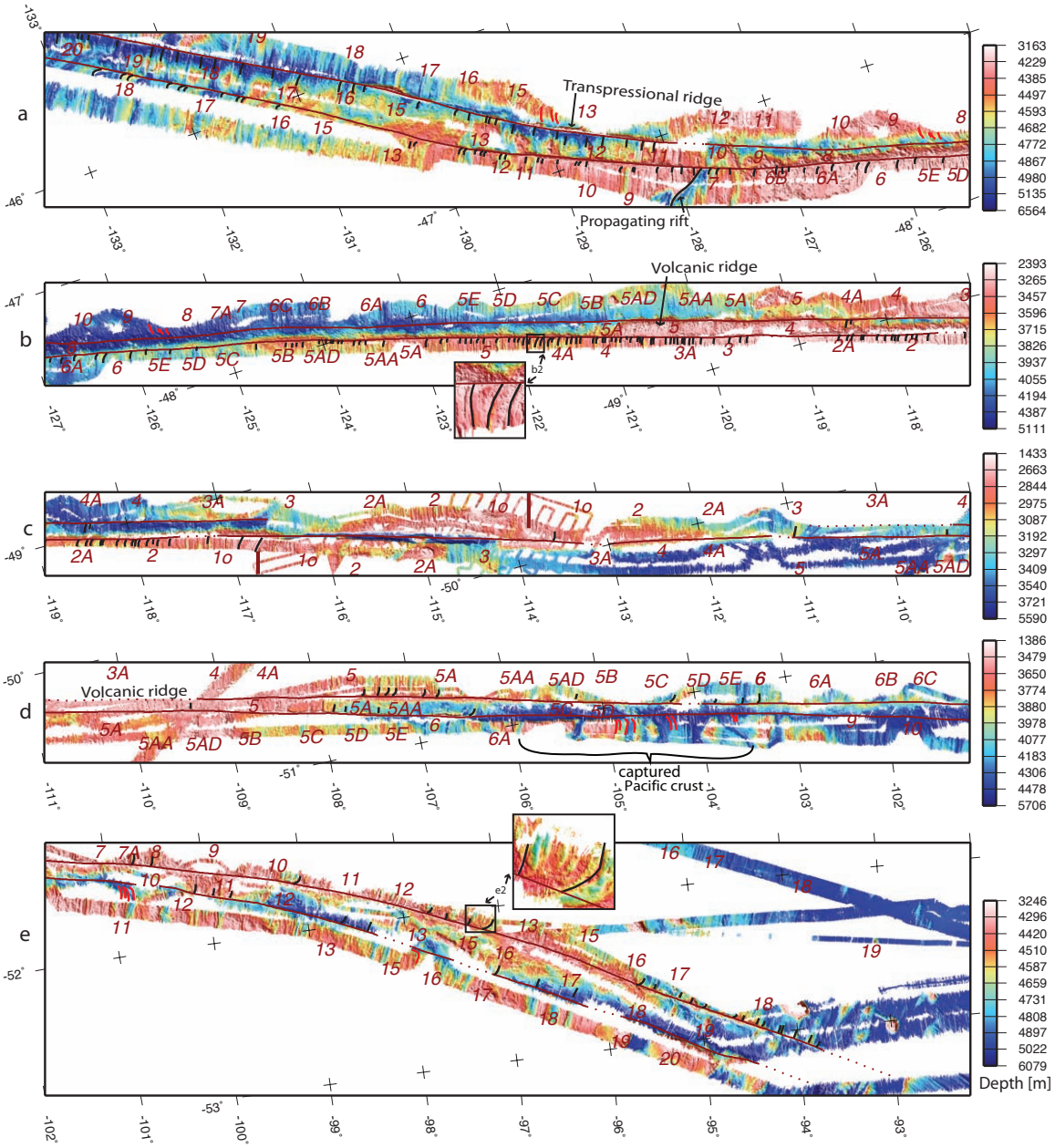

Figure 2.4: J-shaped (black) and anti J-shaped (red) abyssal hills at Menard (Figures 2.4a-e) and Pitman (Figures 2.4f-h) FZs. The FZs are represented with dark red lines. The red numbers show magnetic anomaly identifications. Multibeam bathymetry data at Menard FZ from NBP9707, NBP0007B, NBP0403, NBP0501B, NBP0507, WEST03MV, PACANTARCTIC 2 and RAPA03WT cruises and at Pitman FZ from EW9201, PACANTARCTIC 1, DRFT08RR, KIWI06RR, KIWI07RR, KIWI08RR, KIWI09RR, NBP9604, NBP9605 and NBP9802 cruises (NBP = R/VIB Nathaniel B. Palmer, MV = R/V Melville, RR = R/V Roger Revelle, WT = R/V Thomas Washington, EW = R/V Maurice Ewing). Insets 4b2, 4e2, 4g2 and 4g3 are magnified examples of rapid changes in abyssal hill size and 4g4 illustrates structural interpretation of cracks at Pitman FZ. Map projection same as in Figure 2.1.

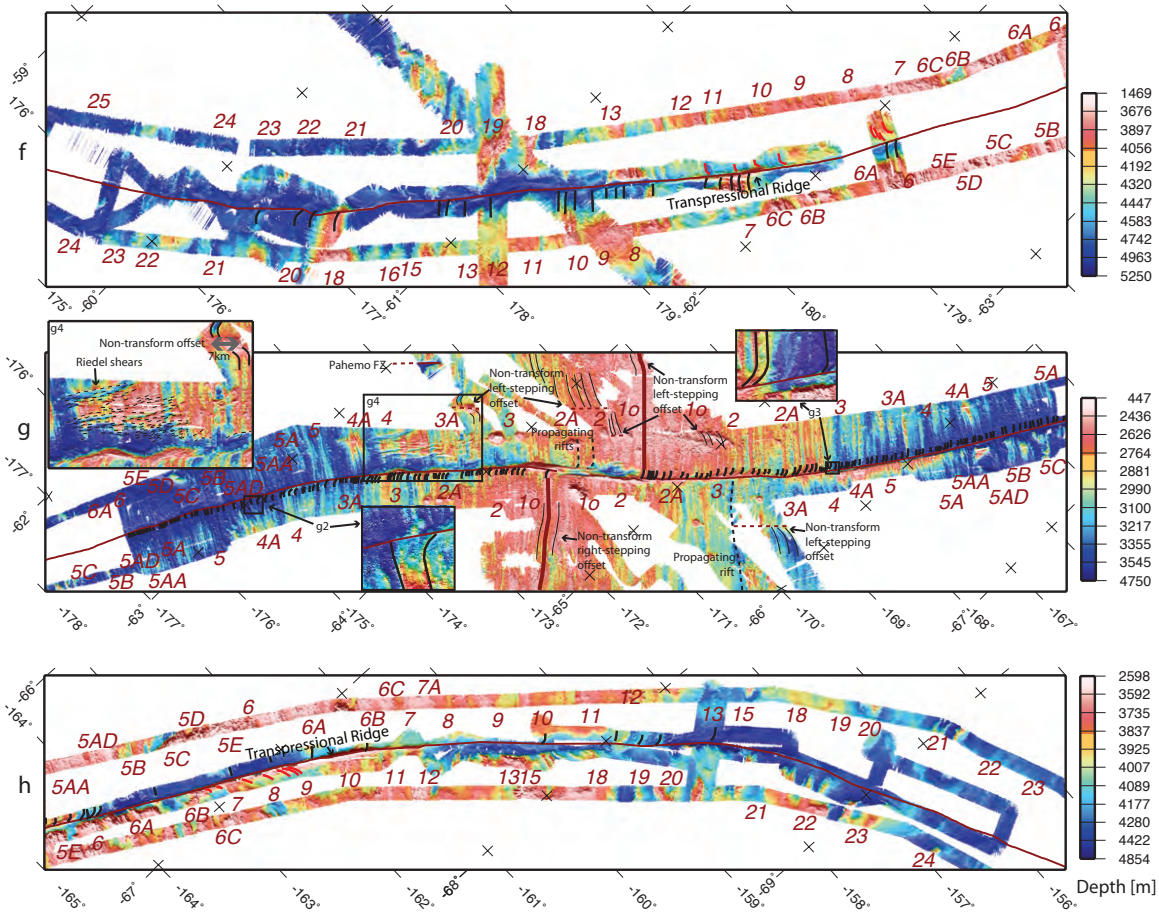

Figure 2.4 (continued)

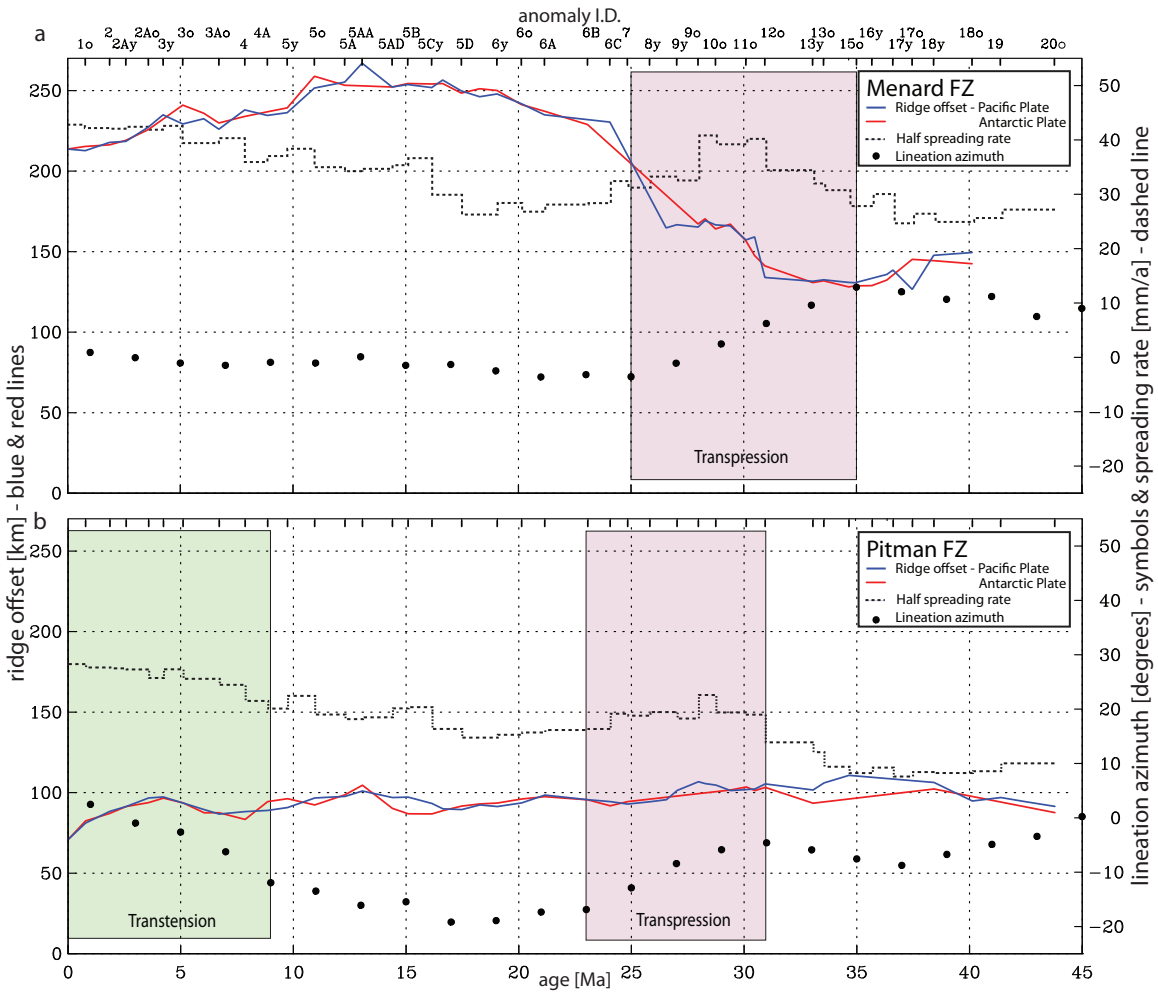

Figure 2.5: The dashed lines indicate half-spreading rates calculated from the rotation parameters along flow lines based on the model for the PAR [*Croon et al.*, 2008] at the Menard (Figure 2.5a) and Pitman (Figure 2.5b) FZs. The black dots represent changes in lineation azimuth based on the synthetic flowline model for Menard and Pitman FZs [*Croon et al.*, 2008]. The red and blue lines represent the ridge offset over time. The ridge offsets on both flanks should be the same; small differences reflect the uncertainties in magnetic anomaly picks [*Croon et al.*, 2008]. Oblique Mercator projection used to calculate abyssal hill curvatures and lineation azimuths same as in Figure 2.1.

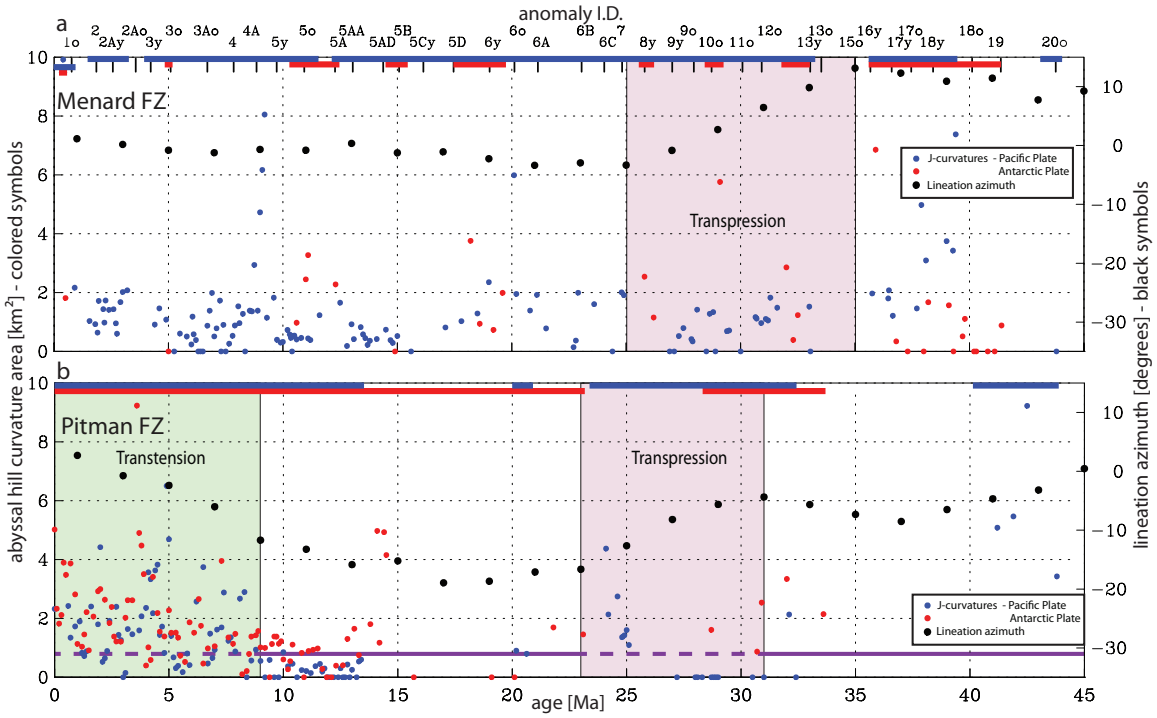

Figure 2.6: The age and the surface area (in km^2) enclosed by the curved part of the abyssal hill, the lineation azimuth trend and the FZ formed at outer RTI corners and mapped on the Pacific (blue dots) and Antarctic (red dots) plates at Menard (Figure 2.6a) and Pitman (Figure 2.6b) FZs during the last 45 Ma (during chron C20r). The black dots represent changes in lineation azimuth based on the synthetic flowline model for Menard and Pitman FZs [*Croon et al.*, 2008]. The thick purple line (Figure 2.6b) marks the arithmetic mean (0.8 km^2 with standard deviation = 1.1 km^2) for time periods that are not associated with transtension or transpression at Pitman FZ, dashed during periods of transtension and transpression. At Menard the thick blue and red lines at the top of Figures 2.6a and b indicate at which crustal age intervals multibeam bathymetry data are available to map abyssal hills on the Pacific and Antarctic plates, respectively. Oblique Mercator projection used to calculate abyssal hill curvatures and lineation azimuths same as in Figure 2.1.

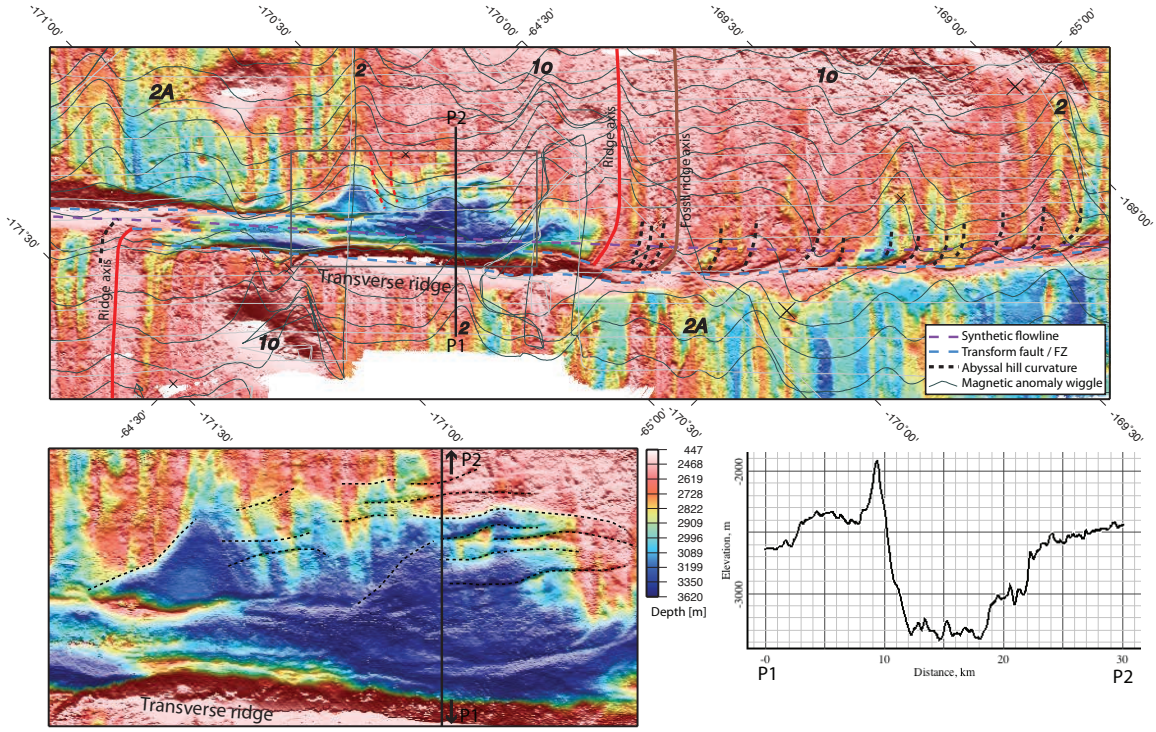

Figure 2.7: Pitman transform fault and surrounding structures. J-shaped abyssal hills are represented by black dashes. The ridge axes bounding the Pitman transform fault are shown solid red, the recently abandoned fossil ridge axis as a solid brown line. The dashed purple line represents the synthetic flowline based on the *Croon et al.* [2008] plate model for the PAR. The dashed blue lines map the locations of the morphologic expression of the Pitman transform fault and FZ. Magnetic anomaly wiggles are presented in grey from EW9201 and PACANTARCTIC 1 cruises. The magnetic anomaly identifications are displayed in bold black. The detailed map shows the Pitman transform fault valley. The dashed black lines mark the location of Riedel shears. The solid black line shows the location of the profile. Map projection same as in Figure 2.1.

Figure 2.8: Anti J-shaped abyssal hills digitized from multibeam bathymetry marked by thick dark red lines (groups 1, 3, 5, 7 and 9) and thick red lines (groups 2, 4, 6, 8 & 10) on multibeam bathymetry maps at Menard (10a & b), Pitman (10c & d) and Heirtzler (10e) FZs. The FZs are represented with thin dark red lines. The red annotations represent magnetic anomaly identifications. Multibeam bathymetry data at Menard FZ from NBP0007B, NBP0403, NBP0501B and NBP0507 cruises, at Pitman FZ from EW9201 cruise and at Heirtzler FZ from NBP9604 cruise. The overview map shows location of detailed maps 10a-e (blue rectangles) plotted on an image of the satellite-derived, free-air gravity field and summarizes the location of magnetic anomaly isochrons. Map projection for all maps same as in Figure 2.1.

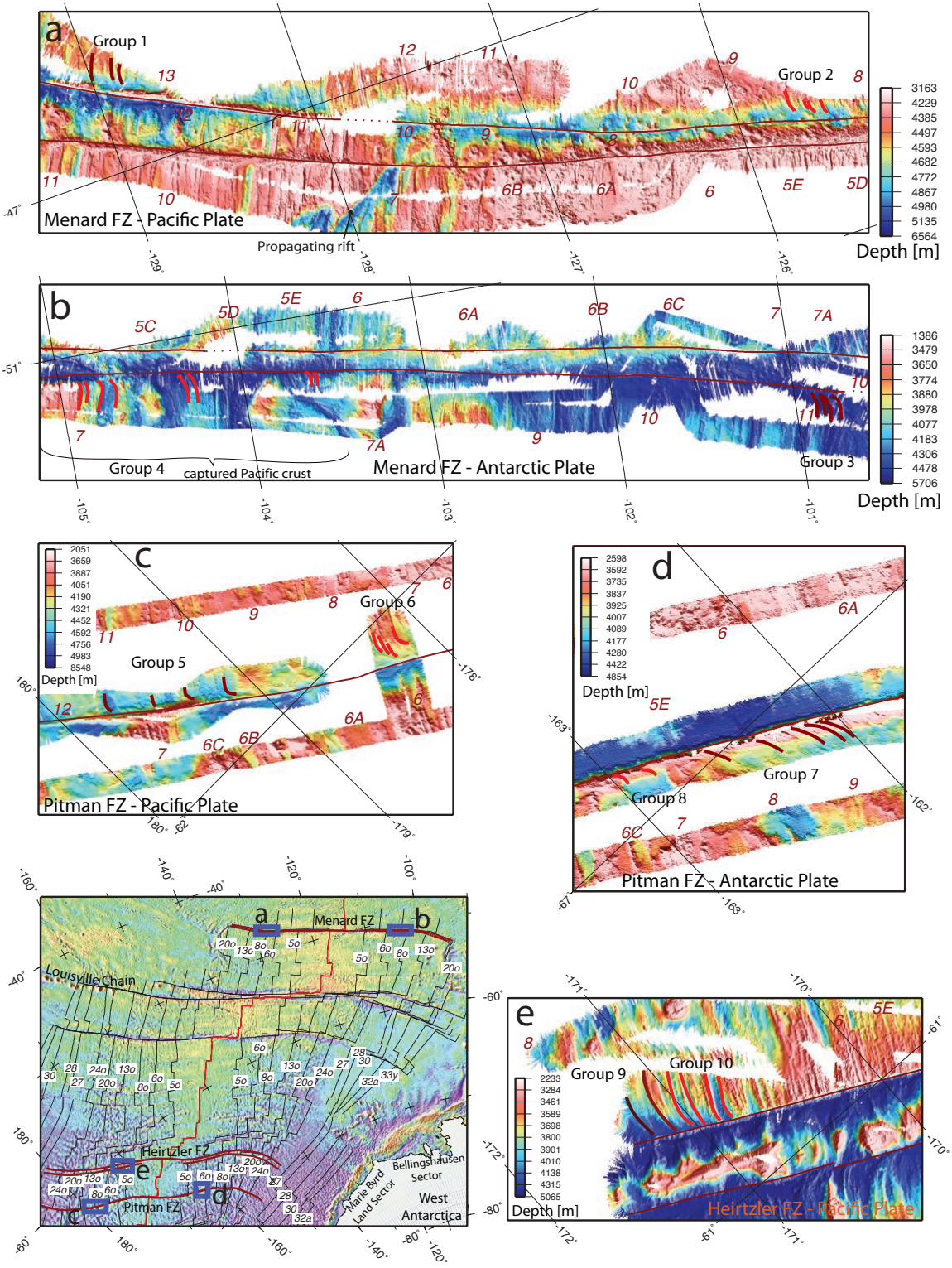
a
Group 1
Group 2
Menard FZ - Pacific Plate
Propagating rift
Depth [m]
b
Group 4
captured Pacific crust
Menard FZ - Antarctic Plate
Group 3
Depth [m]
c
Group 5
Group 6
Pitman FZ - Pacific Plate
Depth [m]
d
Group 7
Group 8
Pitman FZ - Antarctic Plate
Depth [m]
e
Group 9
Group 10
Heirtzler FZ - Pacific Plate
Depth [m]
Louisville Chain
Menard FZ
Heirtzler FZ
Pitman FZ
Bellingshausen Sector
Marie Byrd Land Sector
West Antarctica

Figure 2.9: The age and azimuth of anti J-shaped abyssal hills for the Menard, Pitman and Heirtzler FZs during the last 45 Ma (during chron C20r). The blue and green dots represent anti J-shaped abyssal hills formed at the Pacific and Antarctic, respectively. The blue and green numbers represent the groups of observed anti J-shaped abyssal hills presented in Figure 2.8. The red and blue lines represent the ridge offset over time. The blue line for the northern splay of Heirtzler FZ is dashed since its ridge offset is poorly constrained. The ridge offsets on both flanks should be the same; small differences reflect the uncertainties in magnetic anomaly picks [*Croon et al.*, 2008]. The black dots represent changes in lineation azimuth based on the synthetic flowline model for Menard, Pitman and Heirtzler FZs [*Croon et al.*, 2008]. The thick blue and red lines at the top of Figures 2.9a and b indicate at which crustal age intervals multibeam bathymetry data are available to map abyssal hills on the Pacific and Antarctic plates, respectively. Oblique Mercator projection used to calculate abyssal hill curvatures and lineation azimuths same as in Figure 2.1.

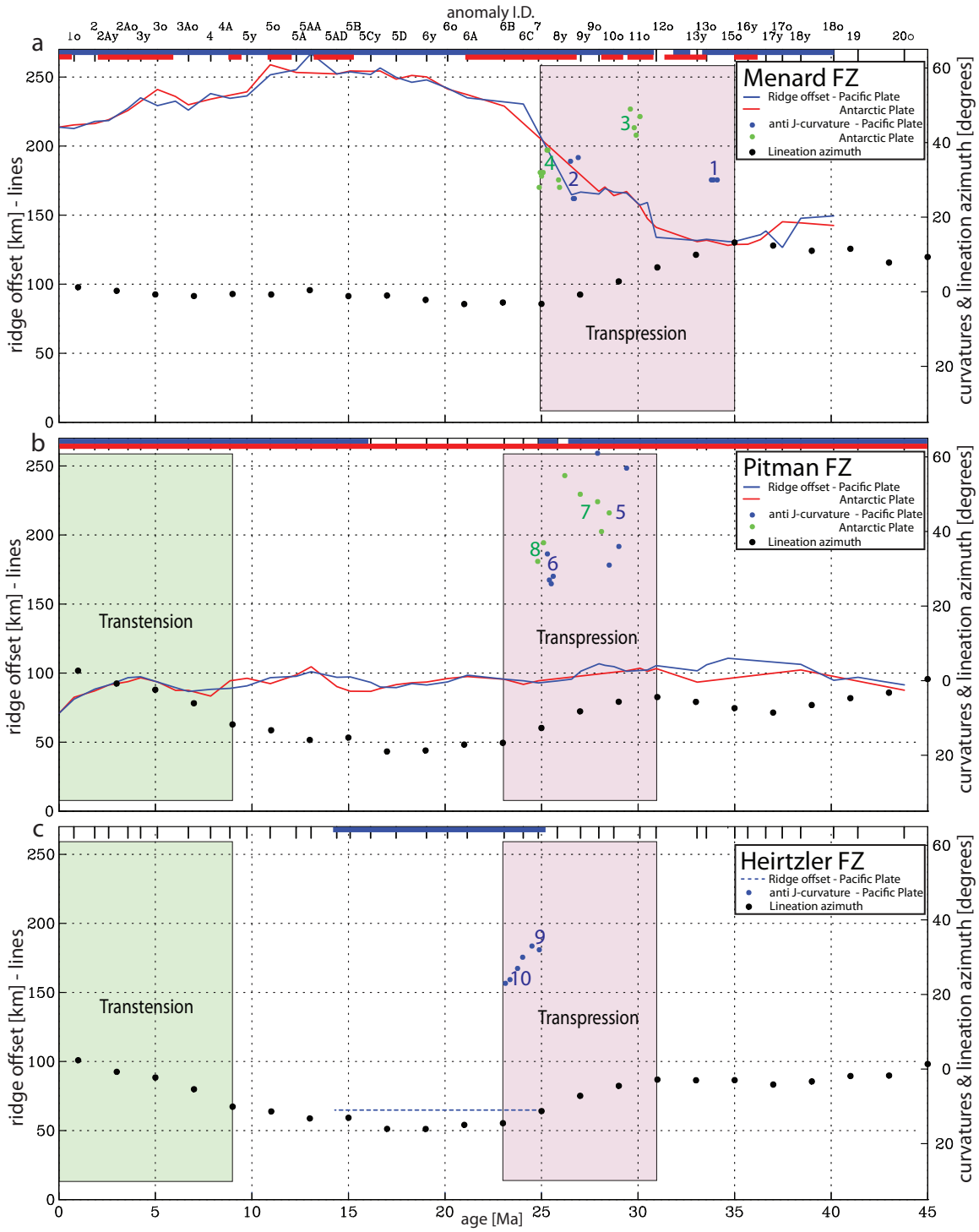
anomaly I.D.
1o 2 2Ao 2Ay 3o 3y 3Ao 4 4A 5o 5y 5AA 5A 5B 5AD 5Cy 5D 6o 6y 6A 6B 6C 7 8y 9o 9y 10o 11o 12o 13o 13y 15o 16y 17o 17y 18o 18y 19 20o
a
Menard FZ
Ridge offset - Pacific Plate
Antarctic Plate
anti J-curvature - Pacific Plate
Antarctic Plate
Lineation azimuth
Transpression
b
Pitman FZ
Ridge offset - Pacific Plate
Antarctic Plate
anti J-curvature - Pacific Plate
Antarctic Plate
Lineation azimuth
Transtension
Transpression
c
Heirtzler FZ
Ridge offset - Pacific Plate
anti J-curvature - Pacific Plate
Lineation azimuth
Transtension
Transpression
ridge offset [km] - lines
curvatures & lineation azimuth [degrees]
age [Ma]

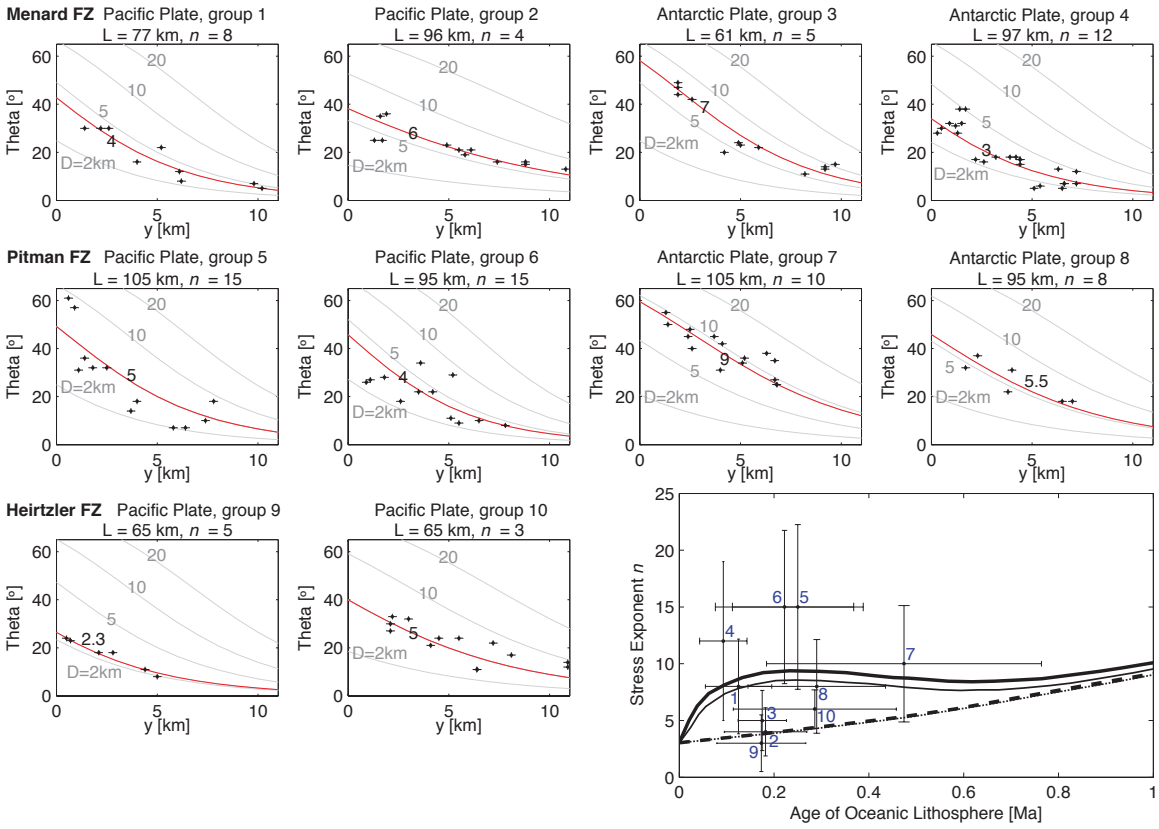

Figure 2.10: Anti J-shaped abyssal hill deflections (θ) vs. distance from transform fault (y). The black dots are the digitized deflections for the ten groups shown in Figures 2.8 and 2.9. Error bars represent measurement errors in θ and y. Red lines represent optimal fitting curve of Equation 1 for paleo-transform fault length L, transform fault displacement D and stress exponent *n*. Curves of Equation 1 for 2, 5, 10 and 20 km transform fault displacement are presented with grey lines. At right bottom comparison of calculated relationship of stress exponent *n*, with lithospheric age [Fig. 4 from *Sonder and Pockalny*, 1999], compared with *n* predicted from curvature of abyssal hills (error bars; numbers represent groups). Solid (dashed) curves represent strong (zero strength) top 2km of oceanic crust. Thick (thin) lines show results with hydrostatic (zero) pore-fluid pressure. Error bars for each group based on errors in best fitting curves for transform fault displacement (age) and stress exponent *n*.

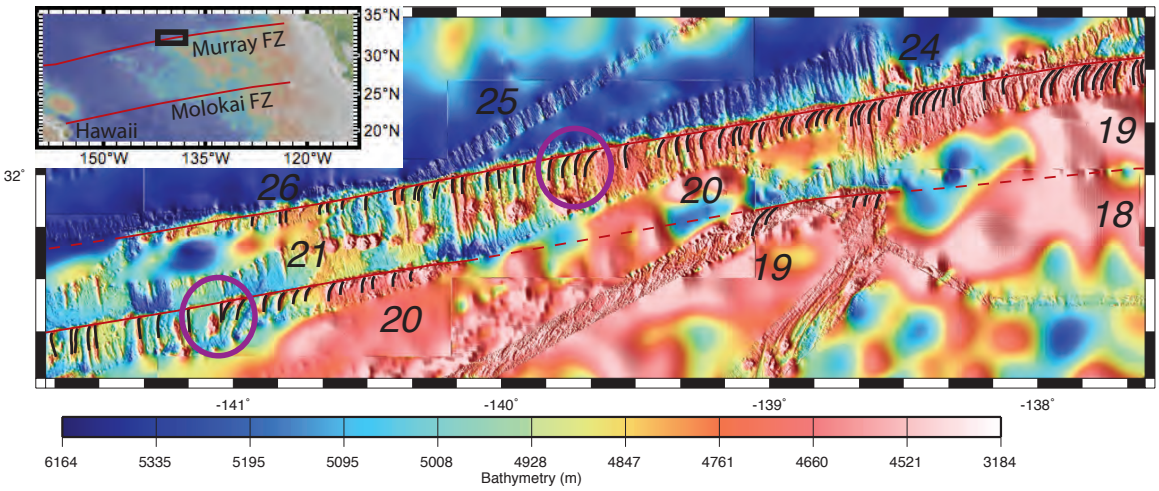

Figure 2B1: Abyssal hill tip morphology (black lines) at the two splays (red lines) of Murray FZ in the North Pacific. The purple circles mark the transition from abyssal hills with little or no curved tips to significant J-shaped deflections. The black numbers show magnetic anomaly identifications. Multibeam bathymetry data at Murray FZ from AVON01MV, COOK25MV, EW9506, MRTN01WT, RNDB01WT and TUNE09WT cruises on a background image of predicted bathymetry [Smith and Sandwell, 1994]. Map projection same as in Figure 2.2b.

Figure 2C1: Figure 2C1a shows the absolute Pacific plate motion relative to a fixed spot in the mantle according to three models (brown, blue and red lines) [*Andrews et al.*, 2006; *Koppers et al.*, 2001; *Wessel and Kroenke*, 2008] and migration of the PAR relative to the mantle (orange, green and purple lines) calculated by combining the finite rotations of the three absolute Pacific plate motion models with the rotations for the motion of the PAR relative to the Pacific plate (black lines representing synthetic flowlines plotted relative to the Pacific and Antarctic plates annotated with magnetic anomaly isochrons) [*Croon et al.*, 2008]. Figures 2C1b and c compare the azimuths of the relative plate motion of the Pacific plate (black dots) to the three models for absolute Pacific plate motion (brown, blue and red lines). Figure 2C1d zooms in to the Pitman transform fault and illustrates the migration (purple arrows) of the RTIs (blue stars) according to the WK08-A model [*Wessel and Kroenke*, 2008]. Map projection of Figures 2C1a and d are stereographic centered on 69°S, 180°W. Oblique Mercator projection used to calculate plate motion azimuths in Figures 2C1b and c same as in Figure 2.1.

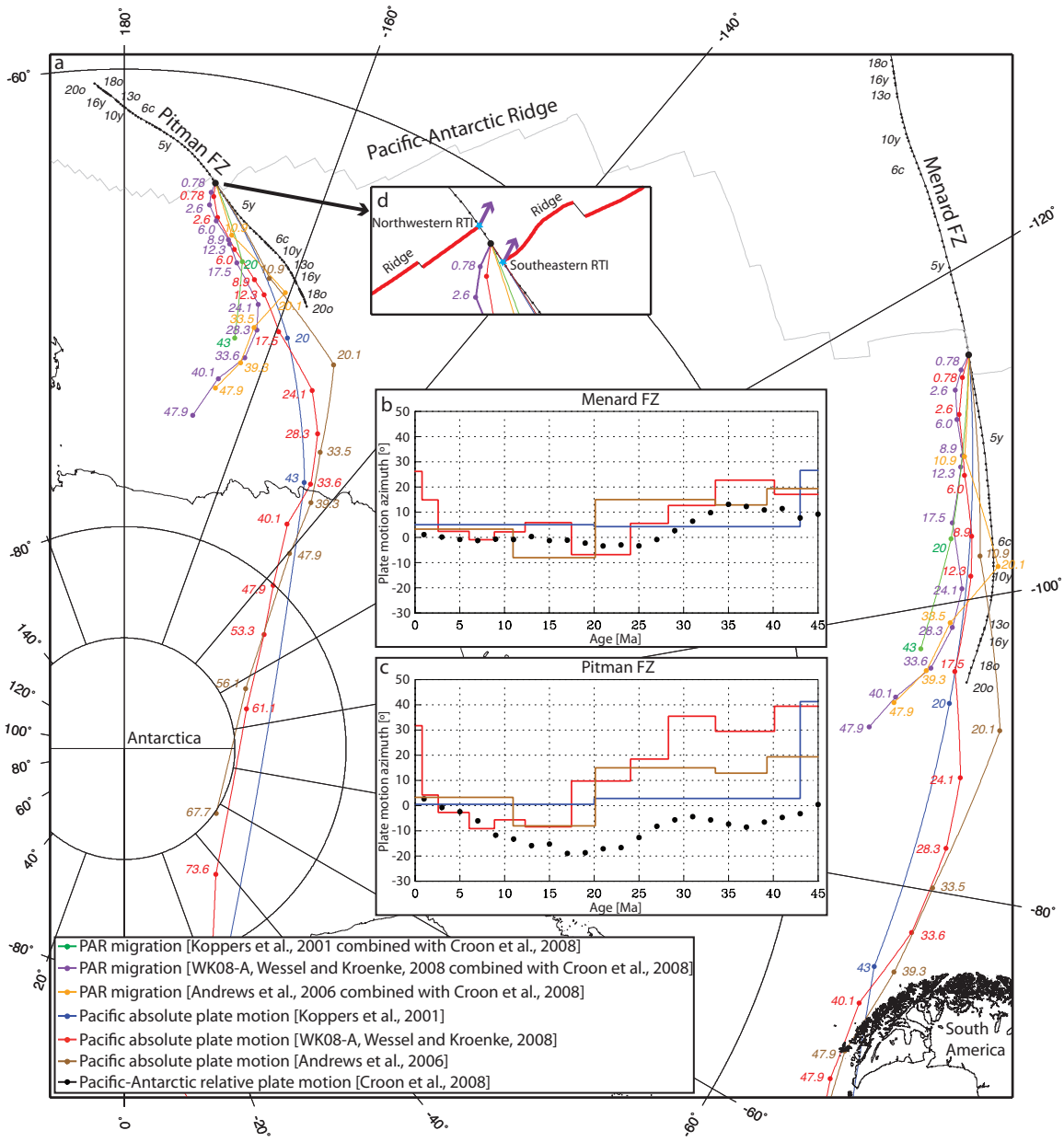
a
Pitman FZ
Pacific-Antarctic Ridge
Menard FZ
Antarctica
South America
d
Northwestern RTI
Southeastern RTI
Ridge
Ridge
b
Menard FZ
Plate motion azimuth [°]
Age [Ma]
c
Pitman FZ
Plate motion azimuth [°]
Age [Ma]
PAR migration [Koppers et al., 2001 combined with Croon et al., 2008]
PAR migration [WK08-A, Wessel and Kroenke, 2008 combined with Croon et al., 2008]
PAR migration [Andrews et al., 2006 combined with Croon et al., 2008]
Pacific absolute plate motion [Koppers et al., 2001]
Pacific absolute plate motion [WK08-A, Wessel and Kroenke, 2008]
Pacific absolute plate motion [Andrews et al., 2006]
Pacific-Antarctic relative plate motion [Croon et al., 2008]

2.10 REFERENCES

Abelson, M., and A. Agnon (1997), Mechanics of oblique spreading and ridge segmentation, *Earth and Planetary Science Letters*, *148*(3-4), 405-421.

Abelson, M., G. Baer, and A. Agnon (2002), Fossil ridge-transform intersection in the Troodos ophiolite: New perspectives from rock magnetism in the gabbro suite and fracture mechanics analysis, *Geochemistry Geophysics Geosystems, 3*, 1046, DOI: 10.1029/2001gc000245.

Andrews, D. L., R. G. Gordon, and B. C. Horner-Johnson (2006), Uncertainties in plate reconstructions relative to the hotspots; Pacific-hotspot rotations and uncertainties for the past 68 million years, *Geophysical Journal International, 166*(2), 939-951, DOI: 10.1111/J.1365-246x.2006.03029.X.

Atwater, T., and J. Severinghaus (1989), Tectonic maps of the Northeast Pacific, in *The Eastern Pacific Ocean and Hawaii, vol. N*, edited by E. L. Winterer, D. M. Hussong and R. W. Decker, pp. 15-20, Geological Society of America, Boulder, Colorado, The Geology of North America.

Behn, M. D., J. Lin, and M. T. Zuber (2002), Evidence for weak oceanic transform faults, *Geophysical Research Letters, 29*(24), Artn 2207, DOI: 10.1029/2002gl015612.

Bonatti, E., M. Ligi, L. Gasperini, A. Peyve, Y. Raznitsin, and Y. J. Chen (1994), Transform Migration and Vertical Tectonics at the Romanche Fracture-Zone, Equatorial Atlantic, *Journal of Geophysical Research-Solid Earth*, *99*(B11), 21779-21802.

Brune, J. N., T. L. Henyey, and R. F. Roy (1969), Heat Flow, Stress, and Rate of Slip Along San Andreas Fault, California, *Journal of Geophysical Research*, *74*(15), 3821-3827.

Cande, S. C., E. M. Herron, and B. R. Hall (1982), The early Cenozoic tectonic history of the Southeast Pacific, *Earth and Planetary Science Letters, 57*(1), 63-74, DOI: 10.1016/0012-821X(82)90173-X.

Cande, S. C., and D. V. Kent (1995), Revised calibration of the geomagnetic polarity timescale for the Late Cretaceous and Cenozoic, *Journal of Geophysical Research-Solid Earth, 100*(B4), 6093-6095, DOI: 10.1029/94JB03098.

Cande, S. C., C. A. Raymond, J. M. Stock, and W. F. Haxby (1995), Geophysics of the Pitman Fracture-Zone and Pacific-Antarctic plate motions during the Cenozoic, *Science, 270*(5238), 947-953, DOI: 10.1126/science.270.5238.947.

Crane, K. (1976), Intersection of Siqueiros Transform Fault and East Pacific Rise, *Marine Geology*, *21*(1), 25-46.

Croon, M. B., S. C. Cande, and J. M. Stock (2008), Revised Pacific-Antarctic plate motions and geophysics of the Menard Fracture Zone, *Geochemistry Geophysics Geosystems, 9*, Q07001, DOI: 10.1029/2008gc002019.

Dietz, R. S., H. W. Menard, and E. L. Hamilton (1954), Echograms of the Mid-Pacific Expedition, *Deep-Sea Research, 1*(4), 258-272, DOI: 10.1016/0146-6313(54)90008-8.

Eakins, B. W. (2002), Structure and Development of Oceanic Rifted Margins, 174 pp, Ph.D. Thesis, Scripps Institution of Oceanography.

England, P., and D. McKenzie (1982), A thin viscous sheet model for continental deformation, *Geophysical Journal of the Royal Astronomical Society, 70*(2), 295-321, DOI: 10.1111/j.1365-246X.1982.tb04969.x.

Ferguson, E. M., and E. M. Klein (1993), Fresh Basalts from the Pacific Antarctic Ridge Extend the Pacific Geochemical Province, *Nature*, *366*(6453), 330-333.

Fornari, D. J., D. G. Gallo, M. H. Edwards, J. A. Madsen, M. R. Perfit, and A. N. Shor (1989), Structure and Topography of the Siqueiros Transform-Fault System - Evidence for the Development of Intra-Transform Spreading Centers, *Marine Geophysical Researches, 11*(4), 263-299, DOI: 10.1007/BF00282579.

Fox, P. J., and D. G. Gallo (1984), A tectonic model for ridge transform ridge plate boundaries-implications for the structure of oceanic lithosphere, *Tectonophysics, 104*(3-4), 205-242, DOI: 10.1016/0040-1951(84)90124-0.

Fujita, K., and N. H. Sleep (1978), Membrane stresses near mid-ocean ridge-transform intersections, *Tectonophysics*, *50*(2-3), 207-221.

Garfunkel, Z. (1974), Model for Late Cenozoic Tectonic History of Mojave-Desert, California, and for Its Relation to Adjacent Regions, *Geological Society of America Bulletin*, *85*(12), 1931-1944.

Géli, L., et al. (1997), Evolution of the Pacific-Antarctic Ridge south of the Udintsev fracture zone, *Science*, *278*(5341), 1281-1284.

Goff, J. A. (1992), Quantitative Characterization of Abyssal Hill Morphology Along Flow Lines in the Atlantic-Ocean, *Journal of Geophysical Research-Solid Earth*, *97*(B6), 9183-9202.

Grindlay, N. R., P. J. Fox, and K. C. Macdonald (1991), 2nd-Order Ridge Axis Discontinuities in the South-Atlantic - Morphology, Structure, and Evolution, *Marine Geophysical Researches*, *13*(1), 21-49.

Grindlay, N. R., and P. J. Fox (1993), Lithospheric stresses associated with nontransform offsets of the mid-atlantic ridge-implications from a finite-element analysis, *Tectonics*, *12*(4), 982-1003.

Gudmundsson, A. (1993), On the Structure and Formation of Fracture-Zones, *Terra Nova*, *5*(3), 215-224.

Haxby, W. F., and E. M. Parmentier (1988), Thermal Contraction and the State of Stress in the Oceanic Lithosphere, *Journal of Geophysical Research-Solid Earth and Planets*, *93*(B6), 6419-6429.

Hayes, D. E., and J. L. LaBrecque (1991), Sediment Isopachs: Circum-Antarctic to 30°S, in *Marine Geological and Geophysical Atlas of the Circum-Antarctic to 30°S, Antarct. Res. Ser., vol. 54*, edited by D. E. Hayes, pp. 29-33, AGU, Washington, D.C.

Hayes, D. E., C. Zhang, and R. A. Weissel (2009), Modeling Paleobathymetry in the Southern Ocean, *EOS Trans., AGU*, *90*(19), 165-166.

Karson, J. A., and H. J. B. Dick (1983), Tectonics of Ridge-Transform Intersections at the Kane Fracture-Zone, *Marine Geophysical Researches*, *6*(1), 51-98.

Kastens, K. A., W. B. F. Ryan, and P. J. Fox (1986), Structural and Volcanic Expression of a Fast Slipping Ridge-Transform-Ridge-Plate Boundary - Sea Marc-I and Photographic Surveys at the Clipperton Transform-Fault, *Journal of Geophysical Research-Solid Earth and Planets*, *91*(B3), 3469-3488.

Klitgord, K. D. (1976), Sea-Floor Spreading - Central Anomaly Magnetization High, *Earth and Planetary Science Letters*, *29*(1), 201-209.

Koppers, A. A. P., J. Phipps Morgan, J. W. Morgan, and H. Staudigel (2001), Testing the fixed hotspot hypothesis using Ar-40/Ar-39 age progressions along seamount trails, *Earth and Planetary Science Letters*, *185*(3-4), 237-252.

Krijgsman, W., F. J. Hilgen, I. Raffi, F. J. Sierro, and D. S. Wilson (1999), Chronology, causes and progression of the Messinian salinity crisis, *Nature, 400*(6745), 652-655, DOI: 10.1038/23231.

Lachenbruch, A. H. (1981), Corrections to 'Heat flow and energetics of the San Andreas fault zone' and some additional comments on the relation between fault friction and observed heat flow, *Journal of Geophysical Research*, *86*(Nb8), 7171-7172.

Ligi, M., E. Bonatti, L. Gasperini, and A. N. B. Poliakov (2002), Oceanic broad multifault transform plate boundaries, *Geology, 30*(1), 11-14, DOI: 10.1130/0091-7613(2002)030<0011:OBMTPB>2.0.CO;2.

Lonsdale, P. (1977), Structural Geomorphology of a Fast-Spreading Rise Crest: The East Pacific Rise Near 3°25'S, *Marine Geophysical Researches, 3*, 251-293, DOI: 10.1007/BF00285656.

Lonsdale, P. (1978), Near-bottom reconnaissance of a fast-slipping transform fault zone at the Pacific-Nazca Plate boundary, *Journal of Geology*, *86*(4), 451-472.

Lonsdale, P. (1986), Tectonic and magmatic ridges in the eltanin fault system, South Pacific, *Marine Geophysical Researches, 8*(3), 203-242, DOI: 10.1007/BF00305484.

Lonsdale, P. (1994a), Geomorphology and structural segmentation of the crest of the southern (Pacific-Antarctic) East Pacific Rise, *Journal of Geophysical Research-Solid Earth*, *99*(B3), 4683-4702.

Lonsdale, P. (1994b), Structural geomorphology of the eltanin fault system and adjacent transform faults of the Pacific-Antarctic plate boundary, *Marine Geophysical Researches, 16*(2), 105-143, DOI: 10.1007/BF01224756.

Macario, A., W. F. Haxby, J. A. Goff, W. B. F. Ryan, S. C. Cande, and C. A. Raymond (1994), Flow line variations in abyssal hill morphology for the Pacific-Antarctic Ridge at 65°S, *Journal of Geophysical Research-Solid Earth*, *99*(B9), 17921-17934.

Macdonald, K. C., D. S. Scheirer, and S. M. Carbotte (1991), Midocean Ridges - Discontinuities, Segments and Giant Cracks, *Science*, *253*(5023), 986-994.

Macdonald, K. C., P. J. Fox, R. T. Alexander, R. A. Pockalny, and P. Gente (1996), Volcanic growth faults and the origin of Pacific abyssal hills, *Nature, 380*(6570), 125-129, DOI: 10.1038/380125a0.

McAdoo, D., and S. Laxon (1997), Antarctic Tectonics: Constraints from an ERS-1 Satellite Marine Gravity Field, *Science, 276*(5312), 556-560, DOI: 10.1126/science.276.5312.556.

McKenzie, D., and J. Jackson (1983), The Relationship between Strain Rates, Crustal Thickening, Paleomagnetism, Finite Strain and Fault Movements within a Deforming Zone, *Earth and Planetary Science Letters*, *65*(1), 182-202.

Menard, H. W. (1960), The East Pacific Rise, *Science*, *132*(3441), 1737-1746.

Menard, H. W., and T. Atwater (1969), Origin of Fracture Zone Topography, *Nature, 222*(5198), 1037-1040, DOI: 10.1038/2221037a0.

Menard, H. W., and T. E. Chase (1970), Fracture Zones, in *The Sea, vol. 4, part 1*, edited by A. E. Maxwell, pp. 421-444, Wiley Interscience, New York, NY.

Nelson, M. R., and C. H. Jones (1987), Paleomagnetism and Crustal Rotations Along a Shear Zone, Las-Vegas Range, Southern Nevada, *Tectonics*, *6*(1), 13-33.

Neves, M. C., M. H. P. Bott, and R. C. Searle (2004), Patterns of stress at midocean ridges and their offsets due to seafloor subsidence, *Tectonophysics, 386*(3-4), 223-242, DOI: 10.1016/j.tecto.2004.06.010.

Phipps Morgan, J., and E. M. Parmentier (1984), Lithospheric stress near a ridge-transform intersection, *Geophysical Research Letters, 11*(2), 113-116, DOI: 10.1029/GL011i002p00113.

Pockalny, R. A. (1997), Evidence of transpression along the Clipperton Transform: Implications for processes of plate boundary reorganization, *Earth and Planetary Science Letters, 146*(3-4), 449-464, DOI: 10.1016/S0012-821X(96)00253-1.

Pollard, D. D., and A. Aydin (1984), Propagation and Linkage of Oceanic Ridge Segments, *Journal of Geophysical Research*, *89*(Nb12), 17-28.

Reasenberg, P. A., and R. W. Simpson (1992), Response of Regional Seismicity to the Static Stress Change Produced by the Loma-Prieta Earthquake, *Science*, *255*(5052), 1687-1690.

Ron, H., R. Freund, Z. Garfunkel, and A. Nur (1984), Block Rotation by Strike-Slip Faulting - Structural and Paleomagnetic Evidence, *Journal of Geophysical Research*, *89*(Nb7), 6256-6270.

Ron, H., A. Aydin, and A. Nur (1986), Strike-Slip Faulting and Block Rotation in the Lake Mead Fault System, *Geology*, *14*(12), 1020-1023.

Ryan, W. B. F., C. A. Raymond, S. C. Cande, W. F. Haxby, S. F. Tebbens, S. O'Hara, R. D. Müller, B. O'Brien, and W. Wilkinson (1992), Documentation of ridge-axis jumps on the Pacific-Antarctic spreading center, *EOS Trans., AGU Spring Meeting Suppl., 295*, *73*(14).

Sandwell, D. T., and W. H. F. Smith (1997), Marine gravity anomaly from Geosat and ERS 1 satellite altimetry, *Journal of Geophysical Research-Solid Earth, 102*(B5), 10039-10054, DOI: 10.1029/96JB03223.

Schouten, H., H. J. B. Dick, and K. D. Klitgord (1987), Migration of Mid-Ocean-Ridge Volcanic Segments, *Nature, 326*(6116), 835-839, DOI: 10.1038/326835a0.

Sclater, J. G., N. R. Grindlay, J. A. Madsen, and C. Rommevaux-Jestin (2005), Tectonic interpretation of the Andrew Bain transform fault: Southwest Indian Ocean, *Geochemistry Geophysics Geosystems, 6*, Q09k10, DOI: 10.1029/2005gc000951.

Searle, R. (1984), GLORIA Survey of the East Pacific Rise near 3.5-Degrees-S - Tectonic and Volcanic Characteristics of a Fast Spreading Mid-Ocean Rise, *Tectonophysics, 101*(3-4), 319-344, DOI: 10.1007/BF00313879.

Searle, R. C., and A. S. Laughton (1977), Sonar Studies of Mid-Atlantic Ridge and Kurchatov Fracture Zone, *Journal of Geophysical Research*, *82*(33), 5313-5328.

Searle, R. C. (1986), GLORIA Investigations of Oceanic Fracture-Zones - Comparative-Study of the Transform-Fault Zone, *Journal of the Geological Society*, *143*, 743-756.

Sempéré, J. C., and K. C. Macdonald (1986), Overlapping Spreading Centers - Implications from Crack-Growth Simulation by the Displacement Discontinuity Method, *Tectonics*, *5*(1), 151-163.

Sharp, W. D., and D. A. Clague (2006), 50-Ma initiation of Hawaiian-Emperor bend records major change in Pacific plate motion, *Science, 313*(5791), 1281-1284, DOI: 10.1126/Science.1128489.

Small, C., and L. V. Danyushevsky (2003), Plate-kinematic explanation for mid-oceanic-ridge depth discontinuities, *Geology, 31*(5), 399-402, DOI: 10.1130/0091-7613(2003)031<0399:PEFMDD>2.0.CO;2.

Smith, W. H. F., and D. T. Sandwell (1994), Bathymetric Prediction from Dense Satellite Altimetry and Sparse Shipboard Bathymetry, *Journal of Geophysical Research-Solid Earth, 99*(B11), 21803-21824, DOI: 10.1029/94JB00988.

Sonder, L. J., and P. England (1986), Vertical Averages of Rheology of the Continental Lithosphere - Relation to Thin Sheet Parameters, *Earth and Planetary Science Letters*, *77*(1), 81-90.

Sonder, L. J., and R. A. Pockalny (1999), Anomalously rotated abyssal hills along active transforms: Distributed deformation of oceanic lithosphere, *Geology, 27*(11), 1003-1006.

Tamsett, D., and R. C. Searle (1988), Structure and Development of the Midocean Ridge Plate Boundary in the Gulf of Aden - Evidence from Gloria Side Scan Sonar, *Journal of Geophysical Research-Solid Earth and Planets*, *93*(B4), 3157-3178.

Tchalenko, J. S., and N. N. Ambraseys (1970), Structural Analysis of Dasht-E Bayaz (Iran) Earthquake Fractures, *Geological Society of America Bulletin*, *81*(1), 41-60.

Thatcher, W., and D. P. Hill (1995), A Simple-Model for the Fault-Generated Morphology of Slow-Spreading Midoceanic Ridges, *Journal of Geophysical Research-Solid Earth*, *100*(B1), 561-570.

Townend, J., and M. D. Zoback (2004), Regional tectonic stress near the San Andreas fault in central and southern California, *Geophysical Research Letters, 31*(15), -, DOI: 10.1029/2003gl018918.

Tucholke, B. E., and H. Schouten (1988), Kane Fracture Zone, *Marine Geophysical Researches, 10*(1-2), 1-39, DOI: 10.1007/BF02424659.

Wessel, P., and L. W. Kroenke (2008), Pacific absolute plate motion since 145 Ma: An assessment of the fixed hot spot hypothesis, *Journal of Geophysical Research-Solid Earth, 113*(B6), Artn B06101, DOI: 10.1029/2007jb005499.

Whittaker, J. M., R. D. Müller, G. Leitchenkov, H. Stagg, M. Sdrolias, C. Gaina, and A. Goncharov (2007), Major Australian-Antarctic plate reorganization at Hawaiian-Emperor bend time, *Science, 318*(5847), 83-86, DOI: 10.1126/science.1143769.

Wilcox, R. E., T. P. Harding, and D. R. Seely (1973), Basic Wrench Tectonics, *American Association of Petroleum Geologists Bulletin*, *57*(1), 74-96.

Wilson, D. S. (1996), Fastest known spreading on the Miocene Cocos-Pacific plate boundary, *Geophysical Research Letters*, *23*(21), 3003-3006.

CHAPTER 3

Revised Pacific-Cocos-Nazca-Antarctic Plate Motions

ABSTRACT

Surface-towed and high altitude aeromagnetic vector magnetometer data enabled us to better constrain the relative motions of the Pacific-Cocos Ridge near the Galapagos Triple Junction in the equatorial Pacific region where the total field magnetic anomaly is very small for oceanic crust formed at the North-South striking East Pacific Rise. These data in combination with available magnetic anomaly profiles for most of the East Pacific ridge systems allowed us to improve plate reconstructions for the Pacific-Cocos, Pacific-Nazca, Cocos-Nazca, Pacific-Antarctic, Chile Ridge and Mathematician paleo-ridge since chron C4A (8.9 Ma). The 3-plate solutions for the Pacific-Cocos-Nazca and the Pacific-Nazca-Antarctic plate circuits agree well for the overlapping Pacific-Nazca rotation parameters. However, our 3-plate model for the Pacific-Cocos-Nazca plate circuit shows a significant non-closure since its solution for the Pacific-Cocos finite rotation poles has a large misfit with the best-fitting 2-plate solutions. The new Pacific-Cocos rotation parameters demonstrate that a ~30° counter-clockwise rotation since chron C4A has put the right-stepping Clipperton transform fault under significant transpression while the left-stepping Siqueiros transform fault has developed three intra-transform spreading centers in response to transtension. Rapidly changing lineation azimuths, based on our new rotation parameters for the Cocos-Nazca Ridge, suggest continuous readjustment of the spreading center since chron C4A.

3.1 INTRODUCTION

The sea-floor spreading history of the East Pacific Rise (EPR) in the eastern tropical Pacific (Figure 3.1) involved several plate boundary readjustments since the split of the Farallon plate into the Cocos and Nazca plates [*Barckhausen et al.*, 2008; *Hey*, 1977; *Lonsdale*, 2005] during the Oligocene after 25 Ma (~chron C7; for this study we used the geomagnetic polarity timescale by *Cande and Kent* [1995] with revisions for chrons C3Ay and C3Ao as given by *Krijgsman et al.* [1999]). Since its birth, the Galapagos Triple Junction (GTJ) has connected the Pacific-Nazca, Pacific-Cocos and Cocos-Nazca spreading centers. A significant part of the oceanic lithosphere, which has been formed at the Cocos-Nazca Ridge (CNR), has been lost by subduction in the Middle America and Peru-Chile Trenches. Evolution of the east-west striking CNR since 8.9 Ma (chron C4A) has been described in detail by *Wilson and Hey* [1995] based, in particular, on several high-amplitude magnetic anomaly profiles. The plate reconstructions in our study have been limited by the availability of a sufficient number of magnetic anomaly picks at the CNR for chron C4A and younger.

A number of studies [*Lonsdale*, 1989; *Okal and Cazenave*, 1985; *Searle et al.*, 1995] provide some constraint on the plate motion history of the fast spreading Pacific-Nazca Ridge (PNR) after 25 Ma (~chron C7). Several readjustments have shaped the structural morphology of the Pacific and Nazca plates since the split, including growth of the prominent Mendoza and Bauer paleo microplates (Figure 3.1), which were actively growing between about 20 to 12 Ma (~chrons C6o to C5A) [*Liu*, 1996; *Lonsdale*, 1989] and 17 to 6 Ma (~chrons C5D to C3Ay) [*Eakins and Lonsdale*, 2003], respectively. After 8 Ma (~chron C4) the EPR rapidly propagated northward and increased in spreading

rate while a ~4° clockwise rotation and decrease of spreading rate occurred at the Bauer-Nazca Ridge. The Bauer microplate was captured by the Nazca plate around 5.8 Ma (during chron C3r). Further readjustment of the PNR occurred after ~6 Ma (chron 3Ay) with the formation of the Easter and Juan Fernandez microplates [*Bird et al.*, 1998; *Naar and Hey*, 1991; *Rusby and Searle*, 1995; *Searle et al.*, 1993] following counterclockwise rotation of the PNR, which led to overlapping spreading centers at long transform fault offsets at the southern end of the PNR. This led to the emergence of the microplates in an intratransform setting [*Bird and Naar*, 1994].

The tectonic evolution of the Pacific-Cocos Ridge (PCR), at the northern part of the EPR, since 25 Ma (~chron C7) has been described in some studies [*Klitgord and Mammerickx*, 1982; *Mammerickx and Klitgord*, 1982; *Menard*, 1978; *Schilt et al.*, 1982]. The PCR is characterized by fast spreading, with highest spreading rates during the Mid-Miocene [*Wilson*, 1996]. Similar to the PNR, the evolution of the PCR is characterized by several readjustments. Most notably, the Mathematician paleo microplate [*Mammerickx et al.*, 1988] was actively growing between the failed Mathematician Ridge and the Moctezuma Trough from ~12 to 3 Ma (chrons C5A to C2A).

The GTJ at the southern end of the PCR is located ~10° north of the magnetic equator (at ~7°S at this longitude). At low magnetic latitudes total field magnetic anomalies over approximately north-south striking bodies such as crust formed at the East Pacific Rise are very small. Therefore, very few reliable magnetic anomaly picks are available in the region of the GTJ. To address this problem, towed vector and total field magnetic data were collected during the DANA05RR cruise (Figure 3.1) in the equatorial Pacific. Except at the poles, the vertical anomaly (Bz) and the horizontal anomaly (Bx) perpendicular to the spreading lineation are always larger than the total

field anomaly. The amplitude of the vector anomalies increases rapidly away from the geographic equator so that in the vicinity of the magnetic equator the vector anomalies are an order of magnitude larger than the corresponding total field anomalies [*Gee and Cande*, 2002]. In this study we evaluate and use the towed vector magnetic anomaly picks from the DANA05RR cruise and several vector aeromagnetic anomaly picks at the CNR in combination with a large number of total field anomaly picks at the CNR, PNR, PCR, Chile Ridge, Pacific-Antarctic Ridge (PAR) and the Mathematician and Bauer paleo-ridges to evaluate and reconstruct the Pacific-Cocos-Nazca and Pacific-Nazca-Antarctic plate circuits for 10 magnetic anomalies between chrons C4A and C1o (8.9 to 0.78 Ma).

The East Pacific ridge geometry includes two main triple junctions linking the Pacific-Nazca-Antarctic and the Pacific-Cocos-Nazca plate circuits. When three plates meet at a triple junction, the circuit is 'closed' when the sum of the three true rotations for each plate pair equals the identity matrix [*Kirkwood et al.*, 1999]. If the sum is not the identity, either the plates are not rigid, or the plate geometry is incorrect, or there is a systematic error in the data. *DeMets et al.* [2010] found a large misfit for the Pacific-Cocos-Nazca plate circuit with their MORVEL global plate circuit model for chron C1o (0.78 Ma). The RMS misfit was 2.8 mm yr^{-1} compared to the best-fitting Pacific-Cocos angular velocity. They evaluated the hypothesis of a diffuse plate boundary within one or both of the Nazca and Cocos plates as the source of the misfit but no evidence, e.g., in the form of earthquakes, has been found for such intra-plate deformation zones. The second possibility, which they evaluated, is a possible inconsistency between the spreading rate and transform fault data, possibly due to a plate readjustment since 0.78 Ma. However, *DeMets et al.* [2010] concluded that the needed directional changes were

unacceptably large. The non-closure, based on MORVEL, is mainly manifested as systematic misfits of the closure-enforced angular velocities to the PNR and PCR spreading rates. In this study we have compared 2-plate solutions for the PCR, PNR, CNR, PAR and Chile Ridge with 3-plate solutions from the Pacific-Nazca-Antarctic and the Pacific-Cocos-Nazca plate circuits for each plate pair and we compare our results for chron C1o with MORVEL.

3.2 DATA

In order to improve the plate kinematic reconstruction of the East Pacific spreading ridges we have included nearly 3300 total field magnetic anomaly picks in our plate reconstruction model. However, in the equatorial Pacific region, where the total magnetic anomaly field is very small for oceanic crust formed at the North-South striking EPR hardly any magnetic anomaly identifications are possible. To address this problem, towed vector magnetometer data and total field data from two Overhauser sensors deployed as a horizontal gradiometer was recorded during the January 2004 DANA05RR cruise aboard R/V Revelle (white solid line in Figure 3.1).

3.2.1 Towed Vector Magnetometer Data

The Scripps vector magnetometer (described in *Gee and Cande* [2002]), which was deployed during the DANA05RR cruise, is based on the Seatex MRU6 motion sensor including a fluxgate by Kongsberg Maritime™. The total field is calculated from the three fluxgate measurements. In order to get accurate total field data from a set of fluxgates, the fluxgates must be properly calibrated [*Merayo et al.*, 2000; *Olsen et al.*, 2003]. Since towed sensors only move in a limited range of roll and pitch angles [*Gee and Cande*, 2002] during a cruise, the nine temperature dependent calibration

parameters were determined in a controlled laboratory environment at several temperatures, that cover the full range of ocean water temperatures. Calibration circles were sailed during the cruise to refine these nine calibration parameters, e.g., a loop that was sailed on the east end of two profiles across the PCR (Figure 3.2a). This refined calibration improves the correspondence between the MRU fluxgate and the SeaSpy Overhauser gradiometer sensors for the total magnetic field.

The internal MRU fluxgate is intended for magnetic north seeking and the sensors are specified with a resolution of ~10 nT. The MRU sensor measures the three magnetic field components and the sensor orientation is determined from accelerometers and angular rate sensors. The yaw angle is estimated using the magnetic data and smoothed GPS data sent to the instrument to provide longer term heading and speed information. The sensor roll and pitch information allow determination of the vertical anomalous field and two orthogonal anomalous field components in the horizontal plane. The fluxgate data are used as a compass to determine a synthetic yaw that when appropriately filtered provides allows an estimate of the north and east components of the magnetic field to be made [*Engels et al.*, 2008]. Then the data are despiked and interpolated. Next, the ambient Definitive Geomagnetic Reference Field (DGRF) for each location is subtracted and a Low Pass (LP)/ High Pass (HP) trapezoidal bandpass filter in space domain of 7 to 200 km is applied to return only wavelengths that could be related to seafloor anomalies. These processing steps were also applied to the Overhauser gradiometer where the total magnetic field is concerned.

To illustrate how the processed total and vertical magnetic field data can be used to identify 2-D magnetic anomalies we show a representative 300 km long profile just East of the PCR (Figure 3.2a). The calibrated raw vector magnetic components (e.g., the

vertical component in Figure 3.2b1) for the MRU sensor have substantially more noise than the presented total magnetic field signals (Figure 3.2b2). The total field signal, measured by the Overhauser gradiometer (red line on Figure 3.2b2), has little noise, which is expected since the instrument is measuring the scalar field intensity, which is independent of orientation. However, the total magnetic field signal from the MRU sensor (gray signal on Figure 3.2b2) shows significantly more noise. This can be explained by the fact that the total magnetic field is calculated from the vector magnetic components for the three axes of the fluxgate. The towed instrument is constantly moving in the water leading to small errors and some noise in the MRU sensor-derived total magnetic field. A median filter is applied during data processing to produce smooth signals (e.g., Figure 3.2c). At ~135 km the processed total field plot (Figure 3.2c2) shows a ~50 nT difference between Overhauser and MRU sensors at the same moment as a 25° roll of the fluxgate towfish (Figure 3.2d). This example shows that the scalar calibration is good since the signals from the two sensors agree everywhere else. However, the misfit between the sensors during the 25° roll is also demonstrative for the limitations of the refined calibration from the circle data due to the limited range of roll and pitch angles during such loops.

We further evaluated the quality of the profile by calculating the cross-spectra between magnetic field component anomalies (Figure 3.2e). A high coherence between field components suggests a 2-D magnetic source (e.g., *Engels et al.* [2008]) whereas a low coherence can be the result of 3-D behavior of the source (e.g., by East-West striking volcanic lineaments or chemical alteration of the oceanic crust) and should be avoided for comparison with 2-D forward models. The best test of two-dimensionality is a high coherence and 90° phase difference for the vertical vs. the calculated horizontal (or

along-track) magnetic field components. However, the cross spectra analysis of the vertical vs. the calculated horizontal magnetic field components hardly shows any coherence for the example profile (Figure 3.2e) or any of the other profiles. In contrast, the example profile (and several others) shows reasonable coherence between the vertical component and the total field anomalies (> 0.5) for wavenumbers between 0.04 and 0.09 (11 to 25 km). It is unclear why the two-dimensionality test for the vertical and horizontal component anomalies is significantly worse than for the vertical component and the total field anomalies (Figure 3.2e). In this study, we have only evaluated the selected profile parts for the vertical field component for comparison with a 2-D forward model in the next section. Since the cross-spectra analysis is applied to the entire 300 km of the profile, we calculated and gridded the coherence for intervals of 50 km centered at each km of the profile (Figure 3.2f1). We also compared the phase difference between the total and vertical field for each interval with a gridded predicted 2-D forward model phase. Zero (white in Figure 3.2f2) means that the profile data and forward model have the same phase. The parts of the profile with reasonable to high (> 0.5) coherence for wave lengths of 7 to 50 km (wavenumbers 0.02 to 0.14) and a similar phase difference between the profile data and forward model for wavenumbers between 0.04 and 0.09 (11 to 25 km) are considered to be of acceptable quality and suitable for 2-D magnetic lineation detection by comparison with a 2-D forward model. We used this method for all DANA05RR profiles across PCR-formed oceanic crust (Figure 3.3). Only a few sections passed our selection criteria. The issues with the DANA05RR data and the applied calibration and processing methods are described more extensively in Appendix A.

3.2.2 Project Magnet Vector Aeromagnetic Profiles

O'Brien et al. [1999] and *Horner-Johnson and Gordon* [2003] demonstrated that magnetic anomalies due to seafloor spreading have been reliably recorded in the Project Magnet vector aeromagnetic profiles. Advantages of the aeromagnetic data compared to a ship-towed magnetometer include:

i) The airplane flies at high speed and therefore the diurnal variation of the magnetic field is mapped into long wavelengths that can easily be filtered with a HP bandpass filter. In contrast, wavelengths of these diurnal variations can interfere with magnetic anomalies due to seafloor spreading for a much slower moving ship-towed magnetometer.

ii) The Project Magnet magnetometer is mounted on an gyro-stabilized airplane. Therefore, the data are significantly less affected by errors introduced by constant motion of the sensor as is often the case for a towfish, which is pulled through surface water currents.

iii) The Project Magnet flights recorded data at ~7 to 8 km altitude. However, the vector aeromagnetic component anomalies can be as large as 100 nT [*Horner-Johnson and Gordon*, 2003]. Despite the diminution of the signal amplitude at the high altitude, the signal to noise ratio was still large.

We downward continued the Project Magnet vector magnetic components data to sea level and applied a geologically significant bandpass filter of 20 to 100 km (wavenumbers: 0.01 to 0.05) [*Horner-Johnson and Gordon*, 2003], e.g., a section of profile 0560-012 in Figure 3.3. Unfortunately, only a few Project Magnet profiles could be selected for comparison with a 2-D forward model since the direction of most Project

Magnet flights in the Equatorial Pacific near the EPR was generally unfavorable and near the strike of the abyssal hill lineation azimuths. The few profiles with a more favorable direction with respect to the seafloor spreading have been included in our plate reconstruction model and the processed vertical magnetic anomaly from these profiles have been presented in the “Tectonic Plate Reconstructions” section.

3.3 FORWARD MODELING OF 2-D MARINE MAGNETIC ANOMALIES

We have used a comparison of observed magnetic anomalies with 2-D forward models [*Blakely*, 1995] to identify nearly 3300 total field magnetic anomalies for finite and stage rotation calculations of the PCR, PNR, CNR, PAR, Chile and Mathematician Ridges. However, the equatorial Pacific and in particular the Southern end of the PCR, where the data were collected for the selected DANA05RR profiles, requires a careful and detailed analysis of the changes in skewness in order to be able to identify any vertical or total field magnetic anomalies in that region. Skewness is a uniform measure of the deviation in shape between the observed magnetic anomaly and the ideal symmetric profile, produced by vertically oriented magnetizations separated by vertical source boundaries. It is a function of effective inclinations of the ambient field and the remanence of the source blocks [*Schouten and Cande*, 1976].

Determination of the skewness parameter of marine magnetic anomalies near the magnetic equator can be a challenging task. Small changes in the orientation of the source blocks, and therefore the effective inclination, can produce a significant change in the shape and amplitude of magnetic anomalies (Figure 3.4). We built a model by determination of the orientation of the source blocks by mapping a large number of abyssal hill lineation (strike) azimuths from the available multibeam bathymetry and

magnetic anomaly data. In addition, we have used the synthetic Apparent Polar Wander paths (APWP) model for the Pacific Plate by *Wessel and Kroenke* [2008] to calculate the remanent inclination and declination for the Pacific Plate. We have rotated the poles from the APWP model by the PCR relative motion poles to calculate the appropriate remanent inclination and declination for the Cocos plate. We took nine trajectories through this dynamic 2D magnetic forward model for the PCR at different latitudes (Figure 3.4). Figure 3.4 demonstrates clearly that the magnetic anomaly field drastically decreases towards the magnetic equator with total and vertical magnetic field anomaly amplitudes dropping as low as 10 and 50 nT, respectively. Small changes (~5°) in the orientation of the magnetic source blocks (measured as changes in abyssal hill lineation azimuths), as a result of a propagating rift or changing spreading direction, near the equator have led to significant changes in skewness over short distances.

In Figure 3.5 we compare and correlate projections of selected DANA05RR and Project Magnet vertical magnetic anomaly data profiles and two additional total magnetic field profiles (VANC01MV and V3210), which cross PCR-formed oceanic crust near the equator, to the forward model. The location of these profiles is mapped in Figures 3.3 and 3.6a. The amplitude and shape of the vertical magnetic anomalies on the Pacific and Cocos plates for chrons C1o, C2, C2Ay and C2Ao (0.78, 1.9, 2.6 and 3.6 Ma) from DANA05RR (Figures 3.3 and 3.5a) correlate well with the forward model. We included both the total magnetic field (Overhauser data) and vertical component anomalies (MRU data) for the DANA05RR data in Figure 3.5a to show the selected segments, with the appropriate phase and coherence above 0.5, which is our criterion to consider these segments for anomaly identification. A 3 km position uncertainty was assigned to these anomaly picks for the rotation parameters calculation (described in the next section).

This number is based upon the uncertainty in position of the magnetic anomaly identification (typically ~1 km) and an additional uncertainty for the imperfect fit in amplitude and shape between the measured and modeled anomalies. DANA05RR anomalies on the Pacific plates for chrons C3o, C3Ay and C3Ao (5.1, 6.0 and 6.7 Ma) have a similar shape as the forward model for these ages but the amplitude is significantly larger for the DANA05RR anomalies. The larger amplitude of the anomalies could possibly be related to an incorrect choice of magnetization value (10 A/m) or source layer thickness (1 km) for the forward model. An alternative explanation is a higher angle between the abyssal hill lineation azimuths and the declination for the data relative to the modeled anomalies. We do indeed observe some rapid changes in these lineations in the multibeam bathymetry data (Figure 3.3a). We included these picks in the rotation parameters calculation with a larger 6 km uncertainty. The amplitude of the magnetic anomalies for chrons C4 and C4A (7.9 and 8.9 Ma) is similar to the forward model but the shape only correlates poorly to moderately well. Unfortunately, these are the only picks we have available for chrons C4 and C4A on the Cocos plate at this section of PCR-formed oceanic crust so we kept these picks in the rotation parameters calculation with an assigned 6 km uncertainty. Note that several of the selected DANA05RR profile segments, with the appropriate phase and coherence above 0.5 for the vertical component and total magnetic anomalies, are short. For example, the chron C2Ay and C2Ao picks on the Cocos plate are at the edges of the profile segment. In a more ideal case, magnetic anomalies would be identified from a longer profile segment.

The shape of the vertical magnetic anomalies for flight 0560-012 of the Project Magnet data (Figures 3.3b, 3.5b and 3.6a) generally correlates well with the forward model for chrons C1o, C2, C3y and C3o (0.78, 1.9, 2.6 and 3.6 Ma) for the Pacific and

Cocos plates. The lower amplitude of the Project Magnet data can be explained by the fact that these data have been collected at 7 to 8 km altitude and some of the wavelengths are lost by the applied bandpass filter. Therefore, the amplitude of the flight profile after downward continuation is expected to be smaller than data collected at sea level. We have assigned a 3 km uncertainty to these picks for rotation parameters calculation.

We have also included several low latitude total magnetic field profiles that correlate well with the forward model. The magnetic anomalies from two of those cruise tracks, VANC01MV and V3210 (Figures 3.5c and d) show good correlation with the forward model for chrons C1o, 2, 2Ao, 3y and 3o (0.78, 1.8, 3.6, 4.2 and 5.1 Ma). An uncertainty of 3 km has been assigned to these picks. Only a few magnetic anomaly picks were available at the segment of PCR-formed oceanic crust near the DANA05RR cruise. We have used abyssal hill morphology to extrapolate the magnetic anomaly pick to the outer edges of the multibeam swath generating two extra picks (Figure 3.3). A 6 km uncertainty was assigned to these picks for the rotation parameters calculation.

3.4 TECTONIC PLATE RECONSTRUCTIONS

The complex sea-floor morphology in the Eastern tropical Pacific reflects the significant changes in relative plate motions since the collision of the EPR with Western North America around 30 Ma [*Atwater*, 1970] and the fissure of the Farallon plate into the Cocos and Nazca plates after 25 Ma [*Barckhausen et al.*, 2008; *Hey*, 1977; *Lonsdale*, 2005]. The resulting GTJ is a ridge-ridge-ridge triple junction where the Pacific, Nazca and Cocos plates meet around the Galapagos microplate.

In order to evaluate the plate tectonic events we have calculated finite rotations for the PCR (Figure 3.6), PNR (Figure 3.7), CNR (Figure 3.8), PAR (see *Croon et al.* [2008]), Chile (Figure 3.9) and Mathematician-Cocos (Figure 3.10) Ridges by using the *Hellinger* [1981] method as implemented by *Chang* [1987; 1988] and *Royer and Chang* [1991]. We have combined the picks of the vector magnetic data from DANA05RR cruise and the Project Magnet vector magnetic data with publically available total field magnetic data (sources: Marine Geoscience Data System and National Geophysical Data Center) from cruise tracks (Figures 3.6 through 3.10) to better constrain the tectonic plate reconstructions of these Pacific ridge systems since chron C4A (8.9 Ma). A large number of the CNR anomaly identifications, which we used for this study, were included to calculate CNR rotation parameters by *Wilson and Hey* [1995]. A significant number of ANR anomaly identifications for chrons 2Ao, 3o and 3Ao (3.6, 5.1 and 6.7 Ma), which we used for this study, were included by *Tebbens and* Cande [1997] to calculate ANR rotation parameters. Anomaly identifications and rotation parameters for the PAR are the same as *Croon et al.* [*Croon et al.*]. Plate reconstruction parameters are determined for calculation of finite rotations by fitting great circles to reconstructed data in each segment defined by magnetic anomalies or FZs. Extra anomaly points were added by extrapolating abyssal hill lineations from multibeam bathymetry data when magnetic anomaly data were sparse to help calculation of rotation parameters. FZ traces have been digitized from available multibeam bathymetry and satellite-derived, free-air gravity field data. We typically assigned an uncertainty of 2 to 3 km for total field magnetic anomaly picks and 3 to 6 km for FZ and abyssal hill lineation picks. A detailed description of the magnetic anomaly picks and the assigned errors at the Southern end of the PCR is given in the previous section. In this section we first present 2-plate

solutions for all plate pairs and then we compare these results with 3-plate solutions for each plate pair from the Pacific-Nazca-Antarctic and Pacific-Cocos-Nazca plate circuits.

3.4.1 Two-Plate Solutions

3.4.1.1 Pacific-Antarctic Ridge

Cande et al [1995] and *Croon et al* [2008] have described the PAR relative plate motions in great detail. The rotation parameters in the *Croon et al* [2008] study were primarily constrained by combining detailed data sets along Menard and Pitman FZs, which are located 3500 km apart and therefore cover a large area of PAR oceanic crust. Most notably, during the recent tectonic history of the PAR a period of clockwise reorientation starting around 9.7 Ma (chron C5y) led to transtension for the right-stepping FZ offsets. We used the magnetic anomaly picks for the PAR from *Croon et al* [2008] to calculate Pacific-Anatarctic-Nazca 3-plate rotations parameters since chron C4A (8.9 Ma), which are described later in this section.

3.4.1.2 Chile Ridge

Plate reconstructions of the Chile Ridge document major plate boundary readjustments in the southeast Pacific around 24.1, 20.1 and 12.3 Ma (chrons C6C, C6o and C5A) and a smaller readjustment around 5.1 Ma (chron C3o) [*Tebbens and Cande*, 1997; *Tebbens et al.*, 1997]. During the chron C6o readjustment a ridge propagated into crust north of the northernmost PAR, which resulted in a northward jump of the Pacific-Antarctic-Nazca triple junction. During the chron C5A readjustment the Chile ridge propagated northward from the Valdivia FZ system to the Challenger FZ resulting in a 500 km northward jump of the Pacific-Antarctic-Nazca triple junction.

We calculated rotation parameters for the Chile Ridge (Figure 3.11). 95% confidence regions for the 2-plate solutions are large. This reflects the fact that the rotation poles are located at ~70° to 100° away from the Chile Ridge. When the pole of rotation is located at about 90° away from the data segments, the great circles that are part of the solution for these segments are positioned more parallel relative to each other producing larger 95% confidence regions. The 2-plate solutions generally agree with the rotation parameters of *Tebbens and Cande* [1997] and 95% confidence regions for chron 1o (0.78 Ma) and MORVEL overlap. Rotation parameters for the 2-plate solutions for Chile Ridge are presented in Table 3.1a.

3.4.1.3 Pacific-Nazca Ridge

The plate kinematic history of the PNR (Figure 3.7) since 25 Ma (~chron C7) is poorly constrained. Only a few 2-plate rotation parameters before chron C1o (0.78 Ma) have been presented (e.g., *Wilder* [2003]). The structural morphology of the Pacific and Nazca plates is characterized by several readjustments since the split of the Farallon plate, including the Mendoza and Bauer paleo microplates (Figure 3.1), which were actively growing between about 20 to 12 Ma (~chrons C6o to C5A) [*Liu*, 1996; *Lonsdale*, 1989] and 17 to 6 Ma (~chrons C5D to C3Ay) [*Eakins and Lonsdale*, 2003], respectively. At about 8 Ma (~chron C4) the Bauer microplate enlarged considerably by capturing a significant piece of Pacific plate as the EPR rapidly propagated northward. This event was followed by ~4° of clockwise rotation and decrease of spreading rate of the Bauer-Nazca Ridge Meanwhile, EPR spreading rates increased proportionally [*Eakins and Lonsdale*, 2003]. Bauer microplate capture by the Nazca plate occurred around 5.8 Ma

(during chron C3r) when the formation of the Quebrada transform fault decoupled the Pacific and Bauer plates.

Further readjustment of the PNR occurred after ~6 Ma (chron 3Ay) with the formation of the Easter and Juan Fernandez microplates (Figure 3.1) [*Bird et al.*, 1998; *Naar and Hey*, 1991; *Rusby and Searle*, 1995; *Searle et al.*, 1993]. Prior to the formation of these microplates the Pacific-Antarctic-Nazca triple junction was of the ridge-fault-fault variety [*McKenzie and Morgan*, 1969]. Counterclockwise rotation of the PNR led to northward propagation of the Chile Ridge and the Juan Fernandez microplate originated from the intratransform setting between chrons C3Ay and C3o (6.0 to 5.1 Ma) [*Bird and Naar*, 1994; *Bird et al.*, 1998]. During this time period a new ridge from within the Chile transform fault started to propagate northward, in response to the counterclockwise rotation of the PNR, leading to emergence of the Easter Microplate [*Bird and Naar*, 1994; *Naar and Hey*, 1991]. North of the Easter Microplate, the PNR has been offset by a series of right-stepping transform faults, which have formed the traces of the Garrett, Wilkes, Yaquina, Gofar and Quebrada FZs (Figure 3.1).

We calculated 2-plate rotation parameter solutions for the PNR (Figure 3.12). Only data south of 17°S latitude was included for chrons C3o through C4A (between 5.1 and 8.9 Ma) since the spreading center of the Bauer paleo microplate was active during that time period. Therefore, any of the magnetic anomaly picks north of the fossil Pacific-Bauer-Nazca triple junction (Figure 3.7) have been excluded in the rotation parameter calculations for the chrons C3o through C4A. 95% confidence regions for the 2-plate solutions are large since the rotation poles are located at ~60° to 90° away from the PNR. Rotation parameters for the PNR are presented in Table 3.2a.

3.4.1.4 Cocos-Nazca Ridge

The CNR (Figure 3.8) developed since after 25 Ma (~chron C7) as a response to the split of the Farallon plate [*Barckhausen et al.*, 2008; *Hey*, 1977; *Lonsdale*, 2005]. A significant part of the oceanic lithosphere, which has been formed since that time, has been lost by subduction in the Middle America and Peru-Chile Trenches. The evolution of the East-West striking CNR since 8.9 Ma (chron C4A) has been described in detail by *Wilson and Hey* [1995] based, in particular, on several high-amplitude magnetic anomaly profiles. Rift propagation has played a dominant role in the continuous readjustment of the CNR. Propagation has predominantly been away from the Galapagos hotspot, which has drifted southward [*Wilson and Hey*, 1995].

Our 2-plate finite rotation solutions for the CNR generally agree well with the rotation poles by *Wilson and Hey* [1995] and MORVEL for chron C1o (0.78 Ma) (Figure 3.13). The somewhat more northerly position of most of our rotation poles compared to the rotation poles by *Wilson and Hey* [1995] can possibly be explained by the fact that since their study a significant amount of additional marine magnetic data has been collected to better constrain magnetic isochron segments and additional multibeam data to better constrain FZ segments. Rotation parameters are presented in Table 3.3a.

3.4.1.5 Mathematician Paleo-Ridge

The recent tectonic evolution of the PCR since chron C4A (8.9) has been characterized by several events. Reorganization of the northern part of the PCR since 12 Ma (~chron C5A), between the now-inactive West O'Gorman FZ and the Rivera FZ, involved the short-lived Mathematician paleo microplate, between the failing Mathematician Ridge (Figure 3.10) and a propagating spreading center: the EPR. The

Mathematician paleo microplate was actively growing between the failed Mathematician Ridge and the Moctezuma Trough between ~12 and 3 Ma (~chrons C5A to C2A), which resulted in the capture of a fragment of lithosphere from the Farallon plate by the Pacific plate (Figure 3.14). The fossil Pacific-Mathematician-Cocos triple junction is located on the Western flank of the Clipperton FZ (Figure 3.14).

Several propagating rifts have complicated the geologic interpretation of magnetic anomalies for the Mathematician paleo-ridge. Identification of magnetic anomalies for chrons C2Ao through C4A (between 3.6 and 8.9 Ma) has therefore only been possible at the northern end of the Mathematician Ridge, near Socorro Island (Figure 3.10). This section is located farthest from the Pacific-Mathematician rotation pole and spreading rates have therefore been highest in that section, which helps with the identification of magnetic anomalies. Possibly, the highest Pacific-Mathematician spreading rates in that section, when the ridge was active, can also explain the volcanic activity at the Socorro and San Benedicto Islands. Even though active spreading at the Mathematician Ridge had stopped (during chron C3A at ~3 Ma), it is perfectly reasonable to argue that extension along the now fossil ridge did not stop at once and that the section furthest from the rotation pole has been affected by some transtension. Since the Mathematician Ridge became locked, the volcanic material that has erupted during the last ~3 Ma has not drifted away from the ridge but instead has accumulated at one spot and has formed the volcanic islands.

The 2-plate solutions (Figure 3.14) for Mathematican-Cocos spreading are poorly constrained due to the limited amount of data. This is expressed in the large 95% confidence regions and the lack of a smooth rotation pole evolution path. However, the three plate solution with the additional constraints from the Mathematican-Cocos (north

of Clipperton FZ) and PCR (south of Clipperton FZ) magnetic anomaly picks has produced significantly smaller 95% confidence regions (Figure 3.14) and constrains the rotation poles to a much more reasonable position near the edge of the Mathematician Paleoplate, which is typical for microplates [*Schouten et al.*, 1993]. Rotation parameters for 2- and 3-plate solutions for the Mathematician ridge are presented in Tables 3.4a and b.

3.4.1.6 Pacific-Cocos Ridge

The evolution of the PCR (Figure 3.14), a plate boundary which is terminated by the Rivera FZ to the north (Figure 3.6b) and the GTJ to the south (Figure 3.6a), has been characterized by several tectonic events. The Oligocene reorganization after 25 Ma was followed by a clockwise reorientation of the spreading ridge. This change led to the formation of the Tehuantepec Ridge, a long transform fault prior to 15 Ma [*Manea et al.*, 2005], and the most prominent ridge feature that can be observed on the Cocos Plate (Figure 3.1). After ~12.3 Ma (chron C5A) transform motion at the Nicaragua, Galapagos, Tehuantepec and Clarion offsets was replaced by a new transform offset pattern, which includes the Siqueiros, Clipperton, Orozco and Rivera offsets in response to a counterclockwise change in the spreading direction. This put the right-stepping Clipperton FZ under transpression and the left-stepping Siqueiros and Orozco FZs under transtension [*Pockalny et al.*, 1997; *Wilson*, 1996]. The recent evolution of the Orozco FZ has been characterized by propagating rift events between 6.5 and 3.5 Ma (between ~chrons C3Ao and C2Ao) when the last segment of the Mathematician Ridge became extinct [*Klitgord and Mammerickx*, 1982; *Mammerickx and Klitgord*, 1982]. The EPR propagated northward into continental crust during this period and significantly

decreased the Orozco transform offset to its present ~85 km [*Madsen et al.*, 1986; *Madsen et al.*, 1992]. Meanwhile, the Rivera transform, which is the northern boundary for PCR plate kinematics, significantly increased its offset to the present ~375 km. The Rivera microplate probably split off the Cocos plate as early as 10 Ma (~chron C5y) [*Lonsdale*, 1995]. In addition to the main transform offsets, the PCR is characterized by several overlapping spreading centers (OCS's) [*Macdonald et al.*, 1984].

Since the Mathematician Ridge was active before ~3 Ma (during chron C3A) we calculated 2-plate solutions for magnetic anomaly data along the entire PCR for chrons C1o, C2 and C2Ay (0.78, 1.9 and 2.6 Ma) and we present the 2-plate solutions for the magnetic anomaly data north of the Clipperton FZ (Figure 3.6b) and the significantly fewer data south of Clipperton FZ (Figure 3.6a) as separate pole rotation evolution paths in Figure 3.14. A much smoother pole rotation evolution path, based on Northern PCR (Mathematician-Cocos) data, suggests that the significantly larger amount of data that is included in the 2-plate rotation parameters calculation for that part of the PCR helps to better constrain its rotation parameters (presented in Tables 3.4c and d).

3.4.2 Three-plate Solutions

The East Pacific ridge geometry includes the Pacific-Nazca-Antarctic and the Pacific-Cocos-Nazca plate circuits (Figure 3.1). Calculating a 3-plate solution allowed us to test if the circuits are 'closed', which is the case when the sum of the three true rotations for each plate pair equals the identity matrix [*Kirkwood et al.*, 1999].

3.4.2.1 Pacific-Nazca-Antarctic Circuit

We combined the magnetic anomaly picks for the PAR with the data from the PNR and Chile Ridge to better constrain rotation parameters since 8.9 Ma (chron C4A)

in a 3-plate Pacific-Nazca-Antarctic solution. In Figure 3.11, 12 and 15 we compare our finite rotation poles for the Chile Ridge, PNR and PAR, based on a 3-plate Pacific-Nazca-Antarctic solution for each plate pair.

The results of the 3-plate solutions for the Chile Ridge (Figure 3.11) and the PAR (Figure 3.15) generally agree with the well-constrained 2-plate solutions. As described previously, the 2-plate solutions for the PNR (Figure 3.12b) are poorly constrained with significant scatter in the rotation pole evolution path and large 95% confidence regions. The better constrained 3-plate solutions for the PNR (Figure 3.12a) show a clear southward pole evolution path since chron C4A (8.9 Ma). 95% confidence regions for 2- and 3-plate solutions for all plate pairs of the Pacific-Nazca-Antarctic circuit overlap and we therefore conclude that the circuit is 'closed' for chrons C4A through C1o (between 8.9 and 0.78 Ma). Moreover, the 95% confidence regions for chron C1o (0.78 Ma) from our 3-plate solutions and MORVEL overlap for all included plate pairs. Rotation parameters for the Pacific-Nazca-Antarctic 3-plate solutions for the Chile Ridge, PNR and PAR are presented in Tables 3.1b, 3.2b and 3.5, respectively.

3.4.2.2 Pacific-Cocos-Nazca Circuit

We calculated 3-plate solutions for the Pacific-Cocos-Nazca circuit as well. Only the magnetic anomaly and FZ picks for Clipperton FZ and southward for the PCR plate pair are included in the solution for chrons C2Ao and C3y (3.6 and 4.2 Ma) since the Mathematician paleo microplate was still active during that time period and affected the area north of Clipperton FZ. No 3-plate rotation parameters were calculated for chrons C3o through C4A (between 5.1 and 8.9 Ma). The Bauer spreading center was still active during that time period [*Eakins and Lonsdale*, 2003]. We tried to find a 3-plate solution

for the Pacific-Cocos-Nazca ciruit for chrons C3o through C4A with magnetic anomaly picks south of the Bauer triple junction (Figure 3.7). However, for none of these chrons we were able to find reasonable rotation parameters. Therefore, we conclude that when the Bauer paleo microplate, which had grown significantly larger than the currently active Easter and Juan Fernandez microplates, was active it affected the PNR plate kinematics on the north end such that the microplate can not be treated as a distinct section within the PNR for that time period. No magnetic anomaly picks are available in the PNR section between the Bauer paleo microplate and GTJ for chrons C3o through C4A (between 5.1 and 8.9 Ma). Hence, we were unable to calculate Pacific-Cocos-Nazca 3-plate solutions for that time period.

95% confidence regions for the 2- and 3-plate (Pacific-Cocos-Nazca circuit) PNR solutions overlap with each other and MORVEL for chron C1o (0.78 Ma) (Figure 3.12). The 2- and 3-plate solutions for the CNR generally agree as well with each other and MORVEL for chron C1o (Figure 3.13). One exception is the 3-plate solution rotation pole for chron C2 (1.9 Ma), which is located near the pole for chron C2Ay (2.6 Ma) and ~6° to the east relative to the rotation pole for our 2-plate solution. A plausible explanation for this misfit is the fact that the relatively poorly constrained magnetic anomaly picks for chron C2 at the PCR, which is part of the 3-plate solution, constrained the CNR rotation pole to a non-realistic easterly position. Interestingly, the 3-plate solution for chrons 1o through 3y (between 0.78 and 4.2 Ma) for the Pacific-Cocos-Nazca plate circuit shows a significant misfit with the rotation parameters calculated for a PCR 2-plate solution (Figure 3.14). The MORVEL pole, which is based on a multi-plate solution by *DeMets et al.* [2010], agrees well with the C1o rotation pole for the 3-plate solution. The RMS misfit

for full spreading rate is 2.8 mm yr^{-1} compared to the best-fitting Pacific-Cocos angular velocity.

DeMets et al. [2010] evaluated the hypothesis of a diffuse plate boundary within one or both the Nazca and Cocos plates as the source of the misfit. The global Central Moment Tensor (CMT) database does not reveal any earthquake activity, e.g., no minor diffuse motion at the fossil Mathematician Ridge or an intra-plate deformation zones elsewhere has been detected to justify the misfit. The second possibility, which they have evaluated, is a possible inconsistency between the spreading rate and transform fault data, possibly due to a plate readjustment since 0.78 Ma. However, *DeMets et al.* [2010] concluded that the needed directional changes were unacceptably large. The non-closure, based on MORVEL, is mainly manifested as systematic misfits of the closure-enforced angular velocities to the PNR and PCR spreading rates. *DeMets et al.* [2010] calculated a systematic 2° difference between best-fitting and MORVEL rotation pole for chron C1o (0.78 Ma). We conclude, based on our Pacific-Cocos-Nazca 3-plate solutions (Figure 3.14), that the misfit and related non-closure for the PCR rotation parameters between the 3-plate and 2-plate (best-fitting) solutions has occurred since at least chron C3y (4.2 Ma). Rotation parameters for the Pacific-Cocos-Nazca 3-plate solutions for the PNR, CNR and PCR are presented in Tables 3.2b, 3.3b and 3.4e, respectively.

3.4.2.3 Comparison of Pacific-Nazca Three-plate Solutions

Our new rotation parameters for chron C1o (0.78 Ma) demonstrate that the 95% confidence regions for the PNR from both Pacific-Nazca-Antarctic and the Pacific-Cocos-Nazca plate circuits overlap with each other (Figure 3.12a). Moreover, both these

95% confidence regions have some overlap with the MORVEL 95% confidence region (the golden triangle at ~Lon 88°W, Lat 55°N in Figure 3.12a). This conforms with the observations by *DeMets et al.* [2010], who found matching Pacific-Nazca rotation parameters for chron C1o (0.78 Ma) based on the Pacific-Cocos-Nazca and Pacific-Nazca-Antarcic plate circuits. We have further tested the quality of the rotation parameters of the two plate circuits by rotating a single point near the GTJ (Figure 3.12c) for the chron C1o (0.78 Ma) rotation parameters. The location of the rotated points as well as the 95% confidence regions for these rotations mostly overlap, which confirms the agreement between the two 3-plate solutions for chron C1o. Figure 3.12a also shows that the evolution path of the rotation poles for the much better constrained Pacific-Nazca-Antarctic plate circuit is smoother compared to the Pacific-Cocos-Nazca plate circuit since chron C3y (5.1 Ma).

3.5 STAGE ROTATIONS, SPREADING RATES AND CHANGES IN LINEATION AZIMUTHS

To evaluate the quality of the new rotation parameters we have calculated stage rotations based on 3-plate rotation parameters for the PCR, PNR, CNR, PAR and Chile Ridge and used these to generate synthetic flow lines. The synthetic flowlines (Figure 3.16) follow a trace similar to several digitized (where sufficient multibeam data is available) FZ traces. This suggests that the predictive quality of rotation parameters is good and can be used to predict changes in spreading rate at different locations for the modeled plate pairs. Moreover, azimuth changes along synthetic flowlines predict clockwise and counterclockwise changes in plate motion direction, which leads to periods of transtension and tranpression at right-stepping transform fault offsets,

respectively [*Sonder and Pockalny*, 1999; *Tucholke and Schouten*, 1988]. The effect is the opposite at left-stepping transform fault offsets.

Between chrons C3y and C1o (4.2 to 0.78 Ma) the stage poles for the PCR migrated south to southeastwards. Spreading rates during that time period remained fairly constant at ~85 mm/a at Orozco FZ, ~105 mm/a at Clipperton FZ and ~130 mm/a near the GTJ (Figure 3.17a). Since we have 3-plate solutions only for chrons C3y to 1o (4.3 to 0.78 Ma), we have included 2-plate solutions for the PCR for the magnetic anomaly picks at Clipperton FZ and southward. These 2-plate solutions are poorly constrained and show a significant misfit in spreading rate and lineation azimuths compared to the 3-plate solution, in particular near the GTJ (Lat: 2.9°N, Lon: 102.1°W, Figure 3.17a). Nevertheless, the 2-plate solutions show that spreading rates were higher between chrons C4A and C3y (8.9 to 4.2 Ma) near the GTJ. The ~30° counter-clockwise rotation of the lineation azimuths between chrons C4A and C1o (8.9 to 0.78 Ma) is remarkable and has put the right-stepping Clipperton FZ under significant transpression during that time period. The transpression resulted in the formation of a median ridge [*Pockalny*, 1997] and anomalously rotated anti-J shaped abyssal hills [*Croon et al.*, 2010; *Sonder and Pockalny*, 1999], both confirming the presence of the significant transpression at the transform fault during at least the last 8.9 Ma (since chron C4A). The multi-splayed Siqueiros transform fault has an opposite sense left-stepping offset of ~135 km and developed three intra-transform spreading centers in response to the transtension [*Fornari et al.*, 1989; *Pockalny et al.*, 1997]. The 85 km left-stepping Orozco offset underwent significant transtension during the same time period and has been characterized by propagating rift events between 6.5 and 3.5 Ma (between ~chrons C3Ao and C2Ao) [*Klitgord and Mammerickx*, 1982; *Mammerickx and Klitgord*, 1982].

Stage poles at the CNR migrated rapidly in a westward direction (Figure 3.16) between chrons C3y and C1o (4.2 to 0.78 Ma). During this time period, full spreading rates near the GTJ (Lat: 3.5°S, Lon: 111.7°W, Figure 3.17b) increased from ~30 to 50 mm/a. At the Ecuador FZ towards the east spreading rates remained somewhat constant at about 60 mm/a, based on both the 3- and 2-plate solutions (before chron C3y). Lineation azimuths changed significantly since chron C4A (8.9 Ma), both clockwise and counter-clockwise, which demonstrates the continuous readjustment of the CNR [*Wilson and Hey*, 1995]. Too few multibeam data are available at CNR FZs to evaluate transtensional and transpressional structural morphology in relation to the changes in CNR lineation azimuths.

At the PNR, the 3-plate solutions of the Pacific-Cocos-Nazca and Pacific-Nazca-Antarctic plate circuits overlap for chrons C1o through C3y (between 0.78 and 4.2 Ma). The synthetic flow lines based on both plate circuits show excellent correlation, which we expect based on the decent agreement between the finite rotation poles (Figure 3.12a). Between chrons C4A and C3o (8.9 to 5.1 Ma) the stage poles migrated in a northwestward direction. During this time period, full spreading rates decreased from ~190 mm/a to ~160 mm/a (Figure 3.17c) while the orientation of lineation azimuths has remained fairly constant. The spreading rates and lineation azimuths at the three synthetic flow line locations, which we evaluated in Figure 3.17c, are very similar since the rotation poles are located at ~60° to 90° away from the PNR. Between chrons C3o and C1o (5.1 to 0.78 Ma) the stage poles migrated back in the southwestward direction (Figure 3.16). During this time period the spreading rate decreased further to ~130 to 150 mm/a for the three evaluated synthetic flow line locations. The lineation azimuths

underwent a small ~5° clockwise rotation, which predicts transtension at the predominantly right-stepping PNR transform offsets.

Between chrons C4A and C1o (8.9 to 0.78 Ma) the stage poles for the Chile Ridge migrated in a northward direction (Figure 3.16). Meanwhile, the full spreading rate decreased from ~100 to ~55 mm/a (Figure 3.17d). The two evaluated synthetic flow lines near the Chile and Guafo FZs (Figure 3.1) had similar full spreading rates since chron C4A, which reflects the fact that the rotation poles are located at ~70° to 100° away from the Chile Ridge. Lineation azimuths for both synthetic flow lines remained fairly constant since chron C4A (8.9 Ma).

Stage poles at the PAR migrated mostly in a northward direction (Figure 3.16) between chrons C4A and C1o (8.9 to 0.78 Ma). The full spreading rates of the evaluated synthetic flow lines near the Menard and Pitman FZs increased gradually from ~75 to 86 mm/a and from ~37 to 48 mm/a, respectively (Figure 3.17e). During this time period both right-stepping FZs were put under transtension by the clockwise rotation of the lineation azimuths. The transtension at Menard and Pitman FZs since chron C4A (8.9 Ma) has been described in detail by *Croon et al.* [2008; 2010].

3.6 PLATE RECONSTRUCTION MODELS AND TECTONIC EVENTS

We have determined 10 rotations since chron C4A (8.9 Ma) for the PCR, PNR, CNR, PAR and Chile Ridge to describe the relative plate motions for these plate pairs in detail. In particular, the understanding of the relative motions between the Pacific and Nazca plates and the Pacific and Cocos plate pairs since chron C4A has been improved significantly with this study.

Following a minor plate reorganization around chron 3Ay (6.0 Ma) in the central Pacific, the Bauer microplate was captured by the Nazca plate [*Eakins and Lonsdale*, 2003] and in the southeast Pacific the Juan Fernandez and Easter microplates began to form [*Bird et al.*, 1998; *Naar and Hey*, 1991; *Rusby and Searle*, 1995; *Searle et al.*, 1993]. Around the same time of these tectonic events the migration of PNR stage poles changed from a northwestward to a southeastward direction (Figure 3.16). Contrary to the findings by *Tebbens and Cande* [1997] we conclude, based on the new rotation parameters, that no significant changes in spreading rate occurred at the PNR, PAR and Chile Ridge around chron 3Ay (Figure 3.17).

The tectonic evolution of the PCR has been described in several studies [e.g., *Klitgord and Mammerickx*, 1982; *Mammerickx and Klitgord*, 1982; *Menard*, 1978]. *Schilt et al.* [1982] calculated stage rotations for intervals between 0, 2, 5, 7.5, 10 and 14 Ma. *DeMets et al.* [2010] presented rotation parameters for chron C1o (0.78 Ma) and *Wilson* [1996] for chron C5Ay (11.9 Ma). *Pockalny et al.* [1997] reported counter-clockwise rotation at the Clipperton and Siqueiros FZs since 3 Ma, based on multibeam bathymetry data. Our 10 new rotation parameters for the PCR describe its plate tectonic evolution in detail and show that ~30° counter-clockwise rotation occurred along the entire PCR since chron C4A (8.9 Ma) (Figure 3.17).

3.7 CONCLUSIONS

In this study we have evaluated all available magnetic anomaly profiles for most of the East Pacific ridge systems, which allowed us to reconstruct the PCR, PNR, CNR, PAR, Chile Ridge and Mathematician paleo-ridge since chron C4A (8.9 Ma). In particular, in the equatorial Pacific region where the total magnetic field anomalies are

small for oceanic crust formed at the North-South striking EPR, data from a towed vector magnetometer and some vector aeromagnetic Project Magnet profiles have helped us to better constrain the relative motions of the PCR near the GTJ. On the basis of our new rotation parameters we draw the following conclusions:

1. *DeMets et al.* [2010] have demonstrated a significant misfit for the PCR between their multi-plate MORVEL model and the best fitting rotation pole estimate for chron C1o (0.78 Ma). We draw the same conclusion based on the misfit between our 3-plate solution, for which the finite rotation pole is located near MORVEL, and our 2-plate best-fitting rotation parameters. Moreover, based on our rotation parameters we have shown that the misfit has occurred since at least chron C3y (4.2 Ma). The cause of this misfit is unclear since no evidence for a diffuse plate boundary, in the form of earthquakes, is detectable from the global Central Moment Tensor (CMT) database. Alternative potential explanations for this misfit are significant systematic errors in the identification of magnetic anomalies or a problem with the setup of the segments for the 2- and 3-plate rotation parameters calculation. However, we have no indication for either of these possible explanations to be valid for our rotation parameters calculation.
2. Our synthetic flow lines for the PCR quantitatively show that a ~30° counter-clockwise rotation since chron C4A (8.9 Ma) has put the right-stepping Clipperton FZ under significant transpression, which is expressed by a prominent median ridge [*Pockalny*, 1997] and anti-J shaped abyssal hills [*Croon et al.*, 2010; *Sonder and Pockalny*, 1999]. The multi-splayed Siqueiros transform fault has an opposite sense left-stepping offset and has developed three intra-transform

spreading centers in response to the significant transtension [*Fornari et al.*, 1989; *Pockalny et al.*, 1997].

3. In agreement with the MORVEL model for chron C1o by *DeMets et al.* [2010] we have found a good correlation between PNR rotation parameters between the Pacific-Cocos-Nazca and the Pacific-Nazca-Antarctic plate circuits for chrons C3y to C1o (4.2 to 0.78 Ma). We have been unable to match finite rotation poles for both 3-plate solutions for chrons C3o through C4A (between 5.1 and 8.9 Ma) when the Bauer paleo microplate was active. We could not find reasonable finite rotation poles for the Pacific-Cocos-Nazca plate circuit, including PNR magnetic anomaly data identified south of the fossil Bauer triple junction, and therefore conclude that the Bauer microplate had grown so large that it affected the PNR plate kinematics on the north end for that time period. The microplate can not be treated as a distinct section within the PNR for that time period as is the case for the currently active Easter and Juan Fernandez microplates.
4. At the CNR, lineation azimuths, based on our new rotation parameters, have changed rapidly and significantly since chron C4A (8.9 Ma), both in clockwise and counter-clockwise directions. Therefore, our synthetic flow line model is in agreement with the findings by *Wilson and Hey* [1995] who have reported continuous readjustment of the CNR since chron C4A.
5. Our new rotation parameters for the Mathematician paleo microplate show that the volcanically active Socorro and San Benedicto Islands are located farthest from the finite rotation poles for the fossil Mathematician paleo-ridge (inactive since ~3 Ma during chron 2A). We suggest that some extension has been ongoing at the northern end of the Mathematician paleo-ridge since that time.

This has resulted in accumulation of volcanic material at one spot resulting in the emergence of the volcanic islands.

3.8 APPENDIX 3A: Towed Vector Magnetometer Data Processing

The vector magnetic data was collected during the DANA05RR cruise in the equatorial Pacific near the EPR (Figure 3.1) with the goal to gain additional insight in the poorly constrained PCR and PNR sea-floor spreading history near the GTJ. Two Seatex MRU6 motion sensors were used during the cruise. Two long profiles across the most northern end of the PNR were collected with sensor 0954 (red track on Figure 3A1). For the second part of the cruise data were collected with a second sensor (serial number 2259) for two long profiles across the PCR and four across the CNR (white track on Figure 3A1).

3.8.1 Vector Magnetic Sensor Calibration

In order to obtain total field and component magnetic anomalies from the towed vector magnetometer, the nine calibration parameters of the three-axis fluxgate, the scale factors, gains and non-orthogonality angles for each axis must be determined [*Merayo et al.*, 2000; *Olsen et al.*, 2003]. Scalar calibration of the two vector magnetometers was done in a controlled laboratory environment in San Diego in April 2005 after the DANA05RR cruise. The advantage of a laboratory setting is that the sensors can be held in many different positions for several temperature increments in order to obtain enough data to properly calibrate the three axes of the vector magnetometer sensor. The results of the laboratory calibration are presented in Figure 3A2. The nine parameters are temperature dependent and the scalar calibration was done at seven incrementally increasing water temperatures to cover the full range of

ocean water temperatures. Next, polynomial fits through the R (Roll), P (Pitch) and Y (Yaw) values for the scale (Figures A2a-2 and A2b-2), offset (in nT) (Figures 3A2a-3 and 3A2b-3) and non-orthogonality (in arc seconds) (Figures 3A2a-4 and 3A2b-4) components were calculated. These polynomial fits are used as the first order set of calibration parameters based on the water/sensor temperature and they explain the total field variations (apart from a DC shift or long wavelength offset) reasonably well prior to any refinement. During the cruise of sea-surface water temperatures varied between 22 and 26°C, (Figure 3A3).

When processing the vector magnetometer data, the sensor temperature is required to properly apply the calibration parameters. Since sensor temperature was not recorded during the DANA05RR cruise, the sea-surface water temperature, which relates linearly to the sensor temperature, was used (Figures 3A2a-1 and 3A2b-1). The sea-surface water temperature was measured at the side of the ship. The RMS misfit for laboratory temperature calibrations was ~35 and ~20 nT for sensors 0954 and 2259, respectively after 10 iterations (following the *Olsen et al.* [2003] method), trying to find the optimal calibration parameters. These values are not much higher than the instrument resolution (< 10 nT) but the RMS misfit for sensor 2259 is clearly lower. Moreover, from Figure 3A2a-3 and A2a-4 it is evident that in particular the R axis for the 0954 sensor shows significant scatter for the offset and non-orthogonality (Figures 3A2a-3 and a-4) when measured at different temperatures. The results after processing of the data collected with the 0954 sensor, which are described later in this Appendix, are indeed poor.

Several calibration loops were sailed during the DANA05RR cruise to refine the nine calibration parameters from the laboratory results with the data from calibration

circles 1 (for sensor 0954) and 2 (for sensor 2259) (Figure 3A1). The disadvantage of using these circle data for calibration of the sensors during the cruise is that only limited roll and pitch variation occurs. Moreover, the data is collected at only one sea-surface temperature. Because the laboratory determined temperature-dependent calibration has already been applied, the scale factors should be near 1 and the offset and non-orthogonality parameters should be near zero. Computing the nine additional circle calibration parameters based on circle 2 for sensor 2259 with the *Olsen et al.* [2003] method resulted in unrealistically additional calibration value of ~1.02 for the scale factors. This compares to an additional 600 nT offset for a magnetic field of 30000 nT intensity, which is unrealistically high and demonstrates that just using the limited data from sailing a calibration loop during a cruise is not sufficient for proper calibration of the sensor. A brute search method was therefore applied where the three scale parameters were kept fixed at their values from the temperature dependent polynomial fits while the other six parameters were allowed to vary. This was tried for all permutations of fixing three parameters but keeping the search range to reasonable values (chosen at ±0.005 for scale factors, ±500nT for offsets and ±100 arcsec for non-orthogonalities) to calculate the smallest RMS misfit for models that are still close to the values determined during the better constrained laboratory calibration. The smallest RMS misfit computed for these nine additional calibration parameters for the SN2259 sensor was 44 nT. The same brute force method was used to compute nine additional calibration parameters for the SN094 sensor for the smallest calculated RMS misfit (116 nT) based on the data from calibration circle 1. These refined calibrations based on parameters with reasonable values have the largest chance of being correct. In Figure 3A4 we demonstrate, with an east to west 300 km long profile just East of the PCR (Figure 3.2),

that the additional circle calibration refinement improves the correlation between the Overhauser and MRU total magnetic field intensity.

3.8.2 Data Processing

After calibration, the DANA05RR cruise data was processed following the *Engels et al.* [2008] method. In this section we summarize the processing steps from calibrated raw data to fluxgate-derived total and vertical magnetic anomalies:

i) Data from all sensors are adjusted for smoothed ship's GPS positions and erroneous data records are replaced by dummy values. Roll, pitch and as first approximation yaw angles from the smoothed ship's GPS course are used for the Euler (rotation) angles. Yaw angles are improved by using the fluxgate as a compass for obtaining the magnetic heading. Difference between the GPS and fluxgate derived yaw measurements reflect the motion of the fluxgate towfish through the water, which is affected by the currents and waves.

ii) The data are despiked, interpolated and resampled by a median filter with a window length of 50 m.

iii) The measured yaw includes a minor part that is contributed by the seafloor anomalies. To obtain that component, a bandpass filter is applied to approximate a synthetic yaw. This value is then subtracted from the measured compass yaw of the MRU sensor. Subsequently the ambient DGRF for each location is subtracted from the total and vector magnetic components.

iv) A LP/HP trapezoidal bandpass filter in space domain is applied to return only wavelengths that could be related to seafloor anomalies. We have chosen a 7

km LP filter, which corresponds to the minimum wavelength that can still be recovered from the research area, which has seafloor depths varying between 3 and 3.8 km. The HP filter gently cuts wavelengths longer than 200 km from long-term trends. These wavelengths include fluxgate baseline instabilities and some external daily geomagnetic field variations.

3.8.2.1 2-D Magnetic Forward Model Profile

In order to test the code for processing the DANA05RR MRU data, following the *Engels et al.* [2008] method, we created a theoretical 2-D magnetic forward model from chron C2A across the ridge axis to chron C2A on the other side. We projected this theoretical forward model on the location of the (arbitrarily chosen) 300 km long profile just East of the PCR (Figure 3.2 and blue profile on Figure 3A1) and 'pseudo' data were produced by using the observed roll, pitch, yaw. We applied the inverse of the Euler rotation matrix for the roll, pitch and yaw data for that profile to the theoretical 2-D magnetic forward model. The idea of this is to test whether after processing all the resultant processed magnetic anomaly components have exactly the same shape and amplitude as the original theoretical 2-D magnetic input model. This is indeed the case for our test profile (Figure 3A5). The total, down, east, north (Figures 3A5b and c) and horizontal and vertical components (Figures 3A5e) are exactly the same as the original theoretical input model.

Figure 3A5 illustrates how the synthetic yaw method of *Engels et al.* [2008] is used to estimate the north and east components of the anomalous field:

i) The horizontal geomagnetic components consist of a geologic anomaly part and a true declination part. The orientation of the sensor is used to calculate the

north, east and down components of the geomagnetic field. The north and east components provide an estimate of the local declination but also include variations due to the geological source (see Figure A5a). The anomaly part is approximated by a 7/200 km LP/HP trapezoidal bandpass filter.

ii) The black line on Figure 3A5f represents the declination derived from the north and east components calculated using the roll, pitch, yaw as recorded by the MRU instrument.

iii) The yaw correction (blue line on Figure 3A5f) is calculated as the sum of the declination and the geologic anomaly part filter (red line on Figure 3A5f) minus the correction for the drift of the magnetic north calculated with the vector magnetic sensors by the MRU instrument relative to the true declination (purple line on Figure 3A5f).

iv) The yaw correction (blue line on Figure 3A5f) is applied as a rotation to the yaw, as measured by the MRU instrument, producing the synthetic yaw relative to a geographical coordinate system. The synthetic yaw was used for processing the east and north field components (Figures 3A5b and c).

The test confirms that we have correctly applied the *Engels et al.* [2008] method and we used the same method that we used for this forward model profile to all other DANA05RR profiles.

3.8.2.2 Cocos-Nazca Ridge Profile

A DANA05RR northwest oriented profile starting at the Galapagos Islands and crossing the CNR (green profile on Figure 3A1) was presented by *Engels et al.* [2008]. Since the magnetic anomaly strike direction at the CNR is nearly orthogonal to the

ambient field declination, large 2-D magnetic anomalies are expected. We processed an additional 280 km long profile that crosses the CNR and is oriented roughly south to north and perpendicular to the abyssal hill strikes (yellow profile on Figure 3A1). The profile data was processed by calibration of the data (Figure 3A2b), correction for the DGRF, replacement of yaw by a synthetic yaw and a bandpass filter (Figures 3A6a-c) following the method by *Engels et al.* [2008]. The ~350 nT difference for the total field between the Overhauser and raw calibrated MRU data (Figures 3A6a and b) indicates that the calibration of the MRU sensor is not optimal. An excellent coherence for the vertical vs. horizontal and for the vertical vs. total magnetic anomalies and a low 3-D index based on the horizontal and vertical field components for most of the profile is observed and magnetic anomalies are easily recognized and identified (Figure 3A6e). To compute the 3-D index a robustly filtered absolute difference between the horizontal and phase-shifted vertical components anomalies is calculated. Next, this is divided by a robustly filtered average of the horizontal and phase-shifted vertical components producing the 3-D index. A low 3-D index suggests 2-D anomalies. This is expected since, similar to the DANA05RR profile presented by *Engels et al.* [2008], the magnetic anomaly strike direction at CNR-formed crust is nearly orthogonal to the ambient field declination resulting in large 2-D magnetic anomalies. Note the change of ~4° in instrument-interpreted geomagnetic north direction (black line on Figure 3A6f) relative to the declination for the profile (purple line on Figure 3A6f). Over time, such a drift could occur for the calculation of IGRF direction based on the vector magnetic components in the instrument. However, during most of the DANA05RR cruise smoothed GPS-based heading of the ship was sent to the MRU instrument to correct for such a drift.

3.8.2.3 Pacfic-Cocos Ridge Profile

Processing of a roughly east to west 300 km long profile just East of the PCR and perpendicular to the abyssal hill strikes is presented on Figures 3.2 and 3A1 (blue profile). After calibration and processing of this PCR profile (Figure 3A7), the resultant coherence for the vertical vs. total and in particular vertical vs. horizontal component (Figure 3A7e) is low for geologically relevant wavenumbers (~0.02 and 0.14 or ~ 7 to 50 km) compared to the forward model (Figure 3A5e) and the CNR profile (Figure 3A6e). Moreover, the 3-D index based on the horizontal and vertical field components is high. Since the coherence between the vertical and total field components is highest, we used these field components for potential 2-D magnetic anomaly interpretation and identification for profile parts with reasonable to high (> 0.5) coherence, as described in the data section. It is not clear why the coherence of the vertical vs horizontal field component, which is independent of any yaw bias, after processing is significantly worse than the coherence from vertical and total field cross-spectra analysis.

3.8.2.4 Pacfic-Nazca Ridge Profile

The coherence between the Overhauser and MRU-calculated total field components for the data that has been collected during the second part of the cruise with MRU sensor 2259 (white track on Figure 3A1) is generally good (e.g., Figures 3A6c and 3A7c). However, this coherence is typically poor for the data that were collected during the first part of the cruise with MRU sensor 0954 (red track on Figure 3A1), e.g., for an east to west 440 km long profile across the PNR (Figure 3A8). The ~150 nT difference for the total field, between the Overhauser and raw calibrated MRU data (Figures 3A8a and b), suggests poor calibration of the MRU sensor, which we described

previously in this appendix. After the calibration refinement based on circle 1 (Figure 3A1) the misfit between the Overhauser and raw calibrated MRU data is still unacceptably large (see Figure 3A8c for best comparison). Unsurprisingly, the resultant coherence for the vertical vs. total and the vertical vs. horizontal component is low for geologically reasonable wavenumbers (~0.02 and 0.14 or ~ 7 to 50 km) and the 3-D index is high. The problems, which are observed for this profile, occur for all data collected with MRU sensor 0954. Therefore, we were unable to use any of these data for 2-D magnetic anomaly interpretation and identification.

3.8.3 Magnetic Boundary Strike Ellipses

We followed the method by *Seama et al.* [1993] as implemented by *Korenaga* [1995] to estimate the location and direction of magnetic boundaries. The magnetization contrast for these boundaries is due to (i) magnetic field reversals, (ii) seafloor structures such as faults and seamount and (iii) magnetization contrasts within a chron. Results for DANA05RR magnetic boundary strike ellipses are presented in Figure 3A9. Ellipses show a general agreement with the abyssal hill strike lineations, which is remarkable considering the low coherence between most of the horizontal and vertical magnetic component anomalies. Ellipses that are large and oriented in different directions typically indicate 3-D structures such as volcanic island lineaments.

3.8.4 Discussion

Unfortunately, the DANA05RR data produced only a limited set of 2-D magnetic anomaly picks (Figure 3.6a). Part of the poor results can be contributed to the issues with calibration, in particular with sensor 0954 during the first part of the cruise. However, the data collected with sensor 2259 for second part of the cruise, where calibration

issues were much less problematic, hardly produced profiles suitable for 2-D magnetic anomaly interpretation and identification since for these data the coherence for the vertical vs. total and the vertical vs. horizontal components is generally too low for geologically reasonable wavenumbers (~0.02 and 0.14 or ~ 7 to 50 km). In particular, the coherence of the vertical vs horizontal field component is poor. It is not clear why since the horizontal field component is independent of any yaw bias. The Project Magnet data profile just north of the DANA05RR profiles (Figures 3.5b and 3.6c) shows excellent 2-D magnetic anomalies. Moreover, the magnetic boundary strike ellipses (Figure 3A9) suggest that many 2-D magnetic lineations should be detected. Therefore, we conclude that it is highly unlikely that the poor results can be attributed to mostly geologic 3-D magnetic anomalies. A possible explanation for the poor results is that the amplitude of the magnetic anomalies in the surveyed region is extremely low with 2-D total and vertical magnetic field anomaly amplitudes dropping as low as 10 and 50 nT, respectively. This may be a plausible, in particular, since the results from the CNR profiles (e.g., Figure 3A5), where 2-D magnetic anomalies are significantly larger, are excellent. Perhaps the poor DANA05RR vector magnetic data results can be attributed to these low 2-D magnetic anomalies for the PCR and PNR profiles in combination with the calibration issues of the sensor, as described previously in this appendix.

3.9 ACKNOWLEDGMENTS

This study was made possible through NSF grants OCE02-42205 and OPP04-40959. We are grateful to Douglas Wilson for generously providing many of the magnetic anomaly picks near the Cocos-Nazca Ridge. We thank Aaron Sweeney for his help with

making the Project Magnet data accessible. We also thank the officers, crew and scientific staff of the R/V Roger Revelle who have sailed on the DANA05RR cruise.

3.10 FIGURES

Figure 3.1: Map of East Pacific Ridge systems on an image of the GEOSAT and ERS-1 satellite-derived, free-air gravity field [*Sandwell and Smith*, 2009], summarizing the location of the DANA05RR cruise track (white solid line), the main tectonic features. Fracture Zones are highlighted in dark-red, troughs in black, the spreading ridges in red and C4A isochrons (8.9 Ma) in blue. Magnetic equator for IGRF2011 model in thick dashed gray. Map is in a Mercator projection.

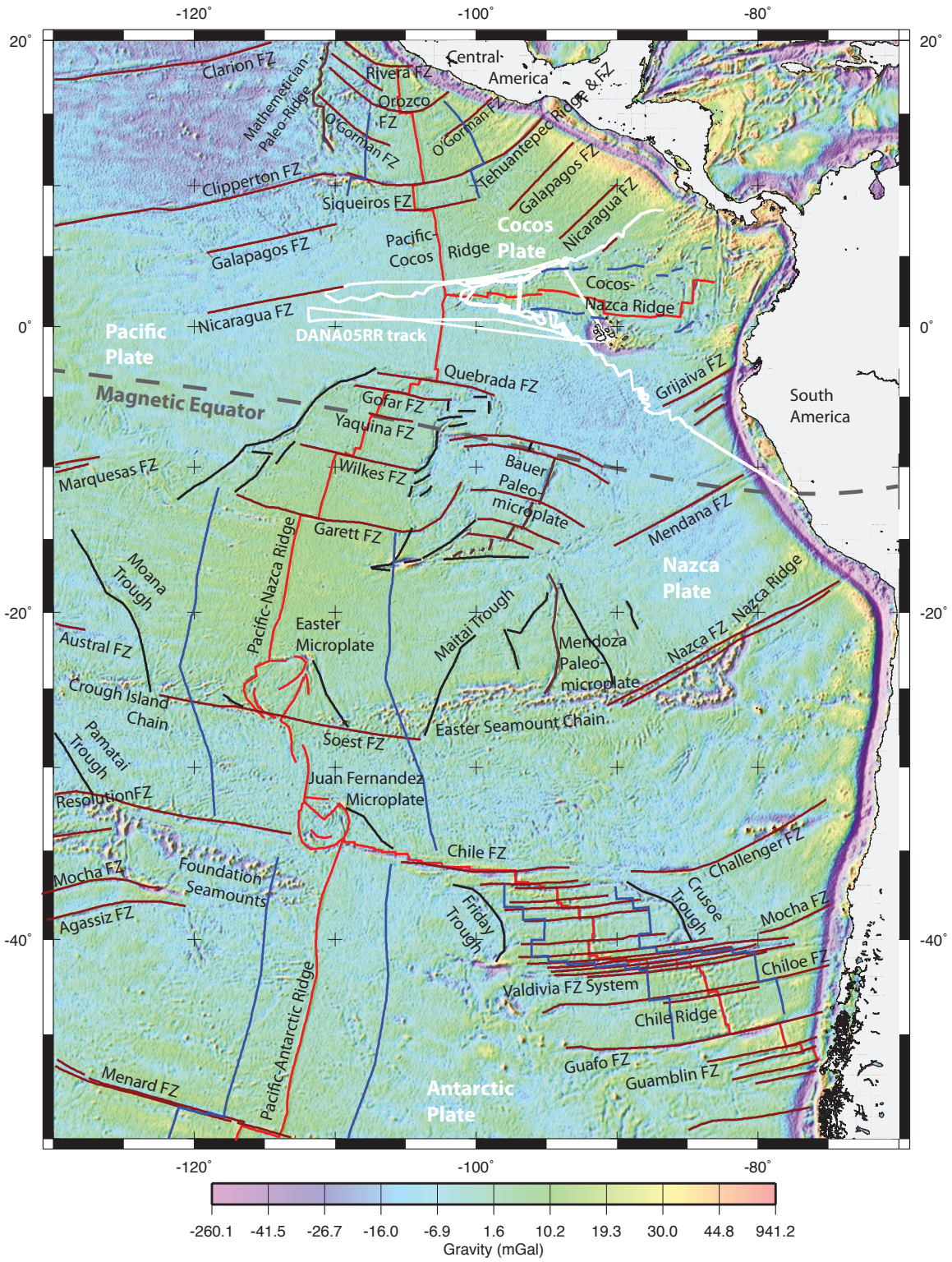
-120˚
-100˚
-80˚
20˚
0˚
-20˚
-40˚
Clarion FZ
Mathematician Paleo-Ridge
Rivera FZ
Central America
Orozco FZ
O'Gorman FZ
Tehuantepec Ridge & FZ
Clipperton FZ
Siqueiros FZ
Galapagos FZ
Nicaragua FZ
Cocos Plate
Pacific-Cocos Ridge
Cocos-Nazca Ridge
DANA05RR track
Pacific Plate
Magnetic Equator
Quebrada FZ
Grijalva FZ
South America
Gofar FZ
Yaquina FZ
Marquesas FZ
Wilkes FZ
Bauer Paleo-microplate
Mendana FZ
Garett FZ
Moana Trough
Pacific-Nazca Ridge
Nazca Plate
Nazca Ridge
Nazca FZ
Austral FZ
Easter Microplate
Maitai Trough
Mendoza Paleo-microplate
Crough Island Chain
Easter Seamount Chain
Pamatai Trough
Soest FZ
Juan Fernandez Microplate
ResolutionFZ
Chile FZ
Challenger FZ
Mocha FZ
Foundation Seamounts
Crusoe Trough
Agassiz FZ
Friday Trough
Chiloe FZ
Valdivia FZ System
Chile Ridge
Pacific-Antarctic Ridge
Guafo FZ
Guamblin FZ
Menard FZ
Antarctic Plate
-260.1
-41.5
-26.7
-16.0
-6.9
1.6
10.2
19.3
30.0
44.8
941.2
Gravity (mGal)

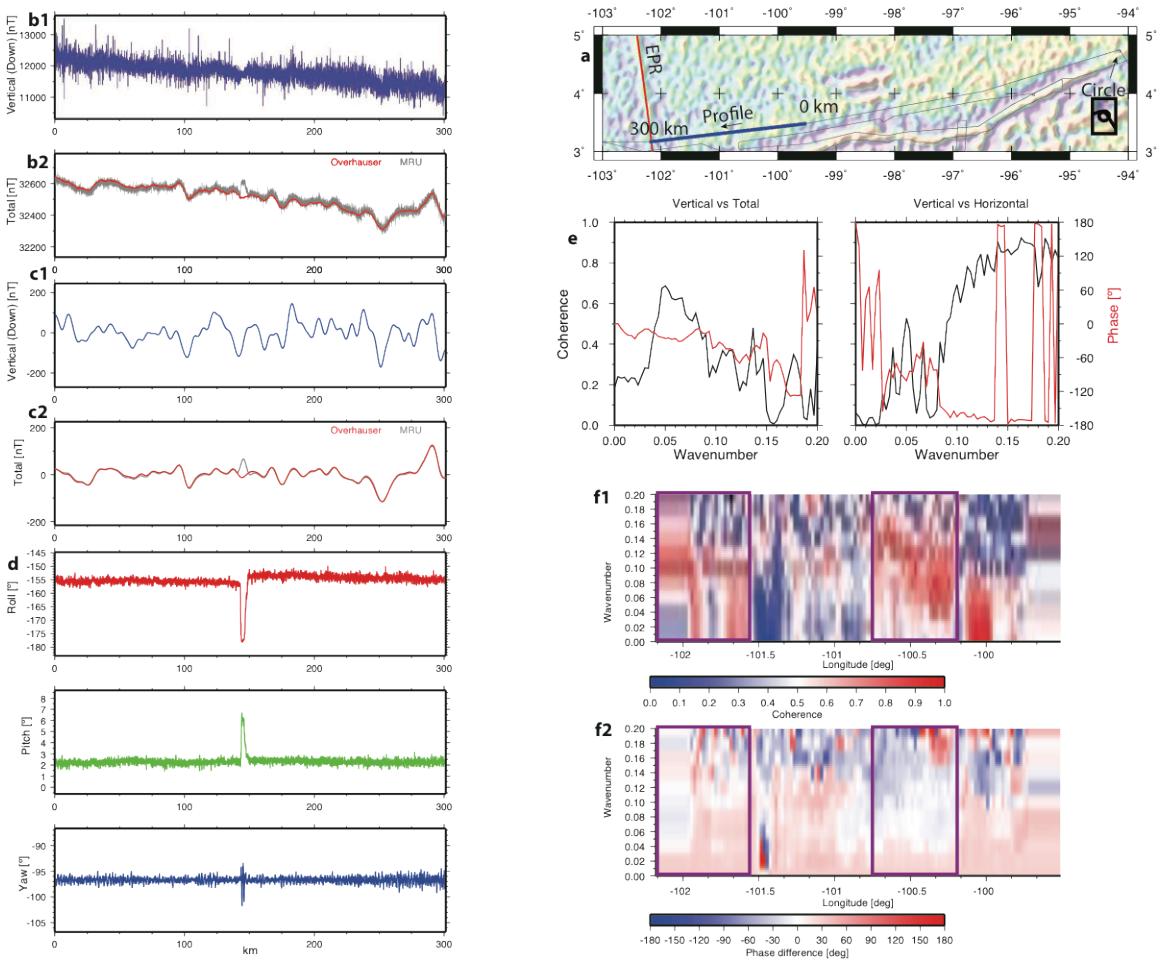

Figure 3.2: (a) Overview map for the 300 km long profile just East of the EPR and the circle data on an image of the satellite-derived, free-air gravity field. Map is in a Mercator projection. (b and c) are profiles of raw calibrated (b1) vertical (MRU) and (b2) total (Overhauser and MRU) and processed (c1) vertical (MRU) and (c2) total field (Overhauser and MRU) data, respectively. (d) Roll, pitch and yaw measurements of the fluxgate towfish along the profile. (e) Cross-spectra coherence plots between the vertical vs. total and vertical vs. horizontal processed anomalies. (f1) Gridded coherence plot for intervals of 50 km centered on each km of the profile along the profile and (f2) the gridded predicted forward model phase difference subtracted from the phase difference from profile data between the total and vertical field components for each interval (zero means the profile data and forward model have the same phase difference). (e and f) Thick purple rectangles mark the profile sections, which have been selected for marine magnetic anomaly identification and interpretation.

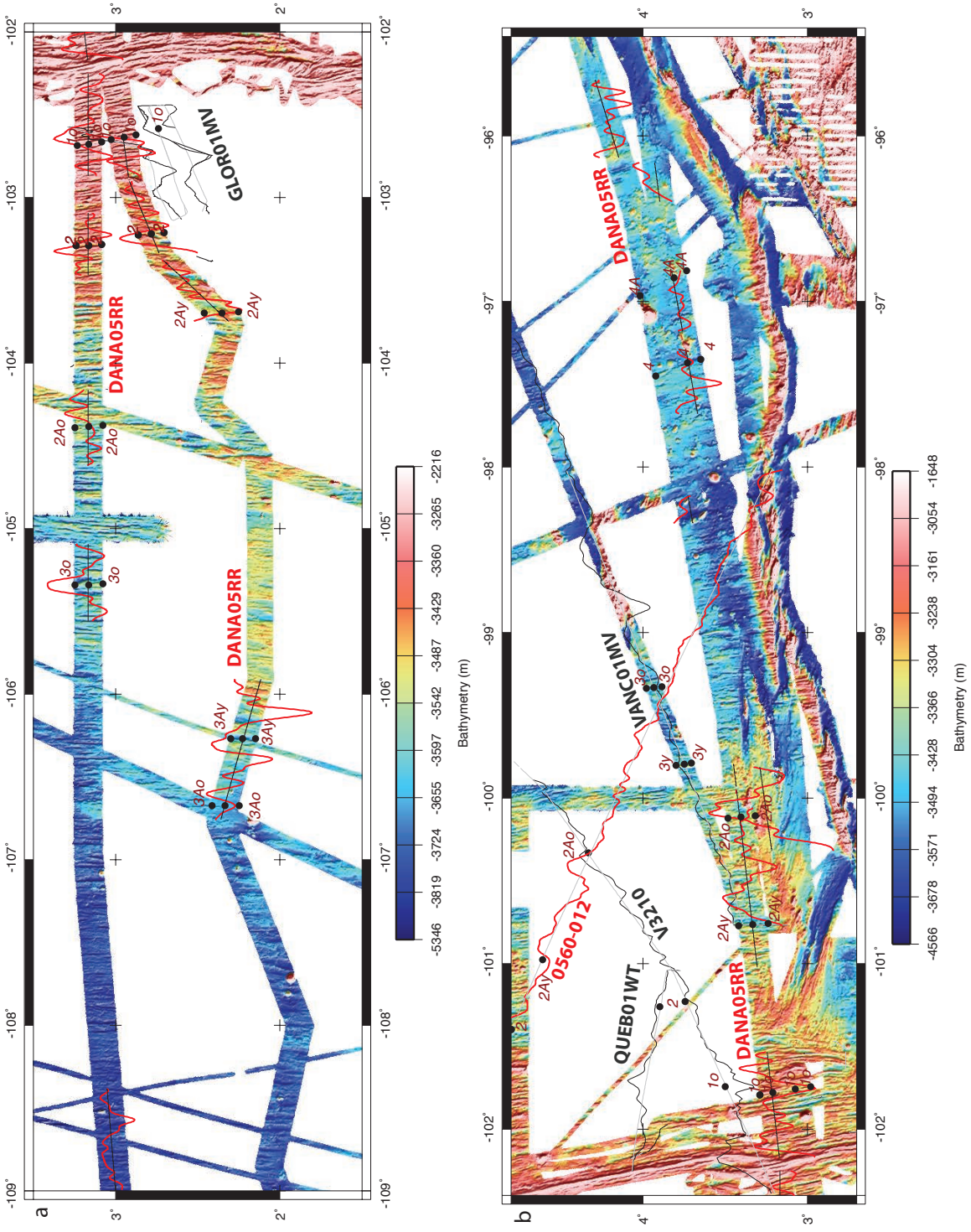

Figure 3.3: Selected vertical magnetic anomaly profiles from DANA05RR and Project Magnet flight 0560-012 in red, selected total field magnetic anomaly profiles in black. Multibeam bathymetry data from DANA05RR and publically available cruises. Map is in a Mercator projection.

Figure 3.4: Nine trajectories through a 2-D magnetic forward model for the Pacific-Cocos Ridge (PCR) based on gridding abyssal hill strike azimuths from the multibeam bathymetry and magnetic anomaly data. In addition, the synthetic Apparent Polar Wander paths (APWP) model for the Pacific Plate by *Wessel and Kroenke* [2008] and PCR rotation parameters were used to calculate the remanent inclination and declination. Map is in a Mercator projection.

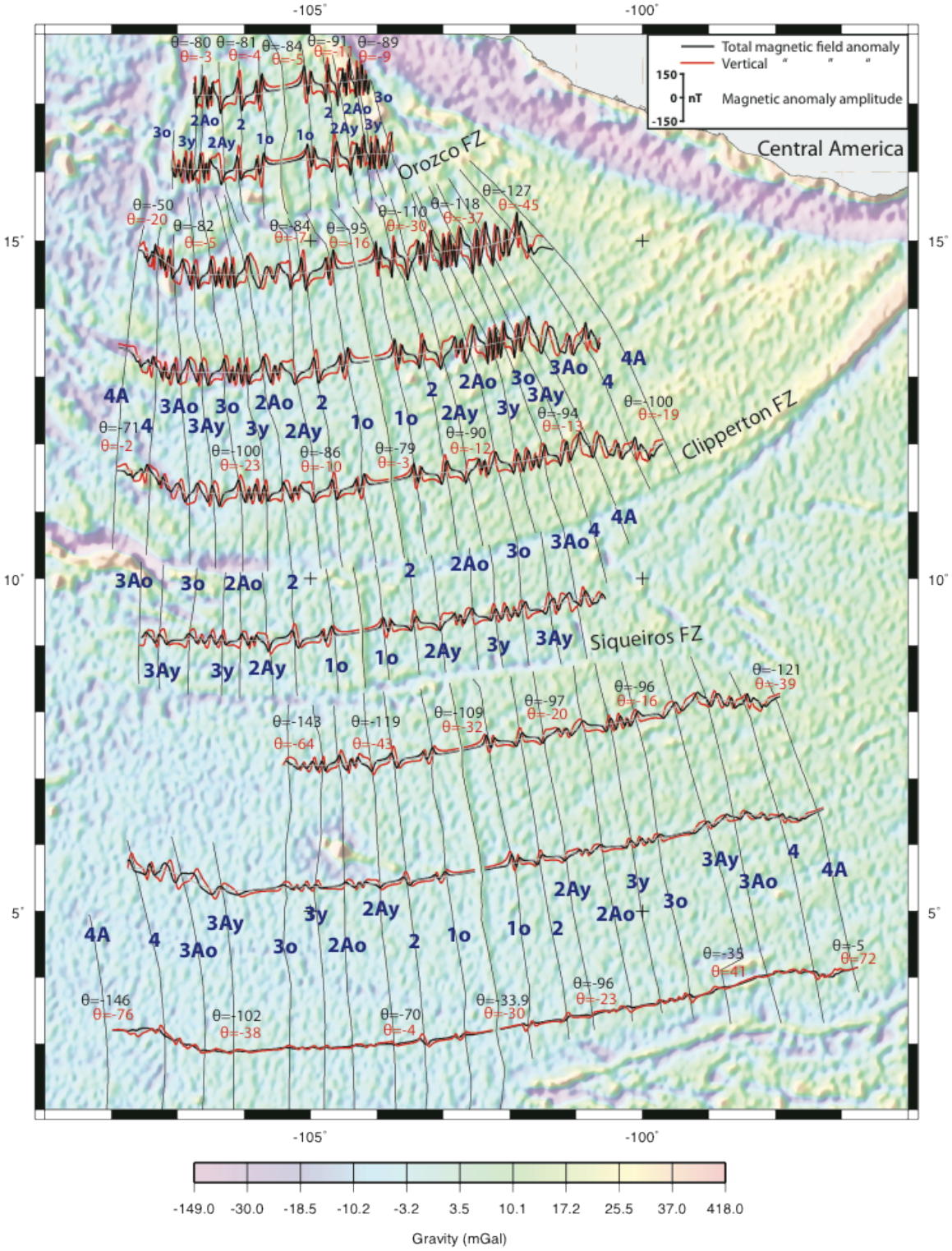
-105°
-100°
15°
10°
5°
Total magnetic field anomaly
Vertical " " "
150
0 nT
-150
Magnetic anomaly amplitude
Central America
Orozco FZ
Clipperton FZ
Siqueiros FZ
-149.0 -30.0 -18.5 -10.2 -3.2 3.5 10.1 17.2 25.5 37.0 418.0
Gravity (mGal)

Figure 3.5: Comparison and correlation of longitudinal projections of (a) selected DANA05RR (thick red lines for vertical component (MRU) and thick black lines for total field (Overhauser) anomalies), the rest of the profiles in gray) and (b) Project Magnet vertical magnetic anomaly (thick red lines) data profiles and (c and d) VANC01MV and V3210 total magnetic field profiles (thick black lines) with the 2-D forward model (thick purple lines for vertical component and thick blue lines for total field anomalies). All forward models are as observed and not reduced to the pole. The location of these profiles is mapped in Figures 3.3 and 3.6a.

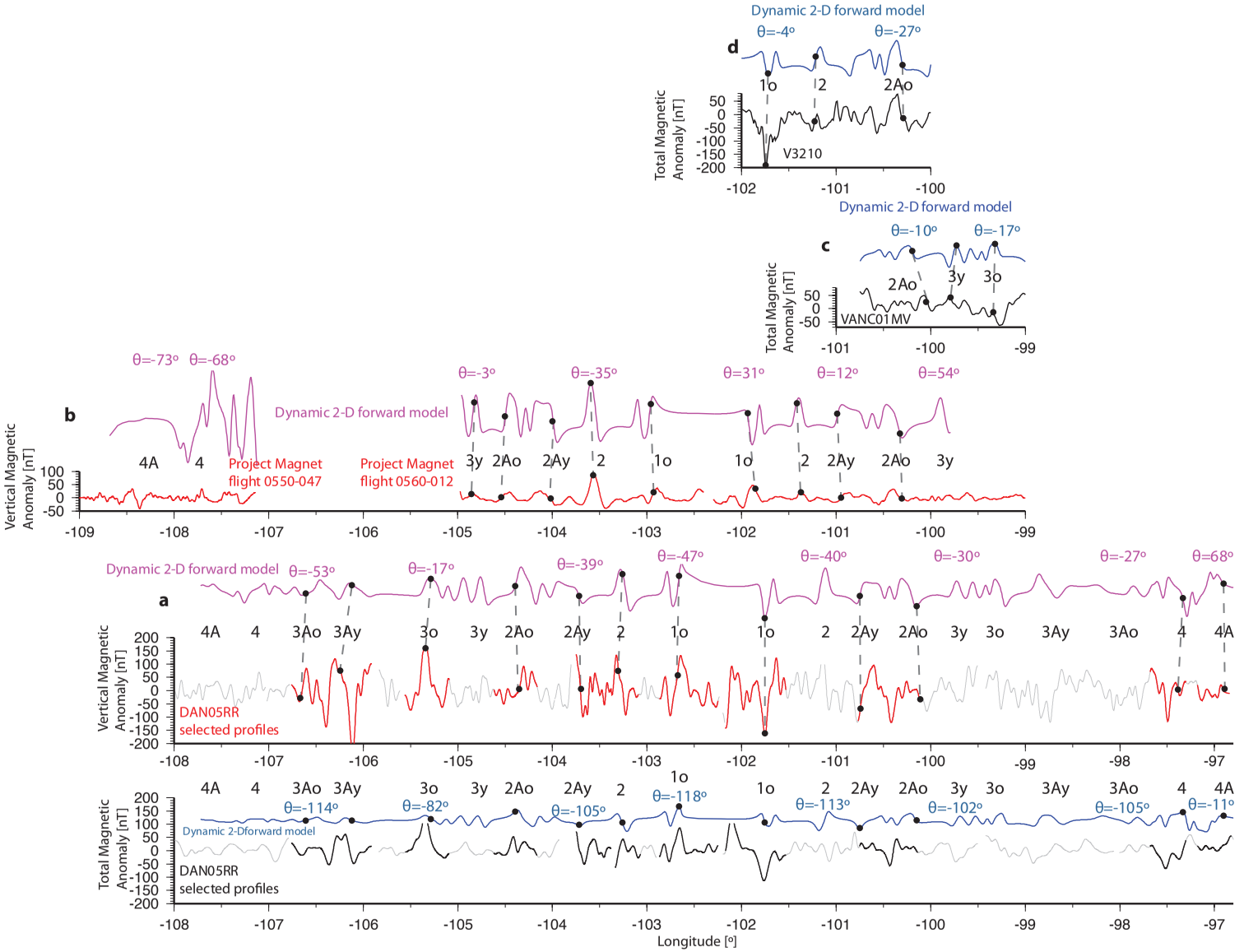
Dynamic 2-D forward model
θ=-4°
θ=-27°
d
1o
2
2Ao
Total Magnetic Anomaly [nT]
V3210
Dynamic 2-D forward model
θ=-10°
θ=-17°
c
2Ao
3y
3o
VANC01MV
θ=-73°
θ=-68°
b
Dynamic 2-D forward model
θ=-3°
θ=-35°
θ=31°
θ=12°
θ=54°
4A
4
Project Magnet flight 0550-047
Project Magnet flight 0560-012
3y
2Ao
2Ay
2
1o
Vertical Magnetic Anomaly [nT]
Dynamic 2-D forward model
θ=-53°
θ=-17°
θ=-39°
θ=-47°
θ=-40°
θ=-30°
θ=-27°
θ=68°
a
3Ao
3Ay
3o
DAN05RR selected profiles
θ=-114°
θ=-82°
θ=-105°
θ=-118°
θ=-113°
θ=-102°
θ=-105°
θ=-11°
Dynamic 2-Dforward model
Total Magnetic Anomaly [nT]
Longitude [°]

Figure 3.6: (a and b) Map of the southern and northern PCR with vertical (red) and total (gray) magnetic anomalies and picks (black triangles with dark-red annotation) on an image of the GEOSAT satellite-derived, free-air gravity field. The PCR is highlighted with thick dark-red lines. Map is in a Mercator projection.

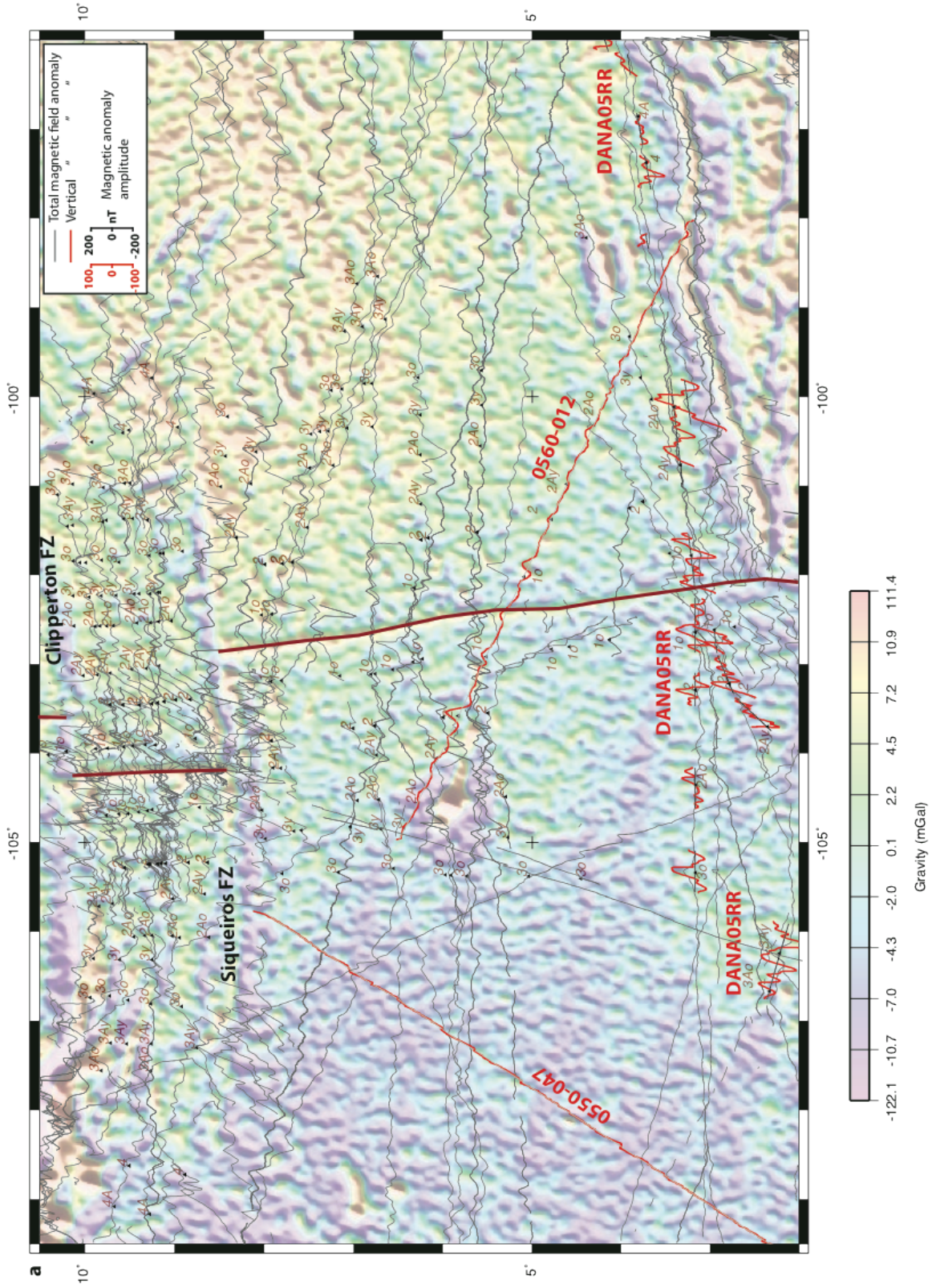
a
10°
5°
-100°
-105°
Clipperton FZ
Siqueiros FZ
0560-012
0550-047
DANA05RR
DANA05RR
DANA05RR
Total magnetic field anomaly
Vertical " "
Magnetic anomaly amplitude
nT
200
0
-200
100
0
-100
Gravity (mGal)
-122.1
-10.7
-7.0
-4.3
-2.0
0.1
2.2
4.5
7.2
10.9
111.4

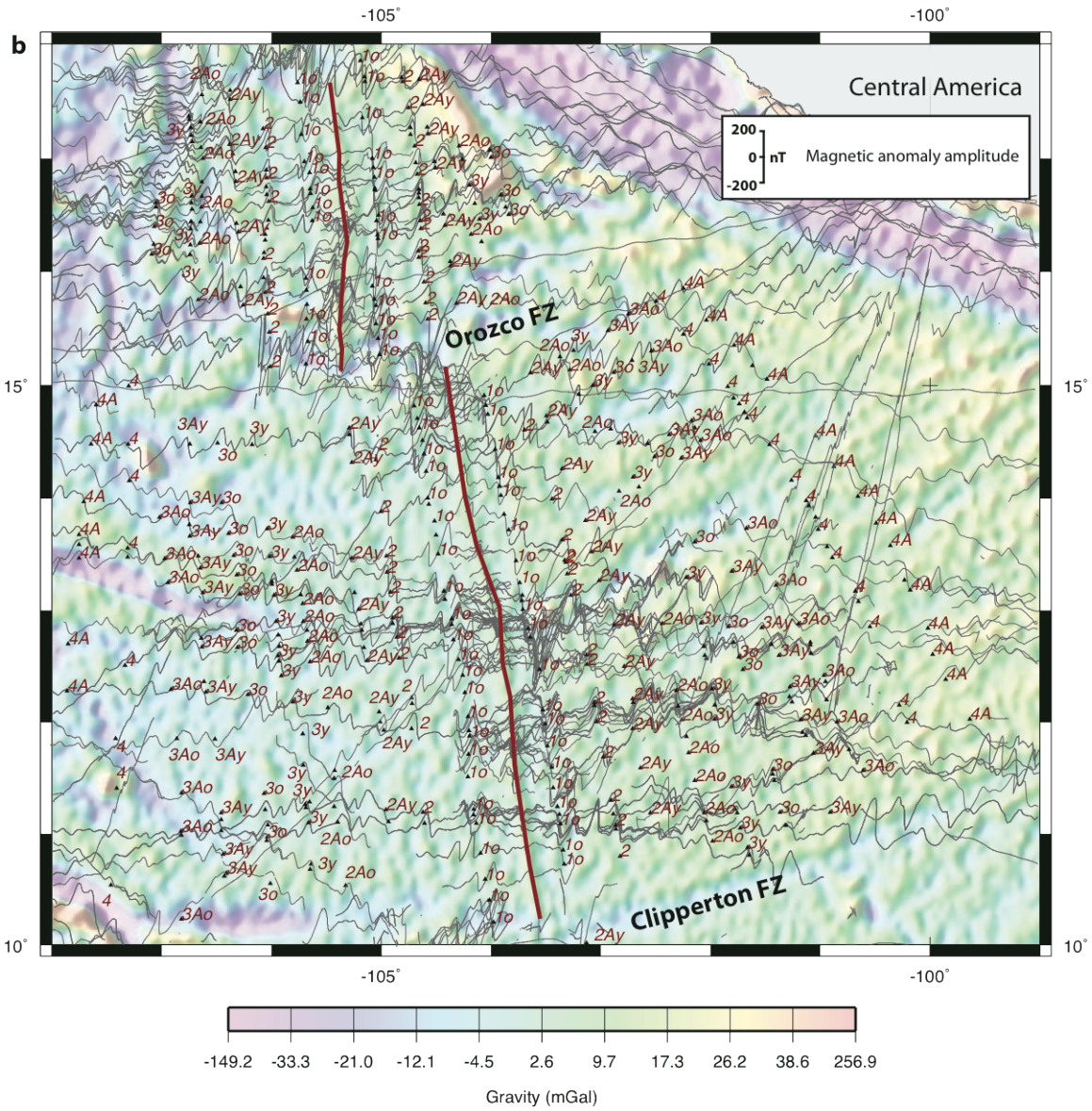

Figure 3.6 (continued)

Figure 3.7: Map of the PNR with total (gray) magnetic anomalies and picks (different colors used for chrons C1o through C4A) on an image of the GEOSAT satellite-derived, free-air gravity field. The PNR is highlighted with thick dark-red lines. Map is in a Mercator projection.

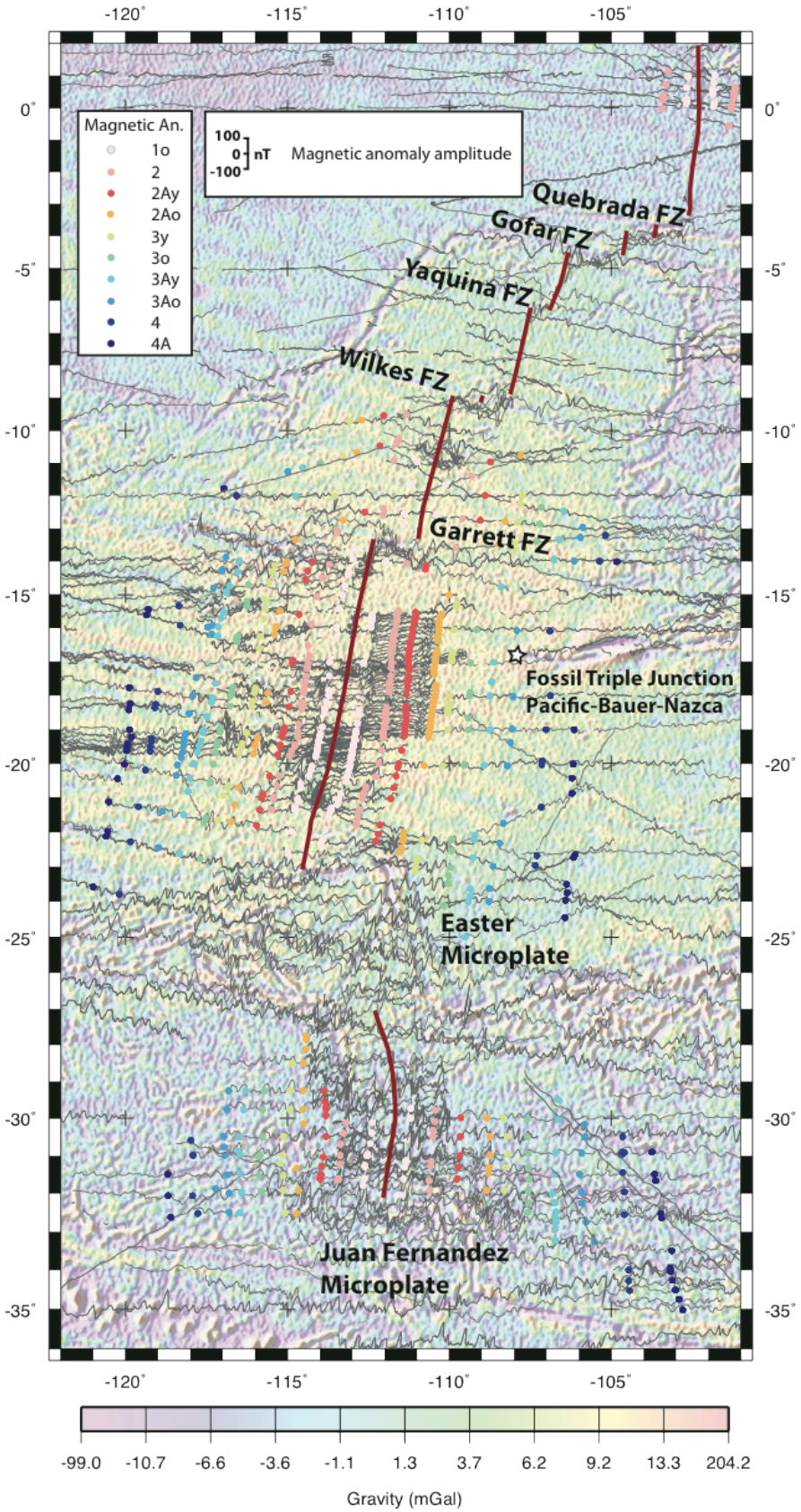
-120°
-115°
-110°
-105°
0°
-5°
-10°
-15°
-20°
-25°
-30°
-35°
Magnetic An.
1o
2
2Ay
2Ao
3y
3o
3Ay
3Ao
4
4A
100
0
-100
nT
Magnetic anomaly amplitude
Quebrada FZ
Gofar FZ
Yaquina FZ
Wilkes FZ
Garrett FZ
Fossil Triple Junction
Pacific-Bauer-Nazca
Easter
Microplate
Juan Fernandez
Microplate
-99.0
-10.7
-6.6
-3.6
-1.1
1.3
3.7
6.2
9.2
13.3
204.2
Gravity (mGal)

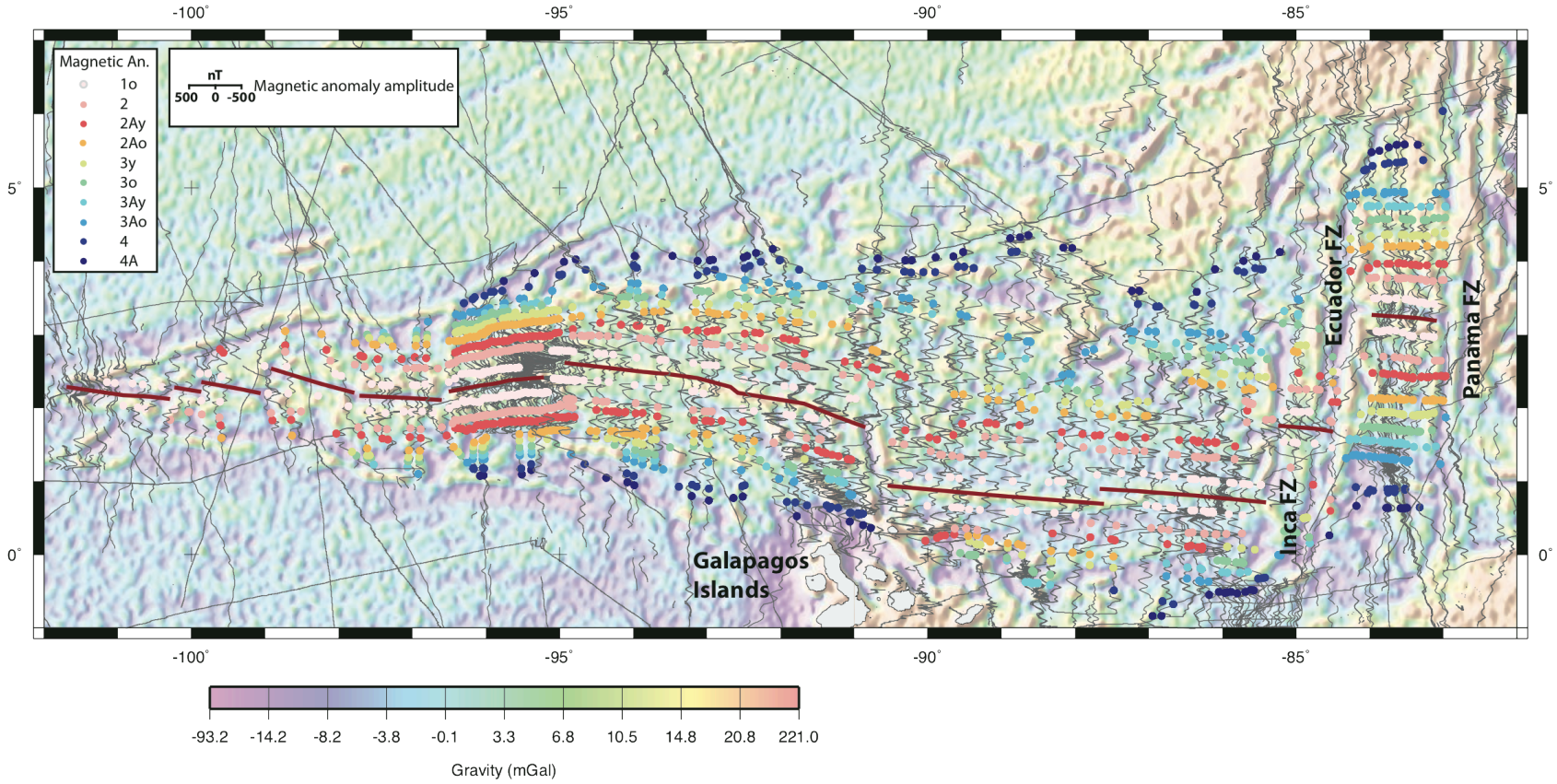

Figure 3.8: Map of the CNR with total (gray) magnetic anomalies and picks (different colors used for chrons C1o through C4A) on an image of the GEOSAT satellite-derived, free-air gravity field. The CNR is highlighted with thick dark-red lines. Map is in a Mercator projection.

Figure 3.9: Map of the Chile Ridge with total (gray) magnetic anomalies and picks (different colors used for chrons C1o through C4A) on an image of the GEOSAT satellite-derived, free-air gravity field. The Chile Ridge is highlighted with thick dark-red lines. Map is in a Mercator projection.

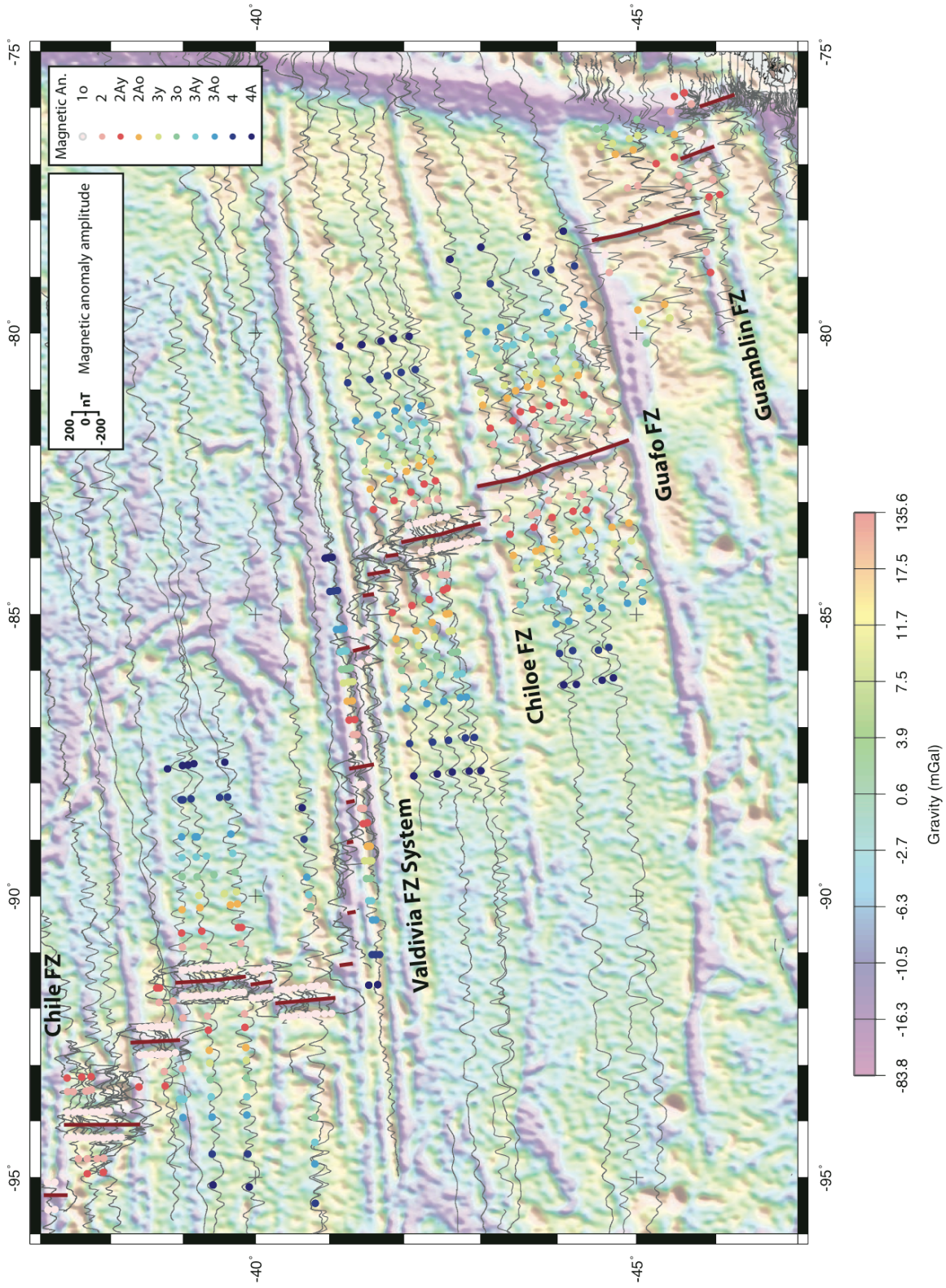
Chile FZ
Valdivia FZ System
Chiloe FZ
Guafo FZ
Guamblin FZ
Magnetic An.
1o
2
2Ay
2Ao
3y
3o
3Ay
3Ao
4
4A
Magnetic anomaly amplitude
200
0
-200
nT
-75°
-80°
-85°
-90°
-95°
-40°
-45°
-83.8
-16.3
-10.5
-6.3
-2.7
0.6
3.9
7.5
11.7
17.5
135.6
Gravity (mGal)

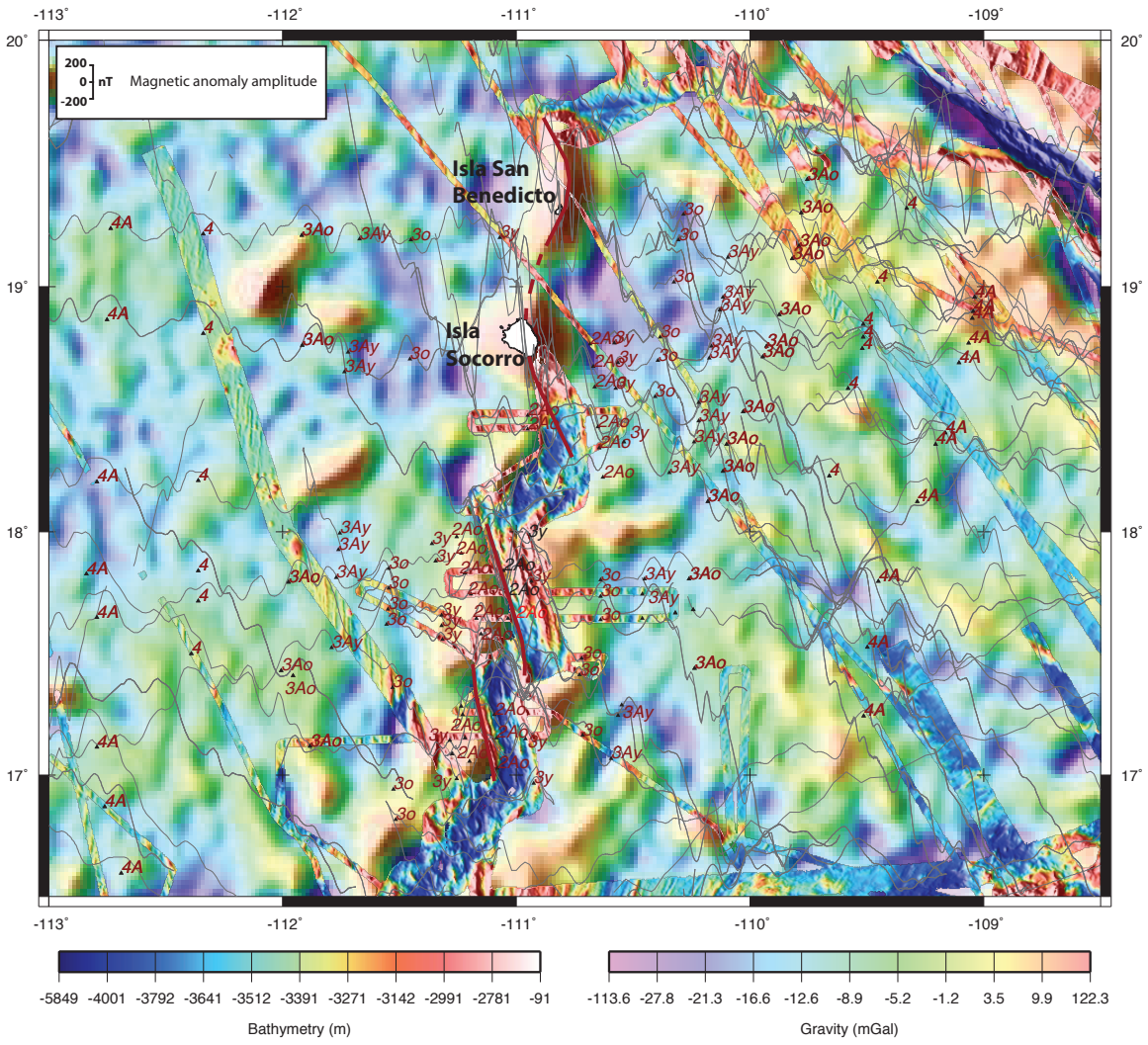

Figure 3.10: Map of the Mathematician paleo-ridge with total (gray) magnetic anomalies and picks (black triangles with dark-red annotation) on an image of the GEOSAT satellite-derived, free-air gravity field and the available multibeam bathymetry data. The Mathematician paleo-ridge is highlighted with thick dark-red lines. Map is in a Mercator projection.

Figure 3.11: Comparison of our Chile Ridge rotation poles based on a Pacific-Nazca-Antarctic 3-plate (blue) and 2-plate (grey) solutions with the *Tebbens and Cande* [1997] poles (purple). MORVEL pole [*DeMets et al.*, 2010] in light-blue. Ellipses represent 95% confidence regions. Rotation parameters are listed in Table 3.2. Map is in a Mercator projection.

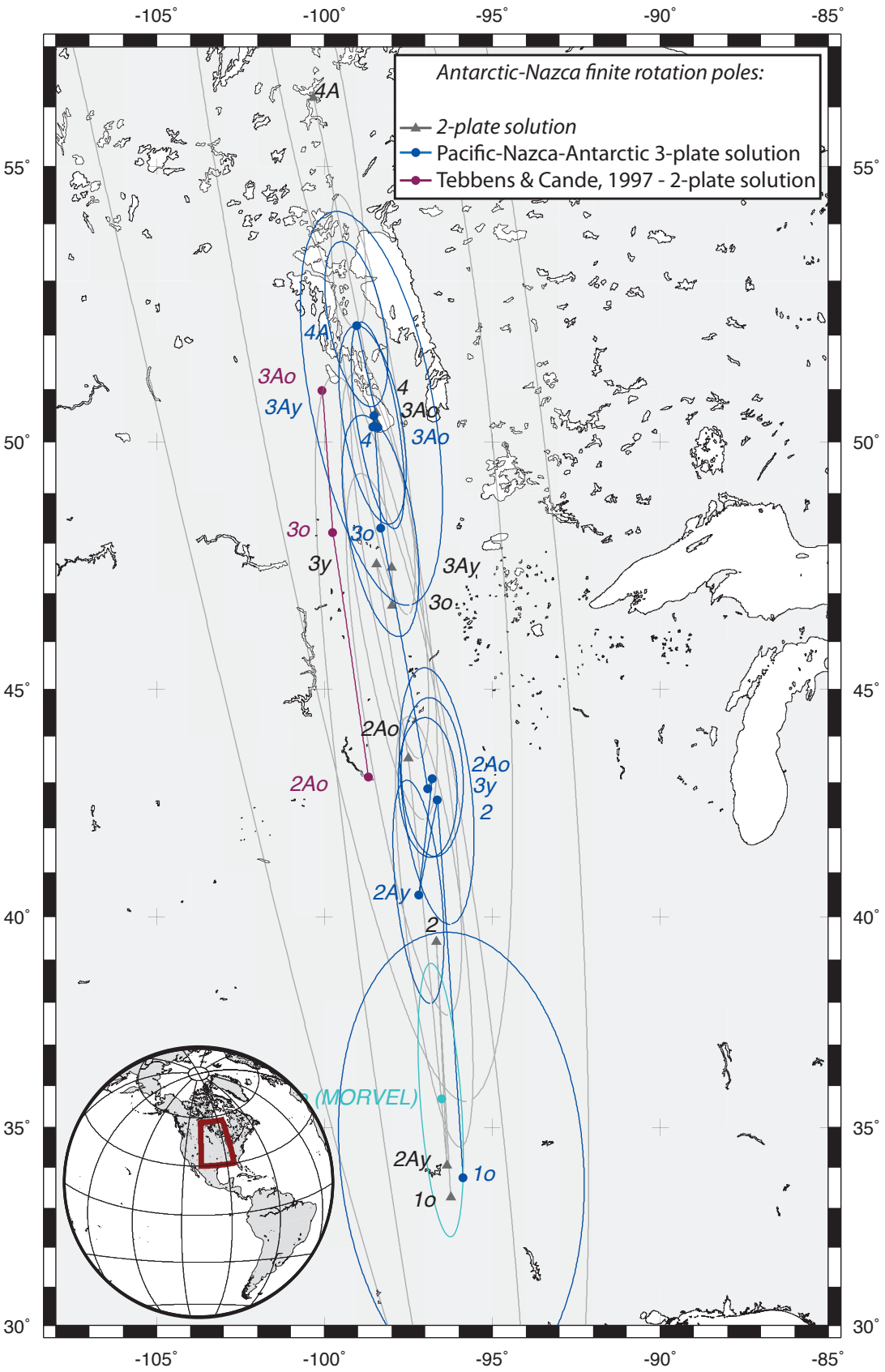
Antarctic-Nazca finite rotation poles:
2-plate solution
Pacific-Nazca-Antarctic 3-plate solution
Tebbens & Cande, 1997 - 2-plate solution
-105˚
-100˚
-95˚
-90˚
-85˚
55˚
50˚
45˚
40˚
35˚
30˚
4A
3Ao
3Ay
4
3Ao
3o
3y
3Ay
2Ao
2Ay
1o
(MORVEL)

Figure 3.12: (a) PNR rotation poles based on a Pacific-Nazca-Antarctic 3-plate (blue), Pacific-Cocos-Nazca 3-plate (red), and 2-plate (grey) solutions. Pole for chron C2A [*DeMets et al.*, 1990] and chrons C3A and C4A [*Wilder*, 2003] in dark-red and MORVEL pole [*DeMets et al.*, 2010] in light-blue. Ellipses represent 95% confidence regions. Rotation parameters are listed in Table 3.5. Map Projection is stereographic centered on 57°N, 90°W. (b) PNR rotation poles on 2-plate (grey) solutions. MORVEL pole [*DeMets et al.*, 2010] in light-blue. Ellipses represent 95% confidence regions. Map projection same as in Figure a. (c) Map of GTJ (black) rotated by the chron C1o PNR pole for the Pacific-Nazca-Antarctic (blue) and Pacific-Cocos-Nazca (red) plate circuits. Multibeam bathymetry data from DANA05RR and publically available cruises. The spreading ridges in solid gray lines. Map is in a Mercator projection.

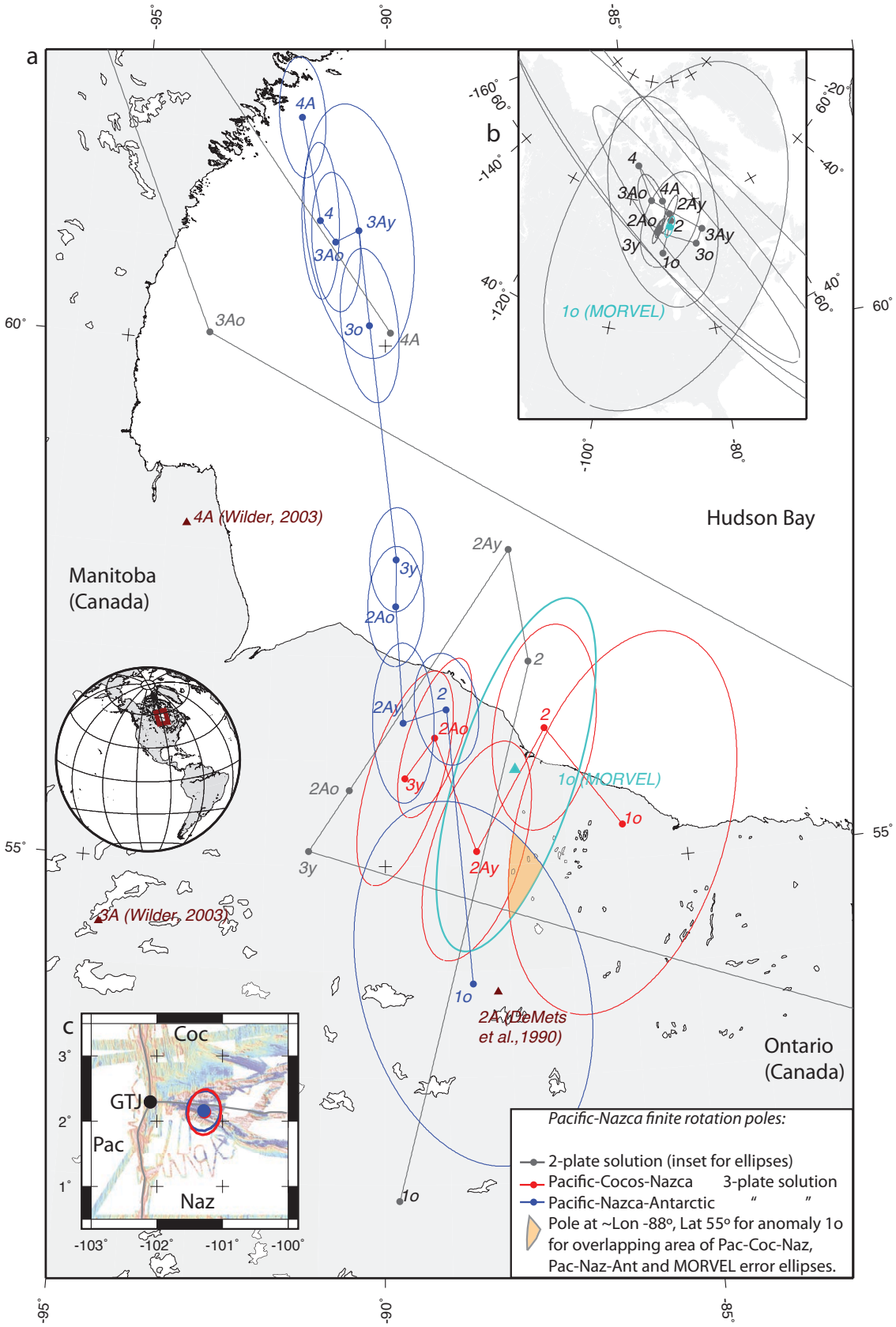
a
b
c
-95°
-90°
-85°
60°
55°
4A
4
3Ay
3Ao
3o
3Ao
4A
4A (Wilder, 2003)
3A (Wilder, 2003)
Manitoba
(Canada)
Hudson Bay
Ontario
(Canada)
3y
2Ao
2Ay
2
2Ay
2Ao
3y
2Ao
3y
2Ay
1o (MORVEL)
1o
1o
2A (DeMets
et al., 1990)
-160°
-140°
-120°
-100°
-80°
60°
40°
-20°
-40°
-60°
4
3Ao
4A
2Ay
2Ao
2
3Ay
3y
1o
3o
1o (MORVEL)
Coc
GTJ
Pac
Naz
3°
2°
1°
-103°
-102°
-101°
-100°
Pacific-Nazca finite rotation poles:
2-plate solution (inset for ellipses)
Pacific-Cocos-Nazca 3-plate solution
Pacific-Nazca-Antarctic " "
Pole at ~Lon -88º, Lat 55º for anomaly 1o
for overlapping area of Pac-Coc-Naz,
Pac-Naz-Ant and MORVEL error ellipses.

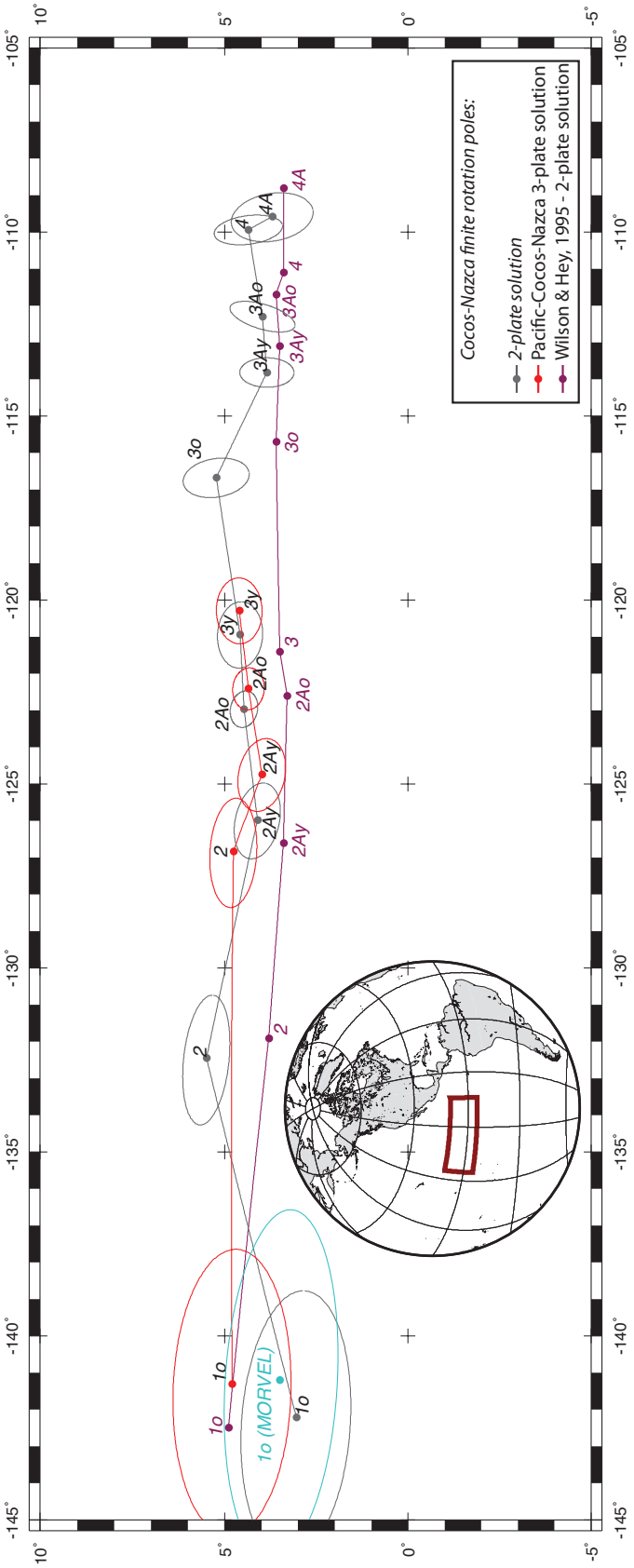

Figure 3.13: Comparison of our CNR rotation poles based on a Pacific-Cocos-Nazca 3-plate (red) and 2-plate (grey) solution with the *Wilson and Hey* [1995] poles (purple). MORVEL pole [*DeMets et al.*, 2010] in light-blue. Ellipses represent 95% confidence regions. Rotation parameters are listed in Table 3.3. Map is in a Mercator projection.

Figure 3.14: PCR rotation poles based on a Pacific-Cocos-Nazca 3-plate (red) and 2-plate (black, blue and grey) solutions. Pacific-Mathematician poles based on 2-plate (green) and Pacific-Mathematician-Cocos 3-plate (orange) solutions. Schilt [1982] PCR poles in purple and MORVEL pole [*DeMets et al.*, 2010] in light-blue. Ellipses represent 95% confidence regions. Background image is the GEOSAT satellite-derived, free-air gravity field. Rotation parameters are listed in Table 3.4. Map is in a Mercator projection.

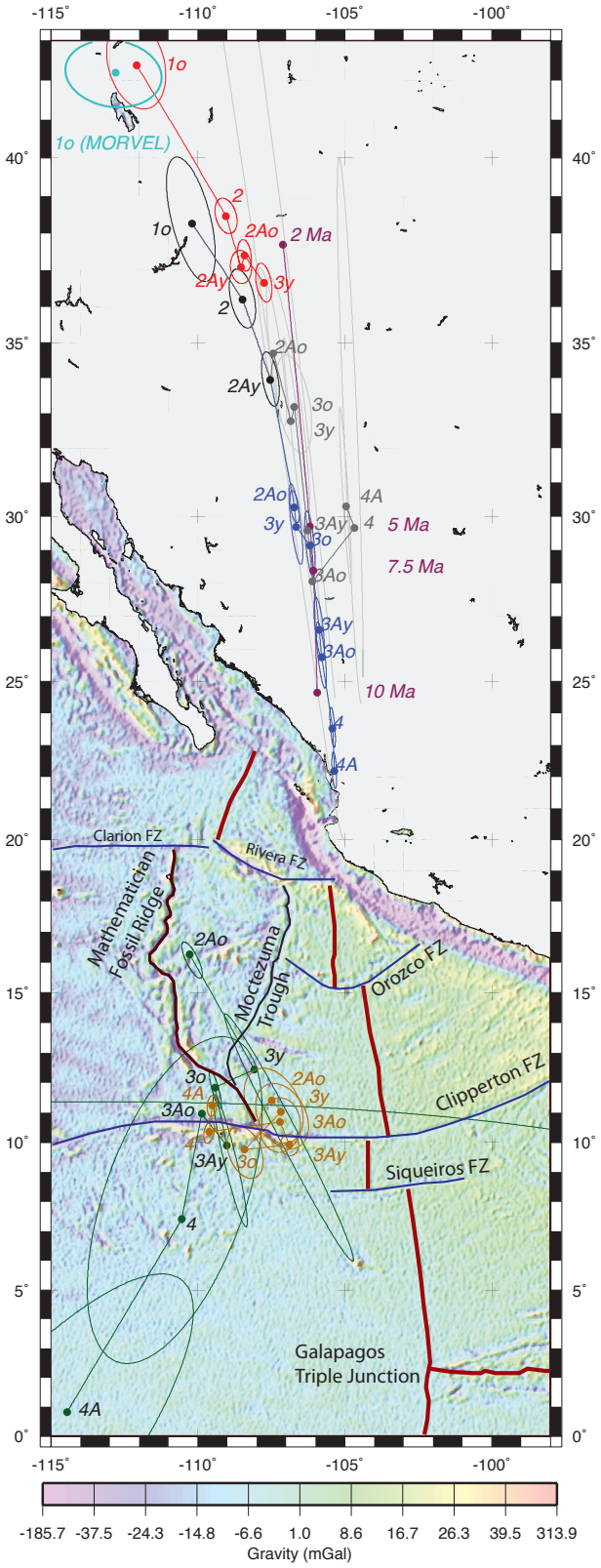

Pacific-Cocos finite rotation poles:

Anomalies 1o, 2 & 2Ay:
2-plate solution

Anomalies 2Ao, 3y, 3o, 3Ay, 3Ao, 4 & 4A:
picks South of Clipperton FZ - 2-plate solution
" North " " "
(Mathematician-Cocos)

Anomalies 1o --> 3y:
Pacific-Cocos-Nazca - 3-plate solution

Schilt et al., 1982 - 2-plate solution

Pacific-Mathematician finite rotation poles:

Anomalies 2Ao, 3y, 3o, 3Ay, 3Ao, 4 & 4A:
2-plate solution
Pacific-Mathematician-Cocos 3-plate solution

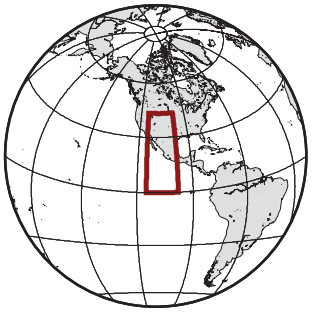

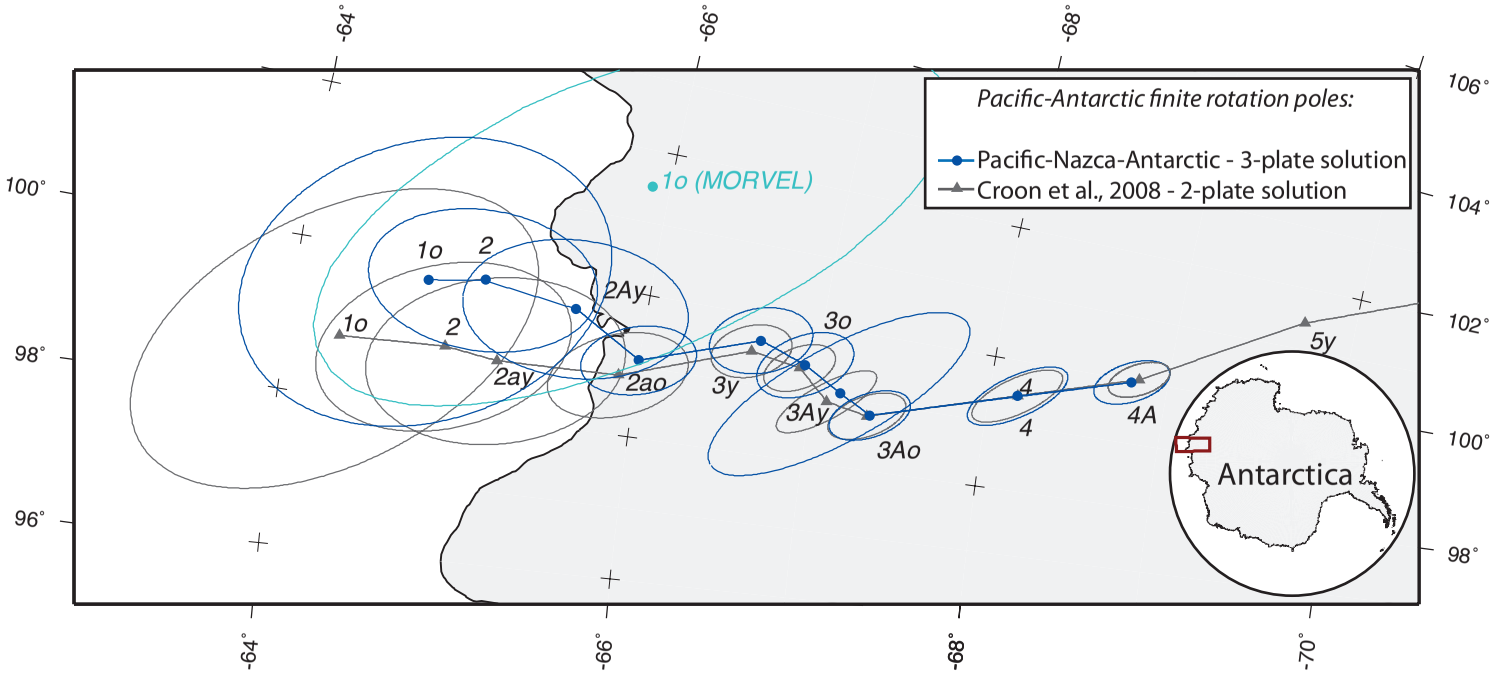

Figure 3.15: Comparison of our PAR rotation poles based on a Pacific-Nazca-Antarctic 3-plate solution (blue) with the *Croon et al.* [2008] poles (grey). MORVEL pole [*DeMets et al.*, 2010] in light-blue. Ellipses represent 95% confidence regions. Rotation parameters are listed in Table 3.1. Map Projection is stereographic centered on 67.2°S, 180°W.

Figure 3.16: Stage poles and synthetic flow lines for PCR, PNR, CNR, PAR and Chile Ridge relative displacements for Pacific-Cocos-Nazca (red) and Pacific-Nazca-Antarctic (blue) plate circuits. Larger dots mark the center points of the flow lines. Ellipses represent 95% confidence regions. The reference frames are marked on the map at each set of stage poles. Digitized FZ traces (from multibeam and satellite-derived, free-air gravity data) in solid orange lines. The spreading ridges in solid gray lines. Map Projection is stereographic centered on 25°S, 110°W.

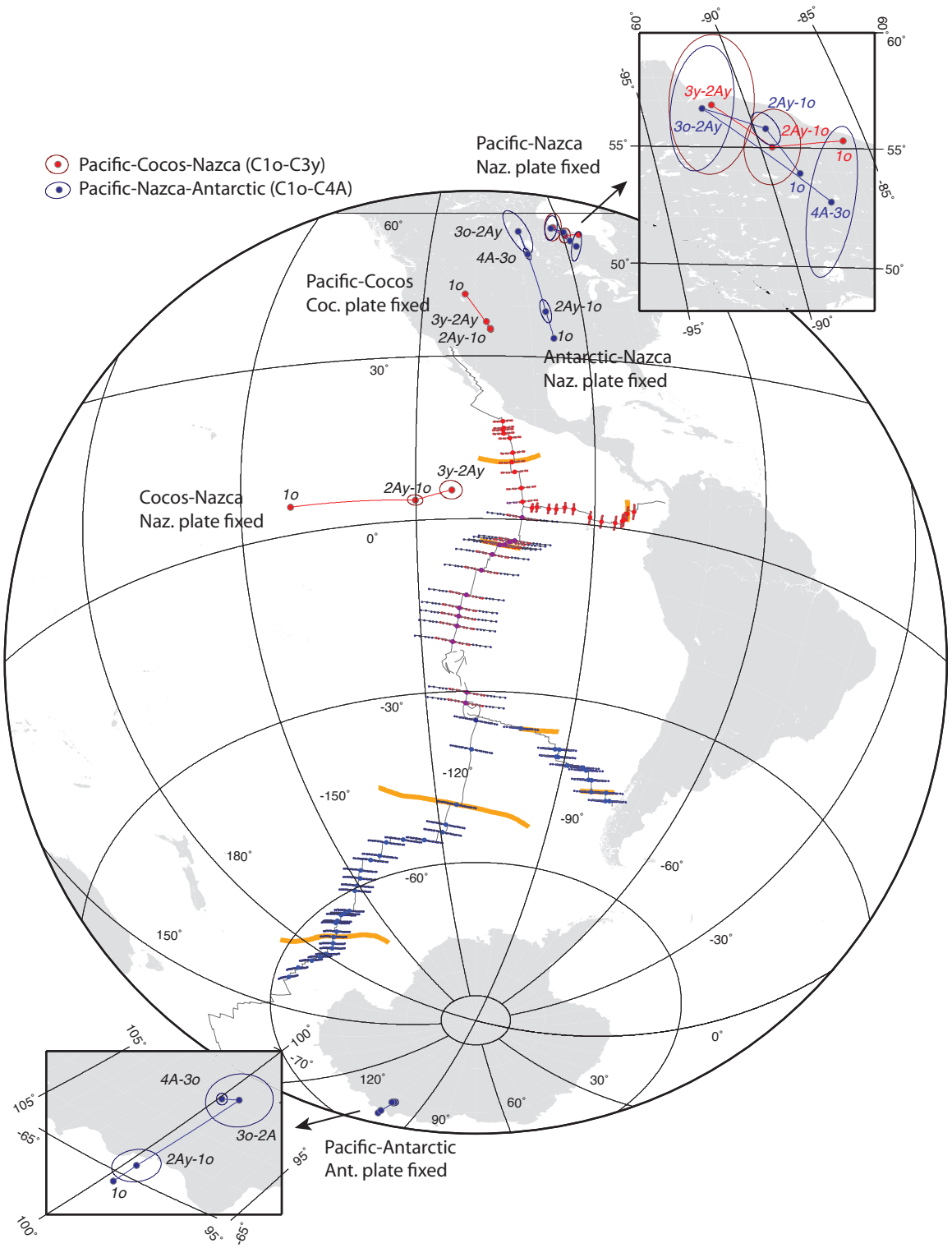
Pacific-Cocos-Nazca (C1o-C3y)
Pacific-Nazca-Antarctic (C1o-C4A)
Pacific-Nazca
Naz. plate fixed
3y-2Ay
2Ay-1o
3o-2Ay
2Ay-1o
1o
1o
4A-3o
Pacific-Cocos
Coc. plate fixed
3o-2Ay
4A-3o
1o
2Ay-1o
3y-2Ay
2Ay-1o
1o
Antarctic-Nazca
Naz. plate fixed
Cocos-Nazca
Naz. plate fixed
1o
2Ay-1o
3y-2Ay
4A-3o
3o-2A
2Ay-1o
1o
Pacific-Antarctic
Ant. plate fixed

Figure 3.17: Full spreading rates (lines) and lineation azimuths (dots, 0° is north and clockwise is positive) calculated from the rotation parameters along flow lines for PCR, PNR, CNR, PAR and Chile Ridge for Pacific-Cocos-Nazca (red shades) and Pacific-Nazca-Antarctic (blue shades) 3-plate circuits. 2-plate solutions for PCR and CNR in grey shades.

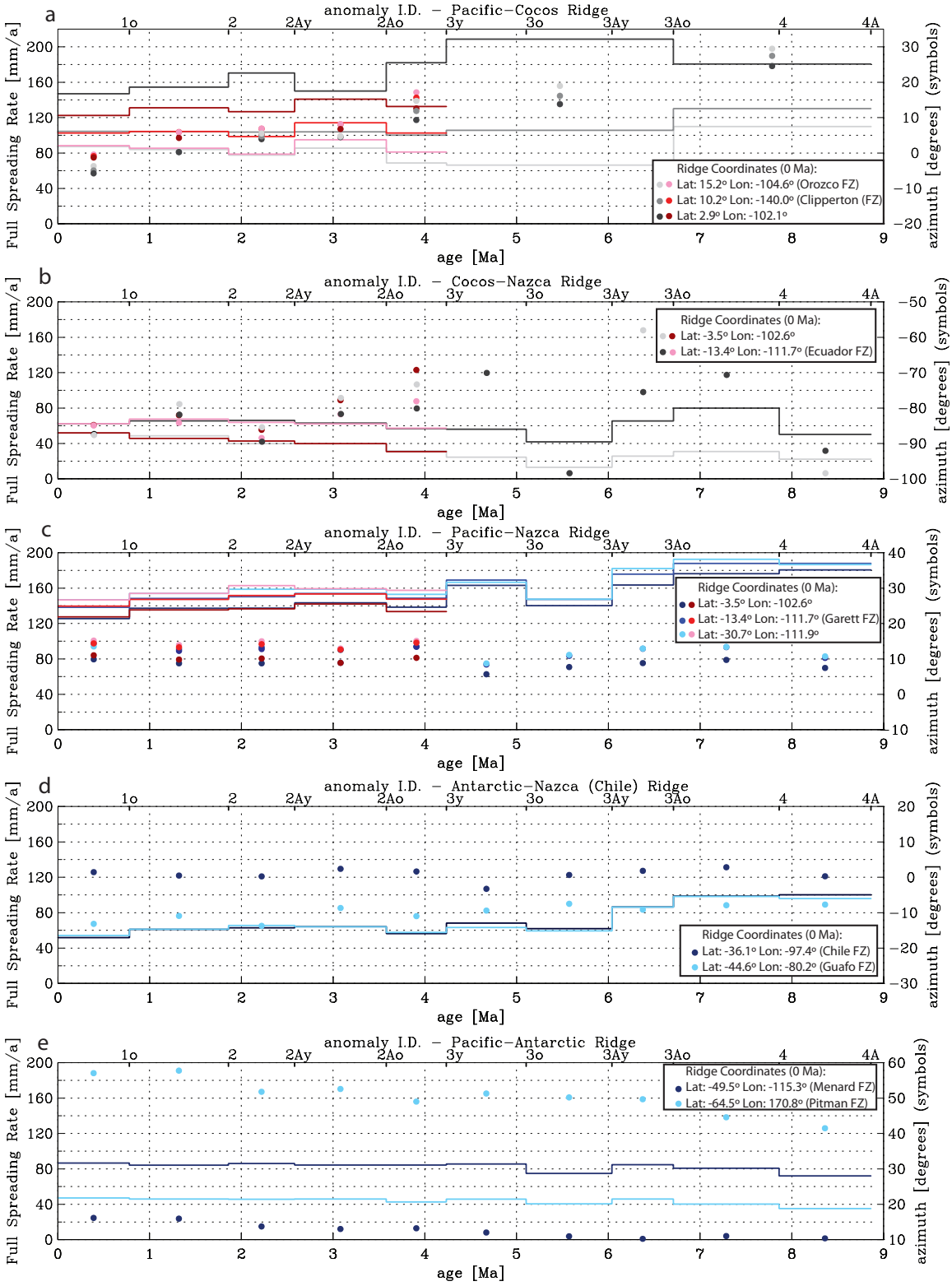
a
anomaly I.D. – Pacific–Cocos Ridge
1o 2 2Ay 2Ao 3y 3o 3Ay 3Ao 4 4A
Full Spreading Rate [mm/a]
azimuth [degrees] (symbols)
age [Ma]
Ridge Coordinates (0 Ma):
Lat: 15.2° Lon: -104.6° (Orozco FZ)
Lat: 10.2° Lon: -140.0° (Clipperton (FZ)
Lat: 2.9° Lon: -102.1°
b
anomaly I.D. – Cocos–Nazca Ridge
Ridge Coordinates (0 Ma):
Lat: -3.5° Lon: -102.6°
Lat: -13.4° Lon: -111.7° (Ecuador FZ)
c
anomaly I.D. – Pacific–Nazca Ridge
Ridge Coordinates (0 Ma):
Lat: -3.5° Lon: -102.6°
Lat: -13.4° Lon: -111.7° (Garett FZ)
Lat: -30.7° Lon: -111.9°
d
anomaly I.D. – Antarctic–Nazca (Chile) Ridge
Ridge Coordinates (0 Ma):
Lat: -36.1° Lon: -97.4° (Chile FZ)
Lat: -44.6° Lon: -80.2° (Guafo FZ)
e
anomaly I.D. – Pacific–Antarctic Ridge
Ridge Coordinates (0 Ma):
Lat: -49.5° Lon: -115.3° (Menard FZ)
Lat: -64.5° Lon: 170.8° (Pitman FZ)

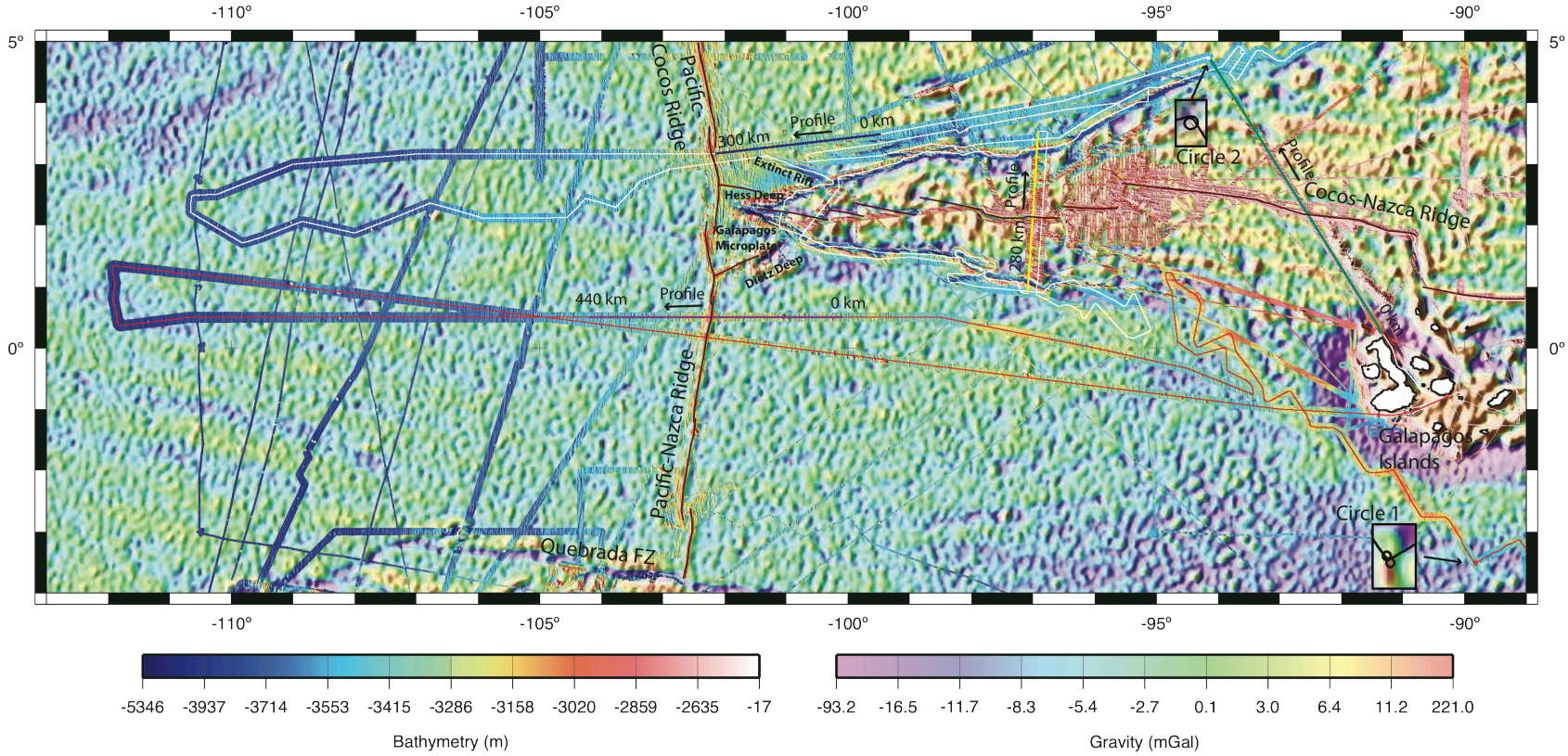

Figure 3A1: Map of the eastern tropical Pacific near the Galapagos Triple Junction on an image of the GEOSAT satellite-derived, free-air gravity field and the available multibeam bathymetry data, summarizing the location of the DANA05RR cruise track for data collected with MRU sensor 0954 (red solid line) and 2259 (white solid line). Thick solid yellow, blue, purple and yellow lines highlight four processed profiles. Calibration circles 1 and 2 are magnified in insets. Spreading ridges in dark red. Map is in a Mercator projection.

Figure 3A2: Laboratory MRU sensor calibration results for (a) Sensor 0954 and (b) Sensor 2259. (a-1 and b-1) Relationship between water and sensor temperature. (a-2,3,4 and b-2,3,4) Polynomial fits for calibration values at seven temperatures. R=Roll, P=Pitch and Y=Yaw sensor.

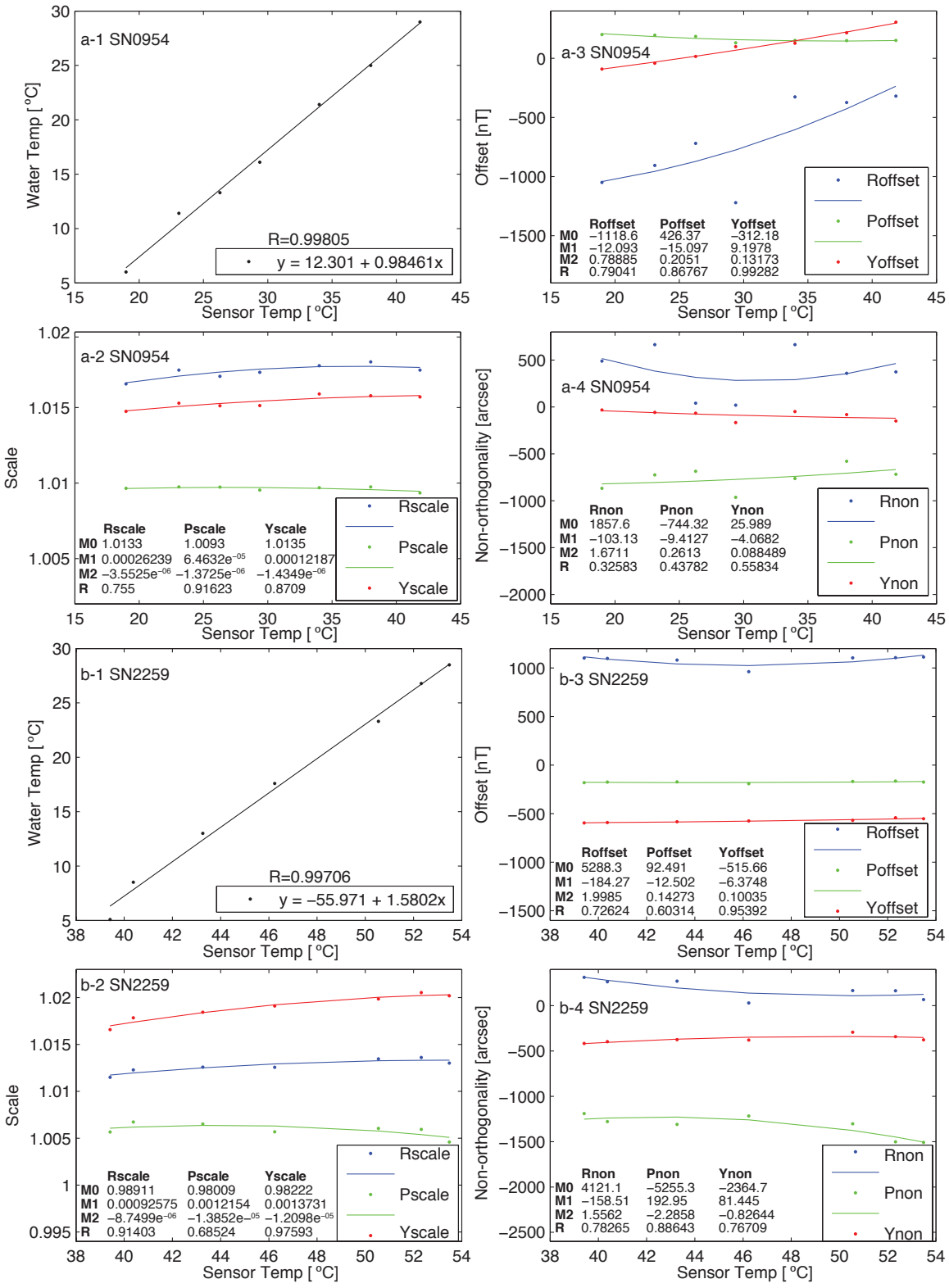
a-1 SN0954
Water Temp [°C]
Sensor Temp [°C]
R=0.99805
y = 12.301 + 0.98461x
a-3 SN0954
Offset [nT]
Sensor Temp [°C]
Roffset
Poffset
Yoffset
Roffset Poffset Yoffset
M0 −1118.6 426.37 −312.18
M1 −12.093 −15.097 9.1978
M2 0.78885 0.2051 0.13173
R 0.79041 0.86767 0.99282
a-2 SN0954
Scale
Sensor Temp [°C]
Rscale
Pscale
Yscale
Rscale Pscale Yscale
M0 1.0133 1.0093 1.0135
M1 0.00026239 6.4632e−05 0.00012187
M2 −3.5525e−06 −1.3725e−06 −1.4349e−06
R 0.755 0.91623 0.8709
a-4 SN0954
Non-orthogonality [arcsec]
Sensor Temp [°C]
Rnon
Pnon
Ynon
Rnon Pnon Ynon
M0 1857.6 −744.32 25.989
M1 −103.13 −9.4127 −4.0682
M2 1.6711 0.2613 0.088489
R 0.32583 0.43782 0.55834
b-1 SN2259
Water Temp [°C]
Sensor Temp [°C]
R=0.99706
y = −55.971 + 1.5802x
b-3 SN2259
Offset [nT]
Sensor Temp [°C]
Roffset
Poffset
Yoffset
Roffset Poffset Yoffset
M0 5288.3 92.491 −515.66
M1 −184.27 −12.502 −6.3748
M2 1.9985 0.14273 0.10035
R 0.72624 0.60314 0.95392
b-2 SN2259
Scale
Sensor Temp [°C]
Rscale
Pscale
Yscale
Rscale Pscale Yscale
M0 0.98911 0.98009 0.98222
M1 0.00092575 0.0012154 0.0013731
M2 −8.7499e−06 −1.3852e−05 −1.2098e−05
R 0.91403 0.68524 0.97593
b-4 SN2259
Non-orthogonality [arcsec]
Sensor Temp [°C]
Rnon
Pnon
Ynon
Rnon Pnon Ynon
M0 4121.1 −5255.3 −2364.7
M1 −158.51 192.95 81.445
M2 1.5562 −2.2858 −0.82644
R 0.78265 0.88643 0.76709

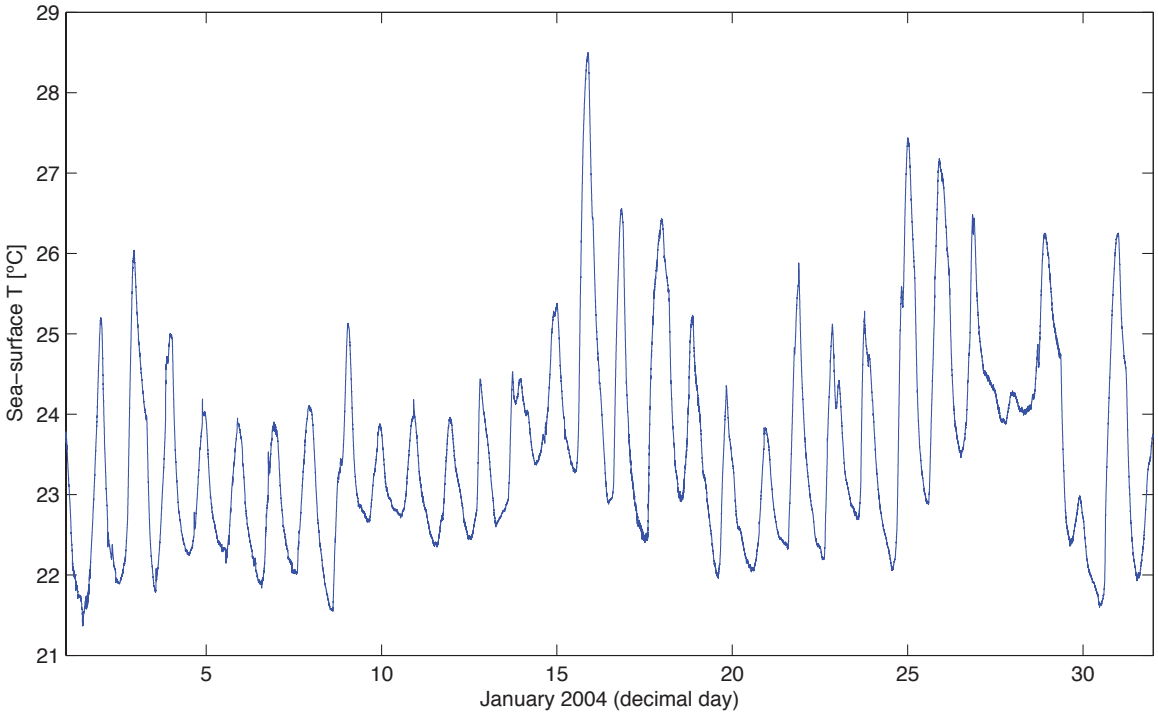

Figure 3A3: Sea-surface water temperatures, collected on the side of the ship in January 2004, for the DANA05RR cruise.

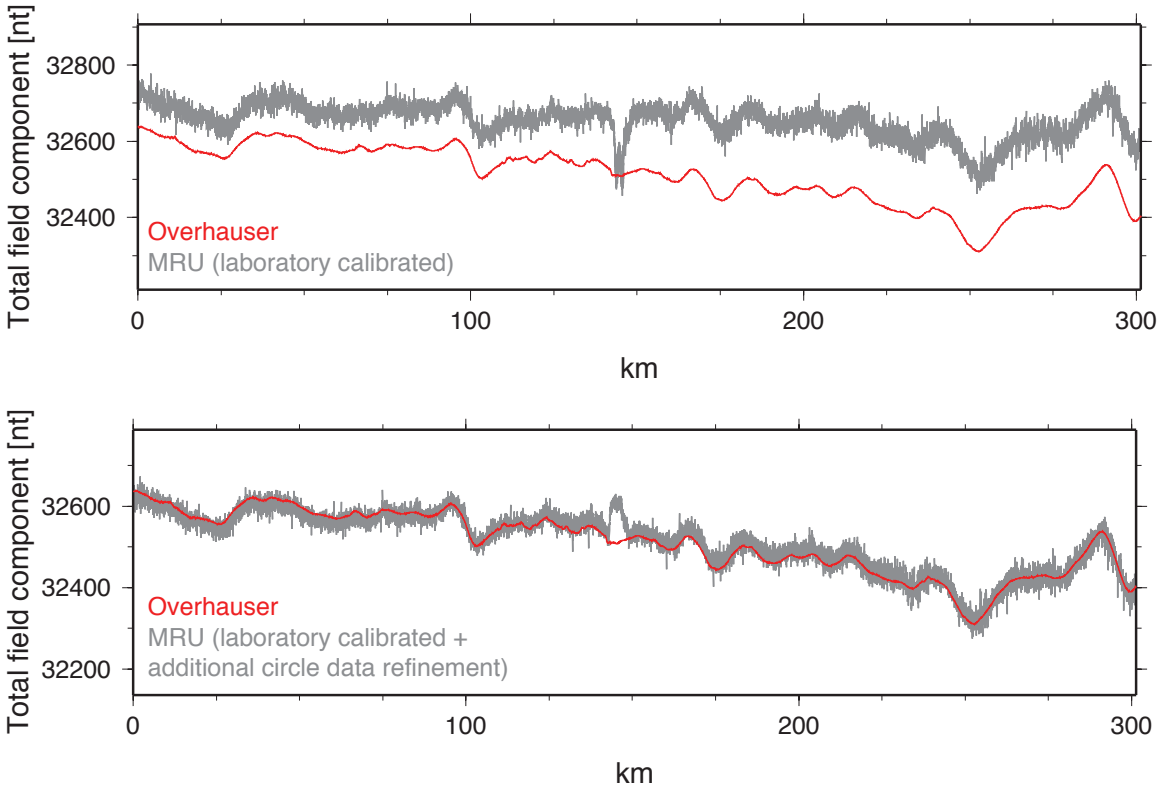

Figure 3A4: Comparison of total magnetic field signal between Overhauser sensor and (top) laboratory calibrated MRU sensor and (bottom) additional calibration refinement from circle data for MRU sensor.

Figure 3A5: Data processing results for a theoretical 2-D magnetic forward model profile with (a) Raw calibrated, (b) DGRF corrected and (c) Bandpass filtered results. (d) Roll, pitch and yaw measurements and calculated sensor temperature of the fluxgate towfish along the profile. (e) Cross-spectra coherence plots between the vertical vs. total and vertical vs. horizontal processed anomalies and profiles for the horizontal and vertical processed anomalies. (f) Synthetic yaw calculation with yaw direction relative to geographic north.

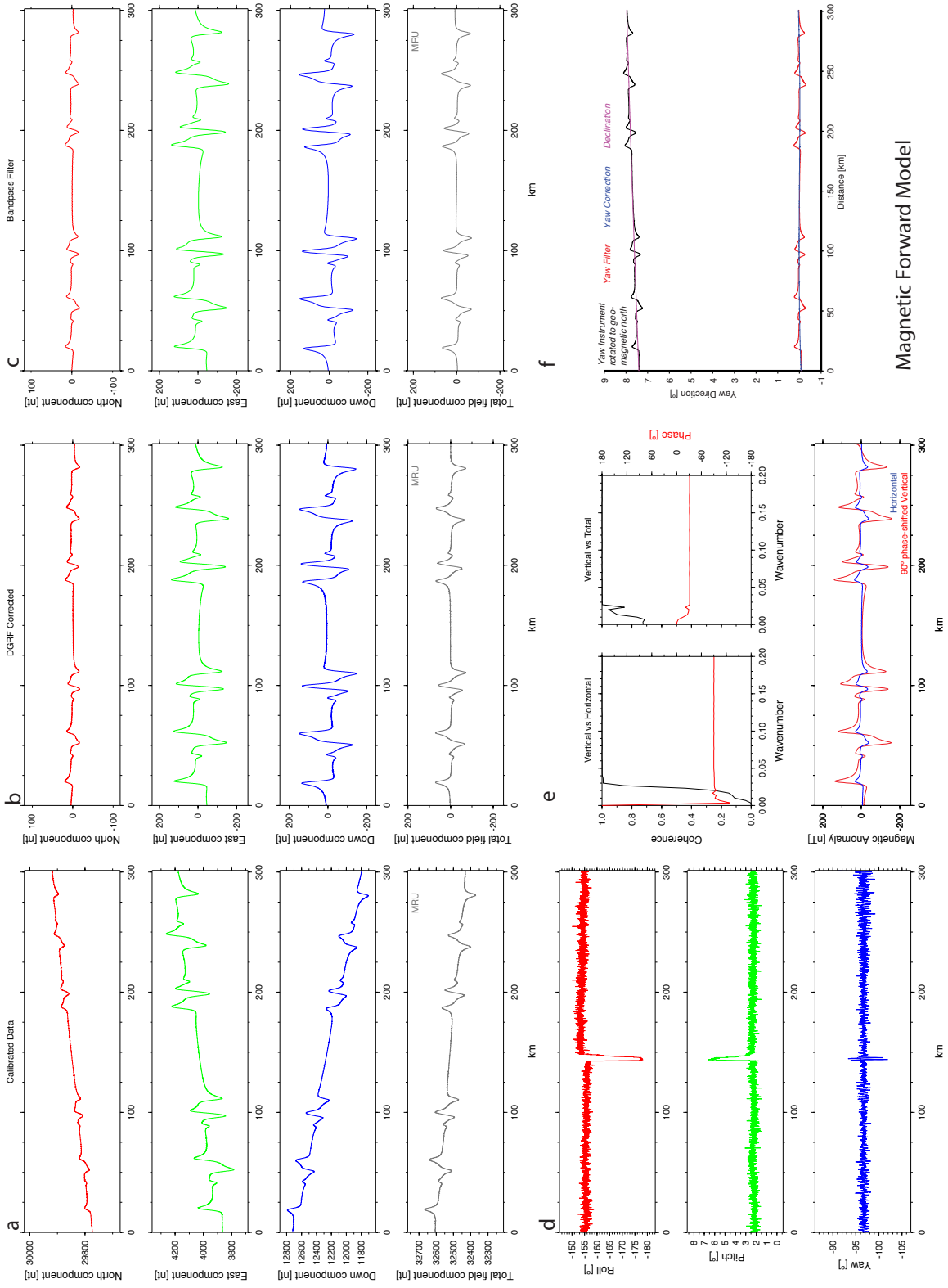
a
Calibrated Data
North component [nt]
East component [nt]
Down component [nt]
Total field component [nt]
MRU
b
DGRF Corrected
c
Bandpass Filter
d
Roll [°]
Pitch [°]
Yaw [°]
e
Vertical vs Horizontal
Vertical vs Total
Coherence
Wavenumber
Phase [°]
Magnetic Anomaly [nT]
Horizontal
90° phase-shifted Vertical
km
f
Yaw Instrument rotated to geo-magnetic north
Yaw Filter
Yaw Correction
Declination
Yaw Direction [°]
Distance [km]
Magnetic Forward Model

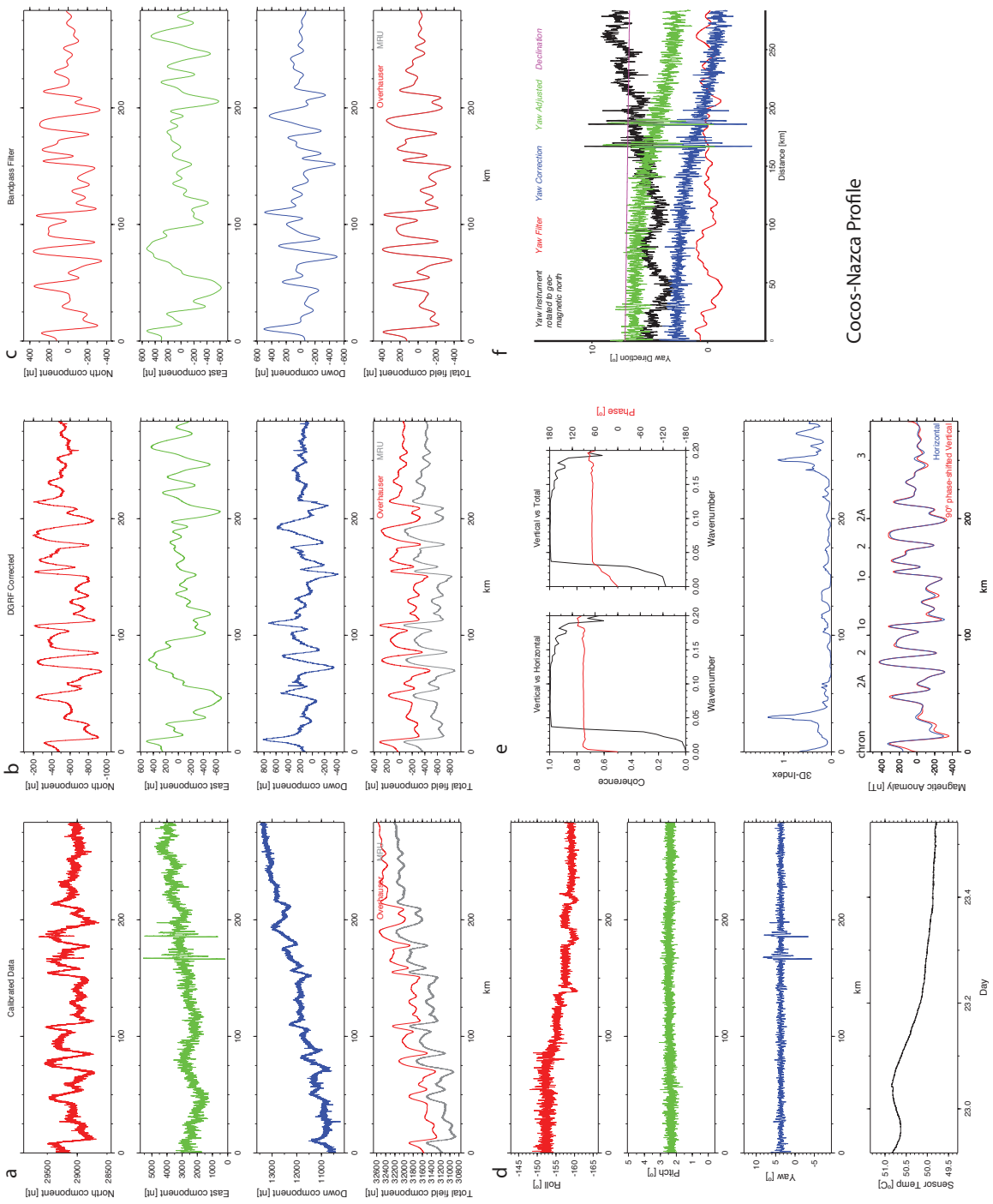

Figure 3A6: Data processing results for a CNR profile. Figure details same as in Figure 3A5 with in addition for (e) a 3-D index.

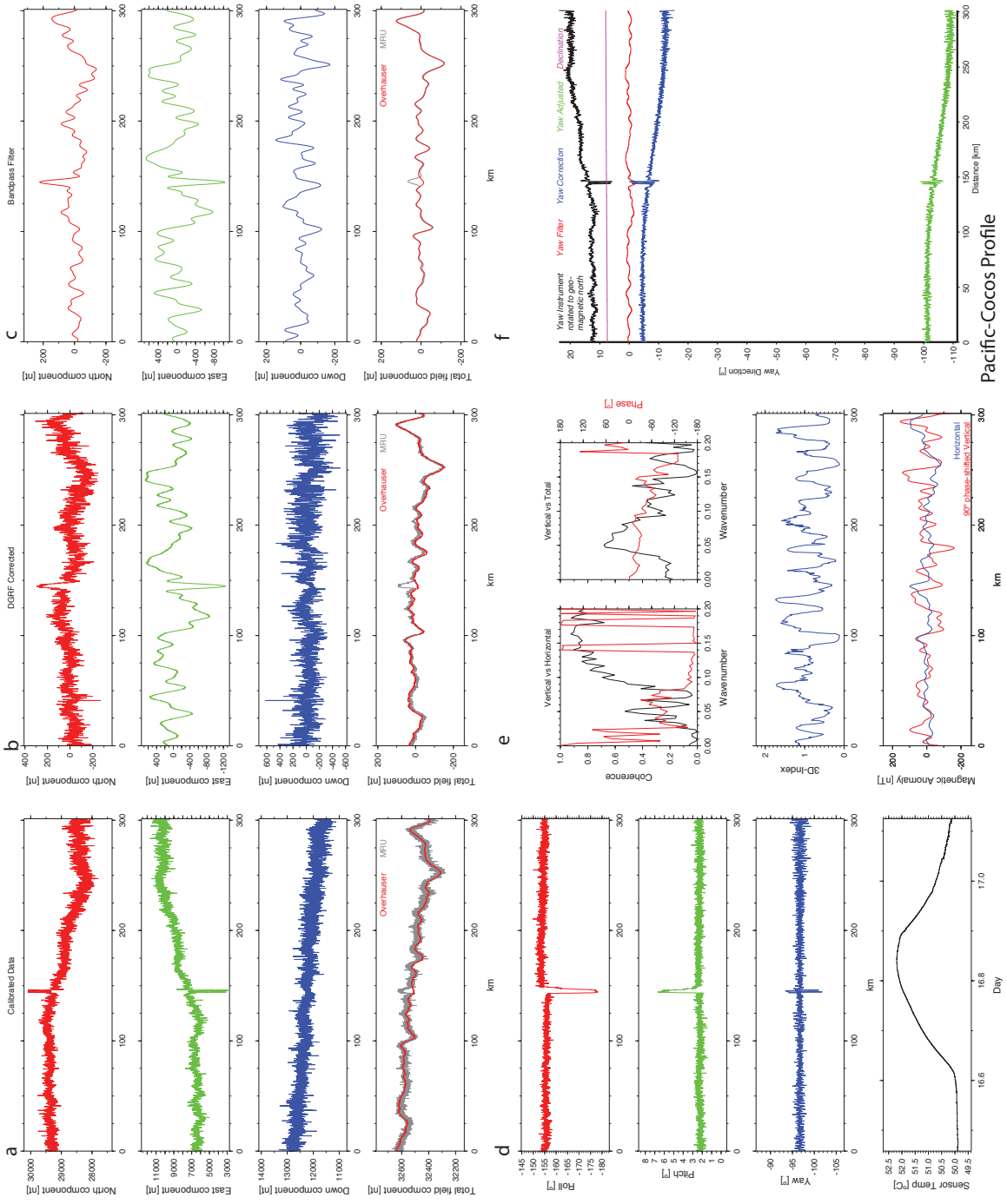

Figure 3A7: Data processing results for a PCR profile. Figure details same as in Figure 3A6.

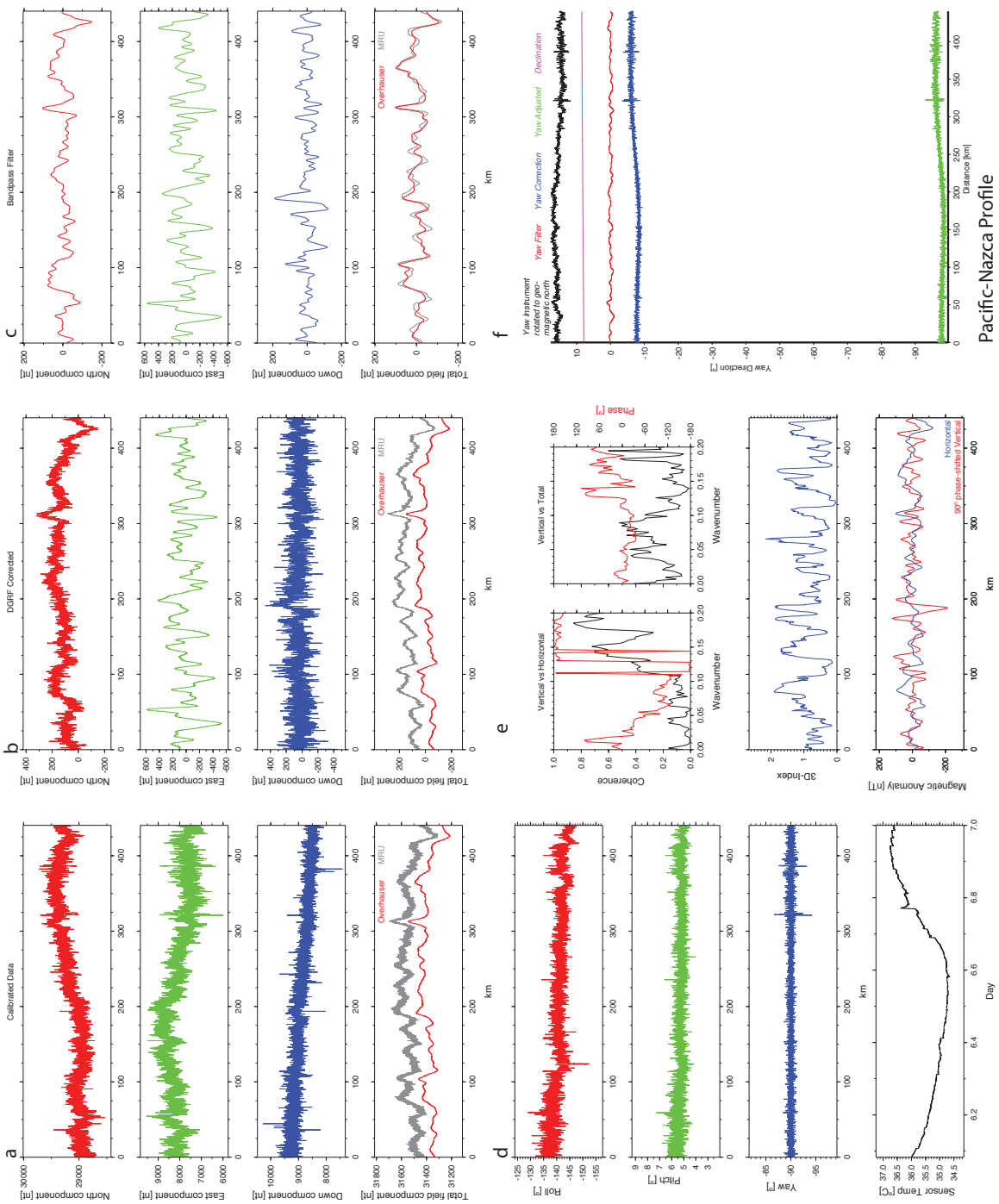

Figure 3A8: Data processing results for a PNR profile. Figure details same as in Figure 3A6.

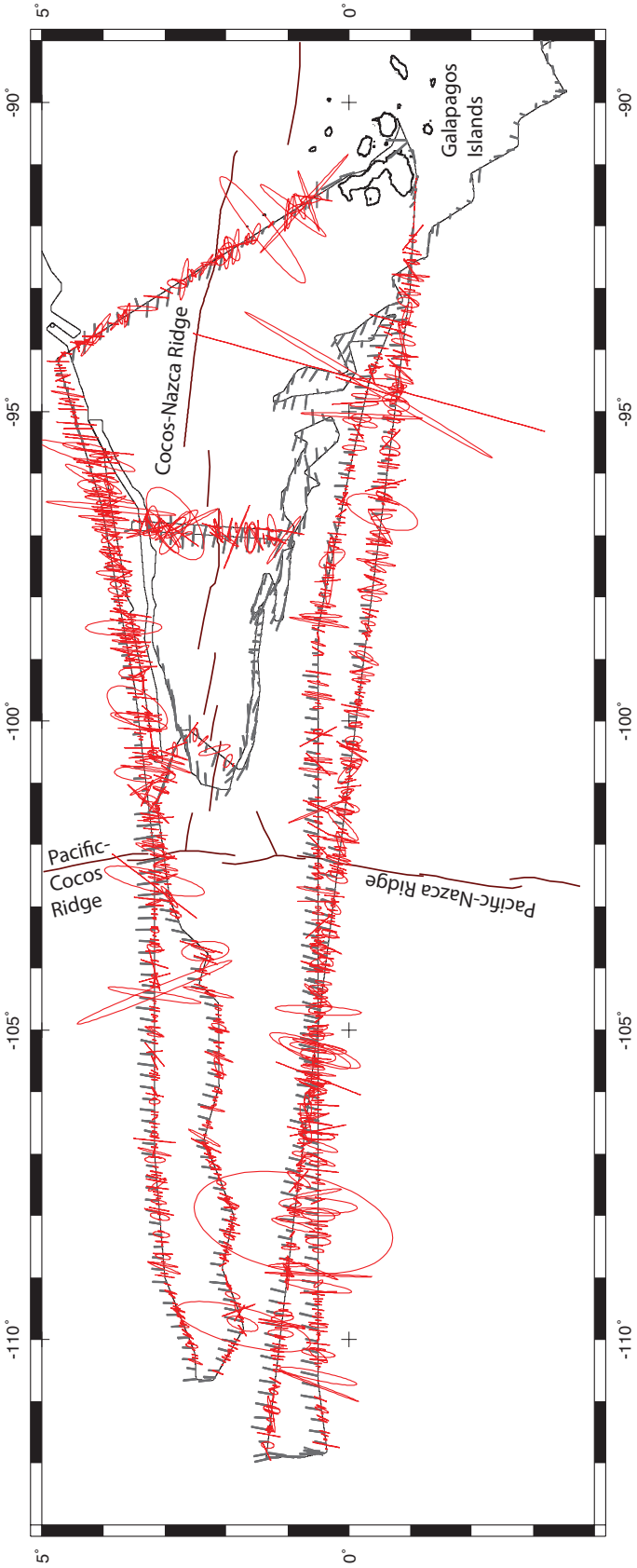

Figure 3A9: Magnetic boundary strike ellipses (red) calculated in the DANA05RR survey area. The magnetic contrast for calculating these ellipses is based on 2 km of data on either side of a point (20 data points at 200 m spacing). Abyssal hill lineation strikes based on the DANA05RR multibeam data in thick gray. Spreading ridges in dark red. Map is in a Mercator projection.

3.11 TABLES

Table 3.1a: Finite rotations and Covariance Matrices of the Antarctic Plate relative to the Nazca Plate for the 2-plate solutions [a].

Age (Ma)	Mag An.	Polarity Chron	Lat. (N)	Long. (E)	Angle (deg)	$\hat{\kappa}$	a	b	c	d	e	f	g	Mag Pts	FZ Pts	A.h Pts
0.78	1o	C1n (o)	33.261	-96.239	0.387	2.27	0.415	-0.327	-0.215	2.71	2.24	1.88	7	130	58	0
1.86	2	C2n (m)	39.419	-96.665	0.984	2.72	0.134	-0.140	-0.115	4.17	3.76	3.45	7	51	58	0
2.58	2Ay	C2An.1n (y)	34.063	-96.345	1.432	6.50	0.143	-0.357	-0.297	10.3	9.11	8.15	7	35	52	0
3.58	2Ao	C2An.3n (o)	43.524	-97.499	1.973	1.94	0.589	-1.06	-0.891	15.9	14.7	13.7	7	30	46	0
4.24	3y	C3n.1n (m)	47.595	-98.452	2.315	1.61	0.568	-0.851	-0.734	14.9	14.3	13.7	7	33	46	0
5.11	3o	C3n.4n (m)	46.749	-97.984	2.820	1.26	0.531	-0.491	-0.390	12.9	11.9	11.1	7	42	46	0
6.04	3Ay	C3An.1n (y)	47.518	-97.992	3.328	2.03	0.669	-0.481	-0.362	21.7	19.9	18.4	7	40	36	0
6.71	3Ao	C3An.2n (o)	50.384	-98.468	3.859	1.55	0.666	-0.210	-0.106	17.8	16.2	14.8	7	31	36	0
7.86	4	C4n.2n (m)	50.558	-98.474	4.885	3.48	0.672	-0.460	-0.358	29.9	26.9	24.4	7	28	36	0
8.86	4A	C4An (m)	56.160	-100.327	5.832	0.80	0.765	-0.350	-0.249	26.2	24.0	22.1	7	21	32	0

[a] Ages are from *Cande and Kent* [1995] except for chrons C3Ay and C3Ao, which are from *Krijgsman et al.* [1999]. Mag. An., magnetic anomaly; (y), (o) and (m), young and old ends and middle of Polarity Chron, respectively. Mag Pts, FZ Pts and A.h Pts, the number of magnetic anomaly, fracture zone, and abyssal hill points, respectively. Mag Segs and FZ Segs, the number of segments with magnetic anomaly and fracture zone data, respectively. The covariance matrix is given by the formula $\frac{1}{\hat{\kappa}} * \begin{pmatrix} a & b & c \\ b & d & e \\ c & e & f \end{pmatrix} * 10^{-g}$, where the values of a-f are given in radians squared. $\hat{\kappa}$ is a statistical parameter related to the error values. Errors are overestimated when $\hat{\kappa} \gg 1$, errors are underestimated when $\hat{\kappa} \ll 1$.

Table 3.1b: Finite rotations and Covariance Matrices of the Antarctic Plate relative to the Nazca Plate for the 3-plate Pacific-Nazca-Antarctic solutions. Table specific details can be found at footnote [a] for Table 3.1.

Age (Ma)	Mag An.	Polarity Chron	Lat. (N)	Long. (E)	Angle (deg)	$\hat{\kappa}$	a	b	c	d	e	f	g	Mag Pts	FZ Pts	A.h Pts
0.78	1o	C1n (o)	33.758	-95.871	0.387	1.79	2.80	-0.271	0.185	6.69	5.46	4.71	8	130	58	0
1.86	2	C2n (m)	42.630	-96.635	0.976	1.80	11.7	-1.63	-0.400	91.9	79.2	73.4	9	51	58	0
2.58	2Ay	C2An.1n (y)	40.502	-97.186	1.403	2.00	11.8	-0.706	1.10	176	148	133	9	35	52	0
3.58	2Ao	C2An.3n (o)	43.090	-96.786	1.978	1.76	35.4	0.83	6.62	140	118	110	9	30	46	0
4.24	3y	C3n.1n (m)	42.871	-96.925	2.319	1.41	35.8	0.24	5.12	116	101	96.2	9	33	46	0
5.11	3o	C3n.4n (m)	48.313	-98.308	2.821	1.30	5.18	-2.11	-1.28	32.5	28.8	26.2	8	42	46	0
6.04	3Ay	C3An.1n (y)	50.504	-98.522	3.334	0.39	6.67	-2.91	-1.86	40.2	35.3	31.9	8	40	36	0
6.71	3Ao	C3An.2n (o)	50.290	-98.550	3.859	1.25	7.14	-5.49	-4.00	44.5	38.3	33.9	8	31	36	0
7.86	4	C4n.2n (m)	50.276	-98.392	4.884	1.60	0.825	-1.27	-1.05	9.92	8.63	7.62	7	28	36	0
8.86	4A	C4An (m)	52.184	-99.037	5.779	0.79	0.856	-0.652	-0.502	4.12	3.47	3.03	7	21	32	0

Table 3.2a:
Finite rotations and Covariance Matrices of the Pacific Plate relative to the Nazca Plate for the 2-plate solutions. Table specific details can be found at footnote [a] for Table 3.1.

Age (Ma)	Mag An.	Polarity Chron	Lat. (N)	Long. (E)	Angle (deg)	$\hat{\kappa}$	a	b	c	d	e	f	g	Mag Pts	FZ Pts	A.h Pts
0.78	1o	C1n (o)	51.849	-89.780	1.049	1.14	12.6	8.87	1.92	27.6	7.99	3.09	8	84	10	6
1.86	2	C2n (m)	56.917	-87.492	2.533	3.55	12.7	9.67	1.66	32.3	7.65	2.94	8	89	10	6
2.58	2Ay	C2An.1n (y)	58.011	-87.769	3.542	1.60	4.49	7.98	2.83	18.4	6.56	2.55	7	71	10	0
3.58	2Ao	C2An.3n (o)	55.722	-90.606	5.027	2.91	4.62	7.71	3.05	17.1	6.66	2.84	7	69	10	0
4.24	3y	C3n.1n (m)	55.137	-91.270	5.962	1.37	4.26	7.02	2.62	15.9	5.84	2.39	7	55	10	0
5.11	3o	C3n.4n (m)	52.999	-81.159	7.388	0.56	7.63	-9.85	-4.25	14.1	6.11	2.64	5	32	0	0
6.04	3Ay	C3An.1n (y)	55.107	-78.934	8.566	0.10	9.30	-9.61	-4.88	11.1	5.60	2.82	5	39	0	0
6.71	3Ao	C3An.2n (o)	60.088	-93.424	9.552	0.76	2.87	-2.13	-0.903	10.7	5.02	2.40	6	29	0	0
7.86	4	C4n.2n (m)	65.624	-99.355	11.478	1.01	2.10	-2.99	-1.17	4.49	1.78	0.709	4	32	0	0
8.86	4A	C4An (m)	60.129	-89.903	13.266	0.46	7.23	-1.77	-0.791	26.0	11.6	5.22	6	36	0	0

Table 3.2b: Finite rotations and Covariance Matrices of the Pacific Plate relative to the Nazca Plate for the 3-plate Pacific-Nazca-Antarctic solutions. Table specific details can be found at footnote [a] for Table 3.1.

Age (Ma)	Mag An.	Polarity Chron	Lat. (N)	Long. (E)	Angle (deg)	$\hat{\kappa}$	a	b	c	d	e	f	g	Mag Pts	FZ Pts	A.h Pts
0.78	1o	C1n (o)	53.880	-88.596	1.033	1.83	2.88	-1.07	-0.333	5.95	2.50	1.63	8	84	10	6
1.86	2	C2n (m)	56.494	-88.945	2.539	3.33	2.38	-0.697	-0.154	6.21	2.57	1.88	8	89	10	6
2.58	2Ay	C2An.1n (y)	56.366	-89.692	3.559	2.00	25.7	-7.42	-0.121	132	70.8	53.0	9	71	10	0
3.58	2Ao	C2An.3n (o)	57.484	-89.814	4.986	1.76	3.74	0.398	0.922	11.9	7.37	6.04	8	69	10	0
4.24	3y	C3n.1n (m)	57.933	-89.801	5.888	1.41	3.78	-0.484	0.244	9.90	6.43	5.49	8	55	10	0
5.11	3o	C3n.4n (m)	60.201	-90.309	7.193	1.30	7.06	-6.03	-2.89	29.5	19.7	15.4	8	32	0	0
6.04	3Ay	C3An.1n (y)	61.125	-90.534	8.441	0.39	1.03	-0.747	-0.411	3.30	2.26	1.74	7	39	0	0
6.71	3Ao	C3An.2n (o)	61.011	-90.994	9.540	1.25	7.13	-0.251	1.37	41.7	28.4	22.0	8	29	0	0
7.86	4	C4n.2n (m)	61.217	-91.313	11.539	1.60	0.892	0.688	0.827	9.45	7.07	5.93	7	32	0	0
8.86	4A	C4An (m)	62.224	-91.741	13.232	0.79	0.823	0.145	0.242	3.84	2.67	2.11	7	36	0	0

Table 3.2c: Finite rotations and Covariance Matrices of the Pacific Plate relative to the Nazca Plate for the 3-plate Pacific-Cocos-Nazca solutions. Table specific details can be found at footnote [a] for Table 3.1.

Age (Ma)	Mag An.	Polarity Chron	Lat. (N)	Long. (E)	Angle (deg)	$\hat{\kappa}$	a	b	c	d	e	f	g	Mag Pts	FZ Pts	A.h Pts
0.78	1o	C1n (o)	55.329	-86.045	1.030	2.27	3.35	2.10	0.351	9.82	2.48	1.24	8	96	10	6
1.86	2	C2n (m)	56.288	-87.271	2.527	1.57	29.7	16.0	0.876	123	26.0	13.9	9	104	10	6
2.58	2Ay	C2An.1n (y)	55.132	-88.488	3.586	1.26	5.44	6.13	1.18	21.9	4.96	2.79	8	71	10	0
3.58	2Ao	C2An.3n (o)	56.219	-89.156	5.017	2.66	1.11	1.52	0.486	4.33	1.33	0.620	7	69	10	0
4.24	3y	C3n.1n (m)	55.836	-89.667	5.946	0.86	8.54	11.9	3.30	36.4	9.94	4.65	8	55	10	0

Table 3.3a: Finite rotations and Covariance Matrices of the Cocos Plate relative to the Nazca Plate for the 2-plate solutions. Table specific details can be found at footnote [a] for Table 3.1.

Age (Ma)	Mag An.	Polarity Chron	Lat. (N)	Long. (E)	Angle (deg)	$\hat{\kappa}$	a	b	c	d	e	f	g	Mag Pts	FZ Pts	A.h Pts
0.78	1o	C1n (o)	3.050	-142.212	0.515	3.59	2.12	7.51	0.947	243	3.71	24.5	9	237	30	0
1.86	2	C2n (m)	5.497	-132.444	1.440	3.26	0.417	0.277	0.101	52.7	0.103	3.00	8	112	28	0
2.58	2Ay	C2An.1n (y)	4.109	-125.977	2.257	1.63	0.262	1.07	0.110	31.5	1.28	3.61	8	208	20	0
3.58	2Ao	C2An.3n (o)	4.474	-122.961	3.307	4.57	0.391	0.103	0.211	45.5	0.277	7.79	8	133	10	0
4.24	3y	C3n.1n (m)	4.582	-120.927	4.021	1.17	0.515	-1.03	0.673	60.1	-1.32	8.01	8	117	10	0
5.11	3o	C3n.4n (m)	5.229	-116.671	5.276	2.37	1.12	-2.10	5.19	91.9	13.3	59.1	8	95	0	0
6.04	3Ay	C3An.1n (y)	3.851	-113.812	6.434	1.39	1.00	-1.21	4.62	55.4	3.09	35.7	8	136	0	0
6.71	3Ao	C3An.2n (o)	3.976	-112.294	7.587	2.59	0.497	-1.46	2.31	12.5	-5.52	12.7	7	90	0	0
7.86	4	C4n.2n (m)	4.354	-109.934	10.114	0.80	0.107	0.156	0.576	11.9	1.60	7.69	7	79	0	0
8.86	4A	C4An (m)	3.705	-109.579	11.310	1.02	0.106	-0.287	0.107	17.4	0.190	6.62	7	54	0	0

Table 3.3b: Finite rotations and Covariance Matrices of the Cocos Plate relative to the Nazca Plate for the 3-plate Pacific-Cocos-Nazca solutions. Table specific details can be found at footnote [a] for Table 3.1.

Age (Ma)	Mag An.	Polarity Chron	Lat. (N)	Long. (E)	Angle (deg)	$\hat{\kappa}$	a	b	c	d	e	f	g	Mag Pts	FZ Pts	A.h Pts
0.78	1o	C1n (o)	4.796	-141.310	0.522	2.27	2.05	5.91	0.397	187	-6.474	19.0	9	237	30	0
1.86	2	C2n (m)	4.763	-126.821	1.622	1.57	4.00	2.78	0.102	296	-12.5	20.3	9	112	28	0
2.58	2Ay	C2An.1n (y)	3.988	-124.729	2.330	1.26	2.52	8.99	-0.264	264	0.903	32.9	9	208	20	0
3.58	2Ao	C2An.3n (o)	4.352	-122.406	3.353	2.66	3.77	1.31	-0.950	400	-21.5	67.9	9	133	10	0
4.24	3y	C3n.1n (m)	4.625	-120.067	4.115	0.86	0.444	-0.675	0.235	48.5	-3.97	7.05	8	117	10	0

Table 3.4a: Finite rotations and Covariance Matrices of the Pacific Plate relative to the Mathematician Plate for the 2-plate solutions. Table specific details can be found at footnote [a] for Table 3.1.

Age (Ma)	Mag An.	Polarity Chron	Lat. (N)	Long. (E)	Angle (deg)	$\hat{\kappa}$	a	b	c	d	e	f	g	Mag Pts	FZ Pts	A.h Pts
3.58	2Ao	C2An.3n (o)	16.263	-110.283	6.424	3.74	6.62	17.1	-5.89	44.4	-15.3	5.25	5	22	19	0
4.24	3y	C3n.1n (m)	12.455	-108.077	3.845	13.20	2.37	6.16	-2.09	16.0	-5.42	1.83	4	15	20	0
5.11	3o	C3n.4n (m)	11.850	-109.422	8.572	12.10	3.83	9.64	-3.36	24.4	-8.47	2.95	5	26	15	0
6.04	3Ay	C3An.1n (y)	9.905	-109.022	9.732	5.60	12.5	30.8	-11.1	76.5	-27.5	9.87	5	18	9	0
6.71	3Ao	C3An.2n (o)	10.966	-109.872	14.121	2.25	1.06	3.04	-1.07	9.18	-3.22	1.13	4	20	0	0
7.86	4	C4n.2n (m)	7.408	-110.550	13.607	2.57	1.43	-2.31	0.436	10.1	-2.60	0.696	3	12	0	0
8.86	4A	C4An (m)	0.817	-114.454	10.922	3.47	1.21	3.73	-1.31	15.7	-5.30	1.80	4	17	0	0

Table 3.4b: Finite rotations and Covariance Matrices of the Pacific Plate relative to the Mathematician Plate for the 3-plate Pacific-Mathematician-Cocos solutions. Table specific details can be found at footnote [a] for Table 3.1.

(Ma)	Mag An.	Polarity Chron	Lat. (N)	Long. (E)	Angle (deg)	$\hat{\kappa}$	a	b	c	d	e	f	g	Mag Pts	FZ Pts	A.h Pts
3.58	2Ao	C2An.3n (o)	11.415	-107.478	1.588	2.16	0.803	2.18	-0.675	6.40	-1.93	0.630	7	22	19	0
4.24	3y	C3n.1n (m)	11.032	-107.166	2.938	1.33	1.45	4.21	-1.21	13.2	-3.67	1.11	7	15	20	0
5.11	3o	C3n.4n (m)	9.760	-108.411	6.280	0.66	1.57	4.02	-1.26	11.1	-3.39	1.10	7	26	15	0
6.04	3Ay	C3An.1n (y)	9.930	-106.882	10.160	1.18	1.59	4.98	-1.22	17.2	-4.11	1.12	7	18	9	0
6.71	3Ao	C3An.2n (o)	10.691	-107.203	14.240	0.32	1.80	5.74	-1.88	20.8	-6.55	2.15	7	20	0	0
7.86	4	C4n.2n (m)	10.362	-109.617	18.687	1.25	3.97	11.1	-3.72	32.2	-10.7	3.64	7	12	0	0
8.86	4A	C4An (m)	11.250	-109.519	27.396	0.45	3.77	9.92	-3.34	26.9	-9.02	3.10	7	17	0	0

Table 3.4c: Finite rotations and Covariance Matrices of the Pacific Plate relative to the Cocos Plate for the 2-plate solutions. Table specific details can be found at footnote [a] for Table 3.1.

Age (Ma)	Mag An.	Polarity Chron	Lat. (N)	Long. (E)	Angle (deg)	$\hat{\kappa}$	a	b	c	d	e	f	g	Mag Pts	FZ Pts	A.h Pts
0.78	1o	C1n (o)	38.262	-110.199	1.531	4.07	1.21	3.57	-0.790	14.2	-3.17	0.791	7	116	30	7
1.86	2	C2n (m)	36.196	-108.478	3.931	2.55	0.691	1.84	-0.401	7.37	-1.61	0.400	7	100	20	4
2.58	2Ay	C2An.1n (y)	33.948	-107.529	5.938	2.35	3.18	10.1	-2.40	37.7	-8.98	2.33	7	59	20	4
3.58	2Ao	C2An.3n (o)	34.694	-107.432	8.009	2.56	2.72	9.68	-1.13	35.8	-4.20	0.545	6	29	10	6
4.24	3y	C3n.1n (m)	32.775	-106.831	10.171	0.79	1.91	6.72	-0.932	24.2	-3.36	0.486	6	30	10	2
5.11	3o	C3n.4n (m)	33.177	-106.735	12.110	4.35	5.39	17.7	-2.18	62.7	-7.60	1.04	6	30	10	5
6.04	3Ay	C3An.1n (y)	29.314	-106.232	16.982	7.00	2.67	8.83	-1.50	29.2	-4.94	0.841	4	15	10	2
6.71	3Ao	C3An.2n (o)	28.059	-106.093	20.315	3.26	5.36	17.3	-3.00	56.2	-9.73	1.69	4	10	10	2
7.86	4	C4n.2n (m)	30.485	-104.708	22.390	7.73	4.23	13.0	-2.20	39.9	-6.77	1.15	4	9	10	2
8.86	4A	C4An (m)	31.000	-105.005	24.542	11.36	1.35	4.07	-0.691	12.3	-2.09	0.363	4	7	10	2

Table 3.4d: Finite rotations and Covariance Matrices of the Mathematician Plate relative to the Cocos Plate for the 2-plate solutions. Table specific details can be found at footnote [a] for Table 3.1.

Age (Ma)	Mag An.	Polarity Chron	Lat. (N)	Long. (E)	Angle (deg)	$\hat{\kappa}$	a	b	c	d	e	f	g	Mag Pts	FZ Pts	A.h Pts
3.58	2Ao	C2An.3n (o)	30.269	-106.710	9.796	6.24	1.26	4.21	-1.04	15.25	-3.76	0.97	6	30	10	0
4.24	3y	C3n.1n (m)	29.686	-106.655	11.893	2.99	5.34	17.95	-3.92	61.44	-13.43	2.97	6	29	10	0
5.11	3o	C3n.4n (m)	29.121	-106.182	14.660	2.59	5.26	17.29	-3.86	57.82	-12.93	2.94	6	26	10	0
6.04	3Ay	C3An.1n (y)	26.576	-105.869	19.979	1.25	6.57	21.39	-4.76	70.73	-15.77	3.55	6	28	10	0
6.71	3Ao	C3An.2n (o)	25.735	-105.791	23.922	1.38	1.22	3.93	-0.86	12.76	-2.80	0.62	5	26	10	0
7.86	4	C4n.2n (m)	23.529	-105.414	33.635	1.57	1.74	5.39	-1.26	16.81	-3.94	0.93	5	29	10	0
8.86	4A	C4An (m)	22.179	-105.357	43.970	0.95	2.20	6.61	-1.67	19.95	-5.05	1.28	5	22	10	0

Table 3.4e: Finite rotations and Covariance Matrices of the Pacific Plate relative to the Cocos Plate for the 3-plate Pacific-Cocos-Nazca solutions. Table specific details can be found at footnote [a] for Table 3.1.

Age (Ma)	Mag An.	Polarity Chron	Lat. (N)	Long. (E)	Angle (deg)	$\hat{\kappa}$	a	b	c	d	e	f	g	Mag Pts	FZ Pts	A.h Pts
0.78	1o	C1n (o)	42.379	-112.086	1.324	2.27	3.35	3.98	-0.555	17.4	-2.78	1.15	8	116	30	7
1.86	2	C2n (m)	38.460	-109.042	3.616	1.57	2.93	4.75	-0.899	21.9	-4.22	1.25	8	100	20	4
2.58	2Ay	C2An.1n (y)	37.084	-108.533	5.189	1.26	5.35	7.11	-0.782	27.3	-3.79	2.02	8	59	20	4
3.58	2Ao	C2An.3n (o)	37.402	-108.416	7.358	2.66	11.0	19.5	0.607	73.6	-0.672	3.92	8	29	10	6
4.24	3y	C3n.1n (m)	36.654	-107.758	8.897	0.86	5.56	12.8	-0.933	75.4	-7.40	2.66	8	30	10	2

Table 3.5: Finite rotations and Covariance Matrices of the Pacific Plate relative to the Antarctic Plate for the 3-plate Pacific-Nazca-Antarctic solutions. Table specific details can be found at footnote [a] for Table 3.1.

Age (Ma)	Mag. An.	Polarity Chron	Lat. (N)	Long. (E)	Angle (deg)	$\hat{\kappa}$	a	b	c	d	e	f	g	Mag Pts	FZ Pts	A.h Pts
0.78	1o	C1n (o)	64.708	-80.373	0.685	1.79	7.57	-0.494	6.38	3.85	5.03	21.8	9	43	45	23
1.86	2	C2n (m)	64.619	-80.338	1.605	1.80	1.77	-0.347	0.332	1.96	2.34	4.63	8	34	32	14
2.58	2Ay	C2An.1n (y)	65.602	-80.358	2.250	2.00	1.91	-0.339	0.408	2.10	2.74	6.02	8	32	31	10
3.58	2Ao	C2An.3n (o)	65.999	-80.918	3.119	1.76	8.74	0.124	8.91	8.02	11.8	35.3	9	31	34	15
4.24	3y	C3n.1n (m)	66.668	-80.360	3.708	1.41	8.76	0.321	7.86	7.44	10.6	30.0	9	29	35	8
5.11	3o	C3n.4n (m)	66.939	-80.603	4.484	1.30	11.5	0.851	14.7	6.94	12.7	51.7	9	30	39	12
6.04	3Ay	C3An.1n (y)	67.160	-80.929	5.216	0.39	2.69	2.20	3.39	3.43	4.11	7.60	8	28	39	6
6.71	3Ao	C3An.2n (o)	67.347	-81.184	5.810	1.25	1.22	0.183	1.87	0.789	1.38	5.71	8	26	41	7
7.86	4	C4n.2n (m)	68.150	-80.564	6.827	1.60	2.20	0.866	3.92	1.46	2.43	10.5	8	30	41	9
8.86	4A	C4An (m)	68.795	-80.030	7.631	0.79	1.09	0.312	1.58	0.949	1.49	4.73	8	29	44	11

3.14 REFERENCES

Atwater, T. (1970), Implications of plate tectonics for the Cenozoic tectonic evolution of western North America, *GSA Bulletin*, *81*(12), 3513-3535.

Barckhausen, U., C. R. Ranero, S. C. Cande, M. Engels, and W. Weinrebe (2008), Birth of an intraoceanic spreading center, *Geology, 36*(10), 767-770, DOI: 10.1130/G25056a.1.

Bird, R. T., and D. F. Naar (1994), Intratransform Origins of Midocean Ridge Microplates, *Geology*, *22*(11), 987-990.

Bird, R. T., D. F. Naar, R. L. Larson, R. C. Searle, and C. R. Scotese (1998), Plate tectonic reconstructions of the Juan Fernandez microplate: Transformation from internal shear to rigid rotation, *Journal of Geophysical Research-Solid Earth*, *103*(B4), 7049-7067.

Blakely, R. J. (1995), *Potential Theory in Gravity & Magnetic Applications*, Cambridge University Press.

Cande, S. C., and D. V. Kent (1995), Revised calibration of the geomagnetic polarity timescale for the Late Cretaceous and Cenozoic, *Journal of Geophysical Research-Solid Earth, 100*(B4), 6093-6095, DOI: 10.1029/94JB03098.

Chang, T. (1987), On the statistical properties of estimated rotations, *Journal of Geophysical Research-Solid Earth and Planets*, *92*(B7), 6319-6329.

Chang, T. (1988), Estimating the Relative Rotations of Two Tectonic Plates from Boundary Crossings, *Journal of the American Statistical Association*, *83*(404), 1178-1183.

Croon, M. B., S. C. Cande, and J. M. Stock (2008), Revised Pacific-Antarctic plate motions and geophysics of the Menard Fracture Zone, *Geochemistry Geophysics Geosystems, 9*, Q07001, DOI: 10.1029/2008gc002019.

Croon, M. B., S. C. Cande, and J. M. Stock (2010), Abyssal hill deflections at Pacific-Antarctic ridge-transform intersections, *Geochemistry Geophysics Geosystems, 11*, Q11004, DOI: 10.1029/2010gc003236.

DeMets, C., R. G. Gordon, D. F. Argus, and S. Stein (1990), Current plate motions, *Geophysical journal international*, *101*(2), 425-478.

DeMets, C., R. G. Gordon, and D. F. Argus (2010), Geologically current plate motions, *Geophysical Journal International, 181*(1), 1-80, DOI: 10.1111/J.1365-246x.2009.04491.X.

Eakins, B. W., and P. F. Lonsdale (2003), Structural patterns and tectonic history of the Bauer microplate, Eastern Tropical Pacific, *Marine Geophysical Researches, 24*(3-4), 171-205, DOI: 10.1007/S11001-004-5882-4.

Engels, M., U. Barckhausen, and J. S. Gee (2008), A new towed marine vector magnetometer: methods and results from a Central Pacific cruise, *Geophysical Journal International, 172*(1), 115-129, DOI: 10.1111/J.1365-246x.2007.03601.X.

Fornari, D. J., D. G. Gallo, M. H. Edwards, J. A. Madsen, M. R. Perfit, and A. N. Shor (1989), Structure and Topography of the Siqueiros Transform-Fault System - Evidence for the Development of Intra-Transform Spreading Centers, *Marine Geophysical Researches, 11*(4), 263-299, DOI: 10.1007/BF00282579.

Gee, J. S., and S. C. Cande (2002), A surface-towed vector magnetometer, *Geophysical Research Letters, 29*(14), Artn 1670, DOI: 10.1029/2002gl015245.

Hellinger, S. J. (1981), The uncertainties of finite rotations in plate tectonics, *Journal of Geophysical Research*, *86*(NB10), 9312-9318.

Hey, R. (1977), Tectonic Evolution of Cocos-Nazca Spreading Center, *Geological Society of America Bulletin, 88*(10), 1404-1420, DOI: 10.1130/0016-7606(1977)88<1404:TEOTCS>2.0.CO;2.

Horner-Johnson, B. C., and R. G. Gordon (2003), Equatorial Pacific magnetic anomalies identified from vector aeromagnetic data, *Geophysical Journal International*, *155*(2), 547-556.

Kirkwood, B. H., J. Y. Royer, T. C. Chang, and R. G. Gordon (1999), Statistical tools for estimating and combining finite rotations and their uncertainties, *Geophysical Journal International, 137*(2), 408-428, DOI: 10.1046/j.1365-246X.1999.00787.x.

Klitgord, K. D., and J. Mammerickx (1982), Northern East Pacific Rise - Magnetic Anomaly and Bathymetric Framework, *Journal of Geophysical Research, 87*(Nb8), 6725-6750, DOI: 10.1029/JB087iB08p06725.

Korenaga, J. (1995), Comprehensive Analysis of Marine Magnetic Vector Anomalies, *Journal of Geophysical Research-Solid Earth*, *100*(B1), 365-378.

Krijgsman, W., F. J. Hilgen, I. Raffi, F. J. Sierro, and D. S. Wilson (1999), Chronology, causes and progression of the Messinian salinity crisis, *Nature, 400*(6745), 652-655, DOI: 10.1038/23231.

Liu, Z. J. (1996), The Origin and Evolution of the Easter Seamount Chain, 266 pp, Ph.D. Thesis, University of South Florida.

Lonsdale, P. (1989), Segmentation of the Pacific-Nazca spreading center, 1°N-20°S, *Journal of Geophysical Research-Solid Earth and Planets, 94*(B9), 12197-12225, DOI: 10.1029/JB094iB09p12197.

Lonsdale, P. (1995), Segmentation and Disruption of the East Pacific Rise in the Mouth of the Gulf of California, *Marine Geophysical Researches, 17*(4), 323-359, DOI: 10.1007/BF01227039.

Lonsdale, P. (2005), Creation of the Cocos and Nazca plates by fission of the Farallon plate, *Tectonophysics, 404*(3-4), 237-264, DOI: 10.1016/J.Tecto.2005.05.011.

Macdonald, K., J. C. Sempéré, and P. J. Fox (1984), East Pacific Rise From Siqueiros to Orozco Fracture Zones: Along-Strike Continuity of Axial Neovolcanic Zone and Structure and Evolution of Overlapping Spreading Centers, *Journal of Geophysical Research, 89*(Nb7), 6049-6069, DOI: 10.1029/JB089iB07p06049.

Madsen, J. A., P. J. Fox, and K. C. Macdonald (1986), Morphotectonic Fabric of the Orozco Transform-Fault - Results from a Sea Beam Investigation, *Journal of Geophysical Research-Solid Earth and Planets, 91*(B3), 3439-3454, DOI: 10.1029/JB091iB03p03439.

Madsen, J. A., D. J. Fornari, M. H. Edwards, D. G. Gallo, and M. R. Perfit (1992), Kinematic Framework of the Cocos-Pacific Plate Boundary from 13°N to the Orozco Transform-Fault: Results from an Extensive Magnetic and Seamarc II Survey, *Journal of Geophysical Research-Solid Earth, 97*(B5), 7011-7024, DOI: 10.1029/91JB01755.

Mammerickx, J., and K. D. Klitgord (1982), Northern East Pacific Rise - Evolution from 25 My Bp to the Present, *Journal of Geophysical Research, 87*(Nb8), 6751-6759, DOI: 10.1029/JB087iB08p06751.

Mammerickx, J., D. F. Naar, and R. L. Tyce (1988), The Mathematician Paleoplate, *Journal of Geophysical Research-Solid Earth and Planets, 93*(B4), 3025-3040, DOI: 10.1016/j.tecto.2006.06.002.

Manea, M., V. C. Manea, L. Ferrari, V. Kostoglodov, and W. L. Bandy (2005), Tectonic evolution of the Tehuantepec Ridge, *Earth and Planetary Science Letters, 238*(1-2), 64-77, DOI: 10.1016/J.Epsi.2005.06.060.

McKenzie, D. P., and W. J. Morgan (1969), Evolution of Triple Junctions, *Nature, 224*(5215), 125-133, DOI: 10.1038/224125a0.

Menard, H. W. (1978), Fragmentation of Farallon Plate by Pivoting Subduction, *Journal of Geology*, *86*(1), 99-110.

Merayo, J. M. G., P. Brauer, F. Primdahl, J. R. Petersen, and O. V. Nielsen (2000), Scalar calibration of vector magnetometers, *Meas Sci Technol, 11*(2), 120-132, DOI: 10.1088/0957-0233/11/2/304.

Naar, D. F., and R. N. Hey (1991), Tectonic Evolution of the Easter Microplate, *Journal of Geophysical Research-Solid Earth and Planets, 96*(B5), 7961-7993, DOI: 10.1029/90JB02398.

O'Brien, M. S., R. L. Parker, and C. G. Constable (1999), Magnetic power spectrum of the ocean crust on large scales, *Journal of Geophysical Research-Solid Earth*, *104*(B12), 29189-29201.

Okal, E. A., and A. Cazenave (1985), A Model for the Plate Tectonic Evolution of the East-Central Pacific Based on Seasat Investigations, *Earth and Planetary Science Letters, 72*(1), 99-116, DOI: 10.1016/0012-821X(85)90120-7.

Olsen, N., L. Toffner-Clausen, T. J. Sabaka, P. Brauer, J. M. G. Merayo, J. L. Jorgensen, J. M. Leger, O. V. Nielsen, F. Primdahl, and T. Risbo (2003), Calibration of the Ørsted vector magnetometer, *Earth Planets Space*, *55*(1), 11-18.

Pockalny, R. A. (1997), Evidence of transpression along the Clipperton Transform: Implications for processes of plate boundary reorganization, *Earth and Planetary Science Letters, 146*(3-4), 449-464, DOI: 10.1016/S0012-821X(96)00253-1.

Pockalny, R. A., P. J. Fox, D. J. Fornari, K. C. Macdonald, and M. R. Perfit (1997), Tectonic reconstruction of the Clipperton and Siqueiros Fracture Zones: Evidence and consequences of plate motion change for the last 3 Myr, *Journal of Geophysical Research-Solid Earth*, *102*(B2), 3167-3181.

Royer, J. Y., and T. Chang (1991), Evidence for relative motions between the Indian and Australian Plates during the last 20 m.y. From plate tectonic reconstructions: Implication for the deformation of the Indo-Australian plate, *Journal of Geophysical Research-Solid Earth and Planets*, *96*(B7), 11779-11802.

Rusby, R. I., and R. C. Searle (1995), A History of the Easter Microplate, 5.25-Ma to Present, *Journal of Geophysical Research-Solid Earth, 100*(B7), 12617-12640, DOI: 10.1029/94JB02779.

Sandwell, D. T., and W. H. F. Smith (2009), Global marine gravity from retracked Geosat and ERS-1 altimetry: Ridge segmentation versus spreading rate, *Journal of Geophysical Research-Solid Earth, 114*, B01411, DOI: 10.1029/2008jb006008.

Schilt, F. S., D. E. Karig, and M. Truchan (1982), Kinematic Evolution of the Northern Cocos Plate, *Journal of Geophysical Research, 87*(Nb4), 2958-2968, DOI: 10.1029/JB087iB04p02958.

Schouten, H., and S. C. Cande (1976), Paleomagnetic Poles from Marine Magnetic-Anomalies, *Geophysical Journal of the Royal Astronomical Society*, *44*(3), 567-575.

Schouten, H., K. D. Klitgord, and D. G. Gallo (1993), Edge-Driven Microplate Kinematics, *Journal of Geophysical Research-Solid Earth*, *98*(B4), 6689-6701.

Seama, N., Y. Nogi, and N. Isezaki (1993), A New Method for Precise Determination of the Position and Strike of Magnetic Boundaries Using Vector Data of the Geomagnetic Anomaly Field, *Geophysical Journal International*, *113*(1), 155-164.

Searle, R. C., R. T. Bird, R. I. Rusby, and D. F. Naar (1993), The development of 2 oceanic microplates - Easter and Juan-Fernandez microplates, East Pacific Rise, *Journal of the Geological Society, 150*, 965-976, DOI: 10.1144/gsjgs.150.5.0965.

Searle, R. C., J. Francheteau, and B. Cornaglia (1995), New Observations on Mid-Plate Volcanism and the Tectonic History of the Pacific Plate, Tahiti to Easter Microplate, *Earth and Planetary Science Letters, 131*(3-4), 395-421, DOI: 10.1016/0012-821X(95)00018-8.

Sonder, L. J., and R. A. Pockalny (1999), Anomalously rotated abyssal hills along active transforms: Distributed deformation of oceanic lithosphere, *Geology, 27*(11), 1003-1006.

Tebbens, S. F., and S. C. Cande (1997), Southeast Pacific tectonic evolution from early Oligocene to present, *Journal of Geophysical Research-Solid Earth, 102*(B6), 12061-12084, DOI: 10.1029/96JB02582.

Tebbens, S. F., S. C. Cande, L. Kovacs, J. C. Parra, J. L. LaBrecque, and H. Vergara (1997), The Chile ridge: A tectonic framework, *Journal of Geophysical Research-Solid Earth, 102*(B6), 12035-12059, DOI: 10.1029/96JB02581.

Tucholke, B. E., and H. Schouten (1988), Kane Fracture Zone, *Marine Geophysical Researches, 10*(1-2), 1-39, DOI: 10.1007/BF02424659.

Wessel, P., and L. W. Kroenke (2008), Pacific absolute plate motion since 145 Ma: An assessment of the fixed hot spot hypothesis, *Journal of Geophysical Research-Solid Earth, 113*(B6), Artn B06101, DOI: 10.1029/2007jb005499.

Wilder, D. T. (2003), Relative Motion History of the Pacific-Nazca (Farallon) Plates since 30 Million Years Ago, 102 pp, Master's Thesis, Department of Marine Science, University of South Florida.

Wilson, D. S., and R. N. Hey (1995), History of Rift Propagation and Magnetization Intensity for the Cocos-Nazca Spreading Center, *Journal of Geophysical Research-Solid Earth*, *100*(B6), 10041-10056.

Wilson, D. S. (1996), Fastest known spreading on the Miocene Cocos-Pacific plate boundary, *Geophysical Research Letters*, *23*(21), 3003-3006.